ANALYTICAL MODELING OF REINFORCED CONCRETE COLUMNS WITH LAP SPLICES

by

Sharmin Reza Chowdhury

B.S., Civil Engineering, Bangladesh University of Engineering and Technology, 1996

M.S., Civil Engineering, Bangladesh University of Engineering and Technology, 2000

Submitted to the Institute for Graduate Studies in
Science and Engineering in partial fulfillment of
the requirements for the degree of
Doctor of Philosophy

Graduate Program in Civil Engineering
Boğaziçi University

2011

ANALYTICAL MODELING OF REINFORCED CONCRETE COLUMNS WITH LAP SPLICES

APPROVED BY:

Assist. Prof. Kutay Orakçal ……..

(Thesis Supervisor)

Prof. Uğur Ersoy …….....

Prof. Alper İlki ……

Prof. Cengiz Karakoç ……

Assoc. Prof. Orhun Köksal ……

DATE OF APPROVAL: 06.06.2011

ACKNOWLEDGEMENTS

I would like to express my sincere gratitude and appreciation to my thesis supervisor Assistant Professor Dr. Kutay Orakçal for his invaluable constant guidance, generous help, invaluable innovative suggestions, continued encouragement, remarkable patience and unfailing enthusiasm throughout the process of completion of this thesis.

I would like to thank to the members of the thesis committee, Professor Dr. Uğur Ersoy, Professor Dr. Cengiz Karakoç, Professor Dr. Alper İlki and Associate Professor Dr. Orhun Köksal for their precious suggestions.

The author also would like to acknowledge Professor Dr. Erol Güler, Prof. Dr. Turan Özturan, Chairman, Department of Civil Engineering, and Associate Professor Dr. Emre Otay for arranging financial support throughout my PhD study.

I would also like to special thank Dr. Murat Melek for providing test data that he obtained during his PhD at University of California, Los Angeles (UCLA).

Thanks also to my friends Yavuz Tokmak, Musa Rahmanlar, Tahir Erdem Öztürk, Ufuk Şahin, Emin Çiftçi, Ernur Akiner, Yusuf Eşidir, Arshiya Abadkon for their support and friendly behavior during my study in Turkey. This research has been financially supported by Boğaziçi University Foundation Fahir İlkel Fellowsip for International Ph.D. Students, and by Boğaziçi University Research Fund, under Project No. 08A403 (859). The author acknowledges the co-operation and support of all the teachers and staff of Department of Civil Engineering to complete the thesis to this stage.

I am indebted to my parents for the endless support, encouragement and love they have given me throughout my life. I cannot forget the support of my dear wife, whose patience and encouragement throughout this study have meant so much to me. Lastly, my son, Rajit of 4 years old, whose innocent, restless attitude always stimulates and refreshes me for the accomplishment of my study.

ABSTRACT

ANALYTICAL MODELING OF REINFORCED CONCRETE COLUMNS WITH LAP SPLICES

A possible source of seismic failure in existing reinforced concrete structures is loss of anchorage in column reinforcement, along deficient lap splices with short lap length and inadequate transverse reinforcement conditions. Reliable modeling of the bond slip behavior and anchorage failures in such columns is important for performance assessment of existing buildings using nonlinear static and dynamic analysis methods.

In this study, a novel analytical modeling approach is proposed, for simulating the lateral load – deformation response of reinforced concrete columns with deficient lap splices. The modeling approach involves implementing bond stress vs. slip springs in the formulation of a fiber-based macro model. Through this methodology, local bond-slip behavior associated with both pullout failure of reinforcing bars and formation of splitting cracks in concrete can be characterized. The proposed model directly considers the influence of bond slip deformations on the lateral load – displacement response of a column under reversed cyclic lateral loading, and successfully represents the distribution of bond stresses and slip deformations, due to either splitting or pullout anchorage failures, along the lap splice region. The model successfully represents the distribution of local bond slip deformations along the length of a reinforced concrete column, as opposed to conventional methods where bond slip deformations are assumed to be localized at prescribed locations. The flexible formulation of the model allows investigating the influence of using smooth reinforcing bars, presence of 180-degreee hooks, the strain penetration effects on the response of a column.

Response predictions of the analytical model were validated against results of cyclic tests on lap-splice-deficient column specimens, and the model was found to consistently represent the experimental behavior, both at global and local response levels, with a reasonable level of accuracy. Additional correlation studies conducted between

model predictions and test results in the literature further verified that the model can effectively reflect the global response characteristics and failure modes of various column configurations incorporating either deficient lap splices or anchorage-deficient continuous reinforcement. Overall, the modeling approach proposed in this study is believed to be a significant improvement, towards realistic consideration of bond slip deformations and anchorage failures on the seismic response and performance of reinforced concrete structures.

ÖZET

EKSİK BİNDİRME BOYLU BETONARME KOLONLARIN ANALİTİK MODELLENMESİ

Mevcut betonarme binaların deprem performansını kötü yönde etkileyen önemli özelliklerden biri kolon donatısındaki bindirmeli ek bölgelerinde eksik bindirme boyu ve yetersiz enine donatı kullanımı nedeniyle oluşan sıyrılma davranışıdır. Bindirme boyu yetersiz kolonlardaki aderans kaybı ve sıyrılma davranışının güvenilir bir şekilde modellenmesi, mevcut betonarme binaların statik ve dinamik hesap yöntemleriyle analizi ve performans değerlendirmesi için açısından önem taşımaktadır.

Bu çalışmada yetersiz bindirme boyuna sahip betonarme kolonların deprem etkileri altında yanal yük – şekildeğiştirme davranışını öngören bir analitik modelleme yöntemi sunulmuştur. Sunulan model, makro-lifli bir betonarme kolon modelinin formülasyonuna aderans gerilmelerinin sıyrılma deformasyonları ile değişimini temsil eden yayların eklenmesinden oluşmaktadır. Önerilen modelleme yöntemi ile bindirmeli ek bölgesinde oluşan sıyrılma deformasyonlarının kolonun tersinir tekrarlanır yükler altında yük–şekildeğiştirme davranışına etkisi etkin bir şekilde temsil edilebilmekte; çekip çıkma ya da yarılma mekanizmaları nedeniyle oluşacak sıyrılma deformasyonlarının ve aderans gerilmelerinin bindirme bölgesi boyunca dağılımı öngörülebilmektedir. Modelin esnek formülasyonu, düz yüzeyli donatının kullanımının, 180-derece kanca davranışının, ve ankraj bölgesindeki sıyrılma deformasyonlarının kolon davranışına etkilerini göz önünde bulundurmaya olanak sağlamaktadır.

Analiz sonuçları yetersiz bindirme boyuna sahip ve nervürlü donatı içeren kolon numuneleri üzerinde yapılan deney sonuçlarıyla detaylı bir şekilde karşılaştırılmış; analitik modelin deneysel sonuçları hem yük – öteleme davranışı hem de yerel şekildeğiştirmelerin dağılımı bakımından doğru ve tutarlı bir şekilde temsil ettiği gözlemlenmiştir. Analitik model sonuçları ayrıca literatürde sunulan farklı konfigürasyon ve ankraj özelliklerine sahip çok sayıda kolon numunesi üzerinde yapılmış olan deneylerin sonuçları ile

karşılaştırılmış; modelin deneylerde gözlemlenen yatay yük davranışı ve kırılma türlerini tutarlı bir şekilde yansıttığı gösterilmiştir. Önerilen analitik modelleme yönteminin, donatıda sıyrılma etkilerinin betonarme yapıların deprem davranışına etkisinin daha iyi irdelenebilmesi için önemli olduğu düşünülmektedir.

TABLE OF CONTENTS

LIST OF FIGURES

LIST OF TABLES

LIST OF SYMBOLS

A_c	Concrete area
A_g	Gross concrete cross sectional area
A_{cc}	Concrete confined core area
A_s	Longitudinal steel area
A_{st}	Longitudinal steel area
A_{sx}, A_{sy}	Transverse steel area in x and y directions
B	Tension stiffening parameter for reinforcing steel
b	Steel strain hardening ratio
b_c	Width of concrete core measured to center of stirrups
c	Relative location of center of rotation for the model element
d	Effective depth of the Column
d_b	Diameter of reinforcing bar
d_c	Height of concrete core measured to center of stirrups
d_s	Distance of a starter bar to the centroid
d_l	Distance of a longitudinal bar to the centroid
E_c	Elastic modulus for concrete
E_I	Concrete tangent modulus at initial point
E_F	Concrete tangent modulus at target point
E_{new}	New concrete tangent modulus upon return to unloading point on monotonic envelope
E_p	Plastic (strain hardening) modulus for bare steel bars
E_p^*	Plastic (strain hardening) modulus for steel bars embedded in concrete
E_{pl}	Concrete plastic modulus upon unloading from monotonic envelope
E_{re}	Concrete tangent modulus at point of return to monotonic envelope

E_s	Elastic modulus for steel
E_{sec}	Concrete secant modulus upon unloading from monotonic envelope
E_{SEC}	Concrete secant modulus between initial and target points and
E_t	Concrete tangent modulus
E_0	Elastic modulus for steel
E_1	Strain hardening modulus for steel
F	Force
F_{int}	Internal resisting force
F_{ext}	External (applied) force
f_b	Axial force in bond slip spring
f_c	Uniaxial concrete stress
f'_c	Peak concrete compressive stress (concrete compressive strength)
f_{cr}	Concrete tensile cracking stress
f_H	Force in horizontal spring
f_i	Force in *i-t*h uniaxial concrete element
f_I	Concrete stress at initial point
f_F	Concrete strain at target point
f_{new}	New concrete stress upon return to unloading point on monotonic envelope
f_{re}	Concrete stress at point of return to monotonic envelope
f_{st}	Axial force in uniaxial steel element
f_t	Peak concrete tensile stress (concrete tensile strength)
f'_t	Peak concrete tensile stress (concrete tensile strength)
f_u	Bar ultimate stress
f_{un}	Concrete stress at unloading point from monotonic envelope
h	Height of a multiple-vertical-line-element
K	Confinement coefficient for concrete

K_{tr}	Transverse Reinforcement Index
k_b	Stiffness of the uniaxial bond slip spring
k_e	Confinement effectiveness coefficient for concrete
k_H	Stiffness of horizontal shear spring
k_i	Stiffness of *i-th* uniaxial element
k_{st}	Stiffness of the uniaxial steel element
m	Number of MVLE model elements
n	Number of uniaxial elements
r	Parameter defining shape of monotonic stress-strain curve for concrete
r	Radious of the steel bar
R	Cyclic curvature coefficient for steel
R	Equation parameter for connecting and transition curves
R	Residual force
R_0, a_1, a_2	Steel parameters defining degradation of cyclic curvature
s'	Clear spacing of stirrups or hoops
S	Center to center spacing of stirrups or hoops
s	Slip
s_h	Center to center spacing of stirrups or hoops
$s_{\max}$	Maximum slip deformation
s_u	Hook end slip
u_H	Deformation in horizontal spring
u	Bond stress
V_c	Concrete Shear-Strength
V_n	Nominal Shear-Strength
V_s	Steel Shear-Strength
V_u	Ultimate Shear
w'	Clear spacing between laterally supported longitudinal reinforcing bars
x^+	Nondimensional strain on concrete tension envelope
x^-	Nondimensional strain on concrete compression envelope

x_{cr}^{+}	Nondimensional critical strain on concrete tension envelope
x_{cr}^{-}	Nondimensional critical strain on concrete compression envelope
x_{crk}	Nondimensional concrete cracking strain
x_i	Horizontal distance of *i-th* uniaxial element to central axis of model element
x_{sp}	Nondimensional concrete spalling strain
δ	Displacement at nodal degree of freedom
δ_n	Key nodal displacement to be incremented
Δ	Displacement
Δ_{top}	Column top flexural displacement
Δf	Reloading stress offset for concrete
$\Delta\varepsilon$	Reloading strain offset for concrete
ε	Longitudinal strain
$\varepsilon_a, \varepsilon_b$	Concrete strain at unloading or target point on a connecting curve
ε_c	Concrete strain
ε_c'	Monotonic strain at peak concrete compressive stress
ε_i	Strain in *i-th* uniaxial element
ε_I	Concrete strain at initial point
ε_{cr}	Concrete strain where monotonic stress-strain relation starts following a straight line
ε_{cr}	Concrete cracking strain
ε_{c0}	Concrete strain at which the cyclic tension envelope originates
ε_F	Concrete strain at target point
ε_m	Concrete strain at unloading point from monotonic compression envelope
$\varepsilon_{\max}$	Absolute maximum strain in steel at strain reversal
ε_n	Strain at intersection of the elastic and plastic lines for steel bars embedded in concrete

ε_{pl}	Concrete plastic strain upon unloading from monotonic envelope
ε_r	Steel strain at reversal point
ε_{re}	Concrete strain at point of return to monotonic envelope
ε_t	Monotonic strain at peak concrete tensile stress
ε_{un}	Concrete strain at unloading point from monotonic envelope
ε_y	Steel yield strain
ε_0	Steel strain at intersection of elastic and yield asymptotes
ε_0	Strain at peak concrete compressive stress
ε_0	Concrete strain at which the cyclic tension envelope originates
ξ	Absolute steel strain difference between current asymptote intersection point and strain at previous reversal point
ψ	Unbalanced (residual) force
ζ_c	Iteration tolerance
λ	Scalar load parameter
ρ	Cross-sectional area ratio of longitudinal steel
ρ_s	Volume ratio of transverse steel
ρ_x, ρ_y	Area ratio of transverse steel in *x* and *y* directions
σ	Uniaxial stress
σ_b	Uniaxial bond stress
σ_c	Uniaxial concrete stress
$(\sigma_c)_i$	Uniaxial concrete stress in *i-th* uniaxial element
σ_n^*	Stress at intersection of the elastic and plastic lines for steel bars embedded in concrete
σ_s	Uniaxial steel stress
σ_r	Steel stress at reversal point
σ_y	Steel yield stress
σ_0	Steel stress at intersection of elastic and yield asymptotes

ϕ	Section curvature
Φ	Column rotation
τ	Bond stress
τ_b	Bond stress
$\tau_{b,\max}$	Maximum bond stress

1. INTRODUCTION

1.1. General

One source of severe seismic damage in poorly-detailed reinforced concrete buildings is the loss of anchorage between reinforcing bars and concrete along short and poorly-confined lap splices in columns, which are located typically above floor levels where large inelastic demands are expected. Typical lap splice lengths of 20 to 30 longitudinal bar diameters, which are commonly encountered in many existing and poorly-detailed reinforced concrete buildings worldwide, have been shown to be inadequate in transferring the tensile stresses in longitudinal reinforcement along the lap splice region of a column. For example, lap splices in reinforced concrete columns in older buildings in the United States, or within the non-participating frames in some newer buildings, were typically designed as compression lap splices. Compression lap splice lengths are typically short (20 to 24 bar diameters), and only moderate transverse reinforcement is provided over the lap length. Under earthquake actions, the columns typically develop significant bending moments, subjecting the longitudinal reinforcement within the splice region to relatively large tensile stresses, particularly if the splice is located just above the floor slab, which is common in older construction. Given that required lap lengths (typically 20 or 24 longitudinal bar diameters) for tension substantially exceed those for compression, bond slip failures along the splice region may occur at load levels less than that required to reach the nominal moment capacity of the column, resulting in loss in column strength, stiffness, and ductility. The load-deformation responses of columns representative of those found in older buildings are not well understood; and in particular, the degradation of strength and stiffness of a column due to splice failure and the ability of the column to undergo inelastic deformation while maintaining axial load capacity, are of interest. The effects of bond deterioration and slip deformations in longitudinal reinforcing bars on the overall response of reinforced concrete columns with inadequate lap-splice lengths must be taken into account in order to develop reliable analytical modeling approaches for such lap-splice-deficient columns, particularly for improvement of nonlinear analysis methods used for seismic performance assessment of existing buildings.

Past experimental observations studies on individual reinforcing bars anchored in concrete have identified two main types of bond failure mechanisms between concrete and reinforcing steel, depending mainly on the amount of concrete confinement provided around the reinforcing steel bar. If the cover concrete is adequate and the concrete is well confined by transverse reinforcement, bond failure typically occurs by pullout. On the other hand, if the cover is inadequate and the concrete is unconfined or poorly confined, bond failure occurs by splitting of the concrete surrounding the bar. A significant number of experimental and analytical studies have been conducted on the anchorage and bond slip characteristics isolated bars embeded in concrete. Several constitutive bond stress vs. slip relationships have been proposed to simulate both pullout and splitting modes of bond failures for individual bars.

However, the current state-of-the-art modeling approach for simulating bond slip behavior in reinforced concrete columns with deficient lap splices consists only of incorporating simple zero-length moment vs. slip rotation springs at the splice regions of column members, which are intended to represent deformations associated with bond slip at critical locations where inadequate anchorage conditions are provided. The moment vs. rotation behavior of the bond slip spring is calibrated via combining results of one-dimensional analysis on isolated reinforcing bars embedded in concrete, which characterizes the bar pull-out force (P) vs. slip deformation behavior of the individual bar, with results of moment–curvature analyses that relate the forces in the reinforcing bars (P) to the moments applied on the member cross-section at a critical location. In general, only monotonic bar pullout vs. slip and moment vs. curvature analyses are employed, in order to generate a moment vs. rotation envelope for the bond slip spring, and the cyclic behavior of the bond slip spring is represented via predefined and somewhat ad-hoc unloading and reloading rules (e.g., Cho and Pincheira, 2004).

This modeling approach, although simple in formulation, introduces certain inconsistencies in the analysis. First, using predefined loading and unloading rules for the rotational bond slip spring introduces incompatibility between flexural and bond slip deformations in a RC member during unloading and reloading, and impairs the reliability of the model in predicting the energy dissipation capacity of the member under reversed cyclic loading. Second, using results of monotonic moment–curvature analyses creates a

conceptual error in calibration of the moment vs. rotation envelope of the bond slip spring. Pronounced bond slip behavior often results in strength-degrading responses associated with the post-peak (degrading) region of the bar pullout force vs. slip response of the individual reinforcing bars, which results in degradation of the lateral load vs. displacement (or the moment vs. rotation) of the member. Therefore, a monotonic moment–curvature analysis should be employed only up to the point (moment) that corresponds to the load where significant slip occurs for an individual reinforcing bar. Subsequently, realistic unloading in the moment–curvature response should be considered, even when the moment vs. rotation envelope of the bond slip spring is being calibrated for monotonic loading. Furthermore, this modeling approach requires multiple steps in the analysis, and bond slip deformations are assumed to be concentrated at pre-defined critical locations on the member, which needs to be specified in the model.

1.2. Scope

Given these shortcomings, the scope of this research study is to develop a more robust and refined modeling approach to simulate the bond-slip responses observed in reinforced concrete columns under reversed cyclic loading. The proposed modeling methodology involves modifying the formulation of a fiber-based flexural model (i.e., the Multiple Vertical Line Element Model), with the fibers representing the hysteretic flexural behavior of concrete only. Reinforcing bar elements, with uniaxial hysteretic stress–strain relationships of their own, are connected to the concrete fibers through uniaxial bond slip springs, the behavior of which are represented with experimentally-derived hysteretic bond stress vs. slip constitutive relationships available in the literature (Eligehausen *et al*., 1983, for pullout, Harajli *et al*., 2009 for splitting, Verderame *et al*., 2009 for smooth reinforcing bars, and Fabbrocino *et al*., 2004 for 180-degree hooks). Through this methodology, local bond slip behavior is incorporated at the fiber level, and full coupling (compatibility) of flexural and bond slip deformations of the model is retained under reversed cyclic loading conditions. The model proposed does not require intermediate steps in the analysis, and successfully represents the distribution of local bond slip deformations along the height of a reinforced concrete member, as opposed to conventional methods where bond slip deformations are assumed to be localized at prescribed locations.

The proposed analytical modelling approach captures many important response characteristics associated with the cyclic behaviour reinforced concrete columns with short lap splices, where failure or degradation in the load-deformation response is initiated by bond slip between longitudinal steel bars and the surrounding concrete in the lap splice region. Several bond stress vs. slip constitutive relationships are implemented in the model formulation, depending based on the type of reinforcing bar (deformed or plain) used, and the failure mode (pullout or splitting) expected. The model allows slip deformations to be distributed over the height of the column, instead of being localized in prescribed regions. Full coupling of flexural and bond slip deformations are enforced at all locations on the column, under generalized and reversed cyclic loading conditions. The model allows monitoring of local responses including longitudinal strains and stresses in concrete and reinforcing steel, as well as bond stresses and slip deformations at any location on the column. Local rotations, strain profiles, and neutral axis locations, and bond stress distributions along either longitudinal or starter splice bars can also be obtained using the analytical model proposed.

Upon development and implementation of the model formulation, detailed and comprehensive correlation studies were conducted between model results and experimental data, in order to identify the capabilities and weaknesses of the proposed model, as well as to provide a better understanding of nonlinear bond slip behaviour of reinforced concrete columns with deficient lap splices. Analytical and experimental response comparisons were made at both global and local response levels, for various column configurations with either deformed or plain reinforcing bars; with various lap splice lengths, cross sections, material properties and reinforcement conditions; subjected to different axial load levels and lateral loading patterns.

1.3. Research Significance

With current modeling approaches available in the literature, it is not possible to fully comprehend and analytically represent the coupled flexural and bond slip behaviour of reinforced concrete columns with short lap splices. The behavioural model proposed in this study is intended to capture many important response characteristics associated with the cyclic behavior of reinforced concrete columns with short lap splices, Detailed

response comparisons conducted between the model results and experimental data, at both global and local response levels, allows a better understanding of the coupled flexural and bond slip responses of lap-splice-deficient columns. The model presented can also be used as an effective tool in nonlinear analysis of structural systems, as part of performance-based evaluation methodologies for existing reinforced concrete buildings.

1.4. Objective

Specifically, the objectives of this study are:

(i) To develop a macroscopic analytical model, which accurately predicts the nonlinear inelastic response of reinforced concrete columns with short lap splices, at both global and local response levels,

(ii) To implement refined constitutive material and bond-slip relationships in the analytical model, and to adopt flexible nonlinear analysis solution strategies for conducting analyses for various column configurations,

(iii) To investigate the sensitivity of model results, at both global and local model response levels, to changes in model parameters,

(iv) To conduct detailed calibration studies on the analytical model and to perform comprehensive correlation studies, at various response levels and locations, between analytical model results and a detailed experimental program involving cyclic loading tests on densely-instrumented reinforced concrete column specimens.

(v) To conduct additional correlation studies between model results and experimental observations in the literature, in order to evaluate various response characteristics, including the influence of using plain bars, presence of hooks, and strain penetration effects on column response,

(vi) To reach conclusions on the effectiveness of the proposed model in predicting the cyclic response of reinforced concrete column with short lap splices and deficient anchorage conditions, and to arrive at recommendations upon further improvements of the model.

1.5. Thesis Outline

Nine chapters are included in this thesis. A general introduction, as well as the scope and objectives of the study are described in chapter one. Chapter two provides a review of the various constitutive bond stress vs. slip models available in literature, previous experimental and analytical studies on the bond slip behavior of reinforced concrete members, and the current state-of-the-art modeling approaches available. The description and numerical formulation of the proposed analytical model is presented in Chapter three. Chapter four describes the cyclic material constitutive relationships used for reinforcing steel and concrete, as well as the bond stress vs. slip constitutive relationships incorporated in the analytical model. Numerical solution strategies adopted to conduct nonlinear analyses using the analytical model are described in Chapter five. Chapter six provides an examination of the characteristic attributes of the analytical model results, and also investigates the sensitivity of the model results to selected model parameters. Chapter seven provides information on correlation of the analytical model results with results of an experimental program on densely instrumented column specimens with deformed reinforcing bars and deficient lap splices. A brief description of the experimental program, detailed information on calibration of the model, and comparisons of model results with the extensive experimental data at both global and local response levels are presented. Chapter eight further compares the analytical model results with additional experimental observations available in the literature on various column specimens with both deformed and plain reinforcing bars, with both deficient lap splices and continuous longitudinal reinforcement (where bond slip behavior in the anchorage zone is of interest). In Chapter nine, the analytical results are summarized, concluding remarks on the abilities and weaknesses of the model are presented, and recommendations on further improvement and application of the model are provided.

2. LITERATURE REVIEW

Past experimental studies on individual reinforcing bars embedded in concrete have identified two main types of bond failure mechanisms, depending on the amount of concrete surrounding the reinforcing bar, as well as the level of confinement. If the surrounding concrete is of significant thickness and the concrete is well confined by transverse reinforcement, bond failure typically occurs by pullout. On the other hand, if the concrete cover is small and the concrete is either unconfined or poorly confined, bond failure occurs by splitting of the surrounding concrete. Several bond stress vs. slip constitutive models to simulate both pullout (for deformed as well as smooth reinforcing bars) and splitting (only for deformed reinforcing bars) modes of bond failures are available in the literature, as described in the following section.

2.1. Constitutive Models for Bond Stress-Slip Relation

Eligehausen *et al*. (1983) first proposed a robust hysteretic constitutive model for the local bond stress vs. slip relationship for a single reinforcing deformed bar anchored within a reinforced concrete beam-column joint. The model was derived using experimental results from tests conducted on 125 specimens with short anchorage lengths, subjected to either monotonic tensile loading or reversed cyclic loading. Effects of loading history, confining reinforcement amount, bar diameter, concrete compressive strength, clear cover, bar spacing, and rate of pull-out on the local bond stress vs. slip relationship were all considered during development of the constitutive model. Cyclic degradation in both bond stress and stiffness was incorporated in the model formulation. The model was shown to agree reasonably well with experimental results, and is still widely used in bond slip modeling applications. Prior to the work by Eligehausen *et al*. (1983), although the bond slip behavior under reversed loading for rather small slip deformation values ($s < s_1$) could be predicted with sufficient accuracy, the influence of loading cycles for larger slip values ($s > s_1$) on the local bond stress vs. slip relationship was not well-defined.

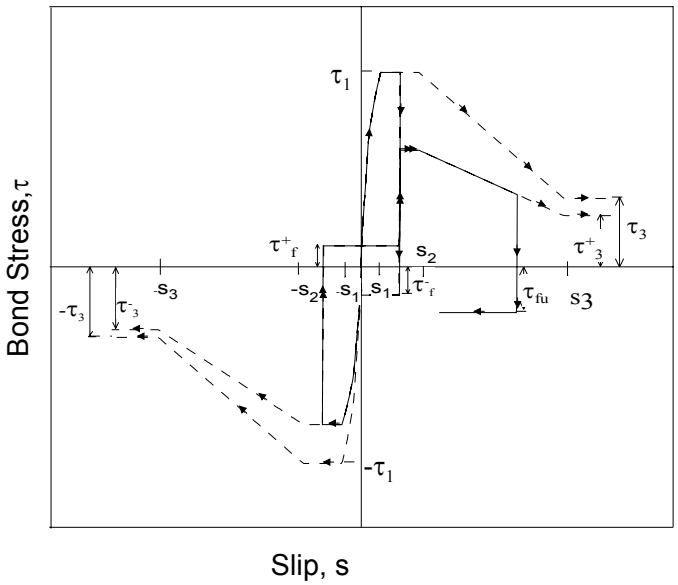

Figure 2.1. Constitutive Model for Local Bond Stress vs. Slip Relationship for Confined Concrete (Eligehausen et al., 1983).

The local bond stress vs. slip constitutive relationships proposed by Harajli *et al*. (1994, 2002, and 2004) apply to reinforcing bars embedded in plain and fiber-reinforced concrete under monotonic tension, and are applicable to both splitting and pull-out type bond failures (Harajli *et al*., 1994). These constitutive models were developed upon compiling a broad database of experimental data, including results of the tests conducted by Eligehausen *et al*. (1983) and Harajli *et al*. (1995). The original version of the model consisted of two monotonic backbone relationships, representing pull-out and splitting failures for unconfined and confined concrete, respectively. These backbone relationships were later improved (reference) to consider the influence of partial confinement on the bond stress vs. slip response of reinforcing bars experiencing splitting type of bond failure.

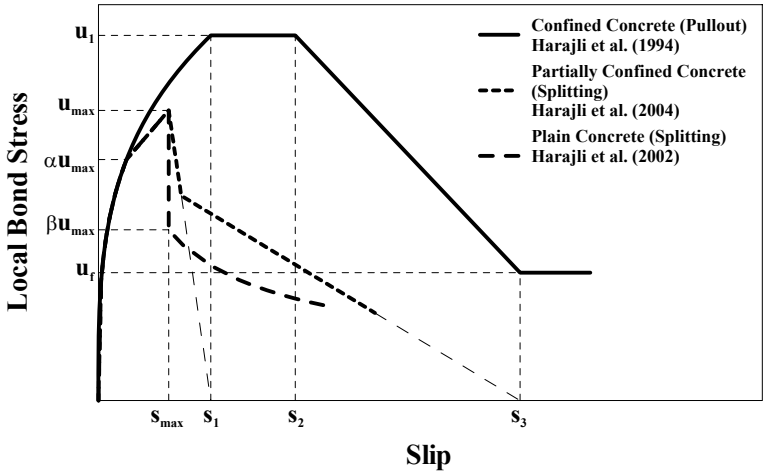

Figure 2.2. Monotonic Bond Stress vs. Slip Constitutive Model (Harajli *et al.*,1994, 2002, 2004).

Harajli (2009) first developed a robust hysteretic local bond stress-slip constitutive model to simulate splitting mode bond failure for deformed reinforcing bars, as shown in Figure 2.3. This cyclic constitutive model accounted for splitting of both unconfined and moderately-confined concrete, and incorporated the effect of several critical bond slip parameters, such as the diameter of reinforcing bars, the ratio of concrete cover to bar diameter, concrete compressive strength, the amount of confining reinforcement, and the type of confinement including steel ties, fiber-reinforced concrete (FRC), and reinforced concrete polymer jackets. Cyclic degradation in both bond stress and stiffness were also incorporated in this constitutive model.

As described above, existing information in the literature on the bond slip behavior of deformed reinforcing bars include extensive experimental data and various constitutive relationships, both monotonic and hysteretic, which account for the governing parameters influencing bond slip response. On the other hand, available information in the literature on the bond stress vs. slip relationship of plain (smooth) bars, which can be important for seismic performance assessment of existing reinforced concrete buildings in many countries, is very limited.

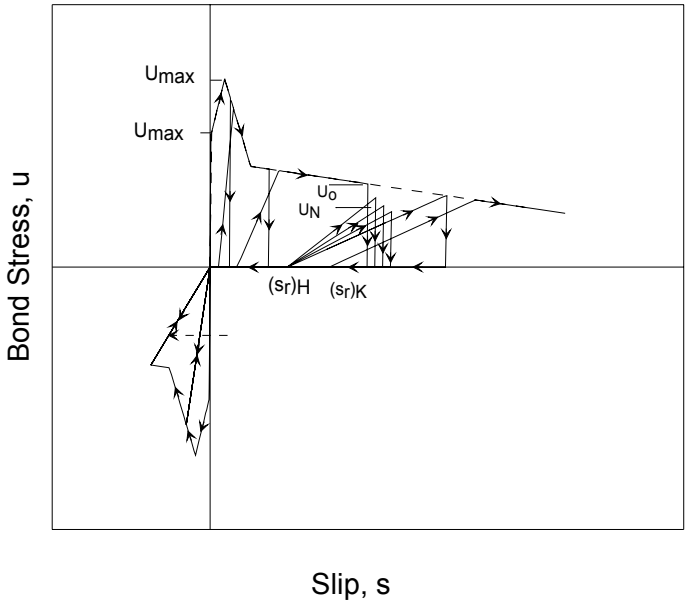

Figure 2.3. Hysteretic Bond Stress vs. Slip Constitutive Model for Splitting Failure (Harajli, 2009).

A robust hysteretic bond stress vs. slip constitutive model for plain reinforcing bars was only recently developed by Verderame *et al*. (2009 a,b), based on experimental results of monotonic and cyclic pull-out tests on plain bars embedded in concrete (Figure 2.4). The monotonic envelope of this constitutive model includes an initial ascending branch up to a peak bond stress capacity value, which corresponding to a very low magnitude of slip deformation. During this phase of the behavior, chemical–physical adhesion, mechanical micro-interlocking, and the friction between the bar surface and surrounding concrete contribute to development of bond stress capacity. Then, a softening branch, represents the progressive degradation of the friction mechanism with increasing slip deformation. Finally, a horizontal branch, at a constant magnitude of bond stress, represents minimum frictional component of bond resistance. Hysteretic rules of the constitutive model are based on experimentally-observed cyclic degradation of the frictional bond resistance component.

The constitutive bond stress vs. slip models adopted in this study for both deformed and plain reinforcing bars are described in detail in Chapter 4 of this thesis.

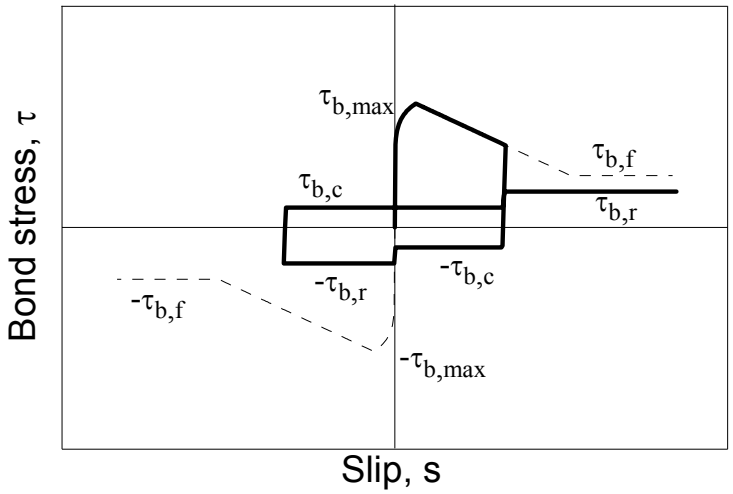

Figure 2.4. Hysteretic Bond-Slip Relationship for Plain Reinforcing Bar (Verderame *et al*., 2009 a,b).

2.2. Experimental Studies on the Bond Slip Behavior of Reinforced Concrete Columns

Experimental observations available in literature on the bond slip behavior of reinforced concrete columns can be categorized in three types; as columns with deformed reinforcing bars incorporating lap splices, columns with smooth reinforcing bars incorporating lap splices and hooks, and columns with continuous deformed reinforcing bars experiencing anchorage slip (strain penetration) effects. Examples of such experimental studies are presented in the following paragraphs. All of these experimental studies were used in experimental calibration and verification of the analytical model proposed in this study, as described in Chapters 7 and 8 of this thesis.

Melek and Wallace (2004) conducted experiments of densely-instrumented full-scale column specimens constructued with deformed reinforcing bars, with various configurations, in order to better characterize the influence of bond slip deformation and slip failure on the lateral load response of lap-splice-deficient reinforced concrete columns. The primary variables in their test program included the level of axial compressive load, the ratio of maximum moment to maximum shear force (shear span), and the loading history. All column specimens had deformed reinforcing bars and a lap splice length equal to 20 bar diameters. The experimental results indicated the lateral strength of specimens

started degrading at lateral drift ratio of 1.0 to 1.5%, due to the deterioration of the bond between the reinforcement and the surrounding concrete. The data showed that higher axial load levels slightly increased the lateral load capacity of the specimens, and that changes in shear demand did not appear to influence the lateral load at which bond deterioration initiated.

Aboutaha (1994) and Aboutaha *et al*. (1996) conducted a series of tests on cantilever type column specimens, representing half the length of an actual column in a real building frame. All column specimens were 2.74 meter high from the top of footing to the point of load application, to ensure flexural-dominated behavior. Cyclic lateral loads were applied at the tip of the column specimens and all columns were loaded in the weak direction. Lateral loads were increased in 22 kN increments until significant inelastic displacement was observed. Lateral displacements were then increased in increments corresponding to 0.5% drift ratios. All columns were tested without axial load. The lap splice length of the specimens were 24 bar diameters. Generally, splice failure was associated with vertical splitting cracks along the full height of the splice. For some specimens, splice failure after yielding of the main longitudinal bars occurred.

Harajli and Dagher (2008) tested full-scale cantilever column specimens with lap-splices located at column. Systematically-varied concrete grades of C14, C16, and C20, and reinforcing bar diameters of 14 mm, 16 mm, and 20 mm were used in the construction of the test specimens. The specimens consisted of columns having a half height of 1.5 m and a 200 mm wide by 400 mm deep rectangular cross section, supported over a 1200 mm long, 500 mm wide, and 500 mm deep footing. The column longitudinal reinforcement was lap-spliced, with starter bars of the same diameter anchored within the footing using standard 90-degree hooks. The lap splice length for all column specimens was selected as 30db, where d_b is the diameter of the column reinforcement. The side cover c_s and bottom cover c_b of the spliced bars in the column section were chosen to produce a range of values of c/d_b that would induce splitting bond failure before steel yielding. The transverse reinforcement in these specimens consisted of φ8 mm diameter ties spaced at 200 mm throughout the height of the column with the first tie placed at 50 mm above the column-footing interface. As the main objective of this experimental study was to investigate the splitting bond strength of column splices and since the splitting bond strength of spliced

bars depends primarily on the tension stresses acting on the spliced bars, the specimens were tested under pure flexure, with no axial compression. Failure was characterized by significant vertical splitting cracks in the lap splice region. The splitting cracks started at the base of the column and propagated upward along the full splice length as the lateral drift increased. Splitting bond failure caused concrete spalling along the splice length and substantial slip of starter bars at the column-footing interface.

Elgawady *et al*. (2010) investigated the cyclic behavior of eight 4/10-scale reinforced concrete column specimens representing construction conditions in the state of Washington prior to 1971. All specimens were tested under constant axial load and incrementally increasing lateral loading cycles. Two modes of failure were observed for the column specimens, which are low-cycle fatigue failure of longitudinal reinforcement and slip failure of the lap splice. In the column specimens, longitudinal bars were lap spliced (over a length of 35 bar diameter), at the base of the column with the starter bars extending from the foundation. All specimens had an approximate longitudinal reinforcement ratio of 1.2%, provided with 12.5 mm diameter deformed rebars, and 6.3 mm diameter smooth mild steel ties at 125 mm spacing as transverse reinforcement. The specimens were subjected to reverse cyclic lateral loading with increasing levels of lateral displacements.

Lynn *et al*. (1996) conducted tests on eight full-scale column specimens representing construction details in the United States prior to the 1970s. The specimens were subjected to reversed cyclic lateral displacements, while the axial load was held constant for the duration of the test, at a level corresponding to approximately 12% of the axial load capacity of the columns. Observed failure modes included localized crushing of concrete, buckling of reinforcement, splitting bond failure at the lap splice, shear failure, and axial load collapse.

The full scale column specimen, ‘L0’, tested by of Harries *et al*. (2006), incorporated a 22 bar diameter lap splice length, and was tested under combined axial and cyclic lateral loads. The column specimen was initially designed so that the lap splice would cause bond slip failure prior to achieving the flexural capacity of the column. The column specimen had 458 mm square cross sections with eight 22 mm – diameter longitudinal reinforcing

bars. 9.5 mm – diameter ties with 356 mm spacing were located over a height of 1780 mm from the base of the column. These ties incorporated deficient 90-degree hooks. The axial load level applied during testing was approximately 25% of the column axial load capacity, and was maintained constant throughout the cyclic lateral load history, using a regulated system of hydraulic rams. The reversed cyclic lateral loads were applied to the column specimen at a height of 2440 mm, which was selected to ensure a sufficiently high moment-to-shear ratio to result in flexure-dominated column behavior. The columns were tested as cantilevers with the lateral loads applied at the top, approximately representing the half the height of an actual column in a building frame, for which the point of inflection is located at the midheight. Failure was characterized by significant vertical splitting cracks in the lap splice region.

Yildiz (2006) conducted an experimental program on reinforced concrete columns with deficient detailing and low material quality, representing older non-ductile buildings in Turkey. Two of her specimens (Specimens AF(COG0)B1 and AF(COG0)B2) incorporated deficient lap splices, with splice lengths equal to 15 bar diameters, and were subjected to constant axial and reversed cyclic lateral loads. All test specimens were designed such that shear failure would be avoided. However, all specimens possessed inadequate confinement and low concrete quality.

Verderame *et al*. (2008) conducted experiments on reinforced concrete column specimens incorporating with smooth reinforcing bars. Two types of specimens were considered, depending on the longitudinal reinforcement details at column base. Type A specimens had lap-spliced and hooked bars with 40 bar diameter long splice length, whereas continuous longitudinal bars were provided for Type B specimens. Two different levels of axial load (12% and 24% of axial load capacity) were applied to represent the behavior of columns in a prototype building. For the specimen types investigated in detail in the present study, the specimens were 2000 mm high, with a 300 mm by 300 mm square cross-section. Longitudinal reinforcement consisted of six 12 mm – diameter smooth bars, while 8 mm – diameter ties were spaced at 100 mm spaced. Cyclic lateral loads were applied at a height of 1570 mm from the top of the specimen foundation A maximum cyclic drift of ±100 mm was applied, and the specimens were cycled three times at 15 target drift levels. Moderate decay of strength due to progressive spalling of concrete cover

and strong pinching effect exhibited for Type A column specimen. Loss of strength due to spalling of concrete cover and buckling of reinforcing bars exhibited for Type B specimen.

Yilmaz (2009) investigated the effect of deficient lap splices with plain bars 180-degree hooks, as well as the influence of low concrete compressive strength on the lateral load behavior of reinforced concrete columns in typical poorly-constructed buildings in turkey. In his experimental study, the column specimens incorporated 14 mm – diameter (φ) smooth longitudinal bars, 10 mm – diameter poorly detailed and wide-spaced ties, and an average concrete compressive strength of approximately 10 MPa. In construction of four specimens, different lap splice lengths (25φ, 35φ, 44φ, 55φ) were used, and one specimen incorporated continuous longitudinal reinforcement. The column specimens were tested under zero axial load and reversed-cyclic lateral loading.

To investigate the influence of bond slip deformations in anchorage zones (i.e., strain penetration effects) on the cyclic lateral load behavior of reinforced concrete columns, Low and Moehle (1987) tested a series of reinforced concrete cantilever column specimens with rectangular cross sections and continuous longitudinal reinforcement anchored into specimen foundations. For the column specimens tested, the anchorage length (within the foundation) of the longitudinal reinforcement corresponded to 23 bar diameters. The specimens were subjected to constant axial load and reversed cyclic lateral loading.

Bousias *et al*. (1995) also tested a column specimen with continuous deformed reinforcing bars to investigate the influence of strain penetration effects (anchorage slip) on column behavior. The column specimen was 1490 mm high, with a 250 mm by 250 mm cross section. An anchorage length (within the specimen foundation) corresponding to 30 bar diameters was used in the construction of the specimen. This column was also subjected to constant axial load and reversed cyclic lateral loading.

2.3. Analytical Studies on the Bond Slip Behavior of Reinforced Concrete Members

Various types of analytical models have been proposed for simulating the bond slip behavior in reinforced concrete structural members. A simple constitutive modeling approach is using the single bar model shown in Figure 2.5, for representing the bond slip

behavior of individual longitudinal bars in a member. The force-deformation response of a reinforcing bar embedded in concrete may be described by this one-dimensional model. In this model, the bar is divided into a finite number of short segments. Each bar segment is connected to a nonlinear spring that represents the local bond resistance on the surface of the bar segment. Knowing the stress-strain characteristics of the materials and assuming a bond stress-slip relationship for the bar embedded in concrete, the pullout force P and the slip deformation Δ_{slip} can be calculated.

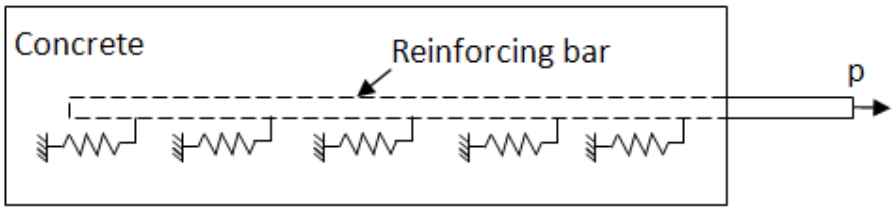

Figure 2.5. Uniaxial Model for an Isolated Bar.

Unlike the behavior of isolated bars, spliced bars interact with each other, following a complex force transfer mechanism. Experimental studies have shown, however, that the cracking, splitting, and bond slip behavior in a lap splice region is similar to that of individual embedded bars; and it is generally accepted that the load-carrying capacity of a spliced bar is almost the same as that of a single embedded bar.

Using the idea of an embedded bar model, Reyes (1999) and Reyes and Pincheira (1999) developed a nonlinear analysis procedure to estimate the lateral strength and displacement capacity of older reinforced concrete columns with short lap splices. Although their procedure provided a good estimate of the lateral strength and failure mode of a splice-deficient column, the lateral deformation capacity was underestimated and the post-peak response was not consistently well represented by their model.

Girard and Bastien (2002) proposed an analytical modeling approach to investigate the response of reinforced coulmns subjected to cyclic loads, which was incorporated in a general purpose finite-element program (CLEF) developed at Laval University. The three-dimensional finite-element model considered the concrete confinement effect, the

softening response of concrete, the strength loss due to bond deterioration, and the slip deformation of the reinforcing bar relative to the surrounding concrete. In their research, it was shown that the use of finite elements with additional degrees of freedom at each node to represent the relative slip between concrete and steel is a reliable method to model the response of structural members for which the progressive deterioration of the bond between steel and concrete influences the general behavior. Comparing with the experimental behavior, the stiffness of the numerical model was found greater due to the initial stiffness of the bond-slip constitutive law was considered constatant for programming simplicity. A bond stress-slip relationship with a reduced envelope , as suggested by Eligehausen *et al*. (1983) could be used to represent the behavior of the interface after some repeated cycles.

Limkatanyu and Spacone (2003) generated a fiber-based frame element model (Figure 2.6) where bond slip deformations are not assumed to be localized at prescribed locations on the member. They applied this model that explicitly accounts for the bond slip deformation of steel reinforcing bars to simulate the response of two experimentally tested reinforced concrete structural specimens, a beam–column joint and a two-story frame. Their frame element consisted of two components: a two-node beam element and a number of two-node rebar elements, which are allowed to undergo slip deformation with respect to beam. The nodal degrees of freedom of the beam and of the rebars were different to permit reinforcement slip. The main objective of this study was to analyze the importance of considering bond slip in evaluating the response of reinforced concrete frame structures subjected to cyclic loading. The study of the beam-column subassembly validated the model accuracy and showed how including the effects of bond slip leads to a spindle-shaped hysteretic loops, and to a better representation of the amount of hysteretic energy dissipation, since excluding the bond-slip effects overestimated the amount of hysteretic-energy dissipation. The bond slip effects were found not to affect the load carrying capacity of the assembly, since no slip failure was observed in either the experimental test or the analytical results. The stress and bond stress distributions on the reinforcing indicated that the bond stress demand within the joint was critical, and that bond slip inside the joint resulted in large fixed-end rotations at the beam-joint interfaces.

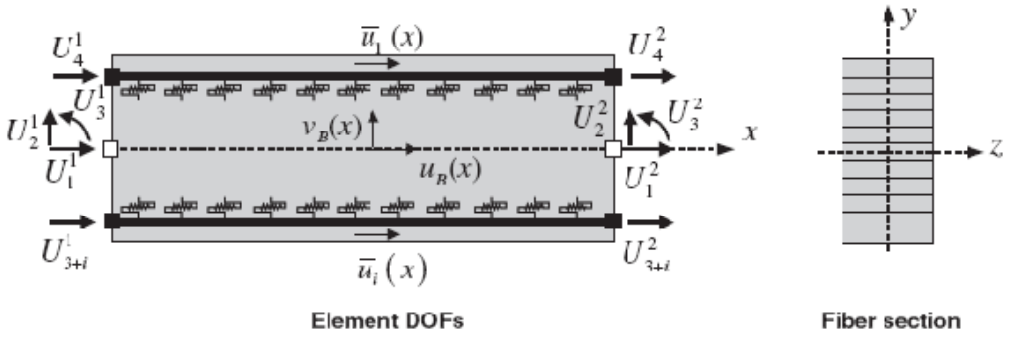

Figure 2.6. RC Frame Element with Bond-Slip: Degrees of Freedom, Fiber Section Discretization (Limkatanyu and Spacone, 2003).

To evaluate the results of these tests, the effect of bond stress vs. slip behavior of lap-spliced longitudinal bars on the overall monotonic column response was analytically modeled by Melek (2006), using a rotational bond slip spring at the column base. Monotonic bond stress vs. slip relationships were used to calibrate the moment vs. slip rotation spring. Investigation of moment vs. rotation responses of the specimens indicated that rotation caused by slippage of longitudinal bars accounted for a significant portion of the total rotation. After bond deterioration initiated, inelastic rotations were dominated by slip deformations. The calculated peak lateral load for the model agreed closely with the peak loads obtained in the tests. However, the monotonic moment versus slip rotation response underestimated the lateral drift (or rotation) at which lateral strength degradation initiates. It was stated that monotonic analyses of the column specimens underestimates lateral stiffness degradation with increasing lateral drift, probably because the monotonic bond stress vs. slip relationships used do not consider the damage caused by a cyclic displacement history.

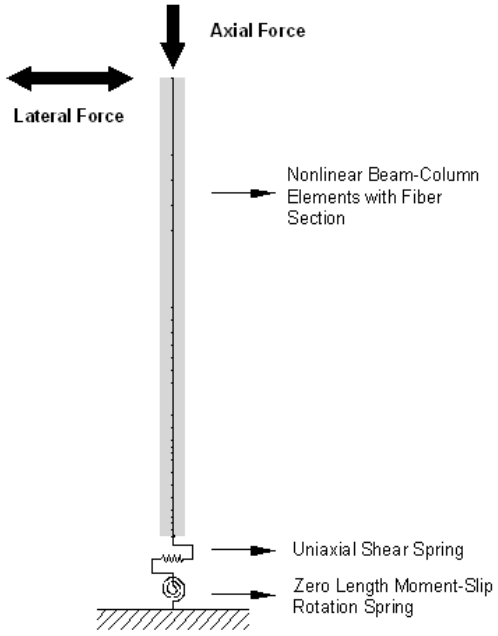

Figure 2.7. Column Model by Melek (2006).

Belmouden and Pierino (2006) proposed an analytical model (Figure 2.8) for simulating the nonlinear hysteretic behavior of reinforced concrete walls, which accounts for strength degradation, stiffness degradation, pinching, inelastic shear deformation, confinement, and bond slip effects. In this study, bond slip behavior was again represented using a rotational slip spring. To establish the validity of the proposed model, correlation studies were conducted between analysis and test results, to compare cyclic load–displacement hysteretic responses and hysteretic energy dissipation capacities. Although the analysis results were generally in good agreement with experimental results, the model was found to be incapable of accurately predicting local deformations on the wall associated with bond slip; indicating that a robust and mechanics-based macro-model which can accurately predict cyclic bond slip responses of columns at both local and global (system) levels was yet to be developed.

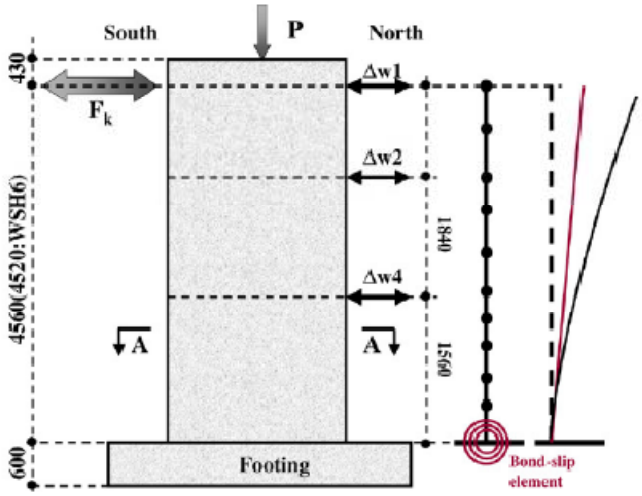

Figure 2.8. Dimensions (mm) and Analytical Model Developed for Reinforced Concrete Structural Walls (Belmouden and Pierino, 2006).

Ayoub (2006) presented a new inelastic element, which was derived from a two-field mixed formulation, where forced and deformations are approximated with independent interpolation functions for analysis of reinforced concrete beam-column elements with bond-slip-dominated responses. He presented an algorithm for implementation of the model in a general purpose nonlinear finite-element analysis program, to consider both slip deformation and pullout failure effects in the analysis. The bond stress-slip model used in his model was based on the work of Eligehausen *et al*. (2003). His model was evaluated by correlation studies with experimentally tested reinforced concrete columns. Although this numerical studies confirmed the accuracy of the model in representing the global behavior, pinching effect was not captured properly.

Cho and Pincheira (2006) recently developed an analytical modelling approach to predict the lateral load behavior of reinforced concrete columns with short lap splices. They considered three basic deformation modes and resistance mechanisms to describe the nonlinear response of a reinforced concrete column as shown in Figure 2.10. The modes of deformation included contributions from flexure, shear, and bond slip of reinforcement at the splice region. Their modeling approach used followed the principles of the lumped plasticity models, and is an extension of the two dimensional, single component model developed by Giberson (1969) modified to include shear response (Pincheira *et al*., 1999).

Figure 2.9 depicts the profile of a reinforced concrete column and its corresponding computer model. An element of length equal to the clear length of the column was used to model the contributions of flexure and shear. This member consisted of an elastic beam-column element with a nonlinear rotational spring at the base and a zero-length shear spring. The deformations due to bond slip in the lap splice region were simulated by a nonlinear rotational bond slip spring at the base of the model element. The moment vs. rotation behavior of the bond slip spring was calibrated via combining results of one-dimensional analysis on isolated reinforcing bars embedded in concrete, which characterizes the bar pull-out force (P) vs. slip deformation behavior of the individual bar, with results of moment–curvature analyses that relate the forces in the reinforcing bars (P) to the moments applied on the member cross-section at a critical location. The backbone relations and hysteretic laws of the rotational bond spring is illustrated in Figure 2.11. The backbone curve was suggested to be tri-linear, with ascending and descending branches.

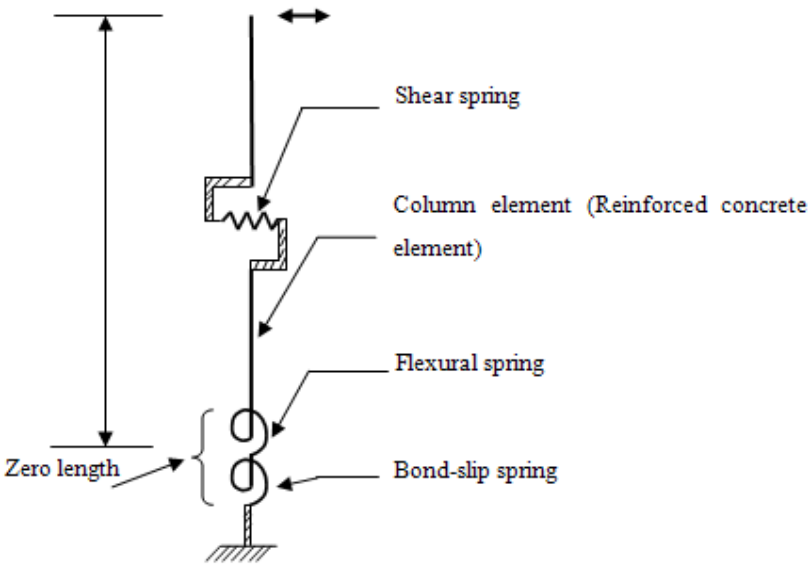

Figure 2.9. Beam-column Model with Bond-slip Spring.

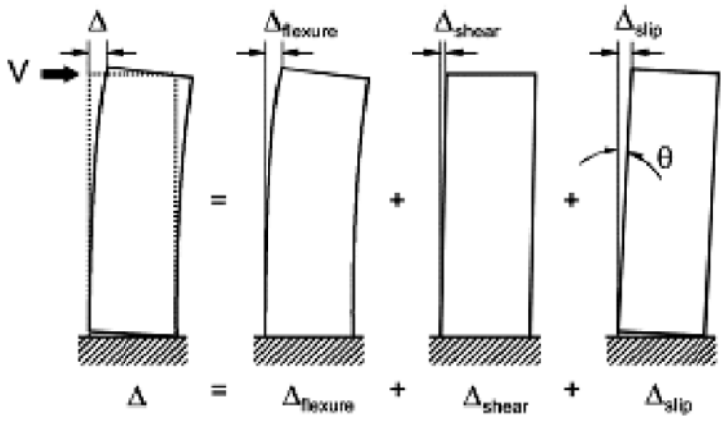

Figure 2.10. Modes of Deformation (Cho and Pincheira, 2006).

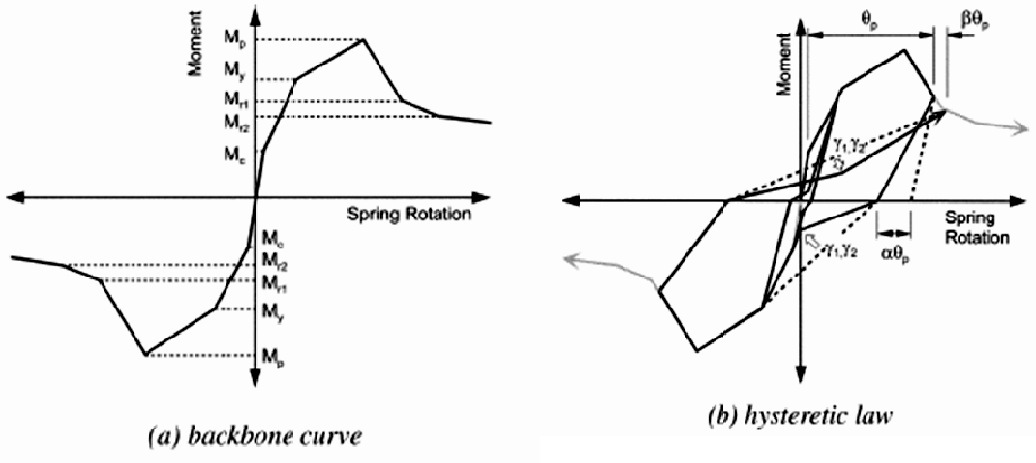

Figure 2.11. Moment vs. Slip Rotation (Cho and Pincheira, 2006).

Analytical results were calibrated with experimental data from cyclic loading tests on reinforced concrete columns with typical constructions details of the early 1970s. In order to develop cyclic response characteristics using monotonic pull-out force versus slip relationships, Cho and Pincheira (2006) suggested implementing hysteretic unloading and reloading rules to the moment versus slip rotation backbone curve (Figure 2.11). Parameters for lateral stiffness degradation with applied cyclic displacement history (β and α); and pinching (γ_1 and γ_2) were determined by doing sensitivity studies for matching of the analytical and experimental results. Investigation of moment vs. rotation responses of the specimens indicated that rotation caused by slippage of longitudinal bars accounted for

a significant portion of the total rotation. After bond deterioration initiated, inelastic rotations rotational were dominated by slip deformations. Although the general characteristics (global response) of the measured response under cyclic loading were represented well by the analytical model, due to the ad-hoc rules hysteretic laws for the flexural and rotational bond slip springs, the pattern of the post peak cycles was not represented accurately. Also, the model did not allow estimation of the distribution of local deformations in the splice region, since similarly to other conventional methods, inelastic flexural and bond slip deformations were assumed to be localized at a prescribed location on the member (at the base of column).

As described in this section, the current state-of-the-art macroscopic modeling approach for simulating bond slip behavior in slender reinforced concrete members involves incorporating zero-length moment vs. rotation springs at the boundaries of beam-column-elements which represent deformations associated with bond slip at critical locations on a member where inadequate anchorage is provided or slip deformations are expected to impact deformations. In general, only monotonic bar pullout vs. slip and moment vs. curvature analyses are employed, in order to generate a moment vs. rotation envelope for the bond slip spring, and the cyclic behavior of the bond slip spring is represented via predefined unloading and reloading rules with typically ad-hoc parameters.

On the other hand, although microscopic modeling approaches can provide a detailed description of the local response, their efficiency, practicality, and robustness are questionable due to complexities in calibrating the model and interpreting the results.

To obtain a more robust, yet practical response prediction, an analytical modeling approach based on a fiber formulation (a distributed plasticity model) has the potential to provide a mechanics-based and reliable, yet practical solution. Therefore, a fiber-based macroscopic modeling approach to simulate nonlinear flexural responses was used as a baseline model for the current study. Characteristics of the flexural macro-model used, which is referred to the Multiple Vertical Line Element Model (MVLEM), are described in the following paragraphs.

The Multi Vertical Line Element Model (MVLEM) was shown to capture important flexural response features (e.g., shifting of the neutral axis and the effect of a fluctuating axial force on strength and stiffness), which are commonly ignored in lumped plasticity (flexural hinge) models. It offers the flexibility to incorporate various material hysteretic models and important response features (for example, confinement and nonlinear shear behavior) in the analysis.

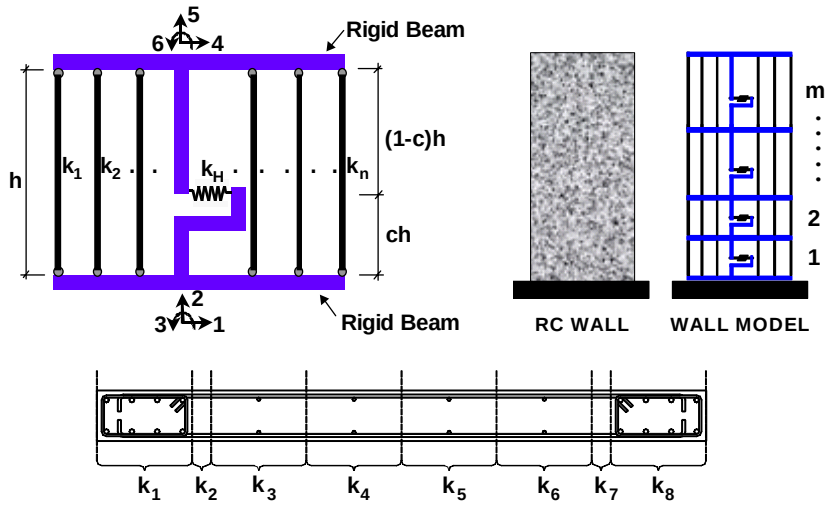

Figure 2.12. MVLE Model for RC Walls (Orakcal, 2004).

In the Multiple-Vertical-Line-Element (MVLE) Model (Figure 2.12), a structural wall is represented as a stack of MVLEs, placed on top of each other. The flexural response of each element is governed by a series of uniaxial elements (or macro-fibers) connected to infinitely rigid beams at the top and bottom levels (at floor levels for example). Therefore, the plane-sections-remain-plane assumption applies. The force-deformation relationships of the uniaxial elements are defined according to uniaxial stress-strain relationships implemented in the model for concrete and steel and the tributary area assigned to each uniaxial element. A horizontal spring simulates the shear response of the model element. The shear response of the model element is simulated by a horizontal spring at the center of rotation and shear deformations are concentrated in this spring. The flexural and shear deformations of the original model are uncoupled; and the shear spring follows a prescribed force-deformation relation, such as the Origin-Oriented-Hysteresis-Model with a trilinear force-deformation envelope (Figure 2.13). Therefore, the model is

incapable of simulating coupled shear-flexural responses in members experiencing significant nonlinear shear deformations. As well, the model formulation incorporates a perfect-bond assumption between concrete and reinforcing steel bars, and thus cannot predict bond-slip responses in members with deficient anchorage conditions.

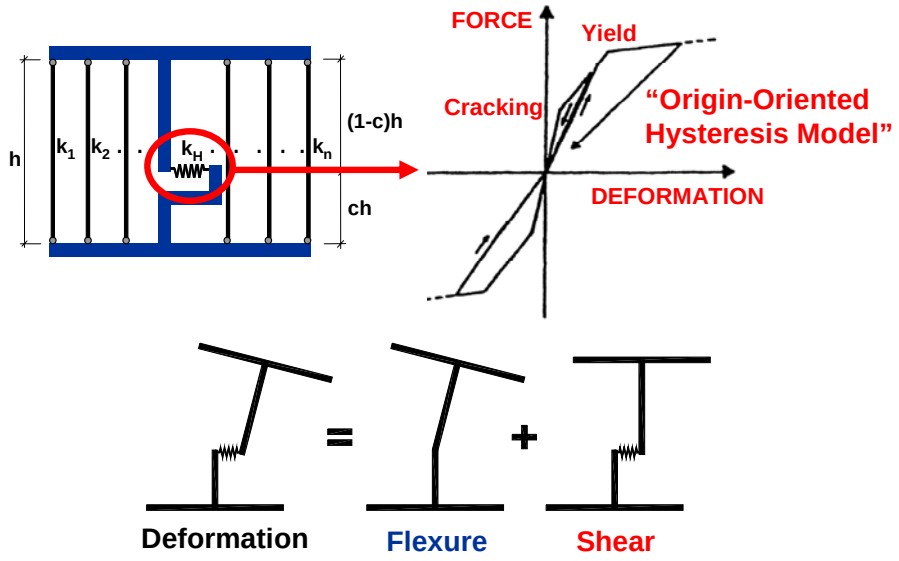

Figure 2.13. Model Shear Response.

Orakcal *et al*. (2004) verified that the improved multiple-vertical-line-element model captures important response characteristics associated with cyclic flexural response of reinforced concrete structural walls with continuous longitudinal reinforcement and adequate anchorage attributes. The scope of the study by Orakcal *et al*. (2004) was to implement state-of-the-art, reliable, robust material constitutive laws into the MVLEM and demonstrate the effectiveness of the MVLEM for modeling and simulating the inelastic response of reinforced concrete structural walls, via detailed correlation studies between model results and experimental (Orakcal and Wallace, 2006) data. Based on the analysis results, it was verified that the MVLEM captures important response characteristics associated with cyclic behavior of slender reinforced concrete structural walls governed by flexure. The analytical model was able to simulate important behavioral features including shifting of the neutral axis along the wall cross section and the effect of fluctuating axial force, which are commonly ignored in simple models. Characteristics of the cyclic

response, including stiffness degradation and strength deterioration, hysteretic shape, and pinching behavior were clearly captured in the analysis results. However, the model was found to underestimate the longitudinal compressive strains in concrete, since it did not consider coupling of nonlinear shear and flexural deformations, as is typically the case for all fiber-based analytical model formulations.

The proposed modeling methodology in this study involves modifying the formulation of the MVLEM, so that the macro-fibers represent the hysteretic axial-flexural behavior of concrete only. Reinforcing bar elements, with uniaxial hysteretic stress–strain relationships of their own, are connected to the concrete fibers through uniaxial bond slip springs, the behavior of which are represented with experimentally-derived hysteretic bond stress vs. slip constitutive relationships available in the literature. Through this methodology, local bond slip behavior is incorporated at the fiber level, and coupling (compatibility) of flexural and bond slip deformations of the model is satisfied under reversed cyclic loading conditions. The description and numerical formulation of the model is presented in the following Chapter.

3. DESCRIPTION OF ANALYTICAL MODEL

The analytical model proposed in this study is based on the formulation of a macroscopic fiber model for modeling the axial-flexural behavior of reinforced concrete members. The Multiple-Vertical-Line-Element Model (MVLEM), the accuracy of which was verified by Orakcal *et al*. (2006), has been used in this study as a baseline model to simulate the coupled axial, flexural and bond slip responses of reinforced concrete columns with lap splices. The analytical model shown in Figure 3.1 represents the modified MVLEM element proposed here, where the fibers (vertical elements) of the MVLEM model element represent the behavior of concrete alone. Uniaxial elements representing the reinforcing steel bars are connected to the rigid beams of the MVLEM element through uniaxial bond slip springs. The model element with 18 degrees of freedom is used over lap splice region of the column. The model element with 12 degrees of freedom, which is used outside the lap splice region, is depicted in Figure 3.2. The reinforced concrete column with the lap splice is modeled as a stack of m model elements, which are placed upon one another, as shown in Figure 3.3.

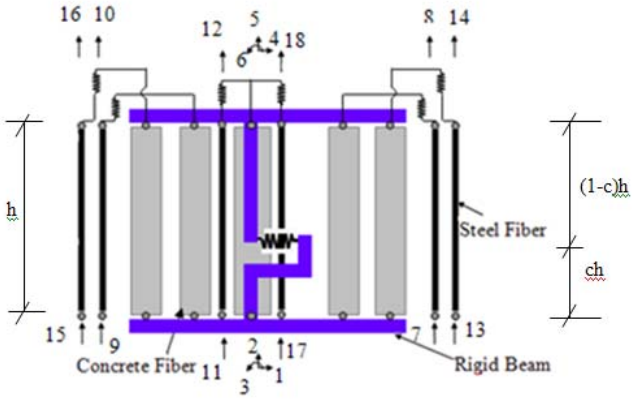

Figure 3.1. Model Element with 18 Degrees of Freedom Used in the Lap Splice Region.

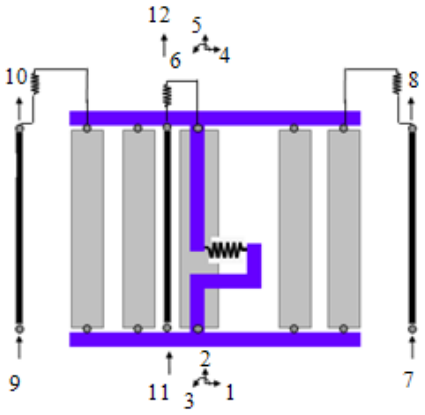

Figure 3.2. Model Element with 12 Degrees of Freedom Used Outside the Lap Splice Region.

The coupled axial, flexural and bond slip responses of the model are simulated by a series of uniaxial elements (or macro-fibers) for concrete, connected to rigid beams at the top and bottom levels of the model elements, which enforce plane sections assumption in the analysis. Steel macro-fibers are connected to the top rigid beams, through uniaxial bond slip springs, the behavior of which are represented via bond stress vs. slip constitutive relations. At the base of the column model, three additional bond slip springs are incorporated to connect the steel macro-fibers to concrete fibers at the bottom rigid beam level, as shown in Figure 3.3. The stiffness properties and force-deformation relationships of the uniaxial elements (concrete macro-fibers) of the element are defined according to cyclic constitutive model implemented for concrete as well as the tributary area assigned to each uniaxial element (Figure 3.4). A cyclic constitutive relationship for reinforcing steel is adopted for the uniaxial steel elements. Cyclic bond characteristics between concrete and steel are represented through constitutive bond stress vs. slip relationships, which are incorporated in the bond slip springs connecting the uniaxial steel elements to the rigid beams. The number of the uniaxial elements (n) can be increased to obtain a more refined description of the column cross-section.

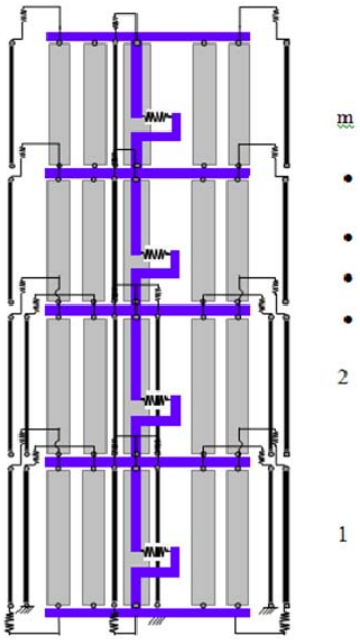

Figure 3.3. Sample Model Assembly.

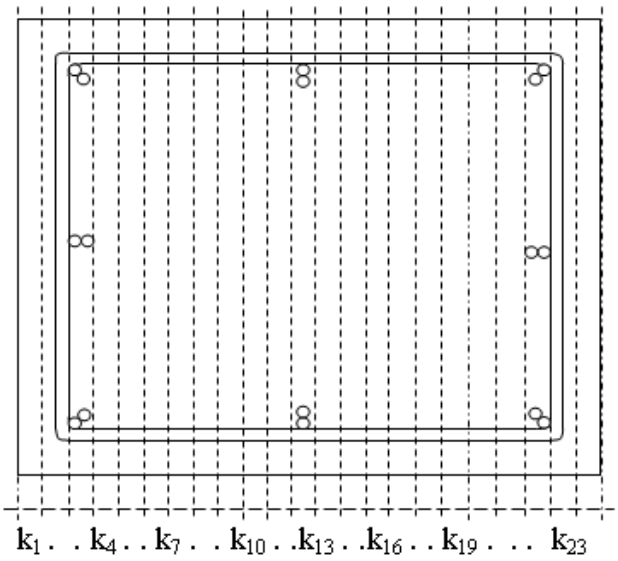

Figure 3.4. Tributary Concrete Area Assignment.

The relative rotation between top and bottom faces of the model element occurs around the point located on the central axis of the element at height *ch* (Figure 3.5), as proposed in the original MVLEM element formulation. Rotations and resulting transverse displacements are calculated based on the average curvature in concrete, derived from

section and material properties, corresponding to the bending moment at height *ch* of each element (Figure 3.5).

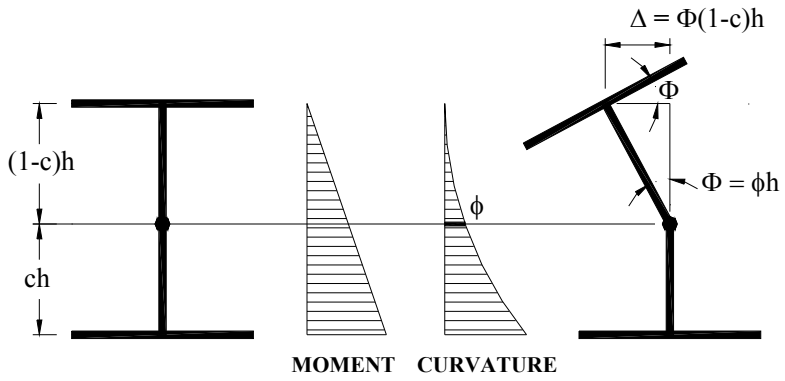

Figure 3.5. Rotations and Displacements of the MVLEM Element (Orakcal, 2004).

A suitable value of the parameter *c* is based on the expected curvature distribution along the element height *h*. A value of $c = 0.4$ recommended by Vulcano *et al*. (1988) based on comparison of the model response with experimental results, is also used in this study.

A horizontal spring located at the the relative height *ch*, with a nonlinear hysteretic force-deformation behavior following an origin-oriented hysteresis rule simulates the shear response of the column element (Figure 3.6). The trilinear shear force vs. shear displacement relation developed by Sezen (2002) defines the backbone of the hysteretic constitutive relationship for the shear spring. It must be mentioned that since the columns investigated in this study are not expected to be shear critical, a detailed constitutive modeling approach was not implemented to define the shear behavior of the horizontal (shear) spring. Improved predictions of column shear response require consideration of the interaction between shear and flexure responses, especially where highly inelastic flexural deformations take place. However, since this study concentrates on modeling of reinforced concrete columns, the behavior of which is dominated by either bond slip, flexure, or simultaneously slip and flexure responses, a simple origin-oriented shear force vs. deformation behavior with a trilinear backbone curve was adopted. For the proposed model formulation, bond slip and flexural mode of deformations are coupled, whereas flexural

and shear modes of deformation are uncoupled (i.e., flexural deformations do not affect shear strength or deformation) (Figure 3.7).

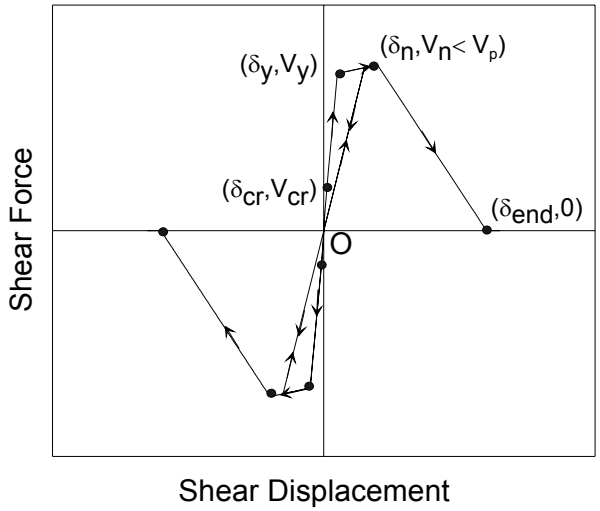

Figure 3.6. Origin-Oriented –Hysteresis Model for Horizontal Shear Spring.

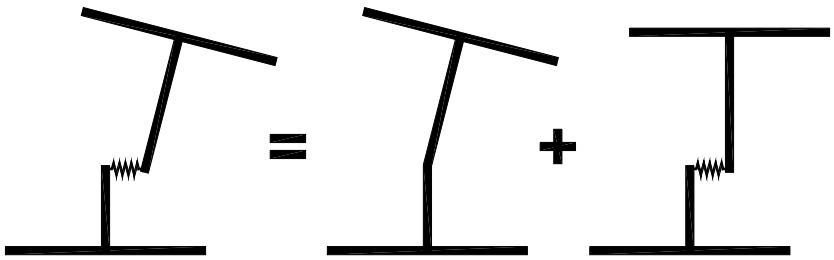

Figure 3.7. Uncoupling of Flexural and Shear Modes of Deformation of the Model Element.

A single model element used in the lap splice region has 18 global degrees of freedom (DOF); with three at the center of each rigid top and bottom beam (6 DOF total for concrete), and two at each end of the six longitudinal steel elements (12 DOF total for reinforcing steel), as shown in Figure 3.1. The average longitudinal strain value for each uniaxial (concrete and steel) element is obtained from the element displacements (translations and rotations) defined at the 18 global degrees of freedom. To relate the average strains in the concrete macro-fibers to the 6 global degrees of freedom for

concrete, the rigid beams enforce the plane-sections-remain-plane kinematic assumption. Accordingly, if $[\delta]$ is a vector that represents the displacement components at the 18 nodal degrees of freedom of each model element (Figure. 3.1):

$$[\delta] = \begin{bmatrix} \delta_1 \\ \delta_2 \\ \delta_3 \\ \delta_4 \\ \delta_5 \\ \delta_6 \\ \delta_7 \\ \delta_8 \\ \delta_9 \\ \delta_{10} \\ \delta_{11} \\ \delta_{12} \\ \delta_{13} \\ \delta_{14} \\ \delta_{15} \\ \delta_{16} \\ \delta_{17} \\ \delta_{18} \end{bmatrix} \tag{3.1}$$

Then, the resulting axial deformations of the uniaxial elements can be obtained as:

$$[u] = [a].[\delta] \tag{3.2}$$

where $[a]$ is a geometric transformation matrix and $[u]$ denotes the axial deformation of the uniaxial elements:

$$[u]=\begin{bmatrix} u_1 \\ u_2 \\ . \\ . \\ u_i \\ . \\ . \\ u_n \\ u_{b1} \\ u_{st1} \\ u_{b2} \\ u_{st2} \\ u_{b3} \\ u_{st3} \\ u_{b4} \\ u_{st4} \\ u_{b5} \\ u_{st5} \\ u_{b6} \\ u_{st6} \end{bmatrix} \tag{3.3}$$

In the formulation above, u_1.... u_n denote the axial deformations of the concrete macro-fibers ('n' denotes the number of concrete macro-fibers), u_{b1} and u_{b2} denote the axial deformations of the uniaxial bond slip springs connected to the exterior starter bars, u_{b3} and u_{b4} denote the axial deformations of the uniaxial bond slip springs connected to exterior longitudinal bars, and u_{b5} and u_{b6} denote the axial deformations of uniaxial bond slip springs connected to the middle starter and longitudinal bars, respectively. Similarly, u_{st1}, u_{st2}, u_{st3}, u_{st4}, u_{st5}, u_{st6} denote the axial deformations of the steel elements representing the exterior and middle starter and longitudinal bars. In a lap splice, a started bar is defined as the reinforcing steel bar extending from the foundation, and the longitudinal bar is the bar extending along the height of the column.

The geometric transformation matrix $[a]$ converts the displacement components at the nodal degrees of freedom to uniaxial element deformations as:

$$[a]=\begin{bmatrix}
0 & -1 & -x_1 & 0 & 1 & x_1 & 0 & 0 & 0 & 0 & 0 & 0 & 0 & 0 & 0 & 0 & 0 & 0 \\
0 & -1 & -x_2 & 0 & 1 & x_2 & 0 & 0 & 0 & 0 & 0 & 0 & 0 & 0 & 0 & 0 & 0 & 0 \\
. & . & . & . & . & . & . & . & . & . & . & . & . & . & . & . & . & . \\
0 & -1 & -x_i & 0 & 1 & x_i & 0 & 0 & 0 & 0 & 0 & 0 & 0 & 0 & 0 & 0 & 0 & 0 \\
. & . & . & . & . & . & . & . & . & . & . & . & . & . & . & . & . & . \\
0 & -1 & -x_n & 0 & 1 & -x_n & 0 & 0 & 0 & 0 & 0 & 0 & 0 & 0 & 0 & 0 & 0 & 0 \\
0 & 0 & 0 & 0 & 1 & d_s & 0 & -1 & 0 & 0 & 0 & 0 & 0 & 0 & 0 & 0 & 0 & 0 \\
0 & 0 & 0 & 0 & 0 & 0 & -1 & 1 & 0 & 0 & 0 & 0 & 0 & 0 & 0 & 0 & 0 & 0 \\
0 & 0 & 0 & 0 & 1 & -d_s & 0 & 0 & 0 & -1 & 0 & 0 & 0 & 0 & 0 & 0 & 0 & 0 \\
0 & 0 & 0 & 0 & 0 & 0 & 0 & 0 & -1 & 1 & 0 & 0 & 0 & 0 & 0 & 0 & 0 & 0 \\
0 & 0 & 0 & 0 & 1 & 0 & 0 & 0 & 0 & 0 & 0 & -1 & 0 & 0 & 0 & 0 & 0 & 0 \\
0 & 0 & 0 & 0 & 0 & 0 & 0 & 0 & 0 & 0 & -1 & 1 & 0 & 0 & 0 & 0 & 0 & 0 \\
0 & 0 & 0 & 0 & 1 & d_l & 0 & 0 & 0 & 0 & 0 & 0 & 0 & -1 & 0 & 0 & 0 & 0 \\
0 & 0 & 0 & 0 & 0 & 0 & 0 & 0 & 0 & 0 & 0 & 0 & -1 & 1 & 0 & 0 & 0 & 0 \\
0 & 0 & 0 & 0 & 1 & -d_l & 0 & 0 & 0 & 0 & 0 & 0 & 0 & 0 & 0 & -1 & 0 & 0 \\
0 & 0 & 0 & 0 & 0 & 0 & 0 & 0 & 0 & 0 & 0 & 0 & 0 & 0 & 0 & -1 & 1 & 0 \\
0 & 0 & 0 & 0 & 1 & 0 & 0 & 0 & 0 & 0 & 0 & 0 & 0 & 0 & 0 & 0 & 0 & -1 \\
0 & 0 & 0 & 0 & 0 & 0 & 0 & 0 & 0 & 0 & 0 & 0 & 0 & 0 & 0 & 0 & -1 & 1
\end{bmatrix} \tag{3.4}$$

where x_i is the distance of the i-th concrete element to the cross-sectional geometric centroid of the model element, d_l is the distance of a longitudinal bar to the centroid of the model element , d_s is the distance of a starter bar to the centroid.

The average uniaxial strain in each concrete macro-fiber and steel element (ε_i) can then be calculated by simply dividing their respective axial deformation by the element height, *h*:

$$\varepsilon_i = \frac{u_i}{h} \tag{3.5}$$

The slip deformation in each bond slip spring is defined directly as the axial deformation of the spring. The average strains in the concrete macro-fibers and steel elements are therefore not necessarily bound by the plane-sections-remain-plane kinematic assumption, and the assumption applies for the concrete macro-fibers only. Slip deformations between concrete and the steel depend on the constitutive bond stress vs. slip properties of the bond slip springs.

The deformation in the horizontal shear spring (u_H) of each model element can be similarly related to the displacement components $[\delta]$ at the 18 element degrees of freedom as:

$$u_H = [b]^T [\delta] \tag{3.6}$$

where the geometric transformation vector $[b]$ is defined as:

$$[b] = \begin{bmatrix} 1 \\ 0 \\ -ch \\ -1 \\ 0 \\ -(1-c)h \\ 0 \\ 0 \\ 0 \\ 0 \\ 0 \\ 0 \\ 0 \\ 0 \\ 0 \\ 0 \\ 0 \\ 0 \end{bmatrix} \tag{3.7}$$

The stiffness properties and force-deformation relationships of the uniaxial elements are defined according to the uniaxial constitutive relationships adopted for concrete and steel, as well as the tributary area assigned to each concrete macro-fiber and the cross-sectional area of the longitudinal steel bars. For the bond slip springs, the stiffness and force-deformation properties depend on the constitutive bond stress vs. slip relationships implemented, as well as the surface area of the longitudinal bar over which bond stresses act.

For a prescribed strain level (ε_i) at the *i*-th uniaxial element (macro-fiber) for concrete, the axial stiffness of the *i*-th uniaxial concrete element (k_{ic}) is defined as:

$$k_{ic} = \frac{(E_c)_i (A_c)_i}{h} \tag{3.8}$$

where $(E_c)_i$ is the concrete tangent modulus (strain derivative of the adopted constitutive stress-strain relationships for concrete) at the prescribed strain level (ε_i); $(A_c)_i$ is the tributary concrete area assigned to the uniaxial element, and *h* is the model element height.

For a uniaxial steel element, the axial stiffness (k_{st}) is defined similarly as:

$$k_{st} = \frac{(E_s)(A_s)}{h} \tag{3.9}$$

where (E_s) is the steel tangent modulus (strain derivative of the adopted constitutive stress-strain relationships for reinforcing steel) at the prescribed strain level, and (A_s) is the cross-sectional area of the longitudinal steel bar represented by the uniaxial element.

For a bond slip spring, the axial stiffness (k_b) is calculated as:

$$k_b = (E_{bond}) h (2\pi r) \tag{3.10}$$

where (E_{bond}) is the bond stress tangent modulus (slip derivative of the adopted constitutive bond stress vs. slip relationship) at a prescribed slip deformation, *r* is the radius of the longitudinal steel bar connected to the bond slip spring, and h is the model element height.

The stiffness of the horizontal shear spring (k_H) and the force in the horizontal spring (f_H) for a prescribed shear deformation (u_H) are derived from the origin-oriented force-deformation relationship (with a trilinear backbone) implemented in the model for the shear spring.

Therefore, if k_H is the stiffness of the horizontal shear spring, k_i is the stiffness of the i-th uniaxial concrete element (macro-fiber), x_i is the distance of the i-th concrete element to the cross-sectional geometric centroid of the model element, d_l is the distance of a longitudinal bar to the centroid of the model element , d_s is the distance of a starter bar to the centroid , n is the number of uniaxial concrete elements, k_{b1} and k_{b2} are the stiffnesses of the uniaxial bond slip springs connected to the two exterior starter bars, k_{b3} is the stiffness of the bond slip spring connected to middle starter bar, k_{b4} and k_{b5} are the stiffnesses of the bond slip springs connected to two exterior longitudinal bars, k_{b6} is the stiffness of the bond slip spring connected to middle longitudinal bar, k_{st1} and k_{st2} are the stiffnesses of the uniaxial steel elements for the two exterior starter bars, k_{st3} is the stiffness of the steel element for the middle starter bar, k_{st4} and k_{st5} are the stiffnesses of the steel elements for the two exterior longitudinal bars, k_{st6} is the stiffness of the steel element for the middle longitudinal bar; the stiffness matrix of the first (bottom) model element relative to the eighteen degrees of freedom is defined by Equation (3.11). Stiffness matrix of the other model elements used over the lap splice region relative to eighteen degrees of freedom is defined by Equation (3.12). The stiffness matrix of the model elements used outside the lap splice region relative to the twelve degrees of freedom is defined by Equation (3.13).

$$
[K_e]=\begin{bmatrix}
k_H c^2+B+A & 0 & -k_H c^2 h-(B/2)h & -k_H c^2-B-A & 0 & -(B/2)h-Ah & 0 & 0 & 0 & 0 & 0 & 0 & 0 & 0 & 0 & 0 & 0 & 0 \\
 & k_{b_7}+k_{b_8}+k_{b_9}+D & k_{b_7}d_l-k_{b_8}d_l+E & 0 & -D & -E & 0 & 0 & 0 & 0 & 0 & 0 & -k_{b_7} & 0 & -k_{b_8} & 0 & -k_{b_9} & 0 \\
 & & k_H c^2 h^2+k_{b_7}d_l^2+k_{b_8}d_l^2+F & k_H c^2 h+(B/2)h & -E & (B/2)h^2-F & 0 & 0 & 0 & 0 & 0 & 0 & -k_{b_7}d_l & 0 & -k_{b_8}d_l & 0 & 0 & 0 \\
 & & & k_H c^2+B+A & 0 & (B/2)h+Ah & 0 & 0 & 0 & 0 & 0 & 0 & 0 & 0 & 0 & 0 & 0 & 0 \\
 & & & & K_b+D & K_b d+E & 0 & -k_{b_1} & 0 & -k_{b_2} & 0 & -k_{b_3} & 0 & -k_{b_4} & 0 & -k_{b_5} & 0 & -k_{b_6} \\
 & & & & & K_b d^2+Ah^2+F & 0 & -k_{b_1}d_s & 0 & k_{b_2}d_s & 0 & 0 & 0 & -k_{b_4}d_l & 0 & k_{b_5}d_l & 0 & 0 \\
 & & & & & & k_{st_1} & -k_{st_1} & 0 & 0 & 0 & 0 & 0 & 0 & 0 & 0 & 0 & 0 \\
 & & & & & & & k_{st_1}+k_{b_1} & 0 & 0 & 0 & 0 & 0 & 0 & 0 & 0 & 0 & 0 \\
 & & & & & & & & k_{st_2} & -k_{st_2} & 0 & 0 & 0 & 0 & 0 & 0 & 0 & 0 \\
 & & & & & & & & & k_{st_2}+k_{b_2} & 0 & 0 & 0 & 0 & 0 & 0 & 0 & 0 \\
 & & & & & & & & & & k_{st_3} & -k_{st_3} & 0 & 0 & 0 & 0 & 0 & 0 \\
 & & & & & & & & & & & k_{st_3}+k_{b_3} & 0 & 0 & 0 & 0 & 0 & 0 \\
 & & & & & & & & & & & & k_{st_4}+k_{b_7} & -k_{st_4} & 0 & 0 & 0 & 0 \\
 & & & & & & & & & & & & & k_{st_4}+k_{b_4} & 0 & 0 & 0 & 0 \\
 & & & & & & & & & & & & & & k_{st_5}+k_{b_8} & -k_{st_5} & 0 & 0 \\
 & & & & & & & & & & & & & & & k_{st_5}+k_{b_5} & 0 & 0 \\
 & & & & & & & & & & & & & & & & k_{st_6}+k_{b_9} & -k_{st_6} \\
 & & & & & & & & & & & & & & & & & k_{st_6}+k_{b_6}
\end{bmatrix}
$$

Symmetry

$$
\begin{aligned}
&k_H(1-c)^2=A;\\
&2k_H c(1-c)=B;\\
&\sum_{i=1}^{n} k_i = D;\\
&\sum_{i=1}^{n} k_i x_i = E;\\
&\sum_{i=1}^{n} k_i x_i^2 = F;\\
&k_{b_1}+k_{b_2}+k_{b_3}+k_{b_4}+k_{b_5}+k_{b_6}=K_b;\\
&k_{b_1}d_s-k_{b_2}d_s+k_{b_4}d_l-k_{b_5}d_l=K_b d;\\
&k_{b_1}d_s^2+k_{b_2}d_s^2+k_{b_4}d_l^2+k_{b_5}d_l^2=K_b d^2;
\end{aligned}
$$

(3.11)

$$
[k_e]=\begin{bmatrix}
k_H c^2+B+A & 0 & -k_H c^2 h-(B/2)h & -k_H c^2-B-A & 0 & -(B/2)h-Ah & 0 & 0 & 0 & 0 & 0 & 0 & 0 & 0 & 0 & 0 & 0 & 0 \\
 & D & E & 0 & -D & -E & 0 & 0 & 0 & 0 & 0 & 0 & 0 & 0 & 0 & 0 & 0 & 0 \\
 & & k_H c^2 h^2+F & k_H c^2 h+(B/2)h & -E & (B/2)h^2-F & 0 & 0 & 0 & 0 & 0 & 0 & 0 & 0 & 0 & 0 & 0 & 0 \\
 & & & k_H c^2+B+A & 0 & (B/2)h+Ah & 0 & 0 & 0 & 0 & 0 & 0 & 0 & 0 & 0 & 0 & 0 & 0 \\
 & & & & K_b+D & K_b d+E & 0 & -k_{b_1} & 0 & -k_{b_2} & 0 & -k_{b_3} & 0 & -k_{b_4} & 0 & -k_{b_5} & 0 & -k_{b_6} \\
 & & & & & K_b d^2+Ah^2+F & 0 & -k_{b_1} d_s & 0 & k_{b_2} d_s & 0 & 0 & 0 & -k_{b_4} d_l & 0 & k_{b_5} d_l & 0 & 0 \\
 & & & & & & k_{st_1} & -k_{st_1} & 0 & 0 & 0 & 0 & 0 & 0 & 0 & 0 & 0 & 0 \\
 & & & & & & & k_{st_1}+k_{b_1} & 0 & 0 & 0 & 0 & 0 & 0 & 0 & 0 & 0 & 0 \\
 & & & & & & & & k_{st_2} & -k_{st_2} & 0 & 0 & 0 & 0 & 0 & 0 & 0 & 0 \\
 & & & & & & & & & k_{st_2}+k_{b_2} & 0 & 0 & 0 & 0 & 0 & 0 & 0 & 0 \\
 & & & & & & & & & & k_{st_3} & -k_{st_3} & 0 & 0 & 0 & 0 & 0 & 0 \\
 & & & & & & & & & & & k_{st_3}+k_{b_3} & 0 & 0 & 0 & 0 & 0 & 0 \\
 & & & & & & & & & & & & k_{st_4} & -k_{st_4} & 0 & 0 & 0 & 0 \\
 & & & & & & & & & & & & & k_{st_4}+k_{b_4} & 0 & 0 & 0 & 0 \\
 & & & & & & & & & & & & & & k_{st_5} & -k_{st_5} & 0 & 0 \\
 & & & & & & & & & & & & & & & k_{st_5}+k_{b_5} & 0 & 0 \\
 & & & & & & & & & & & & & & & & k_{st_6} & -k_{st_6} \\
 & & & & & & & & & & & & & & & & & k_{st_6}+k_{b_6}
\end{bmatrix}
$$

Symmetry

$$
\begin{aligned}
&k_H(1-c)^2 = A;\\
&2k_H c(1-c) = B;\\
&\sum_{i=1}^{n} k_i = D;\\
&\sum_{i=1}^{n} k_i x_i = E;\\
&\sum_{i=1}^{n} k_i x_i^2 = F;\\
&k_{b_1}+k_{b_2}+k_{b_3}+k_{b_4}+k_{b_5}+k_{b_6} = K_b;\\
&k_{b_1} d_s - k_{b_2} d_s + k_{b_4} d_l - k_{b_5} d_l = K_b d;\\
&k_{b_1} d_s^2 + k_{b_2} d_s^2 + k_{b_4} d_l^2 + k_{b_5} d_l^2 = K_b d^2;
\end{aligned}
\tag{3.12}
$$

$$
[K_e]=\begin{bmatrix}
k_H c^2+B+A & 0 & -k_H c^2 h-(B/2)h & -k_H c^2-B-A & 0 & -(B/2)h-Ah & 0 & 0 & 0 & 0 & 0 & 0 \\
 & D & E & 0 & -D & -E & 0 & 0 & 0 & 0 & 0 & 0 \\
 & & k_H c^2 h^2+F & k_H c^2 h+(B/2)h & -E & (B/2)h^2-F & 0 & 0 & 0 & 0 & 0 & 0 \\
 & & & k_H c^2+B+A & 0 & (B/2)h+Ah & 0 & 0 & 0 & 0 & 0 & 0 \\
 & & & & k_{b_1}+k_{b_2}+k_{b_3}+D & k_{b_1}d_l-k_{b_2}d_l+E & 0 & -k_{b_1} & 0 & -k_{b_2} & 0 & -k_{b_3} \\
 & & & & & k_{b_1}d_l^2+k_{b_2}d_l^2+Ah^2+F & 0 & -k_{b_1}d_l & 0 & -k_{b_2}d_l & 0 & 0 \\
 & & & & & & k_{st_1} & -k_{st_1} & 0 & 0 & 0 & 0 \\
 & & & & & & & k_{st_1}+k_{b_1} & 0 & 0 & 0 & 0 \\
 & & & & & & & & k_{st_2} & -k_{st_2} & 0 & 0 \\
 & & & & & & & & & k_{st_2}+k_{b_2} & 0 & 0 \\
 & & & & & & & & & & k_{st_3} & -k_{st_3} \\
 & Symmetry & & & & & & & & & & k_{st_3}+k_{b_3}
\end{bmatrix}
$$

$$
\begin{aligned}
&k_H(1-c)^2=A;\\
&2k_H c(1-c)=B;\\
&\sum_{i=1}^{n} k_i = D;\\
&\sum_{i=1}^{n} k_i x_i = E;\\
&\sum_{i=1}^{n} k_i x_i^2 = F;
\end{aligned}
\qquad (3.13)
$$

The axial force in the *i*-th uniaxial concrete element (f_i) is defined as:

$$f_i = (\sigma_c)_i (A_c)_i \tag{3.14}$$

where $(\sigma_c)_i$ is the uniaxial stress for concrete obtained from the implemented constitutive relationships at the prescribed strain (ε_i).

For a uniaxial steel element axial force (f_{st}) is defined similarly as:

$$f_{st} = (\sigma_s)(A_s) \tag{3.15}$$

where (σ_s) is the uniaxial stress for steel obtained from the implemented constitutive relationships at the prescribed strain level.

For a bond slip spring, the axial force (f_b) is calculated as:

$$f_b = (\sigma_b)(2\pi rh) \tag{3.16}$$

where (σ_b) is the uniaxial bond stress from the adopted constitutive bond stress vs. slip relationship at a prescribed slip deformation, *r* is the radius of the longitudinal steel bar connected to the bond slip spring, and h is the model element height.

Furthermore, if f_H is the force in the horizontal spring, f_i is the force in the i-th uniaxial concrete element, f_{b1} and f_{b2} are the forces in the uniaxial bond slip springs connected to two exterior starter bars, f_{b3} is the force in the bond slip spring connected to middle starter bar, f_{b4} and f_{b5} are the forces in the bond slip springs connected to two exterior longitudinal bars, f_{b6} is the force in the bond slip spring connected to middle longitudinal bar, f_{st1} and f_{st2} are the forces in the uniaxial steel elements for the two exterior starter bars, f_{st3} is the force in the steel element for the middle starter bar, f_{st4} and f_{st5} are the forces in the steel elements for the two exterior longitudinal bars, f_{st6} is the force in the steel element for the middle longitudinal bar, the resisting (internal) force vector for the

first (bottom) model element relative to the eighteen element degrees of freedom is obtained from model element force equilibrium as:

$$[F]=\begin{bmatrix} f_H \\ -\sum_{i=1}^{n} f_i - f_{b_7} - f_{b_8} - f_{b_9} \\ -f_H c h - \sum_{i=1}^{n} f_i x_i - f_{b_7} d_l + f_{b_8} d_l \\ -f_H \\ \sum_{i=1}^{n} f_i + f_{b_1} + f_{b_2} + f_{b_3} + f_{b_4} + f_{b_5} + f_{b_6} \\ -f_H (1-c) h + \sum_{i=1}^{n} f_i x_i + f_{b_1} d_s - f_{b_2} d_s + f_{b_4} d_l - f_{b_5} d_l \\ -f_{st_1} \\ f_{st_1} - f_{b_1} \\ -f_{st_2} \\ f_{st_2} - f_{b_2} \\ -f_{st_3} \\ f_{st_3} - f_{b_3} \\ -f_{st_4} + f_{b_7} \\ f_{st_4} - f_{b_4} \\ -f_{st_5} + f_{b_8} \\ f_{st_5} - f_{b_5} \\ -f_{st_6} + f_{b_9} \\ f_{st_6} - f_{b_6} \end{bmatrix} \tag{3.17}$$

and the resisting force vector for the other model elements used over the lap splice region relative to eighteen degrees of freedom is obtained as:

$$[F]=\begin{bmatrix} f_H \\ -\sum_{i=1}^{n} f_i \\ -f_H c h-\sum_{i=1}^{n} f_i x_i \\ -f_H \\ \sum_{i=1}^{n} f_i+f_{b_1}+f_{b_2}+f_{b_3}+f_{b_4}+f_{b_5}+f_{b_6} \\ -f_H(1-c)h+\sum_{i=1}^{n} f_i x_i+f_{b_1}d_s-f_{b_2}d_s+f_{b_4}d_l-f_{b_5}d_l \\ -f_{st_1} \\ f_{st_1}-f_{b_1} \\ -f_{st_2} \\ f_{st_2}-f_{b_2} \\ -f_{st_3} \\ f_{st_3}-f_{b_3} \\ -f_{st_4}+f_{b_7} \\ f_{st_4}-f_{b_4} \\ -f_{st_5}+f_{b_8} \\ f_{st_5}-f_{b_5} \\ -f_{st_6}+f_{b_9} \\ f_{st_6}-f_{b_6} \end{bmatrix} \tag{3.18}$$

Finally, the resisting force vector for the model elements used outside the lap splice region relative to the twelve degrees of freedom is obtained similarly as:

$$\left[F\right]=\begin{bmatrix} f_H \\ -\sum_{i=1}^{n} f_i \\ -f_H c h-\sum_{i=1}^{n} f_i x_i \\ -f_H \\ \sum_{i=1}^{n} f_i + f_{b_1} + f_{b_2} + f_{b_3} \\ -f_H(1-c)h+\sum_{i=1}^{n} f_i x_i + f_{b_1} d_l - f_{b_2} d_l \\ -f_{st_1} \\ f_{st_1} - f_{b_1} \\ -f_{st_2} \\ f_{st_2} - f_{b_2} \\ -f_{st_3} \\ f_{st_3} - f_{b_3} \end{bmatrix} \tag{3.19}$$

The model formulation described in this Chapter is a robust and efficient approach to relate the coupled flexural and bond slip responses of a reinforced concrete column directly to uniaxial material behavior and uniaxial bond slip behavior, without incorporating any additional empirical assumptions. The primary simplification the model involves applying the plane-sections-remain-plane kinematic assumption to calculate the average longitudinal strains in concrete only (for each uniaxial concrete element). Connecting uniaxial steel elements to concrete elements via bond slip springs permits relative slip deformations between concrete and reinforcing steel, and allows successful coupling flexural and slip deformations of a column, at local response level and in a purely geometric manner. The only geometric parameters that may influence the analytical model response are the number of uniaxial elements used along the length of the column cross section (n), the number of MVLEM elements stacked on top of each other along the height of the column (m), and the parameter defining the location of the center of rotation along the height of each MVLEM element (c). The number of the uniaxial elements (n) and the MVLEM elements (m) can be increased to obtain a more refined description of the column geometry and a more accurate representation of the local response, especially where large inelastic deformations take place (e.g., in the lap splice region). Details of the constitutive relationships implemented in the model formulation for the concrete and reinforcing steel elements, as well as the bond slip springs, are presented in the next chapter.

4. MATERIAL CONSTITUTIVE MODELS

As described in Chapter 3, the analytical model proposed in this study is formulated such that the uniaxial elements (macro-fibers) of the original Multiple-Vertical-Line-Element Model (MVLEM) represent the hysteretic axial-flexural behavior of concrete only. Reinforcing bar elements, with uniaxial hysteretic stress–strain relationships of their own, are connected to the concrete fibers through uniaxial bond slip springs, the behavior of which are represented with experimentally-derived hysteretic bond stress vs. slip constitutive relationships available in the literature. Characteristics of the constitutive relationships implemented in the model for concrete, reinforcing steel, and the bond slip springs directly influence the analytical model response. Therefore, details of the uniaxial hysteretic constitutive relationships adopted in the analytical model for reinforcing steel and concrete, as well as the bond stress vs. slip relationships implemented for deformed bars, plain bars, and 180-degree hooks are described in the following sections.

4.1. Constitutive Model for Reinforcing Steel

The well-known nonlinear hysteretic constitutive model proposed by Menegotto and Pinto (1973) and extended by Filippou *et al*. (1983) is implemented for reinforcing steel, as shown in Figure 4.1. The constitutive model considers Bauschinger's effect and the influence of both kinematic and isotropic strain hardening on the hysteretic uniaxial stress – strain behavior of reinforcing steel bars.

The formulation of the hysteretic stress-strain $(\sigma - \varepsilon)$ relationship of Menegotto and Pinto (1973) can be expressed as:

$$\sigma^* = b\varepsilon^* + \frac{(1-b)\varepsilon^*}{\left(1+\varepsilon^{*R}\right)^{1/R}} \tag{4.1}$$

where

$$\xi^* = \frac{\varepsilon - \varepsilon_r}{\varepsilon_0 - \varepsilon_r} \tag{4.2}$$

and

$$\sigma^* = \frac{\sigma - \sigma_r}{\sigma_0 - \sigma_r} \tag{4.3}$$

Equation (4.1) represents a curved transition from an elastic asymptote with slope E_0 to a yield asymptote, with slope $E_1 = bE_0$ (Figure 4.1). Parameters σ_r and ε_r are stress and strain values at the strain reversal point. R is a cyclic parameter that influences the curvature of the transition curve between the two asymptotes (and thus permits the Bauschinger effect to be represented), Parameters σ_0 and ε_0 are the stress and strain values at the point of intersection of the two asymptotes. Parameter b is the strain hardening ratio. The strain and stress values $(\varepsilon_r, \sigma_r)$ and $(\varepsilon_0, \sigma_0)$ are updated after each strain reversal, as shown in Figure 4.1.

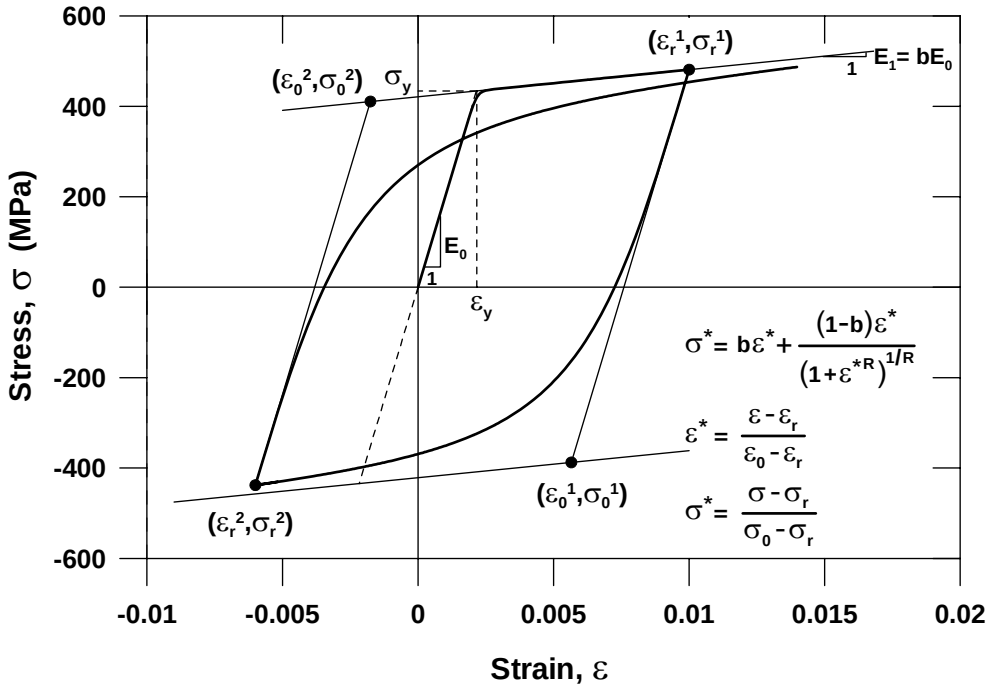

Figure 4.1. Constitutive Model for Steel (Menegotto and Pinto, 1973).

The tangent modulus (E_t) of the stress – strain relationship is given by the following expression:

$$E_t = \frac{d\sigma}{d\varepsilon} = \left(\frac{\sigma_0 - \sigma_r}{\varepsilon_0 - \varepsilon_r} \right) \frac{d\sigma^*}{d\varepsilon^*} \tag{4.4}$$

where

$$\frac{d\sigma^*}{d\varepsilon^*} = b + \left[\frac{1-b}{\left(1+\varepsilon^{*R}\right)^{1/R}} \right] \left[1 - \frac{\varepsilon^{*R}}{1+\varepsilon^{*R}} \right] \tag{4.5}$$

Menegotto and Pinto expressed the cyclic curvature parameter, R, as:

$$R = R_0 - \frac{a_1 \xi}{a_2 + \xi} \tag{4.6}$$

where R_0 is the value assigned to the parameter R for initial (or monotonic) loading, and a_1 and a_2 are experimentally determined parameters that represent the degradation of the curvature within subsequent cycles. The absolute strain difference represented by the parameter ξ (Figure 4.2) can be expressed as:

$$\xi = \left| \frac{\left(\varepsilon_m - \varepsilon_0\right)}{\varepsilon_y} \right| \tag{4.7}$$

where parameter ε_0 is the strain at the current intersection point of the two asymptotes, and ε_m is the maximum or minimum strain, at the previous point of strain reversal. Parameter ε_y is the strain at the monotonic yield point.

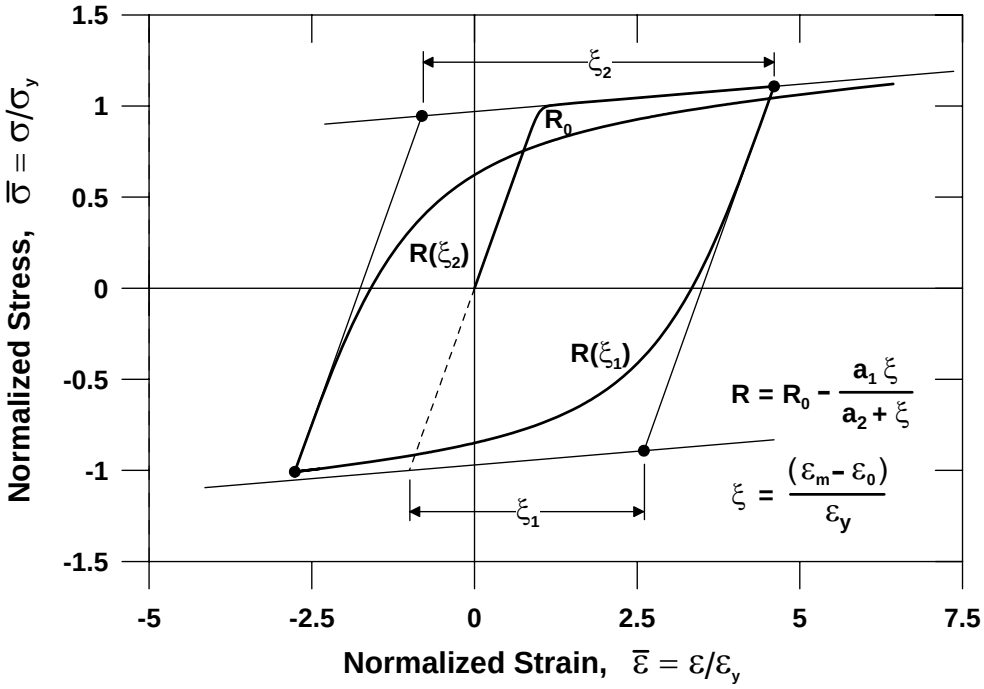

Figure 4.2. Degradation of Cyclic Curvature.

To illustrate the effect of degradation in cyclic curvature, for two different sets of values for parameters R_0, a_1 and a_2 (which were experimentally calibrated by prior researchers based on cyclic test results on reinforcing bars), a comparison of cyclic stress – strain histories generated by the constitutive model (R_0, a_1, a_2 = 20, 18.5, 0.15 by Menegotto and Pinto, 1973; R_0, a_1, a_2 = 20, 18.5, 0.0015 by Elmorsi *et al*., 1998) is shown in Figure 4.3.

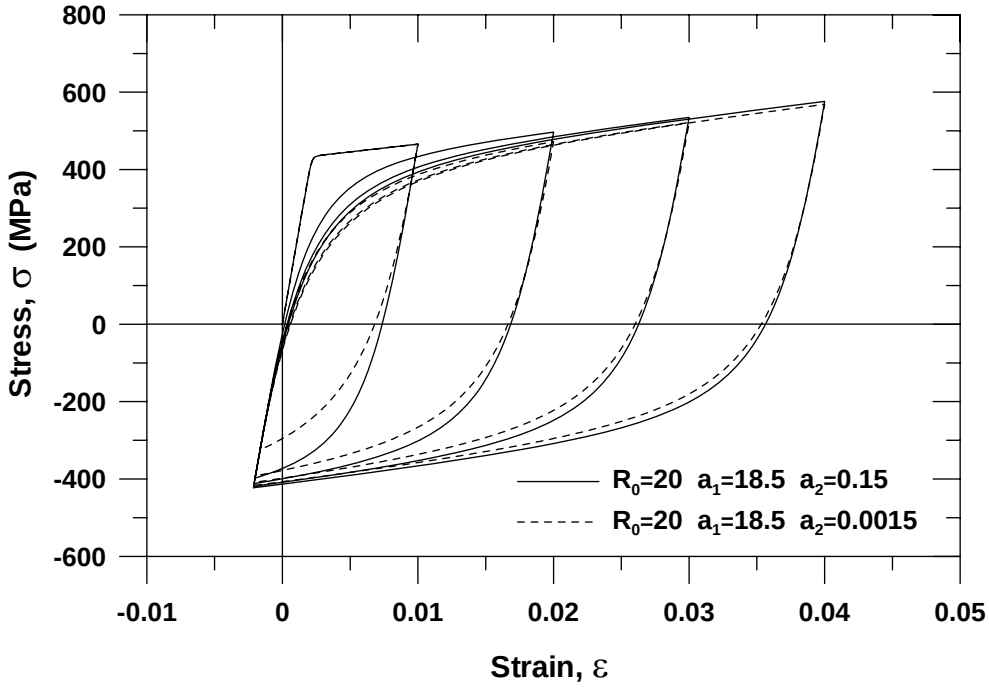

Figure 4.3. Sensitivity of the Stress-Strain Relationship to Cyclic Curvature Parameters.

The original Menegotto and Pinto (1973) model, although simple in formulation, has been shown to accurately represent test results for reinforcing steel bars under typical strain histories. The main limitation of the model is its failure to simulate isotropic strain hardening. Isotropic hardening effects can be influential on the cyclic behavior of reinforcing steel bars in reinforced concrete members, especially during crack closure. Based on experimental observations, Filippou *et al*. (1983) proposed a modification to the original model by Menegotto and Pinto (1973), by introducing a stress shift to the compressive yield asymptote to account for isotropic strain hardening in order to improve the prediction of the stress – strain behavior during crack closure, The shift is arranged by shifting the compressive yield asymptote by a stress magnitude, σ_{st}, in a parallel manner, as shown in Figure 4.4.

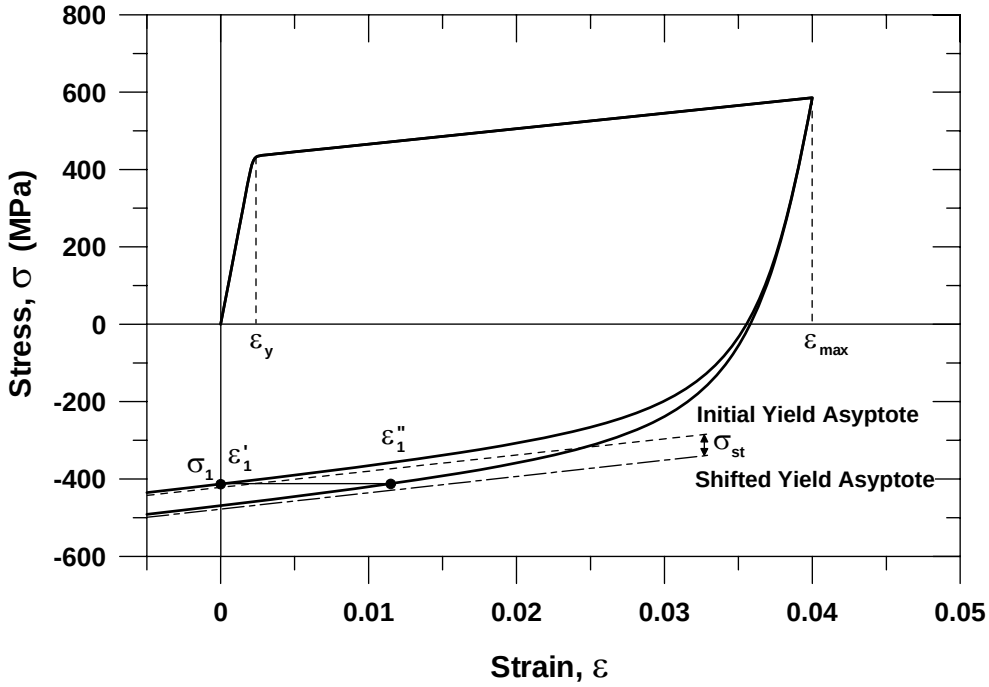

Figure 4.4. Stress Shift due to Isotropic Strain Hardening.

The imposed stress shift on the compressive yield asymptotes (σ_{st}) proposed by Filippou *et al*. (1983) is expressed as:

$$\frac{\sigma_{st}}{\sigma_y} = a_3 \left(\frac{\varepsilon_{\max}}{\varepsilon_y} - a_4 \right) \tag{4.8}$$

where $\varepsilon_{\max}$ is the absolute maximum strain, ε_y, σ_y are, respectively, the strain and stress values at the monotonic yield point, and a_3 and a_4 are experimentally determined parameters. Based on test results, Filippou *et al*. (1983) suggested values of 0.01 and 7 for parameters a_3 and a_4, respectively.

4.2. Constitutive Model for Concrete

The hysteretic constitutive model proposed by Chang and Mander (1994) is implemented in the present model to represent the cyclic stress – strain behavior of the concrete macro-fibers. The Chang and Mander (1994) is an advanced, rule-based, generalized, and non-dimensional constitutive model, which can simulate the hysteretic stress – strain behavior of both confined and unconfined, ordinary and high-strength concrete subjected to cyclic compression and tension. Gradual transition in the cyclic stress-strain behavior upon crack opening and closure, which had not been adequately addressed in previous models, are considered in detail in this model. As well, the cyclic behavior of concrete in tension is modeled similar to that in compression, based on results of a detailed test program conducted by Yankelevsky and Reinhardt (1987).

4.2.1. Compression Envelope Curve

Chang and Mander (1994) defined the compression envelope curve of the model by the initial slope E_c, the strain and stress values at the peak compressive stress point (ε_c', f_c'), a parameter r from Tsai's (1988) equation defining the shape of the envelope curve, and a parameter $x_{cr}^{-} > 1$ to define the spalling strain (Figure 4.5).

The compression and tension envelope curves can be written in non-dimensional form by the use of the following equations:

$$y(x) = \frac{nx}{D(x)} \tag{4.9}$$

$$z(x) = \frac{\left(1 - x^r\right)}{\left[D(x)\right]^2} \tag{4.10}$$

where,

$$D(x) = 1 + \left(n - \frac{r}{r-1}\right)x + \frac{x^r}{r-1} \tag{4.11}$$

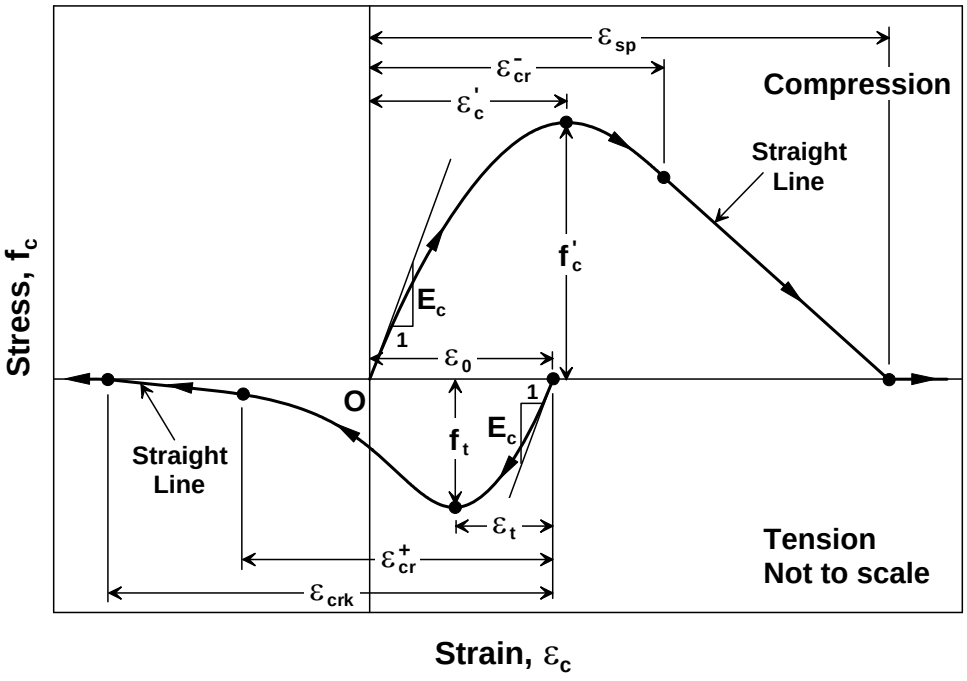

Figure 4.5. Compression and Tension Envelope Curves of the Model by Chang and Mander (1994).

where r not equal to one

$$D(x) = 1 + (n - 1 + \ln x)x \tag{4.12}$$

where r equals to one and n and x are defined for the compression envelope as:

$$x^- = \left| \frac{\varepsilon_c}{\varepsilon_c'} \right| \tag{4.13}$$

$$n^- = \left| \frac{E_c \varepsilon_c'}{f_c'} \right| \tag{4.14}$$

The non-dimensional spalling strain can be calculated by:

$$x_{sp} = x_{cr}^- - \frac{y(x_{cr}^-)}{n^- z(x_{cr}^-)} \tag{4.15}$$

In the equations above, ε_c is the concrete strain, ε_c' is the concrete strain at peak unconfined (or confined) stress, f_c' is the unconfined (or confined) concrete strength, E_c is the concrete initial Young's modulus, x^- is the non-dimensional strain on the compression envelope, x_{cr}^- is the non-dimensional critical strain on the compression envelope curve (used to define a tangent line up to the spalling strain), x_{sp} is the non-dimensional spalling strain, $y(x)$ is the non-dimensional stress function, $z(x)$ is the non-dimensional tangent modulus function, as shown in Figure 4.5.

The stress f_c and the tangent modulus E_t at any given strain on the compression envelope curve can be expressed as below:

$$f_c = f_c^- \left(x^- \right) \tag{4.16}$$

$$E_t = E_t^- \left(x^- \right) \tag{4.17}$$

where $f_c^- \left(x^- \right)$ and $E_t^- \left(x^- \right)$ are defined as:

If $x^- < x_{cr}^-$ (Tsai's equation)

$$f_c^- = f_c' y \left(x^- \right) \tag{4.18}$$

$$E_t^- = E_c z \left(x^- \right) \tag{4.19}$$

If $x_{cr}^- \le x^- \le x_{sp}$ (Straight line)

$$f_c^- = f_c' \left[y \left(x_{cr}^- \right) + n^- z \left(x_{cr}^- \right) \left(x^- - x_{cr}^- \right) \right] \tag{4.20}$$

$$E_t^- = E_c z \left(x_{cr}^- \right) \tag{4.21}$$

If $x > x_{sp}$ (Spalled)

$$f_c^- = E_t^- = 0 \tag{4.22}$$

The minus superscript in the equations above refers to the stress-strain behavior in compression. Once the concrete is considered to be spalled, the stresses are zero for larger compressive strains. A large value of x_{cr}^- should be defined for the case of confined concrete, where the spalling strain value will be larger. The material parameters associated with the compression envelope curve of the model are the concrete compressive strength $f_c^{'}$, the concrete strain at peak stress $\varepsilon_c^{'}$, the concrete initial Young's modulus (modulus of elasticity) E_c, the Tsai's parameter r defining the shape of the compression envelope, and the non-dimensional critical strain x_{cr}^- where the envelope curve starts following a straight line. Parameters E_c, $\varepsilon_c^{'}$ and r associated with the unconfined compression envelope can be empirically related to the unconfined concrete strength $f_c^{'}$ (MPa) as:

Initial modulus of elasticity:

$$E_c = 8200\left(f_c'\right)^{3/8} Mpa \tag{4.23}$$

Strain at peak stress:

$$\varepsilon_c^{'} = \frac{\left(f_c'\right)^{1/4}}{28} \tag{4.24}$$

Shape parameter:

$$r = \frac{f_c'}{5.2} - 1.9 \tag{4.25}$$

For confined concrete, the compressive envelope model by Chang and Mander (1994) complies with the confinement model developed by Mander *et al*. (1988). This

model is applicable to reinforced concrete members with either circular or rectangular cross-sections, and any general type and configuration of transverse reinforcement (Figure 4.6). The effectively confined concrete area for rectangular sections is given by the expression:

$$A_e = \left(b_c d_c - \sum_{i=1}^{n} \frac{\left(w_i'\right)^2}{6} \right) \left(1 - 0.5 \frac{s'}{b_c} \right) \left(1 - 0.5 \frac{s'}{d_c} \right) \tag{4.26}$$

The confined concrete core area is given by:

$$A_{cc} = b_c d_c - A_{st}$$

The lateral pressure for each direction is calculated by:

$$f_{lx}' = k_e \rho_x f_{yh} \tag{4.27}$$

$$f_{ly}' = k_e \rho_y f_{yh} \tag{4.28}$$

where,

$$k_e = \frac{A_e}{A_{cc}} \tag{4.29}$$

$$\rho_x = \frac{A_{sx}}{s\ d_c} \tag{4.30}$$

where A_{sx} = total area of transverse reinforcement parallel to the x axis

$$\rho_y = \frac{A_{sy}}{s\ b_c} \tag{4.31}$$

where A_{sy} = total area of transverse reinforcement parallel to the y axis

The equation proposed by Chang and Mander (1994) to represent the analytical confinement coefficient K is expressed as:

$$K = \frac{f'_{cc}}{f'_c} = 1 + A\overline{x}\left(0.1 + \frac{0.9}{1 + B\overline{x}}\right) \tag{4.32}$$

where,

$$\overline{x} = \frac{f'_{l1} + f''_{l2}}{2f'_c} \tag{4.33}$$

$$r = \frac{f'_{l1}}{f'_{l2}}, where, f'_{l2} \geq f'_{l1} \tag{4.34}$$

$$A = 6.8886 - \left(0.6096 + 17.275r\right)e^{-4.989r} \tag{4.35}$$

$$B = \frac{4.5}{\frac{5}{A}\left(0.9849 - 0.6306e^{-3.8939r}\right) - 0.1} - 5 \tag{4.36}$$

in which the analytical confinement coefficient K is the ratio of the confined concrete strength f'_{cc} to the unconfined concrete strength f'_c.

Equation (4.32) can be expressed in the following form:

$$f'_{cc} = f'_c + k_1 f_l \tag{4.37}$$

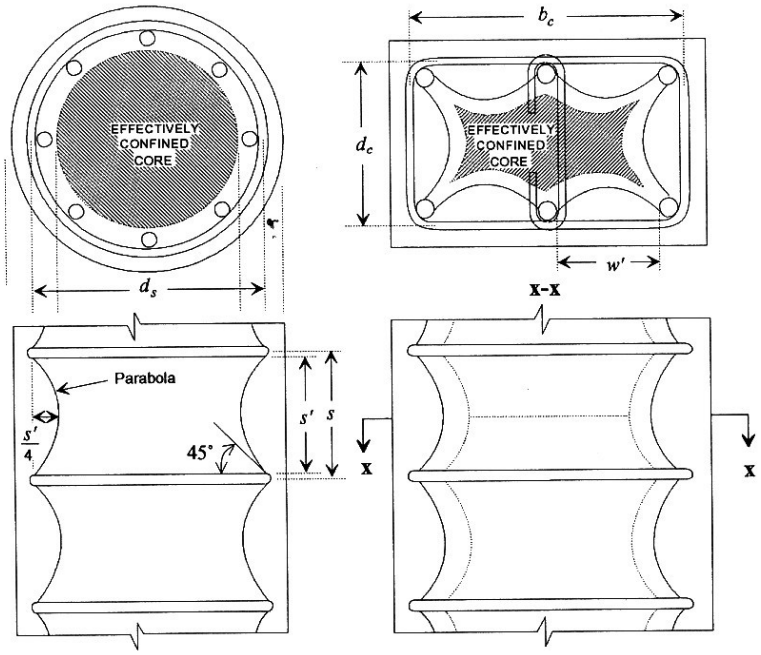

Figure 4.6. Confinement Mechanism for Circular and Rectangular Cross Sections (Chang and Mander, 1994).

By taking f_l as the average of f_{l1} and f_{l2}, this can be rewritten as:

$$K = \frac{f'_{cc}}{f'_c} = 1 + k_1 \overline{x} \tag{4.38}$$

where,

$$k_1 = A\left(0.1 + \frac{0.9}{1 + B\overline{x}}\right) \tag{4.39}$$

The strain at peak stress for confined concrete (ε'_{cc}) as adopted by Chang and Mander takes the form:

$$\varepsilon'_{cc} = \varepsilon'_c\left(1 + k_2 \overline{x}\right) \tag{4.40}$$

with,

$$k_2 = 5k_1 \tag{4.41}$$

where ε_c' is the strain at peak unconfined stress.

4.2.2. Tension Envelope Curve

As stated previously, the shape of the tension envelope curve in the model by Chang and Mander is the same as that of the compression envelope curve (Figure 4.5). However, upon each cycle, the tension envelope curve is shifted to a new origin ε_0 as discussed in the next section. The non-dimensional parameters for the tension envelope curve are expressed as:

$$x^+ = \left| \frac{\varepsilon_c - \varepsilon_0}{\varepsilon_t} \right| \tag{4.42}$$

$$n^+ = \frac{E_c \varepsilon_t}{f_t} \tag{4.43}$$

The non-dimensional cracking strain is given by:

$$x_{crk} = x_{cr}^+ - \frac{y\left(x_{cr}^+\right)}{n^+ z\left(x_{cr}^+\right)} \tag{4.44}$$

where ε_c is the concrete strain, ε_t is the concrete strain at peak tension stress, f_t is the concrete tensile strength, E_c is the concrete initial Young's modulus, x^+ is the non-dimensional strain on the tension envelope curve, x_{crk} is the cracking strain and x_{cr}^+ is the critical strain on the tension envelope curve. The tangent modulus E_t and stress f_c are defined as:

$$f_c = f_c^+\left(x^+\right) \tag{4.45}$$

$$E_t = E_t^+\left(x^+\right) \tag{4.46}$$

where $f_c^+\left(x^+\right)$ and $E_t^+\left(x^+\right)$ are defined as:

If $x^+ < x_{cr}^+$

$$f_c^+ = f_t y\left(x^+\right) \tag{4.47}$$

$$E_t^+ = E_c z\left(x^+\right) \tag{4.48}$$

If $x_{cr}^+ \le x^+ \le x_{crk}$

$$f_c^+ = f_t\left[y\left(x_{cr}^+\right) + n^+ z\left(x_{cr}^+\right)\left(x^+ - x_{cr}^+\right)\right] \tag{4.49}$$

$$E_t^+ = E_c z\left(x_{cr}^+\right) \tag{4.50}$$

If $x > x_{crk}$ (Cracked)

$$f_c^+ = E_t^+ = 0 \tag{4.51}$$

in which the functions y and z are defined by Equations (4.9) and (4.10). The plus superscript refers to the stress – strain behavior in tension. When concrete is fully cracked, it is considered to no longer resist any tensile stress during crack opening. However, upon reversal from a tensile strain, gradual crack closure is considered to take place. Contribution of concrete between the cracks in a reinforced concrete member (the tension stiffening phenomenon) can be considered through an average tensile stress – strain relationship, for which the concrete can be assumed to not fully crack, allowing a large value of x_{cr}^+ to be used.

4.2.3. Hysteretic Properties of the Model

The hysteretic parameters of the Chang and Mander (1994) model for cyclic compression (Figure 4.7) were calibrated based on statistical analysis of extensive test data, and are defined as empirical parameters expressed in the form:

$$E_{\text{sec}}^{-} = E_c \left(\frac{\left| \frac{f_{un}^{-}}{E_c \varepsilon_c'} \right| + 0.57}{\left| \frac{\varepsilon_{un}^{-}}{\varepsilon_c'} \right| + 0.57} \right) \tag{4.52}$$

$$E_{pl}^{-} = 0.1 E_c \exp\left(-2 \left| \frac{\varepsilon_{un}^{-}}{\varepsilon_c'} \right| \right) \tag{4.53}$$

$$\Delta f^{-} = 0.09 f_{un}^{-} \sqrt{\left| \frac{\varepsilon_{un}^{-}}{\varepsilon_c'} \right|} \tag{4.54}$$

$$\Delta \varepsilon^{-} = \frac{\varepsilon_{un}^{-}}{1.15 + 2.75 \left| \frac{\varepsilon_{un}^{-}}{\varepsilon_c'} \right|} \tag{4.55}$$

where $\varepsilon_c^{'}$ is the strain at peak compressive stress, E_c is the initial Young's modulus, and f_{un} and ε_{un} are the unloading stress and strain values.

The plastic (residual) strain upon unloading (ε_{pl}), the new stress (f_{new}) and tangent modulus (E_{new}) values upon return to unloading strain from the envelope curve (ε_{un}), and the strain (ε_{re}), stress (f_{re}) and tangent modulus (E_{re}) at the point of return to the envelope curve can be geometrically related to the empirical parameters (Figure 4.7) as:

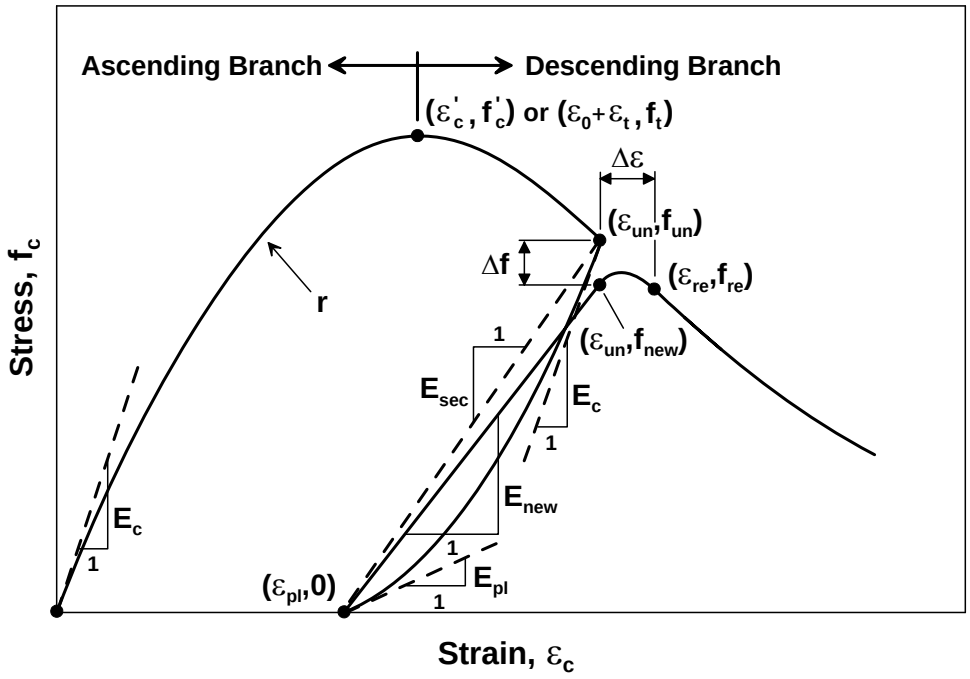

Figure 4.7. Hysteretic Parameters of the Model by Chang and Mander (1994).

$$\varepsilon_{pl}^{-} = \varepsilon_{un}^{-} - \frac{f_{un}^{-}}{E_{\sec}^{-}} \tag{4.56}$$

$$f_{new}^{-} = f_{un}^{-} - \Delta f^{-} \tag{4.57}$$

$$E_{new}^{-} = \frac{f_{new}^{-}}{\varepsilon_{un}^{-} - \varepsilon_{pl}^{-}} \tag{4.58}$$

$$\varepsilon_{re}^{-} = \varepsilon_{un}^{-} + \Delta\varepsilon^{-} \tag{4.59}$$

$$f_{re}^{-} = f^{-}\left(\left|\frac{\varepsilon_{re}^{-}}{\varepsilon_{c}'}\right|\right) \tag{4.60}$$

$$E_{re}^{-} = E^{-}\left(\left|\frac{\varepsilon_{re}^{-}}{\varepsilon_{c}'}\right|\right) \tag{4.61}$$

For cyclic behavior in tension, Chang and Mander (1994) proposed the following empirical parameters:

$$E_{\sec}^{+} = E_c \left(\frac{\left| \frac{f_{un}^{+}}{E_c \varepsilon_t} \right| + 0.67}{\left| \frac{\varepsilon_{un}^{+} - \varepsilon_0}{\varepsilon_t} \right| + 0.67} \right) \tag{4.62}$$

$$E_{pl}^{+} = \frac{E_c}{\left| \frac{\varepsilon_{un}^{+} - \varepsilon_0}{\varepsilon_t} \right|^{1.1} + 1} \tag{4.63}$$

$$\Delta f^{+} = 0.15 f_{un}^{+} \tag{4.64}$$

$$\Delta \varepsilon^{+} = 0.22 \left(\varepsilon_{un}^{+} - \varepsilon_0 \right) \tag{4.65}$$

where ε_t is the strain at peak tensile stress, E_c is the initial Young's modulus and ε_0 is the shifted origin of the tensile envelope curve. The geometrically – derived parameters for cyclic tension therefore defined as:

$$\varepsilon_{pl}^{+} = \varepsilon_{un}^{+} - \frac{f_{un}^{+}}{E_{\sec}^{+}} \tag{4.66}$$

$$f_{new}^{+} = f_{un}^{+} - \Delta f^{+} \tag{4.67}$$

$$E_{new}^{+} = \frac{f_{new}^{+}}{\varepsilon_{un}^{+} - \varepsilon_{pl}^{+}} \tag{4.68}$$

$$\varepsilon_{re}^{+} = \varepsilon_{un}^{+} + \Delta \varepsilon^{+} \tag{4.69}$$

$$f_{re}^{+} = f^{+} \left(\left| \frac{\varepsilon_{re}^{+} - \varepsilon_0}{\varepsilon_t} \right| \right) \tag{4.70}$$

$$E_{re}^{+} = E^{+}\left(\left|\frac{\varepsilon_{re}^{+} - \varepsilon_0}{\varepsilon_t}\right|\right) \tag{4.71}$$

A reversal from the compression envelope curve (Figure 4.8), involves calculating the shifted origin of the tension envelope curve (ε_0) and evaluating the unloading strain from the tension envelope curve. The procedure that describes reversal from the compression envelope (Figure 4.8) is as follows:

(i) Calculate the compression strain ductility as:

$$x_u^{-} = \left|\frac{\varepsilon_{un}^{-}}{\varepsilon_c'}\right| \tag{4.72}$$

(ii) Calculate the tension strain ductility:

$$x_u^{+} = \left|\frac{\varepsilon_{un}^{+} - \varepsilon_0}{\varepsilon_t}\right| \tag{4.73}$$

(iii) If $x_u^{+} < x_u^{-}$, then:

$$x_u^{+} = x_u^{-} \tag{4.74}$$

$$\varepsilon_0 = 0 \tag{4.75}$$

$$\varepsilon_{un}^{+} = x_u^{+}\varepsilon_t$$

$$f_{un}^{+} = f_c^{+}\left(x_u^{+}\right) \tag{4.76}$$

(iv) Calculate:

$$\Delta\varepsilon_0 = \frac{2f_{un}^{+}}{E_{\text{sec}}^{+} + E_{pl}^{-}} \tag{4.77}$$

(iv) Finally,

$$\varepsilon_0 = \varepsilon_{pl}^{-} + \Delta\varepsilon_0 - x_u^{+}\varepsilon_t \tag{4.78}$$

$$\varepsilon_{un}^{+} = x_u^{+}\varepsilon_t + \varepsilon_0 \tag{4.79}$$

Therefore, upon each unloading from the compression envelope, the origin of the tension envelope is shifted based on the unloading strain from the compression envelope. The unloading strain from the tension envelope is re-calculated so that it corresponds to a tension strain ductility equal to the compression strain ductility experienced just before unloading from the compression envelope, or a previously experienced actual tension strain ductility, whichever is greater.

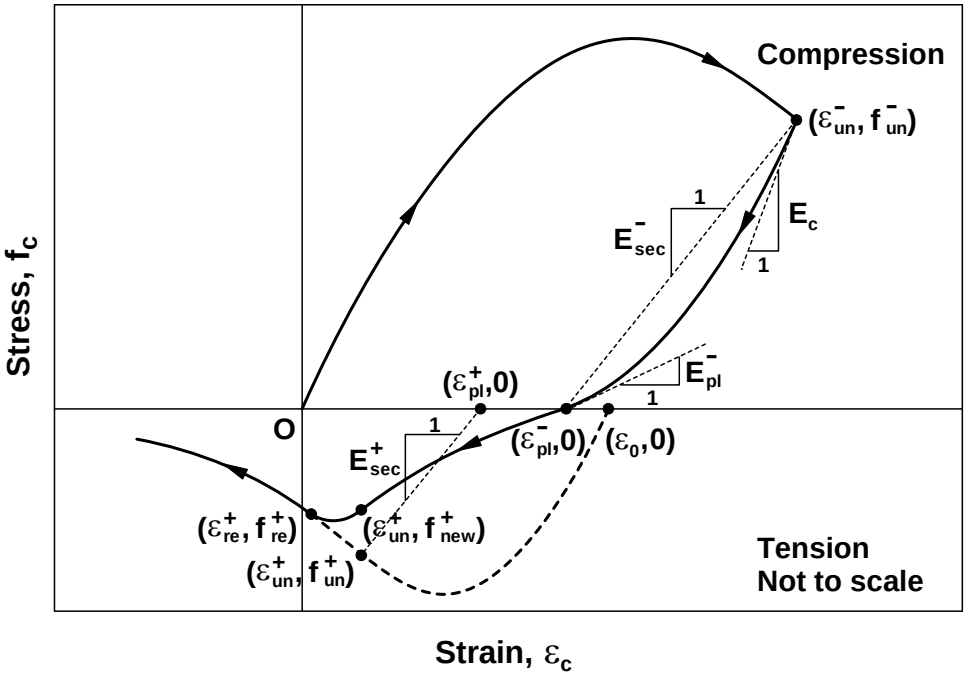

Figure 4.8. Unloading from the Compression Envelope Curve.

To simulate continuous hysteretic behavior, the constitutive model uses smooth "connecting" curves for unloading and reloading between the compression and tension envelope curves, and smooth "transition" curves for partial unloading and reloading between the connecting curves (Figure 4.9). Both connecting and transition curves have slope continuity with uniform sign of curvature in between the starting and final points.

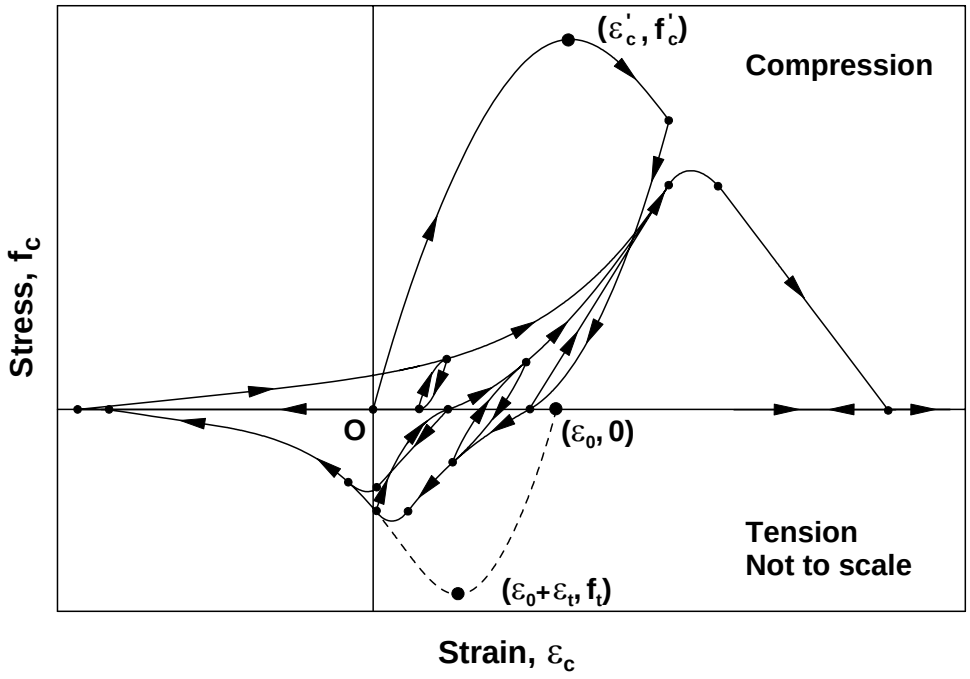

Figure 4.9. Continuous Hysteresis in Compression and Tension.

For the transition curves (Figure 4.10), Chang and Mander (1994) proposed a relationsip between starting and target points $\mathrm{A}(\varepsilon_a, f_a)$ and $\mathrm{B}(\varepsilon_b, f_b)$, based on unloading (ε_{un}) and plastic (ε_{pl}) strain values, which is expressed in the form:

$$\frac{\varepsilon_a - \varepsilon_{pl}^-}{\varepsilon_{un}^+ - \varepsilon_{pl}^-} = \frac{\varepsilon_{un}^- - \varepsilon_b}{\varepsilon_{un}^- - \varepsilon_{pl}^+} \tag{4.80}$$

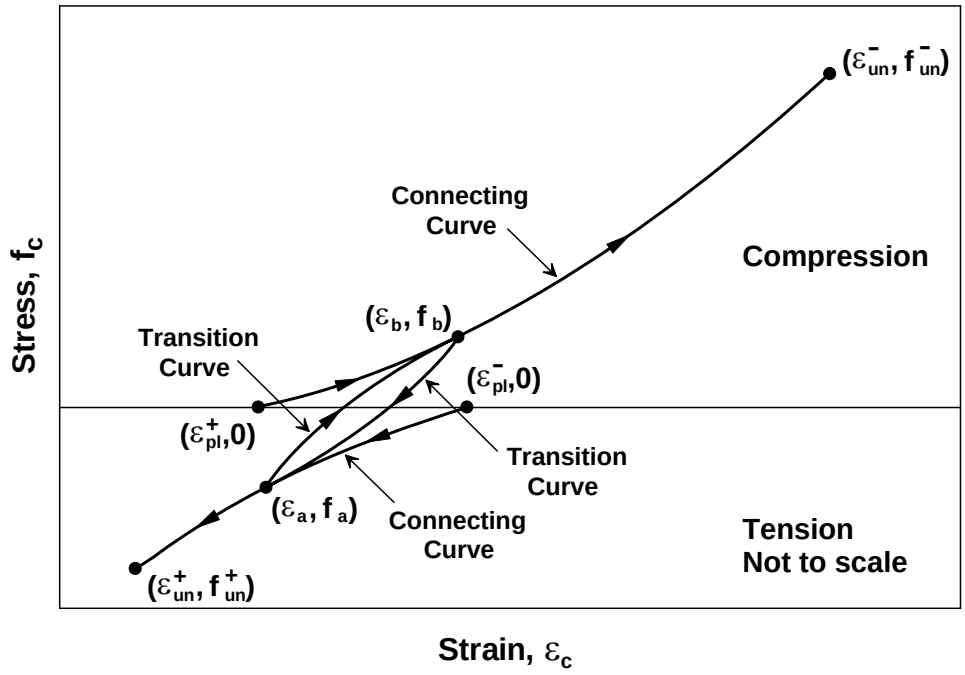

Figure 4.10. Transition Curves Before Cracking.

After full cracking, the tension envelope is reduced to zero, and the connecting curve upon unloading (i.e., strain reversal) represents gradual gap closure (Figure 4.11).

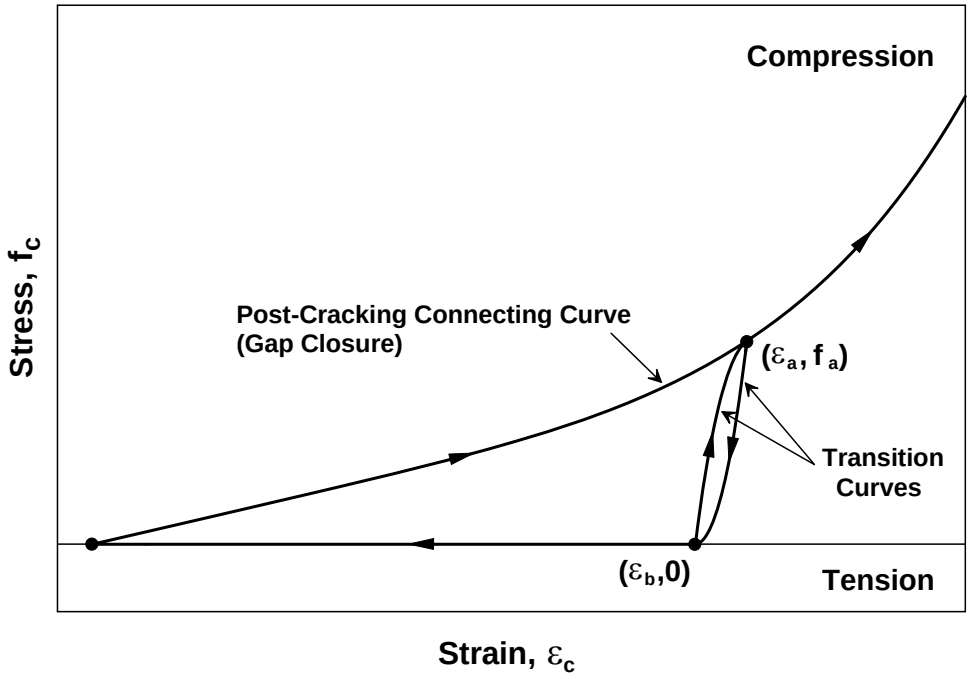

Figure 4.11. Transition Curves After Cracking.

The generalized equation used in the constitutive model to represent the connecting and transition curves takes the form:

$$\varepsilon_b = \varepsilon_a - \frac{f_a}{E_{\text{sec}}^-} \tag{4.81}$$

$$f_c = f_I + \left(\varepsilon_c - \varepsilon_I\right)\left[E_I + A\left|\varepsilon_c - \varepsilon_I\right|^R\right] \tag{4.82}$$

$$E_t = \frac{\partial f_c}{\partial \varepsilon_c} = E_I + A\left(R+1\right)\left|\varepsilon_c - \varepsilon_I\right|^R \tag{4.83}$$

in which,

$$R = \frac{E_F - E_{SEC}}{E_{SEC} - E_I} \tag{4.84}$$

$$A = \frac{E_{SEC} - E_I}{\left|\varepsilon_F - \varepsilon_I\right|^R} \tag{4.85}$$

and,

$$E_{SEC} = \frac{f_F - f_I}{\varepsilon_F - \varepsilon_I} \tag{4.86}$$

where f_c is the concrete stress, ε_c is the concrete strain, E_t is the concrete tangent modulus, f_I is the stress at the initial point, f_F is the stress at the final (target) point, ε_I is the strain at the initial point, ε_F is the stress at the final point, E_I is the tangent modulus at the initial point, E_F is the tangent modulus at the final point, E_{SEC} is the secant modulus between the initial and final points, and R and A are equation parameters. The equations represent a stress-strain curve with a single sign of curvature and slope continuity between the initial and target points.

4.3. Modeling of Tension Stiffening

The contribution of cracked concrete to the tensile resistance of reinforced concrete members is known as the effect of tension stiffening. The concrete between the cracks, which is still bonded to the reinforcing steel bars, contributes to the tensile resistance of the member. In this study, the tension stiffening effect is directly incorporated into the constitutive stress-strain relationships implemented for concrete and steel, as described in the following paragraphs.

Based on extensive tests on reinforced concrete panel specimens subjected to normal stresses, Belarbi and Hsu (1994) developed two constitutive models: one for the average tensile stress-strain relationship of concrete and one for the average tensile stress-strain relationship of steel reinforcing bars stiffened by concrete. The average stress-strain relationship proposed by Belarbi and Hsu for concrete in tension takes the form (Figure 4.12):

If $\varepsilon_c \le \varepsilon_{cr}$ then

$$\sigma_c = E_c \varepsilon_c \tag{4.87}$$

If $\varepsilon_c > \varepsilon_{cr}$ then

$$\sigma_c = f_{cr}\left(\frac{\varepsilon_{cr}}{\varepsilon_c}\right)^{0.4} \tag{4.88}$$

where:

$$E_c = 3875\sqrt{f_c'(MPa)} \tag{4.89}$$

$$f_{cr} = 0.31\sqrt{f_c'(MPa)} \tag{4.90}$$

$$\varepsilon_{cr} = 0.00008 \tag{4.91}$$

In the equation above, ε_c is the average concrete tensile strain, σ_c is the average concrete tensile stress, E_c is the initial Young's modulus of the average stress-strain relationship,

f_{cr} is concrete the tensile cracking stress, and ε_{cr} is the concrete strain at cracking. The expressions for f_{cr}, ε_{cr}, E_c, and the power constant 0.4 in Equation (4.91) are obtained from the average and best fit of experimental results of reinforced concrete panel specimens.

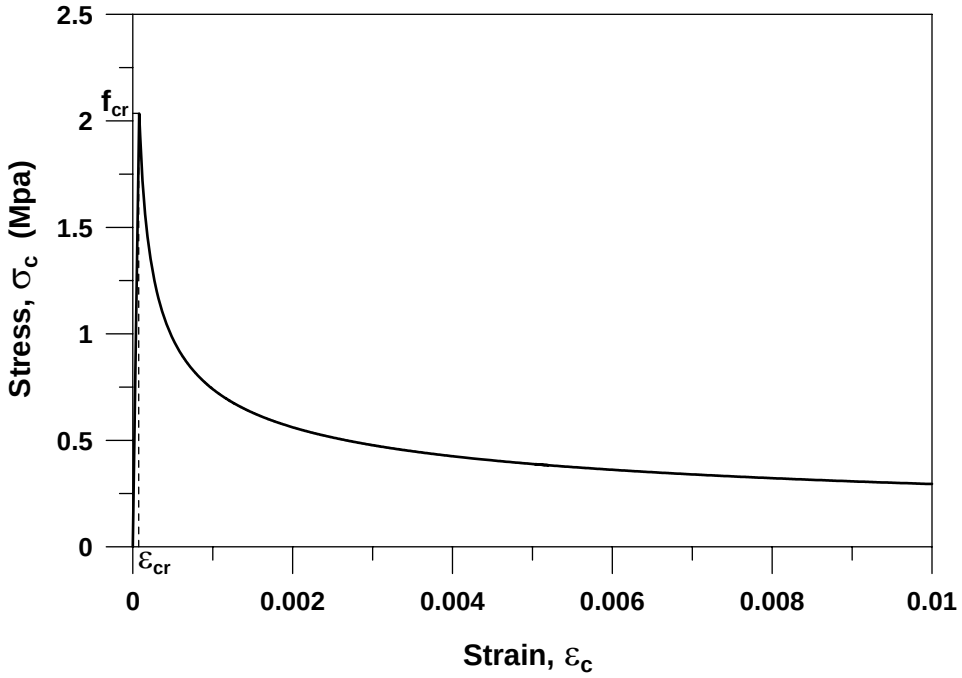

Figure 4.12. Average Stress-Strain Relationship by Belarbi and Hsu (1994) for Concrete in Tension.

Belarbi and Hsu (1994) identified the difference between the average stress–strain relationship of reinforcing steel bars surrounded by concrete and the stress–strain relationship of bare steel bars (Figure 4.13). The most important difference was found to be the reduction of the yield stress, σ_y, as yielding of a reinforced concrete element occurs when the steel stress at the cracked section reaches the yield strength of the bare bar. At the same time, the average steel stress smeared along the length of the element reaches a level lower than that of the yield stress of the bare bar. Based on experimental data from the RC panels, the reduction of the yield stress of bars embedded in concrete were found to be empirically dependent on the cross-sectional area ratio of the longitudinal steel in the panel (ρ), and the ratio of concrete cracking stress (f_{cr}) to the steel yield stress (σ_y). The strain-hardening slope (plastic modulus) of the steel bars embedded in concrete was also

observed to differ from the plastic modulus of bare bars with the variation also dependent on the above parameters.

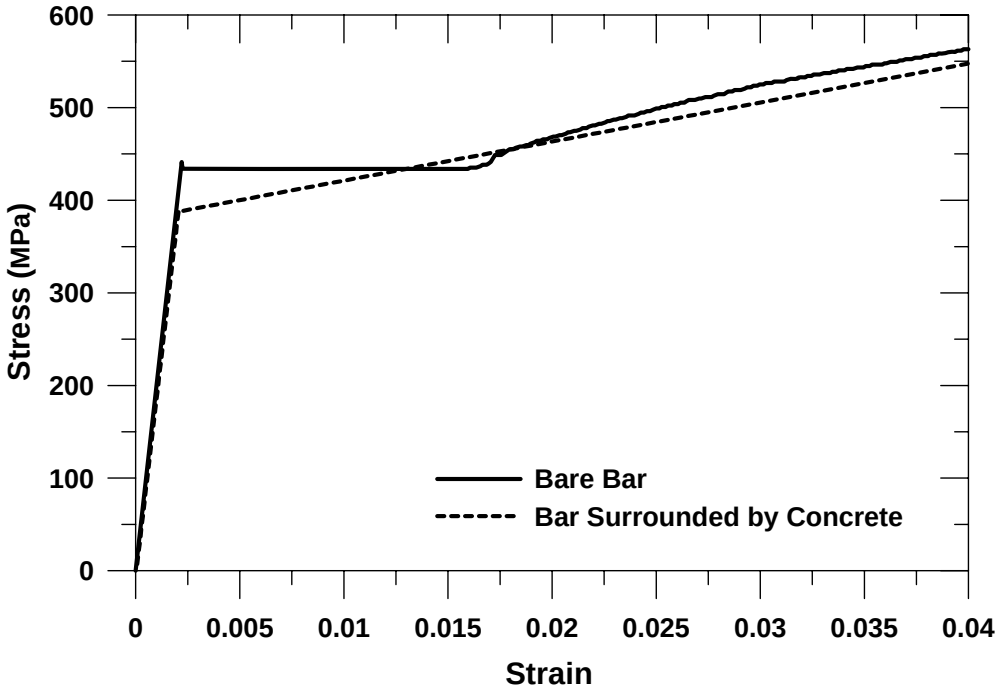

Figure 4.13. Effect of Tension Stiffening on Reinforcing Bars.

Based on evaluation and characterization of experimental data, Belarbi and Hsu (1994) proposed the simple bilinear constitutive model shown in Figure 4.14. for reinforcing steel bars embedded in concrete

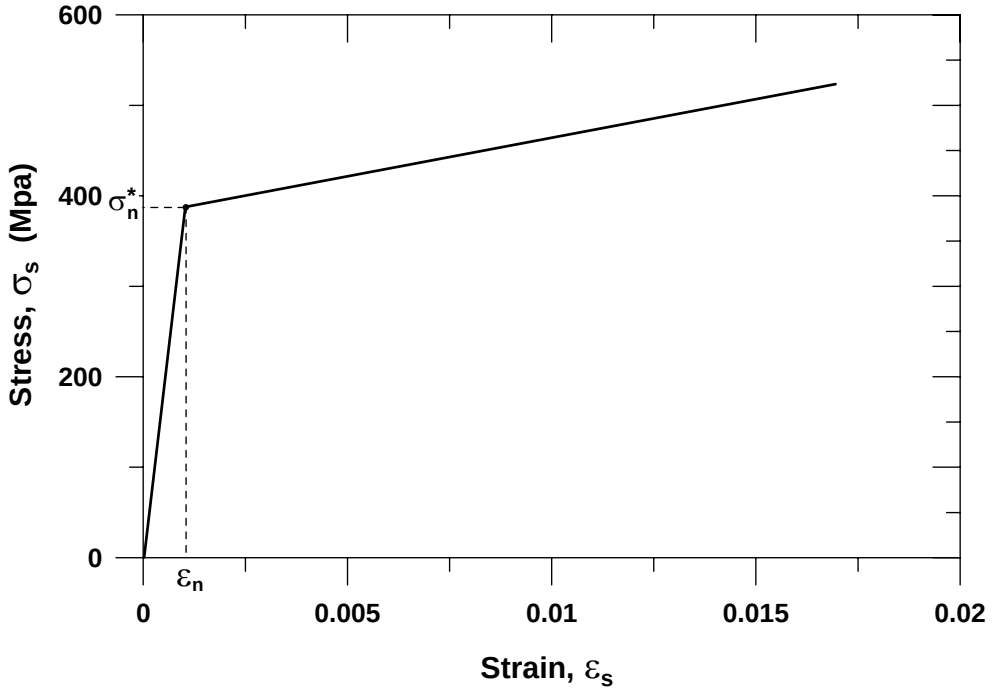

Figure 4.14. Average Stress-Strain Relationship by Belarbi and Hsu (1994) for Reinforcing Bars Embedded in Concrete.

The effective yield stress at the intersection of the two lines $\left(\sigma_n^*\right)$ and the plastic slope $\left(E_p^*\right)$ are determined using the following expressions:

$$\sigma_n^* = \left(0.93 - 2B\right)\sigma_y \tag{4.92}$$

$$E_p^* = (0.02 + 0.25B)E_s \tag{4.93}$$

where the parameter B is defined as:

$$B = \frac{1}{\rho}\left(\frac{f_{cr}}{\sigma_y}\right)^{1.5} \tag{4.94}$$

In the equations above, σ_y and E_s are the yield stress and modulus of elasticity of the bare steel bars, (ρ) is the cross-sectional area ratio of the longitudinal steel bars in the

reinforced concrete section, and (f_{cr}) is the concrete cracking stress, obtained according to the relationship in Equation (4.90). Equation (4.93) was derived assuming that the plastic modulus of "bare" steel bars (E_p) is approximately equal to 2.5% of the modulus of elasticity $(E_p = 0.025E_s)$. For a more general case, Equation (4.93) can be expanded as:

$$E_p^* = (0.8b + 0.25B)E_s \tag{4.95}$$

where b is the strain hardening ratio (E_p/E_s) defined for the bare steel bars.

Accordingly, the bilinear model of Belarbi and Hsu (1994) for modeling the average (smeared) stress-strain behavior of steel reinforcing bars embedded in concrete, takes the form (Figure 4.23):

If $\varepsilon_s \le \varepsilon_n$,

$$\sigma_s = E_s\varepsilon_s \tag{4.96}$$

If $\varepsilon_s > \varepsilon_n$,

$$\sigma_s = (0.93 - 2B)\sigma_y + (0.8b + 0.25B)E_s(\varepsilon_s - \varepsilon_n) \tag{4.97}$$

where σ_s is the average (smeared) stress, ε_s is the average strain, and ε_n is the average strain defined at the intersection of the two lines:

$$\varepsilon_n = \frac{\sigma_n^*}{E_s} = \frac{(0.93 - 2B)\sigma_y}{E_s} \tag{4.98}$$

and E_s, σ_y, and b are the modulus of elasticity, yield stress, and strain-hardening ratio measured experimentally for bare steel bars.

4.4. Constitutive Model for Shear

The empirical model developed by Sezen (2002) to simulate the shear force – deformation behavior of lightly reinforced concrete columns under monotonic lateral loading is implemented in the analytical model to represent the behavior of the horizontal shear spring. The model uses four points (Figure 4.15) to represent a piecewise linear lateral load – shear deformation response of a column element. The four points that define the shear deformation – lateral load (shear force) relationship correspond to cracking (δ_{cr}, V_{cr}), yielding (δ_y, V_y), and peak strength (δ_n, V_n) pointes, as well as the shear deformation at complete loss of shear capacity (δ_{end}, 0).

The shear deformation and lateral load at onset of cracking is calculated using equations (4.99) and (4.100).

$$V_{cr} = \frac{7.5 \cdot \sqrt{f_c'} \cdot I_g}{c \cdot h_{col}} \tag{4.99}$$

$$\delta_{cr} = \frac{6 \cdot V_{cr} \cdot h_{col}}{5 \cdot G \cdot A_g} = \frac{3 \cdot V_{cr} \cdot h_{col}}{E_c \cdot A_g} \tag{4.100}$$

where G is shear modulus, E_c is the modulus of elasticity of concrete, A_g is gross cross-sectional area, c is the neutral axis depth and I_g is the uncracked cross-sectional moment of inertia.

Shear deformation at first yielding of longitudinal reinforcement is determined using:

$$\delta_y = \left(\frac{3}{0.2 + 0.4 \cdot P_r} \right) \cdot \frac{V_y \cdot h_{col}}{E_c \cdot A_g} \tag{4.101}$$

where P_r is the ratio of applied axial load (P) to the axial load capacity of the column (P_0) [$P_0 = 0.85 f_c' A_g (1 - \rho_l) + f_y A_{sl}$ where ρ_l = longitudinal reinforcement ratio (= A_{sl}/A_g), and A_{sl} = total area of longitudinal reinforcement, f'_c is the compressive strength of concrete] and V_y

is the shear force at yielding [$V_y = \frac{2M_y}{L}$ for double-curvature specimens (M_y = moment capacity at yield) where L is the length of column]

The shear deformation corresponding to the peak strength is calculated using:

$$\delta_n = \frac{V_s \cdot h_{col}}{d \cdot b} \cdot \left[\frac{1}{\rho_w \cdot E_s} + \frac{4}{E_c} \right] \tag{4.102}$$

where ρ_w is the transverse reinforcement ratio, V_s is the shear force carried by transverse reinforcement [$V_s = \alpha \frac{A_s f_{yw} d}{s}$ where α is the slope of the line fitted to test data (for most shear strength models α =1), f_{yw} is the yield strength of transverse reinforcement, A_s is the transverse reinforcement area within a spacing s and d is the distance from the extreme compression fiber to centroid of tension reinforcement], b is the section width and h_{col} is the height of the column.

The Peak lateral strength is calculated using:

$$V_n = k\left(V_c + V_s\right) = k\left(\frac{6\sqrt{f_c'}}{a/d} \sqrt{1 + \frac{p}{6\sqrt{f_c'} A_g}} \right) 0.80 A_g + k \frac{A_s f_{yw} d}{s} \tag{4.103}$$

where 'a' is shear span, V_c is the shear carried by concrete and V_s is shear carried by transverse reinforcement.

The peak lateral strength V_n, must be smaller than the lateral load, V_p, required to reach the maximum flexural capacity, M_p, at column end ($V_p = 2M_p / L$, for double-curvature specimens)

The shear displacement at the end of monotonic loading, δ_{end}, is calculated from

$$\delta_{end} = \delta_{total,end} - \delta_{flex,n} - \delta_{slip,n} \geq \delta_n \tag{4.104}$$

where, $\delta_{total,end}$ = total displacement of column at loss of axial capacity. If the final failure is dominated by shear, then the column does not develop its maximum flexural and slip deformation potential. Therefore, flexure and bar slip displacements at axial failure are the same as flexure and bar slip displacements corresponding to peak later strength, $\delta_{flex,n}$ and $\delta_{slip,n}$, respectively. δ_n is calculated from Equation (4.102).

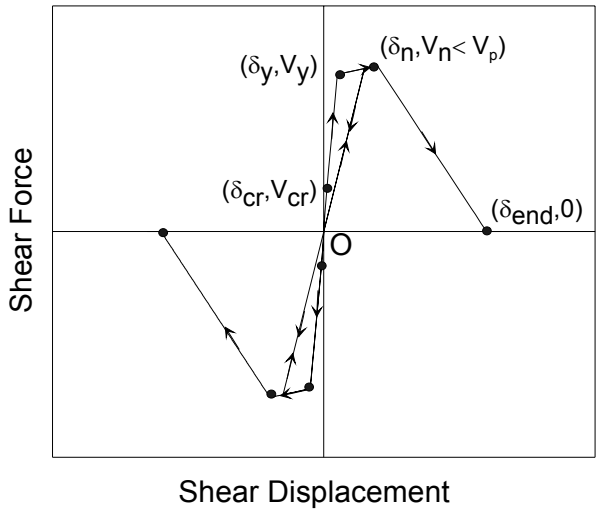

Figure 4.15. Origin-Oriented –Hysteresis Model for Horizontal Shear Spring.

For a given axial load ratio, P/P_0 and transverse reinforcement parameter $A_{sw}f_yh/(sP_0)$, the drift ratio at axial load failure could be obtained from Figure 4.16 ($\delta_{total,end} = driftratio * L$)

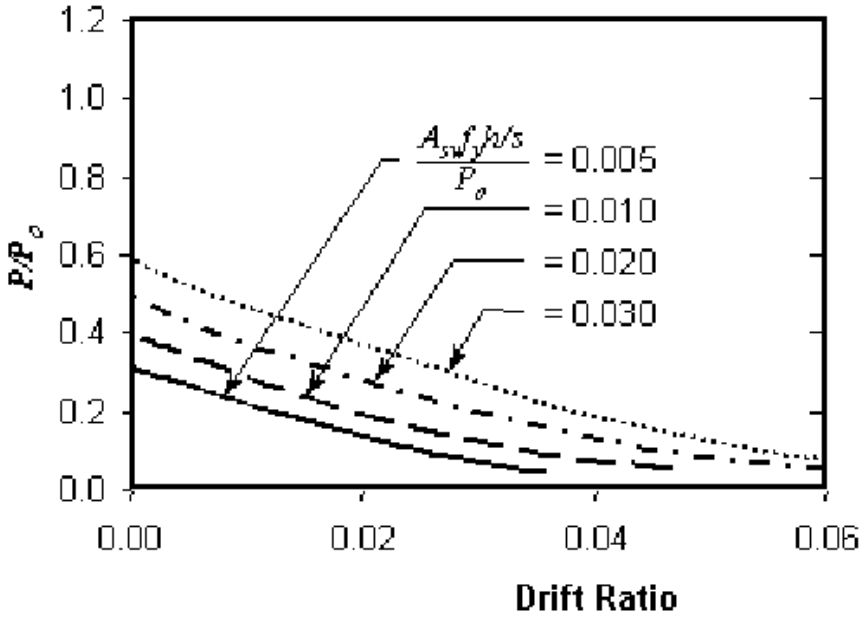

Figure 4.16. Drift Capacity at the Loss of Axial Load Capacity (Sezen, 2002).

The trilinear shear force vs. shear displacement relation developed by Sezen (2002) defines the backbone of the hysteretic constitutive relationship for the shear spring. An origin-oriented hysteresis rule simulates the shear response of the column element (Figure 4.15). It must be mentioned that since the columns investigated in this study are not expected to be shear critical, a detailed constitutive modeling approach was not implemented to define the shear behavior of the horizontal (shear) spring. Improved predictions of column shear response require consideration of the interaction between shear and flexure responses, especially where highly inelastic flexural deformations take place. However, since this study concentrates on modeling of reinforced concrete columns, the behavior of which is dominated by either bond slip, flexure, or simultaneously slip and flexure responses, a simple origin-oriented shear force vs. deformation behavior with a trilinear backbone curve was adopted.

4.5. Constitutive Models for Bond Stress vs. Slip Deformation

Uniaxial hysteretic bond stress vs. slip constitutive models are used to represent the cyclic force – deformation behavior of the bond slip springs of the analytical model. Past experimental studies on individual reinforcing bars embedded in concrete have identified

two main types of bond failure mechanisms, depending on the amount of concrete surrounding the reinforcing bar, as well as the level of confinement. If the surrounding concrete is of significant thickness and the concrete is well confined by transverse reinforcement, bond failure typically occurs by pullout. On the other hand, if the concrete cover is small and the concrete is either unconfined or poorly confined, bond failure occurs by splitting of the surrounding concrete. Several bond stress vs. slip constitutive models to simulate both pullout (for deformed as well as smooth reinforcing bars) and splitting (only for deformed reinforcing bars) modes of bond failures are available in the literature. Among them, for deformed reinforcing bars, the bond stress vs. slip relationship developed by Eligehausen *et al*. (1983) for pullout mode of bond failure; and the bond stress vs. slip relationships developed by Harajli *et al*. (1994, 2002, 2004, 2009) for splitting mode of bond failure were selected in this study. For pullout failure of plain reinforcing bars, the hysteretic bond stress vs. slip constitutive model recently developed by Verderame *et al*. (2009) was adopted, and a constitutive model for 180-degree hooks developed by by Fabbrocino *et al*. (2002, 2005) was implemented. Details of the constitutive bond slip relationships used are described in the following subsections.

4.5.1. Constitutive Bond Stress vs. Slip Model by Eligehausen *et al.* (1983)

Eligehausen *et al*. (1983) proposed the well-known and robust constitutive model for the local bond stress vs. slip relationship for single reinforcing bars, based on results of tests on deformed bars embedded in beam-column joints. The model was derived using experimental results from tests conducted on 125 specimens with short anchorage lengths subjected to either monotonic tensile loading or reversed cyclic loading. Effects of loading history, confining reinforcement, bar diameter, concrete strength, clear cover, bar spacing, transverse pressure, and the rate of pullout on the local bond stress vs. slip relationship were investigated. The model proposed compares reasonably well with experimental results, and is widely used in modeling applications. Although the model is originally developed for single bars embedded in concrete, it has also been shown to be suitable to be used for modeling the bond stress vs. slip behavior of lap–spliced reinforcing bars (e.g., Reyes, 1999).

4.5.1.1. Monotonic Envelope. The monotonic (envelope) bond stress vs. slip relationship of the constitutive model includes four branches (Figure 4.17): (1) a nonlinear ascending branch (Equation (4.105)), (2) a plateau after the peak stress is reached (Equation (4.106)), (3) a linearly descending branch (Equation (4.107)), and (4) a second plateau after the residual stress is reached (Equation (4.108)).

For $s \leq s_1$

$$\tau(s) = \tau_1 \cdot \left(s / s_1\right)^{\alpha} \tag{4.105}$$

For $s_1 \leq s \leq s_2$

$$\tau = \tau_1 \tag{4.106}$$

For $s_2 \leq s \leq s_3$

$$\tau(s) = \tau_1 - \frac{\left(\tau_1 - \tau_3\right)}{\left(s_3 - s_2\right)} \cdot \left(s - s_2\right) \tag{4.107}$$

For $s \geq s_3$

$$\tau = \tau_3 \tag{4.108}$$

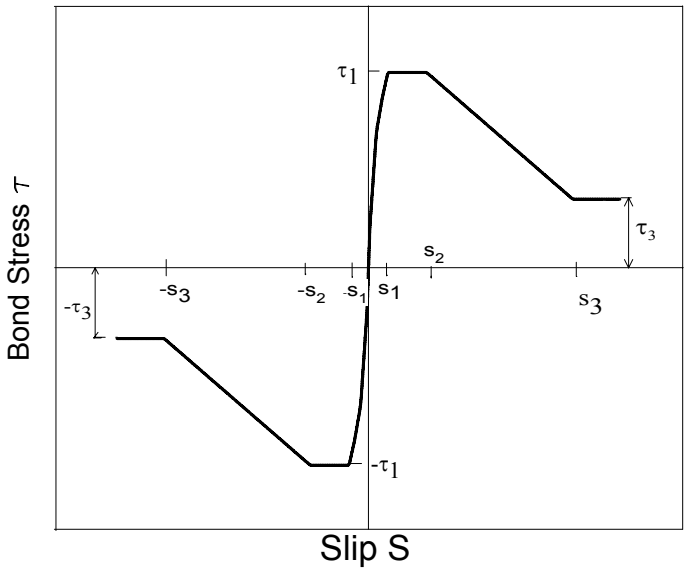

Figure 4.17. Proposed Analytical Model for Monotonic Local Bond Stress-slip Relationship for Confined Concrete (Eligehausen *et al*. ,1983).

Default parameters of the monotonic envelope for confined and unconfined concrete, for a reference concrete compressive strength value of 30 MPa, are presented in Table 4.1. Modifications to the default envelope parameters were suggested by Eligehausen *et al*. (1983) to account for variability in the following conditions:

Bar Diameter: The default values were calibrated for #8 (d_b = 25.4 mm) reinforcing bars. Peak bond stress (τ_1) values are increased or decreased by 10% for #6 (d_b = 19.05 mm) or #10 (d_b = 32.26 mm) longitudinal reinforcement, respectively.

Deformation Pattern: Envelope parameters need to be modified if the deformation pattern of the reinforcement bars used in the construction of the columns specimens are different than the test specimens used in the calibration of the Eligehausen *et al*. (1983) model. Clear spacing between lugs affects the bond stress vs. slip behavior substantially. As the clear spacing between lugs increases, the slip also increases. Since the slip parameters (s_1, s_2 and s_3) of the monotonic bond stress vs. slip model were calibrated using experimental results with clear lug distance of 10.5 mm, Eligehausen *et al*. (1983) proposed to scale the slip parameters (s_1, s_2 and s_3) by c_1 (mm)/10.5 mm, but not more than +/- 30%.

Concrete Strength: Default model parameters were derived for test results from specimens with compressive concrete strength values of 30 MPa. For specimens with different concrete compressive strengths, it is suggested to modify the parameters τ_1 and τ_3 with a factor of $(f_c'/30)^{\beta}$, where f'_c is in MPa and β = 1/2 to 2/3.

Clear Spacing: Peak (τ_1) and residual (τ_3) bond stresses values are reduced if the clear spacing between longitudinal reinforcing bars is smaller than $4d_b$.

External Pressure: If external transverse load (pressure) is applied along the anchorage or lap-splice length, then the maximum and residual bond stresses should be increased. In typical cases, especially for lap splices in columns, no external transverse loads are applied along the splice region; therefore, no modification to the default value is necessary.

Table 4.1. Eligehausen *et al*. (1983) Local Bond Stress – Slip Material Model Parameters for Confined and Unconfined Concrete.

	Confined Concrete		Unconfined Concrete	
	Tension Side	Compression Side	Tension Side	Compression Side
u1	13.5 MPa	13.5 MPa	5 MPa	20 MPa
u3	5 MPa	5 MPa	0	7.5 MPa
s1	1 mm	1 mm	0.3 mm	1 mm
s2	3 mm	3 mm	0.3 mm	s2 = 3 mm
s3	10.5 mm	10.5 mm	1 mm	10.5 mm
α	0.4	0.4	0.4	0.4

Loading Rate: The envelope relationship is based on pull-out tests where the loading rate (slip per minute) was controlled. The test results indicated that the slip rate influenced the maximum (τ_1) and residual (τ_3) bond stresses values achieved during the tests, where the maximum and residual bond stresses increased as the slip rate increased. Eligehausen *et al*. (1983) proposed a modification to account for slip rate, where the default bond stresses are modified by -/+15% for slip rates between 0.01 mm/min and 100 mm/min using a logarithmically linear relation.

4.5.1.2. Hysteretic Rules. The hysteretic unloading/reloading behavior of the constitutive model by Eligehausen *et al*. (1983) consists of several branches as shown in Figure 4.18, in which the dashed line represents test results and the solid line indicates the constitutive model response. Figure 4.19 illustrates the characteristics of the complete hysteretic bond stress vs. slip constitutive relation, which is described in the following paragraphs.

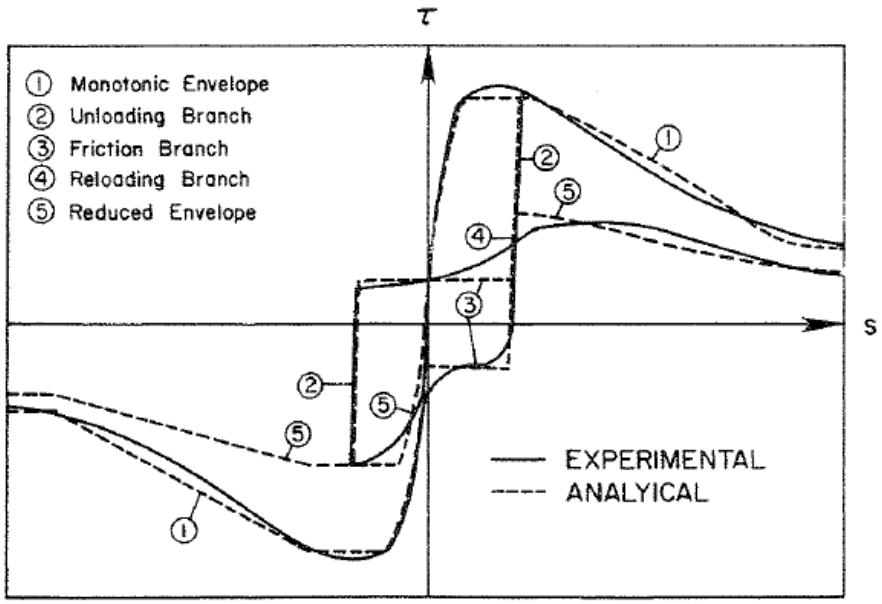

Figure 4.18. Hysteretic Branches of Bond Stress vs. Slip Constitutive Model for Confined Concrete (Eligehausen *et al*. ,1983).

Upon each successive unloading and reloading, reduced bond stress vs. Slip envelopes are derived from the monotonic envelopes, by reducing the characteristic bond stress $\tau 1$ and $\tau 3$ through reduction factors, which are formulated as a function of a parameter, called the "damage factor" (d). It can be observed in Figure 4.19 that maximum bond resistance ($\tau 1$) deteriorates faster than the ultimate frictional resistance (τ_3). However, there is a strong correlation between the deterioration rate of the maximum and frictional bond resistance values. This can be observed in Figure 4.21, which illustrates the reduction of the frictional resistance τ_3 as a function of the damage parameter d, deduced from the reduction in the maximum bond resistance τ_1. Figure 4.20 illustrates the correlation between the measured damage factor,d as a function of the calculated dimensionless dissipated energy factor, E/E_0.

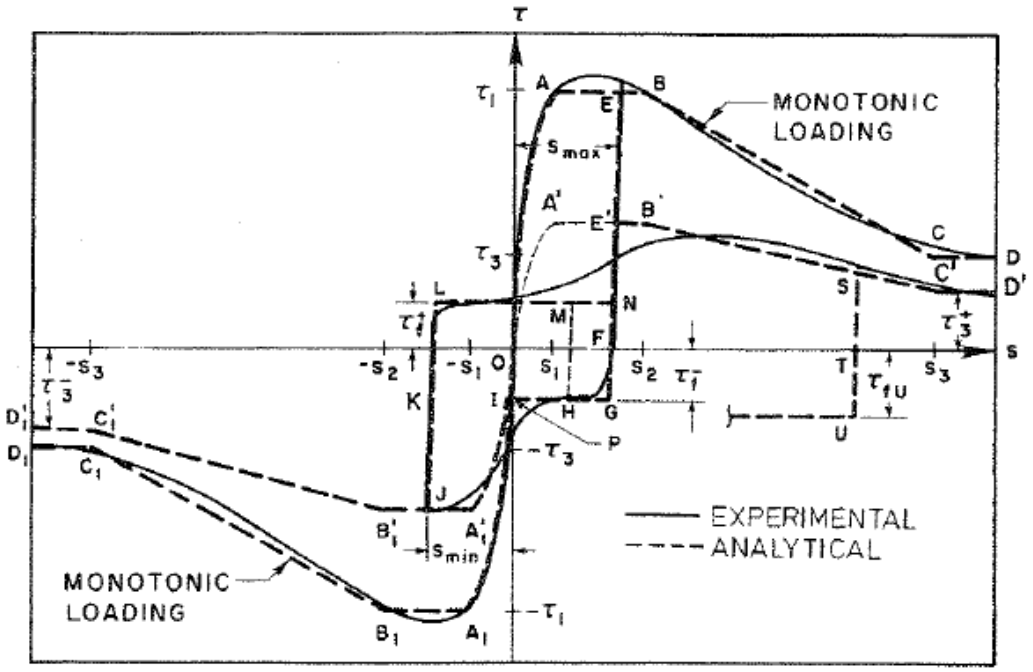

Figure 4.19. Proposed Analytical Model for Local Cyclic Bond Stress-slip Relationship for Confined Concrete (Eligehausen *et al*. ,1983).

The normalized energy, E_0, corresponds to the absorbed energy under monotonically increasing slip deformation up to a value of s_3. Therefore, from Figure 4.20,

$$\tau_1(N) = \tau_1(N=1)(1-d) \tag{4.109}$$

where N is the number of cycles and $d = 1 - e^{-1.2(E/E_0)^{1.1}}$

$$\tau_3(N) = \tau_3\left(1 - \frac{d}{2-d}\right) \tag{4.110}$$

τ_3^-, τ_3^+ as shown in Figure 4.19, can be solved from Equation (4.110)

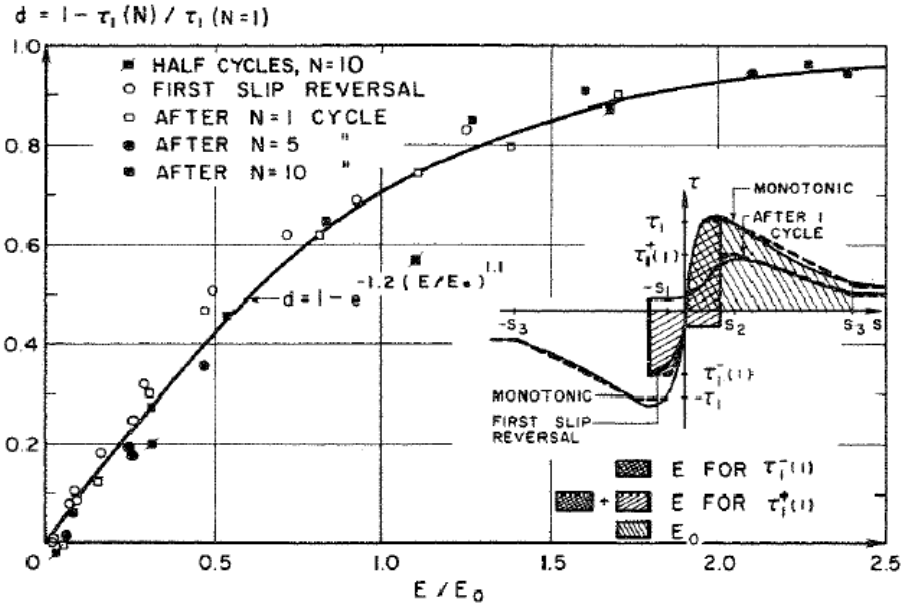

Figure 4.20. Damage Factor, d, for the Reduced Envelope as a Function of the Dimensionless Energy Dissipation Ratio E/E_0 (Eligehausen *et al*. ,1983).

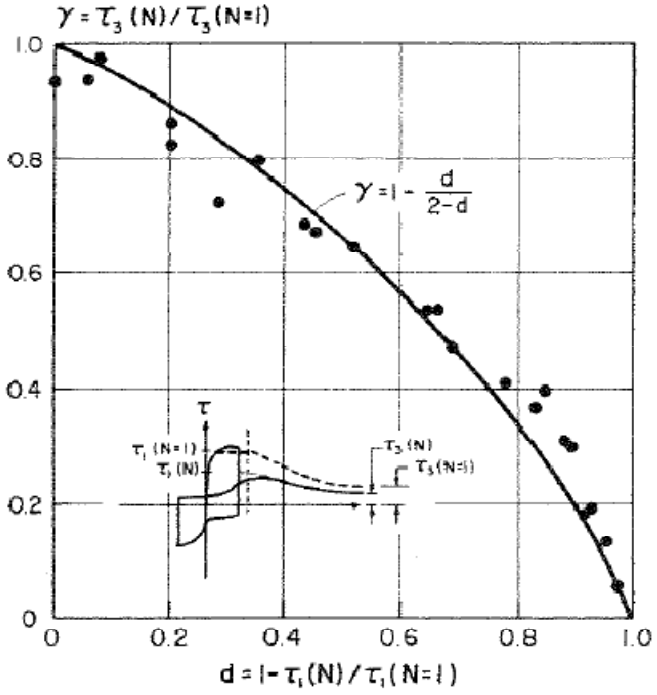

Figure 4.21. Ratio of the Ultimate Frictional Bond Resistance of the Reduced Envelope to that of the Monotonic Envelope as a Function of the Damage Factor, d (Eligehausen *et al*. ,1983).

No reduction of the envelope (monotonic or reduced) is assumed for partial unloading or reloading (e.g. path EFE, Figure 4.19). In the tests, cycles were always carried out between increasing peak values of slip deformation. However, during generalized excitations, it is possible that a cycle is not completed to the envelope values of s_{max} and s_{min} (e.g. path GHM in Figure 4.19). In this case, the damage parameter is interpolated between the values valid for the last slip reversal and for the completed cycle (point E and point P in this example) using following equation:

$$d = d_L + (d_c - d_L)\frac{s_L - s}{s_L - s_C} \tag{4.111}$$

where,

d : damage factor of current inversion point (point H in example)

d_L: damage factor of last inversion point (point E in example)

d_C: damage factor for the completed cycle (point P in example)

s_L:slip value of last inversion point (slip of point E in example)

s_C: slip value of completed cycle (slip of point P in example)

s: slip value of current inversion point (slip of point H in example)

The frictional bond resistance (τ_f in Figure 4.19) is related to the value of the ultimate bond resistance of the corresponding reduced envelope (τ_3 in Figure 4.19). The relationship between τ_f and τ_3 as a function of the ratio s_{max}/s_3 deduced from the tests is shown in Figure 4.23. The following relationships were derived by Eligehausen *et al*. (1983) based on results presented in Figure 4.23:

if $(s_{max}/s_3) < 0.50$

$$\tau_f(N) = \tau_3(N)\left(0.10 + 1.8\,s_{max}/s_3\right) \tag{4.112}$$

if $(s_{max}/s_3) > 0.50$

$$\tau_f(N) = \tau_3(N) \tag{4.113}$$

The expression above is used only for the calculation of the frictional resistance for the first slip reversal (τ_f^- in Figure 4.19).

Figure 4.22 illustrates the correlation between the measured reduction factor d_f as a function of the computed dimensionless dissipated energy factor E_f/E_{of}, as well as the proposed function for d_f. E_f is the energy dissipated by friction alone and the normalizing energy E_{of} is equal to the product of τ_3 and s_3. Based on results presented in Figure 4.22 the following expression was proposed by Eligehausen *et al*. (1983):

$$\tau_f(N) = \tau_{f0}\left(1 - d_f\right) \tag{4.114}$$

where

$$d_f = 1 - e^{-1.2(E_f/E_{of})^{0.67}} \tag{4.115}$$

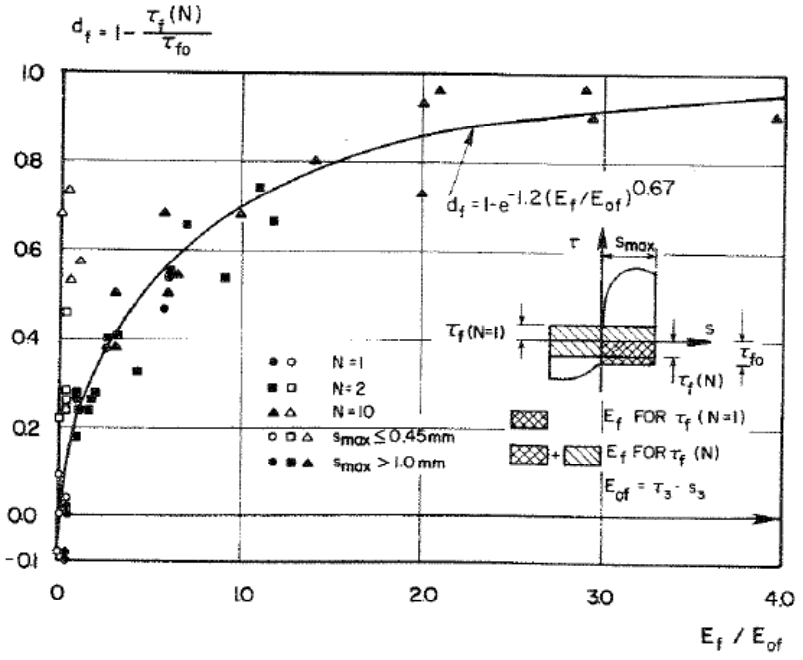

Figure 4.22. Damage Factor, d_f, for Frictional Bond Resistance during Cycles, as a Function of the Dimensionless Energy Dissipation E_f/E_{of} (Eligehausen *et al*. ,1983).

If unloading is from a larger slip deformation value than the peak slip in the previous cycle (e.g. path STU in Figure 4.19), the new frictional bond resistance, τ_{fu}, is interpolated between two values (Figure 4.24). The first value is related to the τ_3 (residual bond stresses) value of the corresponding new reduced envelope using the analytical function given in Figure 4.23 and the second value is the τ_f (frictional bond resistance) value reached in the last cycle (τ_f (1) in Figure 4.24).

Regarding variability of the cyclic parameters with testing conditions, Eligehausen *et al*. (1983) stated that the cyclic parameters described above may be assumed valid valid for different test conditions than those based on which they have been determined. Details of the complete constitutive model formulation are presented in the report by Eligehausen *et al*. (1983).

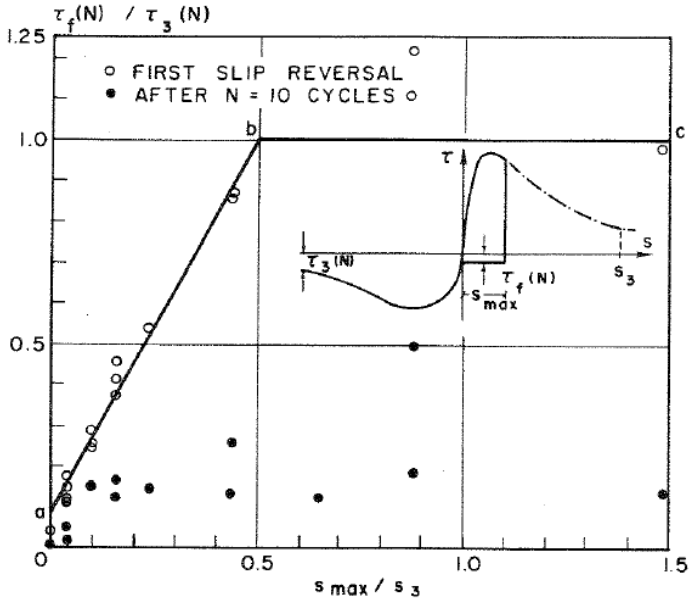

Figure 4.23. Relationship Between Frictional Bond Resistance during Cycling, $\tau_f(N)$, and the Corresponding Ultimate Frictional Bond Resistance $\tau_3(N)$ (Eligehausen *et al*. ,1983).

4.5.2. Constitutive Bond Stress vs. Slip Models by Harajli *et al.* (1994, 2002, 2004, 2009)

Harajli *et al*. (1994, 2002, and 2004) proposed constitutive bond stress vs slip relationships which may be applied to reinforcing bars embedded in plain (unconfined) concrete and fiber reinforced concrete under monotonic tension, and are applicable to both bond splitting and pull-out type failures (Harajli *et al*., 1994). The models were developed upon compiling a broad database of experimental results, including the tests conducted by Eligehausen *et al*. (1983) and Harajli *et al*. (1995).

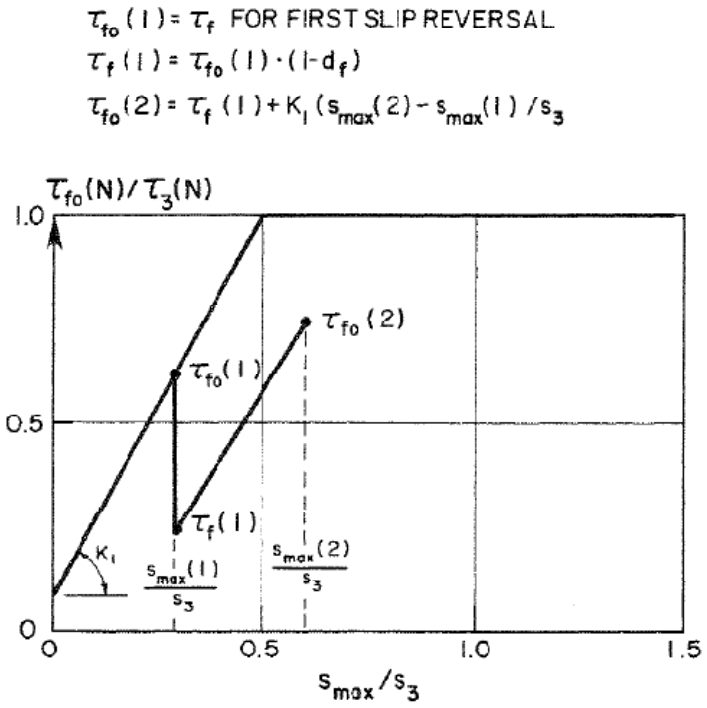

Figure 4.24. Calculation of Zero Initial Frictional Bond Resistance for Unloading from Larger Value of Peak Slip s_{max} than Previous Cycles (Eligehausen *et al.* ,1983).

4.5.2.1. Monotonic Envelope. The original model formulation consisted of two monotonic backbone relationships, representing pull-out and splitting failures for confined and unconfined concrete, respectively (Figure 4.25). The model has been updated since it was first proposed in 1994. Harajli *et al*. (2004) proposed modifications to incorporate the influence of partial confinement on the bond stress vs. slip response of reinforcing bars experiencing splitting type failures.

The ascending branch of the local bond stress – slip relationship proposed by Harajli *et al*. (1994) is very similar to the one proposed by Eligehausen *et al* (1983), and takes the form:

$$u(s) = u_1 \cdot \left(s/s_1\right)^{0.3} \tag{4.116}$$

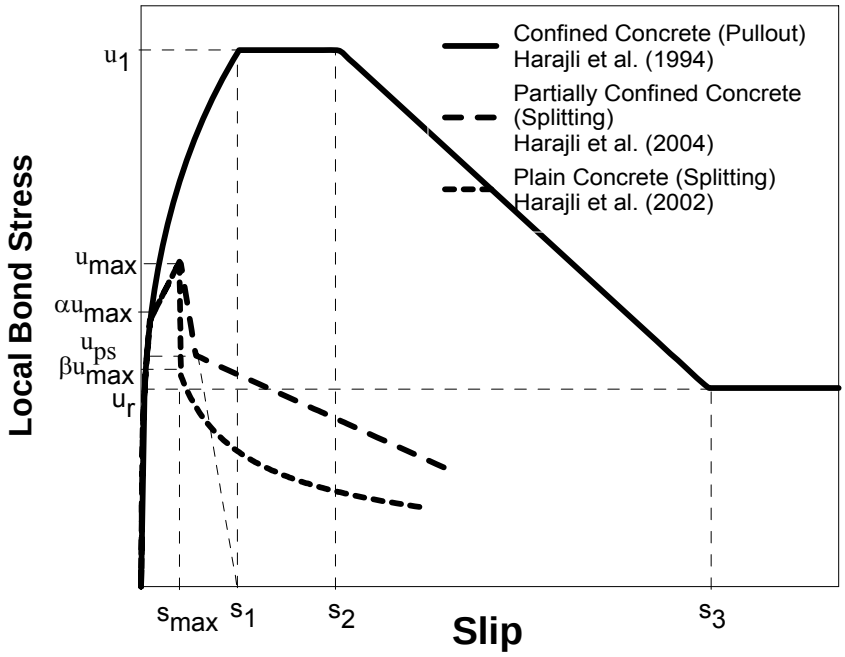

Figure 4.25. Monotonic Bond Stress – Slip Model (Harajli *et al.* ,1994, 2002, 2004).

where $s \leq s_\alpha$ and u_1 is the maximum bond stress of a reinforcement bar with a pull-out type failure and s_1 is the amount of slip deformation corresponding to the maximum bond stress (u_1). The maximum bond stress for pull-out failure (u_1) is calculated as:

$$u_{1(MPa)} = 2.57 \cdot \sqrt{f'_{c(MPa)}} \tag{4.117}$$

For members with splitting type failure, once a bond stress of αu_{max} is reached, the bond stress vs. slip relationship increases linearly until the maximum bond stress (u_{max}) is reached (Figure 4.24), according to the following expression:

$$u(s) = \alpha \cdot u_{\max} + \frac{u_{\max} - \alpha \cdot u_{\max}}{s_{\max} - s_\alpha} \cdot \left(s - s_\alpha\right) \tag{4.118}$$

where u_{max} and s_{max} are given by Equations (4.119) and (4.120), respectively, and the coefficient α is taken as 0.7.

$$u_{\max} = 0.78 \cdot \sqrt{f'_{c(MPa)}} \cdot \left(\frac{c + K_c}{d_b} \right)^{2/3} \leq u_1 \tag{4.119}$$

$$s_{\max} = s_1 \cdot e^{(1/0.3)\cdot \ln\left(\frac{u_{\max}}{u_1}\right)} + s_0 \cdot \ln\left(\frac{u_1}{u_{\max}} \right) \tag{4.120}$$

In the equations above, s_0 is 0.15 mm for plain (unconfined) normal-strength concrete and 0.40 mm (0.016 in.) for concrete confined with ordinary transverse reinforcement, and K_c is equal to $7.0 \cdot A_{tr} / (s \cdot n)$ (Harajli *et al*., 2004). The addition of the terms $((c + K_c)/d_b)$ and s_0 in Equations (4.117) and (4.118), respectively, represent improvements (Harajli *et al*., 2002) to the original model by Harajli *et al*. (1994).

These improvements are especially useful when modeling local bond stress vs. slip behavior of reinforcing bars embedded in partially (or moderately) confined concrete. For the column tests selected for this study (Chapters 7 and 8), where the transverse reinforcement spacing is too large to prevent a global splitting type failure, it is possible to account for the impact of the transverse reinforcement on the local bond stress vs. slip behavior using this model improvement. For unconfined concrete, the third branch of the monotonic bond stress – slip relationship involves a sudden drop of the bond stresses from u_{max} to $\beta\tau_{max}$ after the maximum bond stress is reached ($u = u_{max}$ and $s = s_{max}$), where β is a taken between 0.6 and 0.7. For the partially confined condition, the local bond stress vs. slip relationship does not degrade as rapidly, as shown in Figure 4.26, and follows the following expression:

$$u_{ps} = u_{\max} \cdot (0.5 + K_{cs}) \tag{4.121}$$

where K_{cs} is equal to $7.5 \cdot A_{tr} / (s \cdot c \cdot n)$. The final branch of the relationship for unconfined concrete is expressed as:

$$u(s) = \beta \cdot u_{\max} \cdot (s / s_{\max})^{-0.5} \tag{4.122}$$

where $s \geq s_3$, as shown in Figure 4.26, until the bond stress degrades to zero.

The experimental results used in development of the model indicated that the amount of slip deformation, and thus the slip parameters of the monotonic model, are dependent on the clear spacing between the lugs of the reinforcing bar. For known lug spacing, the following values for s_1 are recommended by Harajli *et al*. (1994):

$s_1 = 0.15c_1 = 1.95$ mm (0.08 in.)
$s_2 = 0.35c_1 = 4.55$ mm (0.18 in.)
$s_3 = c_1 = 13.00$ mm (0.51 in.)

If specific information on reinforcement geometry is not available, Harajli *et al*. (2002) recommends that slip parameters s_1, s_2 and s_3 be taken as 1.5 mm, 3.5 mm, and 10 mm, respectively.

4.5.2.2. Hysteretic Rules. Harajli (2009) proposed hysteretic unloading and reloading rules for the bond stress vs. slip relationship, which are applicable for the monotonic envelope shown in Figure 4.25 for partially confined concrete representing splitting mode of bond failure. Harajli (2009) proposed to adopt the idealization shown in Figure 4.26 to describe the cyclic bond stress–slip response for one cycle. Figure 4.27 illustrates the proposed idealized response for several successive cycles. The proposed hysteretic rules were generated as a function of the following characteristic cyclic response parameters: (1) slope of the unloading branch k_0, (2) slip s_r at which the rate of bond resistance experiences a sudden increase, (3) bond degradation ratio u_N/u_0.

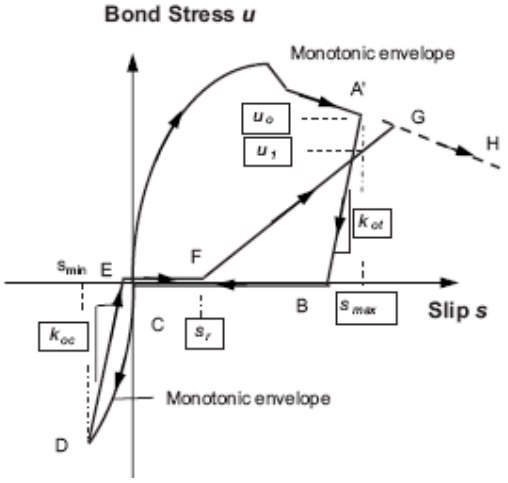

Figure 4.26. Proposed Idealized Cyclic Response for One Complete Cycle (Harajli, 2009).

Based on the observed trends in the experimental data, the following empirical expression is recommended for evaluating the slope k_{0t} of the unloading branch of the bond stress vs. slip response in tension for all values of maximum slip deformation, s_{max}:

$$k_{0t} = \frac{u_0}{s_{\max}/2} \geq \frac{u_{sp}}{s_{sp}/2} \tag{4.123}$$

provided that $k_{0t}/\sqrt{f_c'}$ is not taken less than 6.0 per mm. Because slip deformations in compression (defined when the reinforcing bar is in compression) is negligibly small, it would be sufficiently accurate to assume that first loading in compression would occur along the monotonic envelope curve in compression. For unloading or reloading in subsequent compression cycles, the slope k_{0c} would be such that the response follows a line that joins the point of zero slip to the point of maximum negative slip mobilized during the loading history (Figure 4.26).

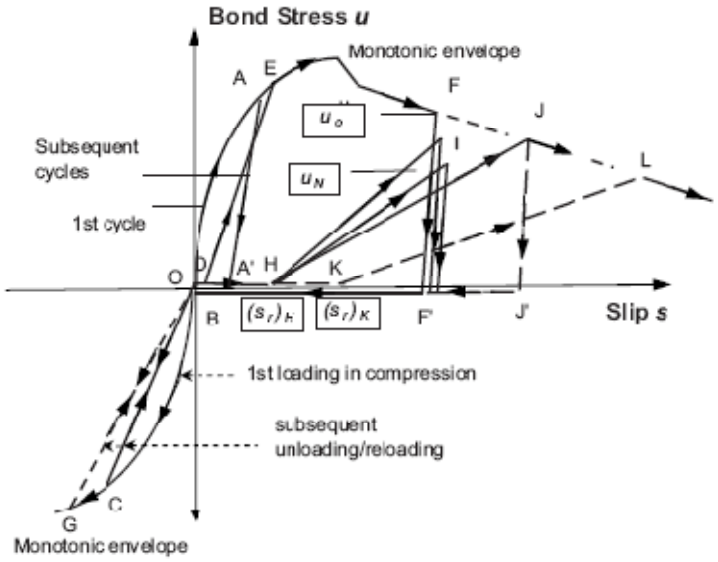

Figure 4.27. Proposed Model of Cyclic Bond Stress-Slip Response (Harajli, 2009).

Experimentally-observed variation of the slip ratio s_r / s_{max} at different values of the maximum slip deformation s_{max} for the first two reloading cycles in tension is presented in Figure 4.27. Based on the trend shown, and neglecting the expected slight increase in

s_r / s_{max} with subsequent loading cycles, the following regression equation for estimating s_r was derived by Harajli (2009):

$$\left(\frac{s_r}{s_{max}}\right) = 0.44 + 0.035\ln(s_{max}) \tag{4.124}$$

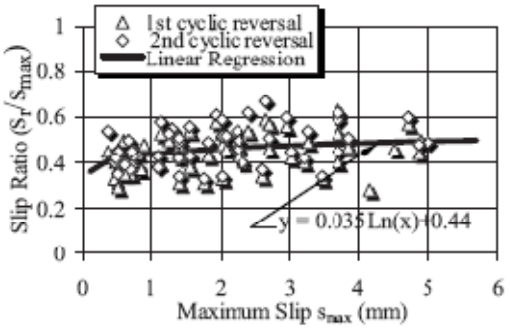

Figure 4.28. Variation of Slip Ratio s_r / s_{max} with Maximum Slip Deformation (Harajli, 2009).

The bond degradation response associated with cyclic loading is simulated through a bond degradation ratio u_N/u_0, where u_0 =bond resistance at slip s_{max} on the envelope curve from which first unloading occurred, and u_N is the bond stress at slip $s=s_{max}$ corresponding to tension reloading cycle. The bond degradation ratio was observed to be mostly dependent on the number of cycles and maximum slip s_{max} value mobilized during the loading history; however, it was practically insensitive to the bar diameter or ratio of concrete cover to bar diameter and type of confinement used. For larger slip deformation values beyond splitting, the average bond degradation ratio decreases considerably but is practically independent of the maximum slip s_{max}.

Figure 4.29 shows variation of the bond degradation ratio u_N/u_0 with number of cycles N corresponding to the limited number of cycles generated for two different ranges of maximum slip s_{max}. Regression analysis to the experimental data presented in Figure 4.29 leads to the following expressions for evaluating the bond degradation ratio with number of cycles for complete half-cycles:

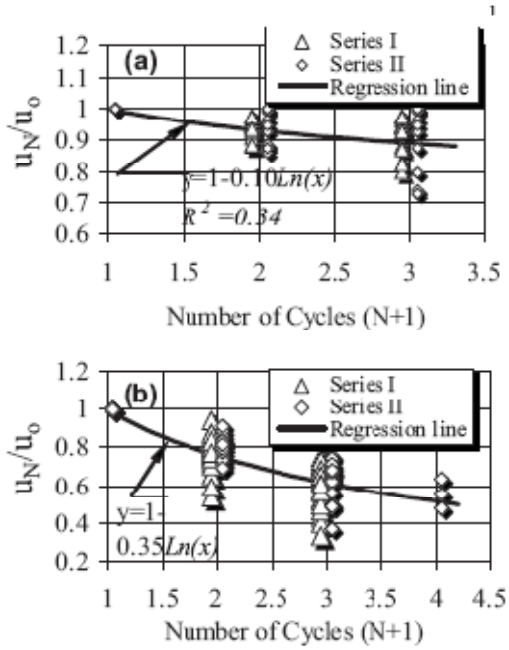

Figure 4.29. Variation of Bond Degradation Ratio u_N / u_0 with Cycle Number N: (a) $s \le s_{sp}$ and (b) $s \ge s_{sp}$ (Harajli, 2009).

For slip deformation *s* less than or equal to s_{sp},

$$\frac{u_N}{u_0} = 1 - 0.1\ln(N+1) \tag{4.125}$$

For slip deformation *s* greater than s_{sp},

$$\frac{u_N}{u_0} = 1 - 0.35\ln(N+1) \tag{4.126}$$

For the case of incomplete cycles, the bond stress vs. slip behavior is assumed to follow the simple bilinear response shown in Figure 4.30. Details of the constitutive model are presented in the paper by Harajli (2009).

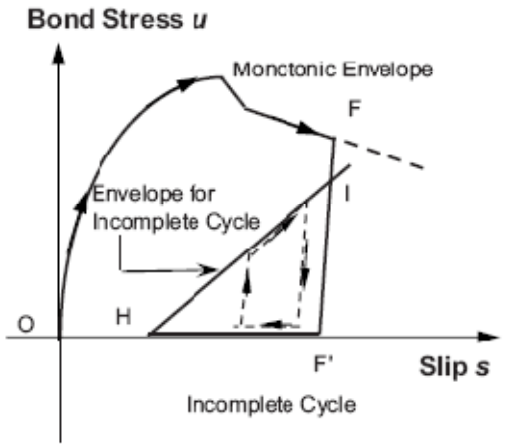

Figure 4.30. Simplified Response for Incomplete Cycle (Harajli, 2009).

4.5.3. Constitutive Bond Stress-Slip Model by Verderame *et al.* (2009) for Smooth Reinforcing Bars

The existing literature does not offer significant contribution on the definition of numerical models representing the bond and interaction mechanisms between plain reinforcing bars and concrete. The only code instructions relative to the local constitutive bond–slip relationship for plain bars can be found in CEB-FIP Model Code 90 (1993). This model (Figure 4.31(a)) is constituted by a first monomial branch, given by the following expression:

$$\tau_b = \tau_{b,\max}\left(\frac{s}{s_{\max}}\right)^{\alpha} \tag{4.127}$$

and a second constant branch, for s > s_{max}, with $\tau_b = \tau_{b,\max}$. Model Code 90 (1993) suggested to assume, for plain hot rolled bars, parameter α is equal to 0.5 and s_{max} = 0.10 mm. The maximum bond strength value was assumed equal to $\tau_{b,\max} = 0.30\sqrt{f_c}$ for good bond conditions and to $\tau_{b,\max} = 0.15\sqrt{f_c}$ for poor bond conditions, where f_c is the cylindrical compressive strength of concrete.

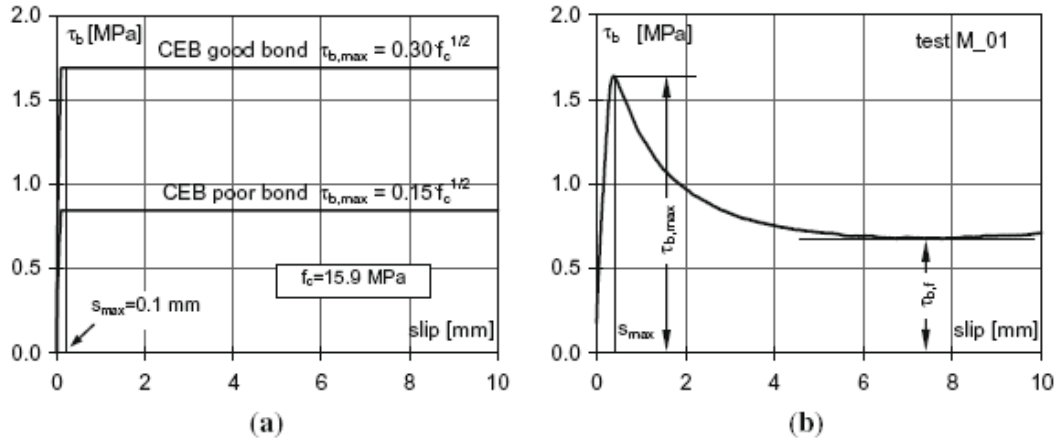

Figure 4.31. Monotonic Bond Stress vs. Slip Relationship for Plain Bars: (a) from CEB-FIP Model Code 90 (1993) and (b) from Experimental Results Reported in Verderame *et al*. (2009).

It was debated that this model cannot fully represent the effective interaction mechanisms between plain reinforcing bars and concrete. As a matter of fact, the wide experimental program carried out by Abrams (1913) and the phenomenological description proposed by Tassions (1979) and Rehm (1969) highlighted that the experimental response of a plain bar, in terms of bond stress vs. slip relationship, follows a first ascending branch up to a peak strength value corresponding to very low values of slip deformation. During this phase, chemical–physical adhesion, mechanical micro-interlocking between concrete and indentations of surface of the bar and also the friction component contribute to the bond strength. Then, a softening branch (transition curve) related to the progressive degradation of friction mechanism is present, which differs from the formulation proposed by Model Code 90 (1993). This softening branch continues until a minimum frictional value of bond stress (Figure 4.30(b)). Recent experimental results reported by Fabbrocino *et al*. (2005), Feldman and Bartlett (2005); and Verderame *et al*. (2009 a) confirmed what was asserted first by Abrams (1913) and later by Tassions (1979).

4.5.3.1. Monotonic envelope. The monotonic constitutive model which best fits the experimental bond stress vs. slip behavior for plain reinforcing bars is the one proposed by Eligehausen *et al*. (1983) (also known as BPE model, Figure 4.32), modified by removing the plateau branch with the aim of modeling the bond behavior of FRP bars Cosenza *et al*.

(1997). In Figure 4.32(a) and 4.32(b),the original and modified BPE models are shown, and respective characteristic parameters are reported. In both cases the ascending branch is expressed by the monomial expression in Equation (4.127).

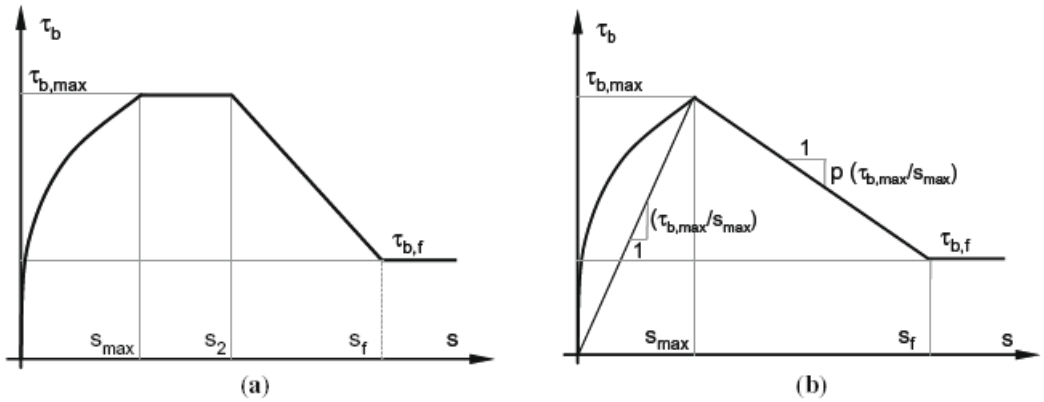

Figure 4.32. BPE Model (a) Original (b) Modified by Eligehausen *et al*. (1983).

The modified BPE model, has no horizontal branch for slippage values higher than s_{max}. A linear softening branch's expression is expressed as follows:

$$\tau_b = \tau_{b,\max} - p\frac{\tau_{b,\max}}{s_{\max}}\left(s - s_{\max}\right) \tag{4.128}$$

On the basis of the modified BPE model and experimental results obtained by Verderame *et al*. (2009, part 1), maximum bond strength $\tau_{b,max}$ was expressed to be proportional to the square root of the cylindrical compressive strength of concrete fc, through a factor equal to 0.31, with a coefficient of variation equal to 0.39 as:

$$\tau_{b,\max} = 0.31\sqrt{f_c} \tag{4.129}$$

where f_c is the cylindrical compressive strength of concrete. Equation (4.127) is consistent with the experimental observations of Fabbrocino *et al*. (2005) and with the proposal of the Model Code 90 (1993) for good bond conditions. The purely frictional bond strength was evaluated in relation with the maximum bond strength value, $\tau_{b,f}/\tau_{b,\max}$. Again, based

on experimental results, the mean value of the purely frictional bond strength is expressed as:

$$\tau_{b,f} = 0.43\tau_{b,\max} \tag{4.130}$$

with a coefficient of variation equal to 0.18. This result confirmed the theoretical observation reported in Tassions (1979), where the value of the ratio $\tau_{b,f}/\tau_{b,\max}$ was assumed to be equal to at least 0.30. Using Equation (4.128), the above relationship can be rearranged as:

$$\tau_{b,f} = 0.13\sqrt{f_c} \tag{4.131}$$

which is consistent with the proposal of Model Code 90 (1993) for poor bond conditions.

4.5.3.2. Hysteretic Rules. The hysteretic unloading and reloading rules proposed by Verderame *et al*. (2009, part II) for the modified BPE backbone relationship are illustrated in Figure 4.33. Characteristics of the hysteretic behavior are based on experimental results from cyclic pull-out tests, with different target values of maximum imposed slip deformation, as reported in Verderame *et al*. (2009 a). The hysteretic rules were derived to simulate the test results, in a simple, yet representative manner.

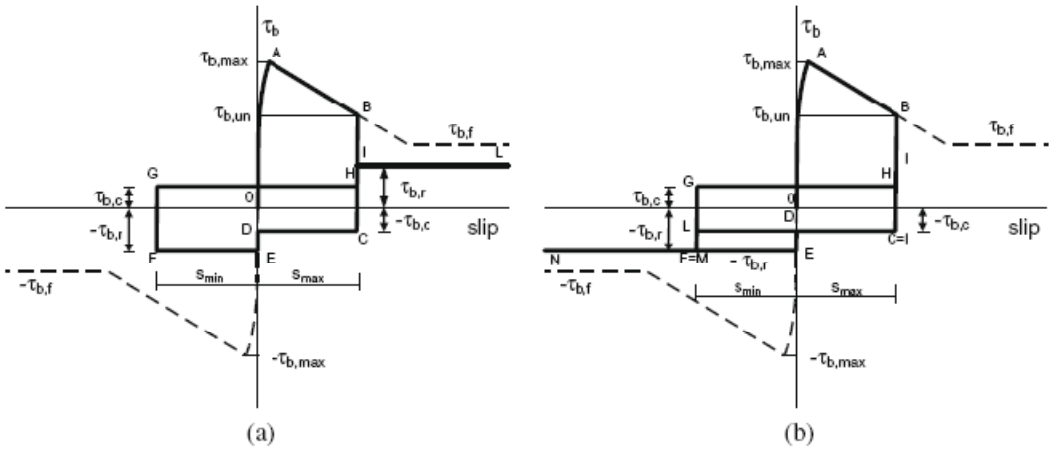

Figure 4.33. Hysteretic Bond Stress vs. Slip Relationship (Verderame *et al*. ,2009a).

When the smooth reinforcing bar is loaded for the first time, the bond stress vs. slip behavior follows the monotonic envelope curve (path 0AB). When a reversal is imposed from an arbitrary value of slip deformation, a linear unloading branch, with stiffness k_{un} is followed, until the so-called cyclic bond resistance, $\tau_{b,c}$ (path BC). This resistance value is kept constant when slip deformation decreases until the reinforcing bar reaches the initial position, which corresponds to zero slip deformation between steel and concrete. When the sign of the slip is reversed, the bond stress increases on a linear branch, with a stiffness (slope) of k_{un}, until the residual bond resistance value, $\tau_{b,r}$ (path DEF).

When a second slip reversal is imposed, the bond stress vs. slip relationship first follows an unloading branch with stiffness k_{un}, followed by a cyclic frictional branch with $\tau = \tau_{b,c}$ until the point H, located on the unloading branch (path FGH). As the slip deformation increases, a reloading branch with stiffness k_{un} is followed until the residual bond resistance ($\tau_{b,r}$) is reached, after which the bond stress is kept constant with the increasing value of slip (path HIL). On the other hand, if the slip is reversed again from point H (Figure 4.33 (b)), the bond stress decreases following an unloading branch with stiffness k_{un} until the cyclic bond resistance ($\tau = \tau_{b,c}$) is reached, after which is the bond stress is kept constant for increasing negative values of slip up to the maximum slip value attained previously. When this maximum slip value is reached, the relationship follows a reloading branch up to the constant bond stress branch, corresponding to $\tau = \tau_{b,r}$ (path HILMN).

In this constitutive model, under cyclic excitations and in correspondence with values of slip higher than the maximum one previously attained, the bond stress vs. slip relationship does not reach the monotonic envelope curve, but to reduced bond stress values bounded by the purely frictional bond resistance, $\tau_{b,r}$. During the cycles, the bond stress is kept constant at a value of $\tau_{b,c}$, both during pulling out and pushing in of the bar. Therefore, to completely define the hysteretic model, only two parameters are required, which are the residual bond resistance ($\tau_{b,r}$) and the cyclic bond resistance ($\tau_{b,c}$). Finally, assuming that no further degradation of the bond resistance takes place as the number of

partial loading cycles increases, the proposed model yields symmetric bond stress vs. slip behavior, which is consistent with experimental observations, which also do not highlight significant asymmetry associated with the first loading direction.

Verderame *et al*. (2009b) assumed that the hysteretic parameters of the constitutive bond slip behavior mainly depend on the compressive strength of concrete and the surface roughness of the bar, because of the nature of the interaction mechanisms at the interface between plain bars and concrete. Therefore, as done with $\tau_{b,f}$ in the definition of the monotonic envelope curve, parameters $\tau_{b,r}$ and $\tau_{b,c}$ are evaluated to be proportional to the maximum bond resistance. Neglecting the variability in the surface roughness of reinforcing bars, it is possible to extend the proposed model to different values of the concrete strength, basing on the defined ratios between the maximum bond resistance and the square root of the cylindrical compressive strength of concrete. It was stated that this assumption is yet to be better investigated by executing cyclic pull-out tests with different values of concrete strength (Verderame *et al*., 2009 b).

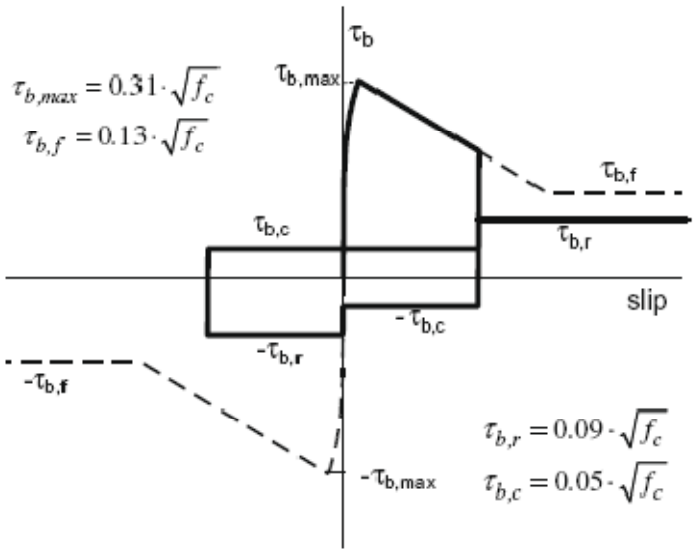

Figure 4.34. Hysteretic Bond-slip Relationship for Plain Reinforcing Bar (Verderame *et al.*, 2009b).

Details on the characteristic parameters of the constitutive bond stress vs. slip relationship, as well as possible maximum and minimum values and coefficients of variation are described in Verderame *et al*. (2009b). Figure 4.34 illustrates a brief summary of the model, with characteristic values used for the parameters. For the model implemented in this study, the slope of the linear unloading and reloading branches were taken as is k_{un} = 15 MPa/mm, based on the overall average experimental value observed . by Verderame *et al*. This value was assumed to be constant and not depending on the number and the magnitude of cycles. The progressive stiffness degradation due to the increase of the maximum imposed slip was therefore neglected. As a matter of fact, according to the experimental data, this stiffness changes from an average value of about 28 N/mm3, corresponding to s_{max} = 0.5 mm, to a value of 8 N/mm3 when s_{max} = 8.0 mm. It was observed that this simplification has no significant influence on the structural response modeling, as long as this stiffness does not assume values significantly higher than the experimental variability range..

4.5.4. Constitutive Model for Axial Stress in Bar vs. Slip Deformation for 180-degree Circular Hooks by Fabbrocino *et al*. (2002, 2005)

4.5.4.1. Monotonic Envelope. Fabbrocino *et al*. (2005) conducted out pull-out type tests in order to evaluate the response, in terms of axial stress in reinforcing bar vs. slip deformation relationship, of 180° circular hooks, which is the most common anchorage condition for smooth bars in column splices. In the experimental program, three different specimen configurations were considered, including ‘full’ type specimens, ‘end’ type specimens and ‘full-H’ type specimens. Here, only the ‘full’ type specimen configuration (Figure 4.35 (b)) is discussed, as this configuration is applicable to 180-degree hooks in typical column splices. The tests were conducted in such a way that only the hook was embedded in the concrete specimen (Figure 4.35(b)), and a direct measure of the slip deformation at the end of the hook could be obtained. The loading was applied under displacement control. The main parameters investigated during the experimental study were the bar diameter, the concrete cover thickness, the cast direction, and the type of loading (monotonic or cyclic).

Figure 4.35(a) provides an overview of experimental results on hooks made of 12 mm diameter reinforcing bars. The test results given are in terms of σ_{hook} (bar stress) vs. s_{hook} (hook end slip) relationships for specimens that fit the bond conditions for hooks at column base or anchored in interior beam column joints. Test results indicate that the hook shows a very high initial stiffness, followed by a pronounced nonlinear behavior even at low stress levels. However, and interestingly, the bar shows the capacity to reach yield stress, under progressively increasing slip deformations. Therefore, a pure slip failure does not occur. The bar stress vs. slip response is not characterized at yield by a well-defined yield plateau (due to the limited yield spreading along the circular branch, so that yielding develops only in the straight unbounded region), and significant increase in slip deformation can be observed only after strain hardening starts.

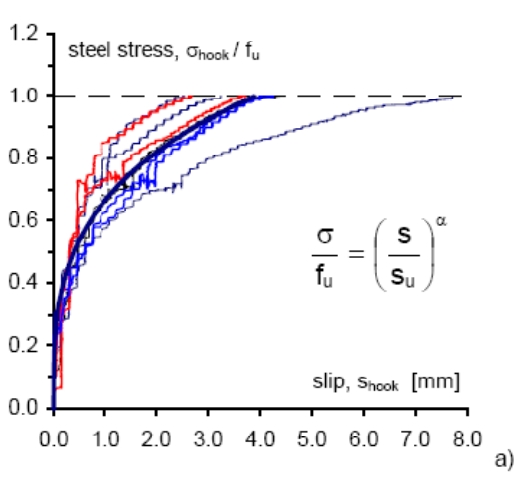

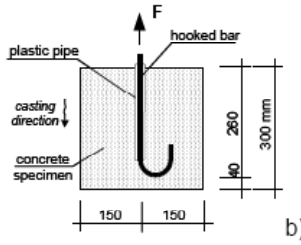

Reference test group	α	s_u (mm)
(a)	0.30	4.10
(b)	0.25	3.10
(c)	0.37	4.00
All	0.30	3.90

Figure 4.35. Results of Experimental Tests and Stress-slip Relation for 180-degree Hooks Fabbrocino *et al*. (2005).

Based on the test results, a constitutive bar stress vs. hook end slip deformation relationship was derived by Fabbrocino *et al*. (2005), the formulation of which resembles the first monotonic branch of the constitutive relationship by Eligehausen *et al*. (1983) (Figure 4.35):

$$\sigma = f_u \left(\frac{s}{s_u} \right)^{\alpha} \tag{4.132}$$

where s is the hook end slip, s_u is the hook end slip at bar failure, f_u is the bar ultimate stress, and α is a dimensionless positive exponent that is generally smaller than 1. Ultimate

stress and slip at bar failure are used as basic parameters of the theoretical formulation; the first of which is a parameter depending upon the steel grade, and the second of which can be evaluated using statistical analysis of available test results. Regression analysis results on the experimental data is shown in Figure 4.35(a), with reference to different hook orientations (test groups a, b, and c denote hook being parallel to concrete casting direction, and perpendicular to casting direction with hook downward and upward respectively). Optimal parameters depending on hook orientation as well as based on all test data is reported in Figure 4.35. In this study, the overall average values ($\alpha = 0.30$, s_u, = 3.90 mm) were used to represent the constitutive behavior of 180-degree hooks.

4.5.4.2. Hysteretic Behavior. Fabbrocino *et al*. (2002) also carried out cyclic tests on 180° circular hooks. Some minor changes in the experimental setup was done in order to avoid buckling of the reinforcing bar when subjected to compressive stresses. Tests were carried out up to bar fracture, at longitudinal strain values higher than 0.2. Figure 4.36(a) shows the load history (bar end displacement) that was applied on the reinforcing bar specimen. Figure 4.36(b) reports the measured bar axial stress vs. bar end displacement relationship. The yielding stress level is reported on the same plot, highlighting an asymmetrical behavior. In fact, for a given displacement, the stress level reached under compression is higher than the corresponding stress level under tension. This behavior continues until concrete spalling (pushing-out) at the bottom of the concrete block (Figure 4.35(b)), which is clearly represented in the experimental results as a sudden loss in bar compressive stresses.

After this spalling occurs, the compressive strength of the hook rapidly deteriorates, and a pinching-type behavior develops . From a local point of view, the asymmetric behavior becomes more pronounced,, as shown in Figure 4.36(c), where the bar stress is plotted against hook end slip. In fact, a very stiff behavior occurs under compression during the early cycles; as the slip deformation under compression increases, a large permanent slip deformation accumulates related to progressive pulling out of the bar. This effect is however counterbalanced by an increasing level of deformation under compression, which leads to spalling concrete cone in the bottom region of the specimen block (Figure 4.35(b)). This phenomenon starts a sudden reduction of the compressive

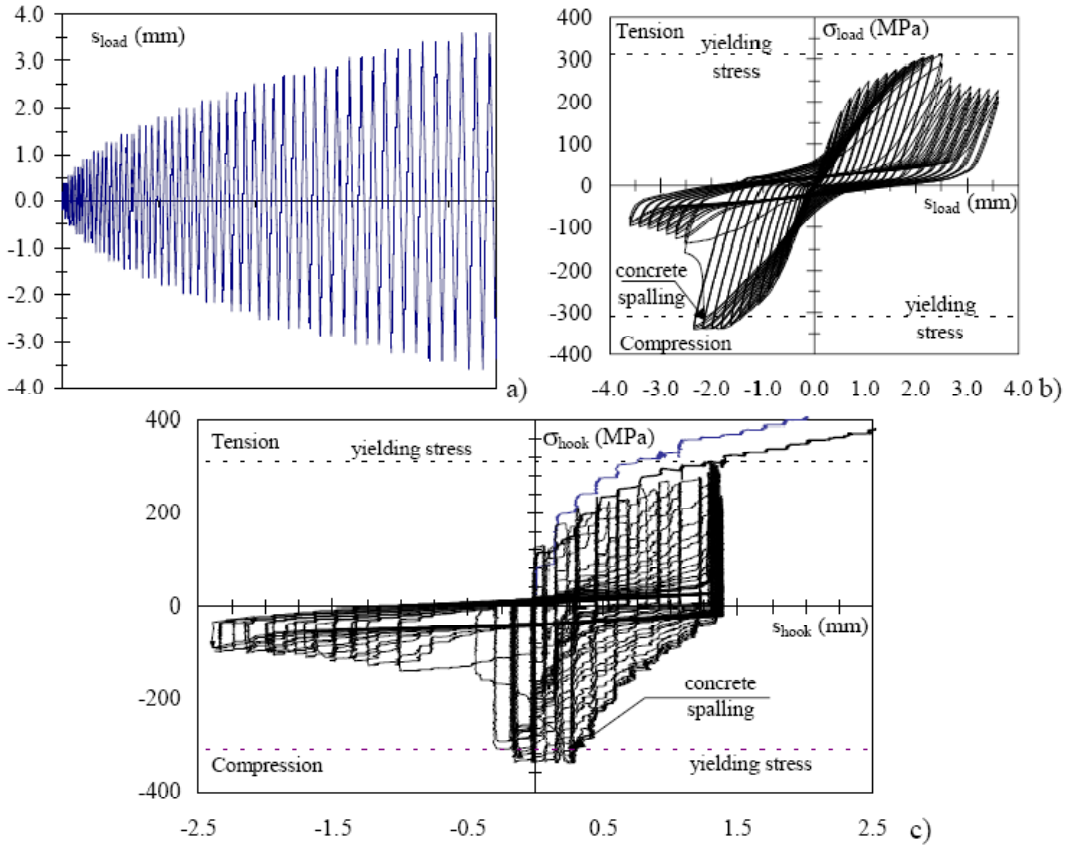

Figure 4.36. Experimental Results of Cyclic Test on 180-degree Hook Made of 12 mm Diameter Smooth Bar (Fabbrocino *et al*.i, 2002).

stress capacity and a pronounced increase of slip deformation under compression. However, this behavior is specific to the test setup, and will not be applicable to a hook in the lap splice region of a column. Therefore, and especially since a representative hysteretic behavior is not available for hooks in column splices, a simple origin-oriented hysteretic response was implemented in the present analytical model for column hooks (Figure 4.37), together with the monotonic envelope described in Figure 4.35 to relate axial stresses in a smooth bar with hook end slip deformations.

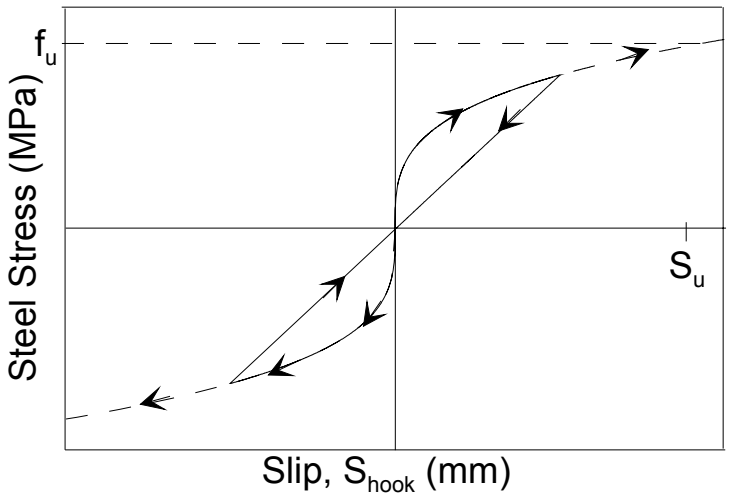

Figure 4.37. Implemented Origin-Oriented Hysteretic Constitutive Model for 180-degree Hooks.

Together with the material constitutive models for steel and concrete, and the constitutive relationships for deformed bars, smooth bars, and hooks described in this chapter, as well the nonlinear analysis solution strategy to be described in Chapter 5, the formulation of the model described in Chapter 3 was implemented in Matlab ("Matlab"), to perform nonlinear quasi-static (monotonic or cyclic) analyses using the analytical model proposed.

5. NONLINEAR ANALYSIS SOLUTION STRATEGY

The model element formulations described in Chapter 3 (with elements of 18 degrees of freedom used in the lap splice region and elements of 12 degrees of freedom used outside the lap splice region as shown in Figure 5.1) were assembled together in Matlab, using a direct stiffness assembly approach, to form a component model for an individual reinforced concrete column with a lap splice. The constitutive relationships described in Chapter 4 were implemented in the model for concrete, steel, and the bond slip springs. An appropriate incremental-iterative solution strategy was adopted for conducting nonlinear quasi-static (monotonic or cyclic) analyses of individual columns.

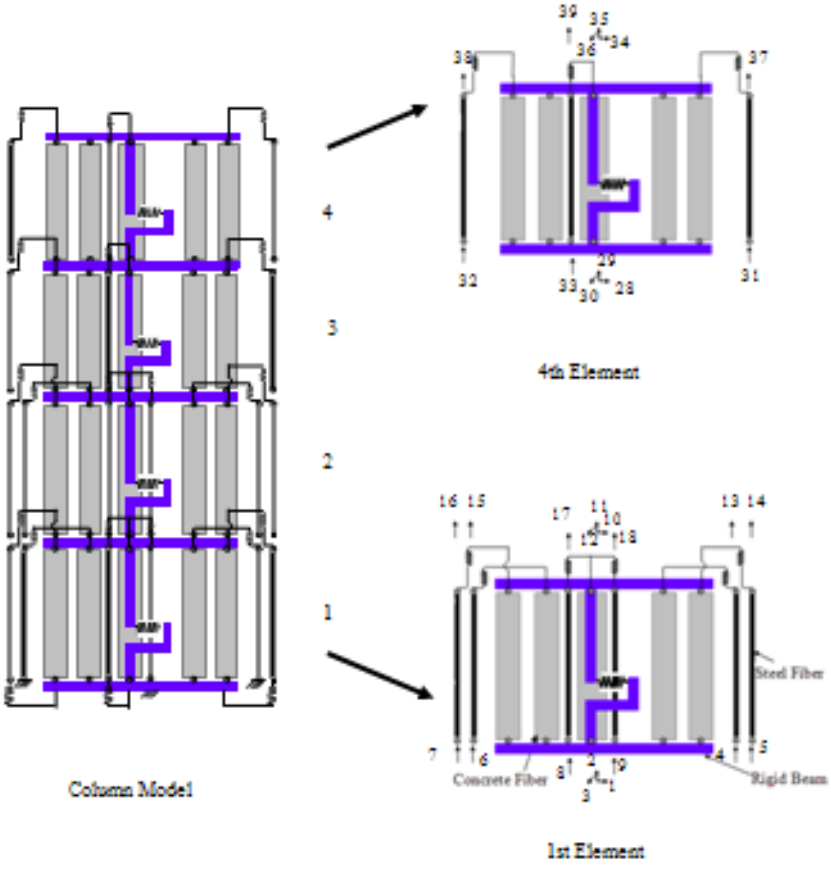

Figure 5.1. Sample Model Assembly with Degrees of Freedom.

Selection of a suitable incremental-iterative numerical solution strategy for nonlinear analysis depends on type of loading (static or dynamic) and type of analysis (load-

controlled, displacement-controlled, or combination). A displacement-controlled iterative solution strategy was implemented in this study for conducting a nonlinear quasi-static analyses, using the model formulation developed. The reason behind choosing this displacement-controlled iterative solution strategy is that the experimental programs selected for this study to calibrate and correlate the experimental results with the analytical results are drift-controlled reverse cyclic reinforced concrete column tests which are subjected to prescribed lateral displacement histories at the top of the column. Descriptions of numerical solution strategies are given below. Details of the nonlinear solution analysis strategy implemented in this study are presented in this Chapter.

5.1. The Nonlinear Quasi-Static Problem

Figure 5.2 illustrates a generic nonlinear quasi-static response, in the form of analytically-obtained lateral load vs. top displacement behavior of a reinforced concrete column subjected to a reverse cyclic lateral loading imposed at the top. In order to generate a quasi-static response, the external load or displacement effects are applied with a sufficiently slow rate, such that they do not induce dynamic effects on the analytical (or experimental) response.

The general equilibrium equation for nonlinear quasi-static response can be expressed as:

$$\left\{F_{\text{int}}\left(\delta\right)\right\} = \left\{F_{ext}\right\} \tag{5.1}$$

where $\left\{F_{\text{int}}\left(\delta\right)\right\}$ denotes the internal resisting force vector, which is a nonlinear functional of system (nodal degree of freedom) displacements, and $\left\{F_{ext}\right\}$ is the external force vector, representing the externally applied forces at the nodal degrees of freedom. In the case of a linear elastic system, the static problem would reduce to the linear equation as

$$\left[K\right]\left\{\delta\right\} = \left\{F_{ext}\right\} \tag{5.2}$$

where $\left[K\right]$ denotes the stiffness matrix and $\left\{\delta\right\}$ is the vector of nodal displacements.

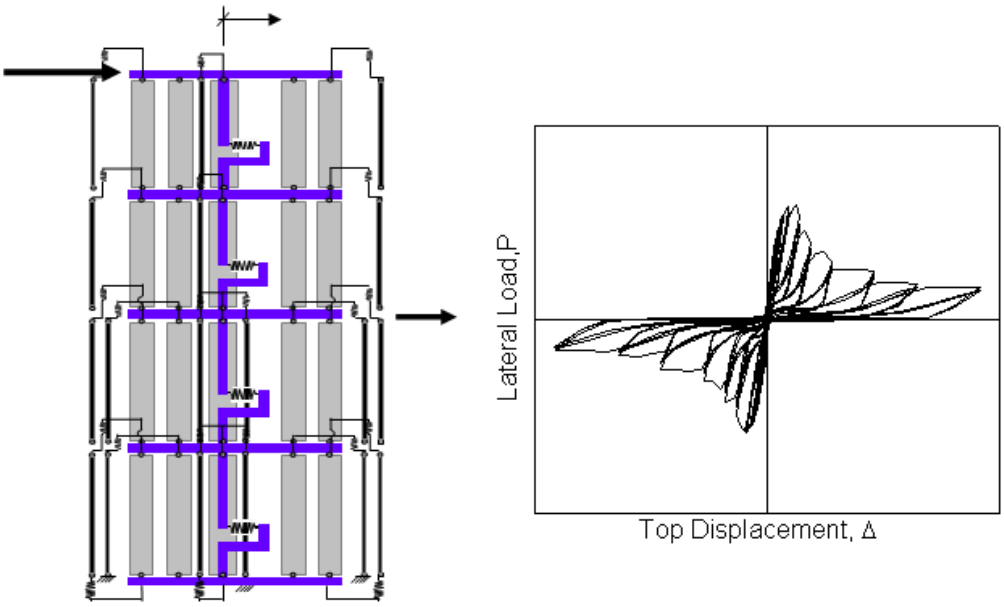

Figure 5.2. Generic Nonlinear Quasi-static Response.

5.2. Incremental Iterative Approach – Newton-Raphson Scheme

The conventional Newton-Raphson solution scheme is capable of linearizing the nonlinear equilibrium equation, through an incremental iterative strategy. Figure 5.3 illustrates a schematic of the Newton-Raphson iterative solution algorithm, with the incremental equation of equilibrium expressed as:

$$\left\{\Delta F_{\text{int}}\left(\Delta\delta\right)\right\} = \left\{\Delta F_{ext}\right\} \tag{5.3}$$

where $\left\{\Delta F_{\text{int}}\left(\Delta\delta\right)\right\}$ is the incremental restoring force vector being a nonlinear functional of the incremental nodal displacement vector $\left(\Delta\delta\right)$, and $\left\{\Delta F_{ext}\right\}$ is the incremental external load vector. Equation (5.3) is linearized within an arbitrary load step *i* about $\left\{\delta\right\} = \left\{\delta\right\}_i$, providing the equation for the first iteration within the load step as:

$$\left[K\right]_i^1 \left\{\Delta\delta\right\}_i^1 = \left\{\Delta F_{ext}\right\}_i \tag{5.4}$$

where $[K]_i^1$ denotes the tangent stiffness matrix of the system at the beginning of the load step, obtained by differentiating the internal (restoring) force resisting vector with respect to displacements at the degrees of freedom:

$$[K]_i^1 = \left.\frac{d(F_{\text{int}})}{d(\delta)}\right|_{\delta=\delta_i} \tag{5.5}$$

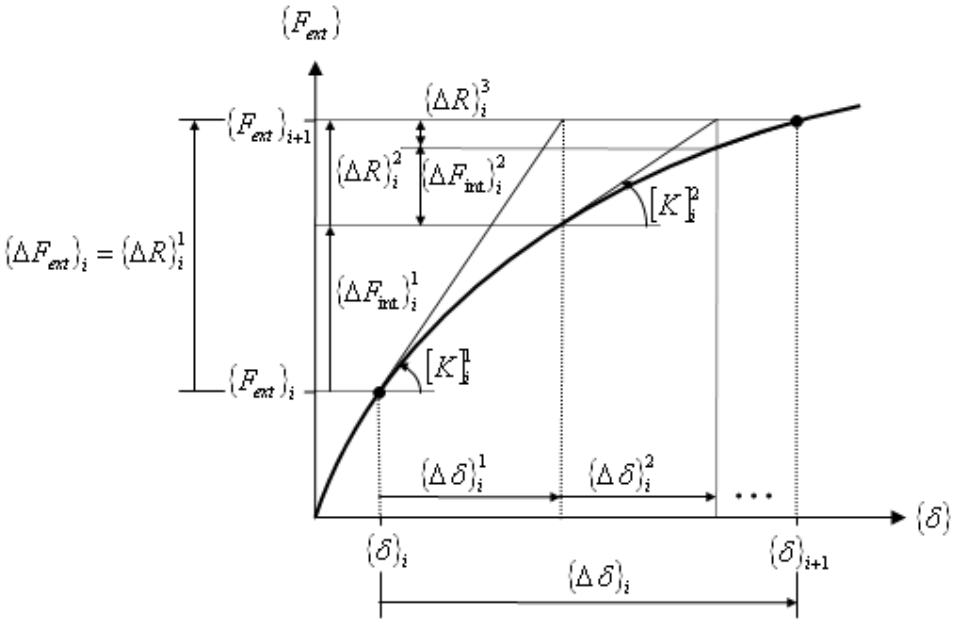

Figure 5.3. Newton-Raphson Iteration Scheme.

The linearized incremental equilibrium equation for the j'th iteration of the Newton-Raphson scheme within the load step i can be written as:

$$[K]_i^j \{\Delta\delta\}_i^j = \{\Delta R\}_i^j \tag{5.6}$$

where

$$\{\Delta R\}_i^j = \{\Delta R\}_i^{j-1} - \{\Delta F_{\text{int}}\}_i^{j-1} \tag{5.7}$$

The term $\{\Delta R\}_i^j$ represents the vector of residual forces (Figure 5.3) and the term $\{\Delta F_{\text{int}}\}_i^{j-1}$ is the increment of internal resisting forces for the iteration being equal to the difference in between the two internal resisting force vectors: $\{F_{\text{int}}\}_i^{j-1} - \{F_{\text{int}}\}_i^{j-2}$ (Figure 5.4).

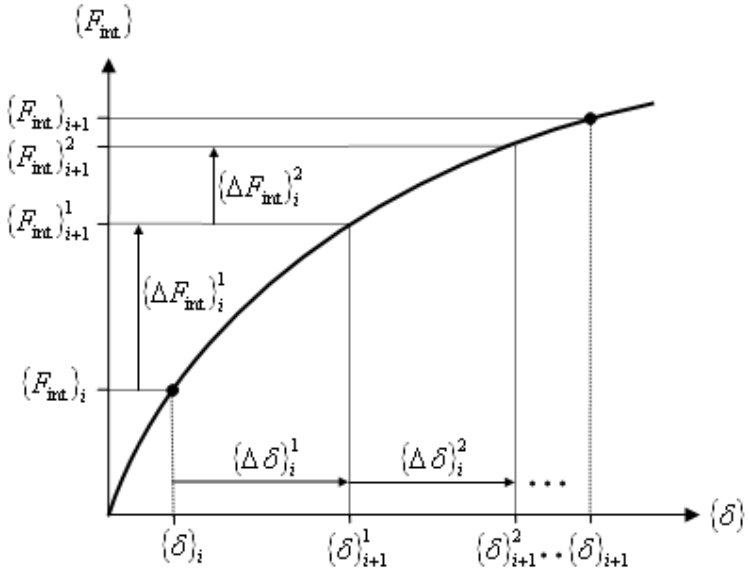

Figure 5.4. Nodal Displacement and Internal Resisting Force Increments.

After successive iterations on the incremental nodal displacement vector, Convergence is achieved by minimizing the vector of residual forces to a specified value of tolerance. The resulting incremental nodal displacement vector for the *i*'th load step can be computed as the sum:

$$\{\Delta\delta\}_i = \{\Delta\delta\}_i^1 + \{\Delta\delta\}_i^2 + \ldots\ldots\ldots + \{\Delta\delta\}_i^l \tag{5.8}$$

where *l* is the number of iterations performed in order to achieve convergence.

Although the conventional Newton-Raphson strategy successfully linearizes the equilibrium equation to obtain an iterative solution, it is incapable of passing load limit points within the quasi-static load-displacement path of the system, because the load level

is held constant while iterations are conducted to achieve convergence. Passing load limit points for incremental nonlinear analysis approaches is extremely difficult due to the near singular nature of the tangent stiffness matrix in the neighborhood of a load limit point. Iterations should be performed on externally applied loads as well as nodal displacements by introducing constraint equations within the solution strategy to proceed beyond a load limit point. Several different techniques have been proposed to pass beyond the load limit and the most well known being 'iteration at constant arc-length' introduced by Wempner (1971) and updated by Ricks (1979). An adaptation of the 'arc-length' method, with a displacement-controlled iterative strategy, based on incrementation of selected displacement components of the model (Clarke and Hancock, 1990) is used in this study as the iterative solution technique. Details of the iterative solution strategy used are described in the following section.

5.3. Applied Nonlinear Analysis Solution Strategy

The solution strategy used in this study is based on a modified Newton-Raphson iterative approach, where the tangent stiffness matrix is computed at the beginning of each load step and held constant for each load step. An iterative strategy, based on incrementation of a selected displacement component and iterations at constant value of the selected displacement component was used for the purpose of passing load limit points as well as for comparison of analysis results with results of displacement-controlled experiments conducted on column specimens.

In the incremental-iterative method implemented, each load step consists of the application of an increment of external load with subsequent iterations required to satisfy the total equilibrium equations within a specified tolerance. In this text, the notation adopted is to use the subscript *i* to denote load step number *i*, and the superscript *j* to denote the iteration cycle *j* (within load step *i*). Iteration cycles begin at $j = 1$, which is defined to correspond to an increment of external load. The equilibrium iterations commence at $j = 2$. The scalar λ denotes a load parameter to be used in combination with a reference external load vector (assuming external loading to be proportional), and $\{\delta\}$ is the vector of nodal displacements at the model degrees of freedom. There are two

distinct strategies required for the successful completion of a single load step in an incremental-iterative scheme:

(i) Selection of a suitable external load increment $\Delta\lambda_i^1$ for the first iteration cycle. The selected increment is referred to as the "initial load increment", and the particular strategy used to determine it is referred to as the "load incrementation strategy".

(ii) Selection of an appropriate "iterative strategy" for use in subsequent iterative cycles ($j \geq 2$), where the aim is to restore equilibrium as rapidly as possible. If iterations are performed on the load parameter $\Delta\lambda_i^j$ as well as the nodal displacements $\{\delta\}_i^j$, then an additional constraint equation involving $\Delta\lambda_i^j$ is required. It is the form of this constraint equation, which distinguishes the various iteration strategies.

A description of the incremental-iterative technique for a single load step i is described in the following subsections. It is assumed that perfect convergence has been achieved at the conclusion of load step $(i-1)$, so that the solution $\left(\lambda_{i-1,}\{\delta\}_{i-1}\right)$ is known to satisfy total equilibrium (Figure 5.5).

5.3.1. The First Iteration Cycle, j = 1

The new load step starts with the computation of the tangent stiffness matrix $[K_I]_i$, based on the known displacements (strains) and loads (stresses) at the conclusion of the previous load step. The initial 'tangent' displacements' $\{\delta_I\}_i$ for this load step are then computed as the solution of:

$$[K_I]_i \{\delta_I\}_i = \{F_I\}_i \tag{5.9}$$

in which $\{F_I\}_i$ is the reference external load vector, typically as specified in the input data for the problem. The magnitude of the tangent displacements is arbitrary, only their direction is important. Next, the value of the initial load increment $\Delta\lambda_i^1$ is determined

according to a particular load incrementation strategy, referred to as the "incrementation of a selected displacement component" in this study. The incremental displacements are then evaluated by scaling the tangent displacements:

$$\{\Delta\delta\}_i^1 = \Delta\lambda_i^1 \{\delta_I\}_i \tag{5.10}$$

The total displacements and load level are updated from those existing at the conclusion of the previous load step (Figure 5.5) as:

$$\{\delta\}_i^1 = \{\delta\}_{i-1} + \{\Delta\delta\}_i^1 \tag{5.11}$$

$$\lambda_i^1 = \lambda_{i-1} + \Delta\lambda_i^1 \tag{5.12}$$

At this stage the solution does not satisfy global equilibrium within the specified tolerance, so additional iterative cycles are required to restore equilibrium.

5.3.2. Equilibrium Iteration Cycles, j ≥ 2

The Newton-Raphson or modified Newton-Raphson iterative strategies are incapable of passing limit points because the load level is held constant while iterating to obtain convergence; therefore, the load parameter $\Delta\lambda_i^j$ must be allowed to vary if limit points are to be overcome. With a varying load parameter, a general solution technique evolves if it is assumed that, for any iteration $j \geq 2$ within load step *i*, the change in the incremental displacements can be expressed as:

$$[K_I]_i \{\Delta\delta\}_i^j = \Delta\lambda_i^j \{F_I\}_i - \{\psi\}_i^{j-1} \tag{5.13}$$

where,

$$\{\psi\}_i^{j-1} = \{F_{\text{int}}\}_i^{j-1} - \{F_{ext}\}_i^{j-1} \tag{5.14}$$

The vector $\{F_{\text{int}}\}_i^{j-1}$ represents the internal nodal forces obtained at equilibrium from element contributions (forces in the uniaxial elements and horizontal springs in the present model). For proportional loading, the external forces $\{F_{ext}\}_i^{j-1}$ at the conclusion of the previous iteration may be expressed as:

$$\{F_{ext}\}_i^{j-1} = \lambda_i^{j-1}\{F_I\}_i \tag{5.15}$$

The right-hand side of the Equation (5.13) is linear in $\Delta\lambda_i^j$, thus the final solution can be written as the linear combination of two vectors:

$$\{\Delta\delta\}_i^j = \Delta\lambda_i^j\{\delta_I\}_i + \{\Delta\delta_R\}_i^j \tag{5.16}$$

in which $\{\delta_I\}_i$ are the tangent displacements, already computed for $j=1$, and $\{\Delta\delta_R\}_i^j$ are the 'residual' displacements (Figure 5.6) obtained from Equation (5.17):

$$[K_I]_i\{\Delta\delta_R\}_i^j = -\{\psi\}_i^{j-1} \tag{5.17}$$

The incremental change on the nodal displacements for this iteration is computed using Equation (5.16), and the total displacements and load level are updated from the previous iteration (Figure 5.5) as:

$$\{\delta\}_i^j = \{\delta\}_i^{j-1} + \{\Delta\delta\}_i^j \tag{5.18}$$

$$\lambda_i^j = \lambda_i^{j-1} + \Delta\lambda_i^j \tag{5.19}$$

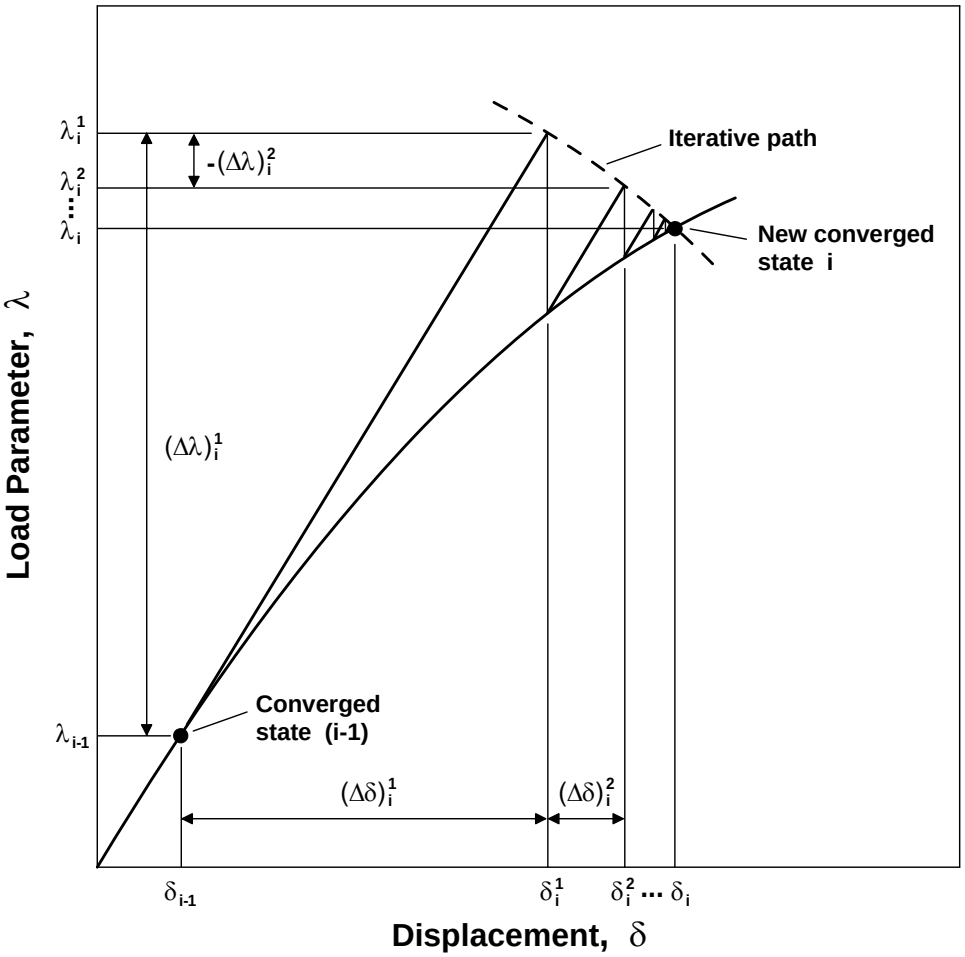

Figure 5.5. Representation of the Adapted Nonlinear Analysis Solution Scheme for a Single Degree of Freedom System.

Iteration cycles are continued until a convergence criterion based on either the forces or displacements is satisfied. If convergence is not achieved within a specified number of cycles, or if divergence of the solution is detected, a re-solution strategy may be adopted, with the application of a reduced initial load increment. The convergence criterion and the re-solution strategy used in this study are described in later subsections.

5.3.3. Load Incrementation Strategy: Incrementation of a Selected Displacement Component

The initial load increment of each load step is chosen to limit a specified 'key' displacement δ_n (being the lateral top displacement of the column in this study) in the

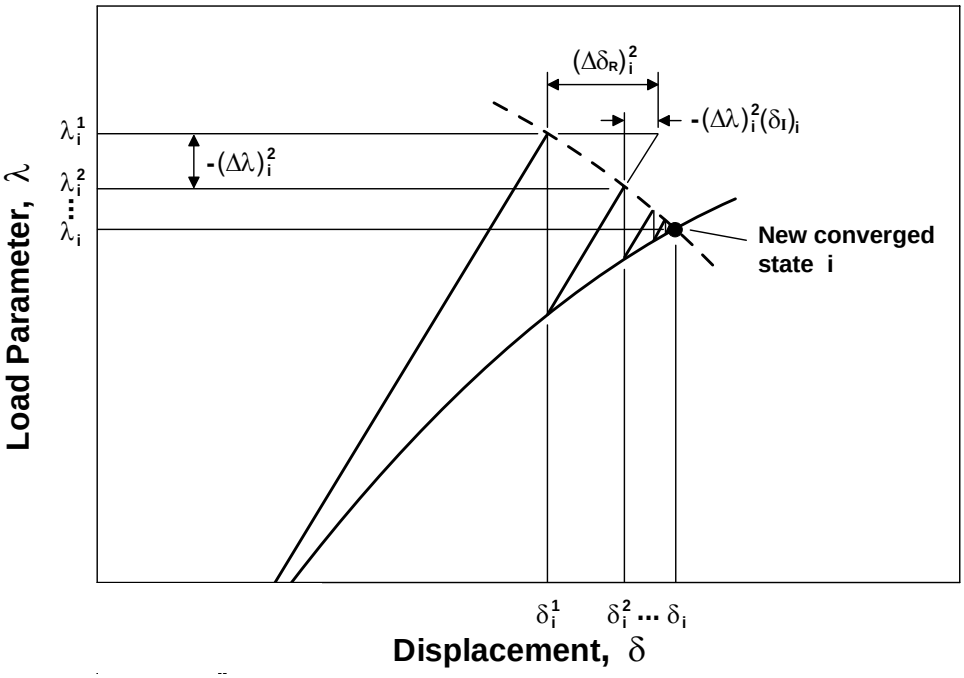

Figure 5.6. Iterative Strategy and Residual Displacements.

structure. If it is assumed that perfect convergence is achieved at the conclusion of the previous load step, the displacement increment $(\Delta\delta_n)_i$ can be expressed as:

$$(\Delta\delta_n)_i = \Delta\lambda_i^1 \{b_n\}^T \{\delta_I\}_i \tag{5.20}$$

in which $\{b_n\}$ is a vector containing unity in the *n*'th row and zero elsewhere. Hence,

$$\Delta\lambda_i^1 = \frac{(\Delta\delta_n)_i}{\{b_n\}^T \{\delta_I\}_i} \tag{5.21}$$

5.3.4. Iterative Strategy: Iteration at Constant Displacement

The constant displacement iteration strategy described here is an example of a more general technique presented by Powell and Simons (1981). In this strategy, for the first iteration ($j = 1$), the 'key' displacement component in the structure (δ_n in this case) is incremented by a prescribed amount as described in the preceding subsection. This

displacement component is held constant during subsequent iterations ($j \geq 2$). Denoting the 'key' displacement component as δ_n, the *n*'th component in the vector of nodal degrees of freedom, the increment in δ_n can be expressed as:

$$\Delta\delta_n = \{b_n\}^T \{\Delta\delta_R\}_i^j \tag{5.22}$$

in which $\{b_n\}$ is a vector of zero entries except for unity in the *n*'th row. From Equation (5.16),

$$\Delta\delta_n = \Delta\lambda_i^j \{b_n\}^T \{\delta_I\}_i + \{b_n\}^T \{\Delta\delta_R\}_i^j \tag{5.23}$$

If the value of δ_n is to remain unchanged during the equilibrium equations (constant displacement) then $\Delta\delta_n$ =0, giving the iterative change in the load parameter:

$$\Delta\lambda_i^j = \frac{-\{b_n\}^T \{\Delta\delta_R\}_i^j}{\{b_n\}^T \{\delta_I\}_i} \tag{5.24}$$

5.3.5. Convergence Criteria and Re-Solution Strategy

Iteration cycles are continued until a convergence criterion based on nodal displacements is satisfied at the end of each load step. If convergence is not achieved within a specified number of cycles, or if divergence of the solution is detected, a re-solution strategy is implemented for the load step.

A convergence criterion based on the incremental nodal displacements is used. The stringent maximum norm is adopted in the present study to test for convergence, that is:

Maximum norm:

$$\|\varepsilon\|_\infty = \max_k \left| \frac{\Delta\delta_k}{\delta_k} \right| \tag{5.25}$$

where $\Delta\delta_k$ is the change in the displacement component k during the current iteration cycle and δ_k is the value of that displacement component updated at the end of the previous iteration. Convergence is attained when:

$$\|\varepsilon\|_\infty < \zeta_c \tag{5.26}$$

where the tolerance ζ_c is typically in the range of 10^{-2} to 10^{-5} depending on the desired accuracy and the non-linear characteristics of the particular problem.

A re-solution strategy was incorporated in the iterative solution technique, if convergence is not attained at each load step within the maximum specified number of iterative cycles, or if the solution appears to be diverging. Within a single load step an increase of stiffness is the principal reason for non-convergence of the analytical model. The re-solution strategy adopted includes recovering the previous converged load step, and starting the current load step, using the initial stiffness matrix of the first load step of the nonlinear solution strategy. If convergence is still not attained within the number of specified iterations, the value of the prescribed displacement increment is reduced and the iterative strategy is repeated until convergence is attained for progressively smaller increments of the prescribed displacement component.

The incremental-iterative nonlinear solution strategy described in this chapter is ideal for obtaining the complete quasi-static load vs. deformation response of the analytical model proposed for this study, and for comparison of the model results with drift-controlled test results on column specimens. During the iterations, the lateral displacement imposed at the top of the column (selected displacement component) remains constant, and iterations are performed on both displacement and load components to obtain static equilibrium within a specified tolerance. The analytical model results obtained using this solution strategy are presented in the following Chapter (Chapter 6), where the sensitivity of the analytical results to model parameters are also discussed.

6. ANALYTICAL MODEL RESULTS AND PARAMETRIC SENSITIVITY STUDIES

The analytical model formulation presented in Chapter 3 and the constitutive relationships described in Chapter 4 were implemented in Matlab ("Matlab") together with the incremental-iterative solution strategy described in Chapter 5, for conducting nonlinear quasi-static analyses of lap-spliced columns using the analytical model proposed. Characteristics of the analytical model response and sensitivity of the model results to model parameters are presented in this chapter.

6.1. Review of the Analytical Model

The analytical model proposed in this study is capable of predicting the inelastic response of reinforced concrete columns with lap splices, considering coupling of axial, flexural and slip deformation components. The main feature of the model is that it allows distribution of the bond slip deformations over the height of the column. The model can efficiently capture neutral axis migration along the cross section, as well as the effects of, tension-stiffening, progressive gap closure, concrete confinement, nonlinear shear behavior, variation in axial force, on the response. A brief review of the model and material constitutive features is provided in this section, before presenting characteristic attributes of the model response.

In the proposed model, a reinforced concrete column is formulated as a stack of 'm' model elements, which are placed upon one another (Figure 6.1 (a)). The coupled flexural and bond slip response response is simulated by a series of uniaxial elements (or macro-fibers) of concrete connected to rigid beams at the top and bottom (e.g., floor) levels, and uniaxial steel elements connected to the rigid beams (and therefore to concrete) through uniaxial bond slip springs at top level of each model element. At the base of model, three additional bond slip springs are included for better representation of bond stresses at column base. The model element shown in lower part of Figure 6.1(b) (with 18 degrees of freedom) is used over the lap splice region (to represent spliced bars), and the element shown in upper part (with 12 degrees of freedom) is used outside the lap splice region. A

horizontal spring placed at the height *ch*, with a nonlinear hysteretic force-deformation behavior following an origin-oriented hysteresis rule with the trilinear monotonic envelope by Sezen (2002) simulates the shear response of the model element.

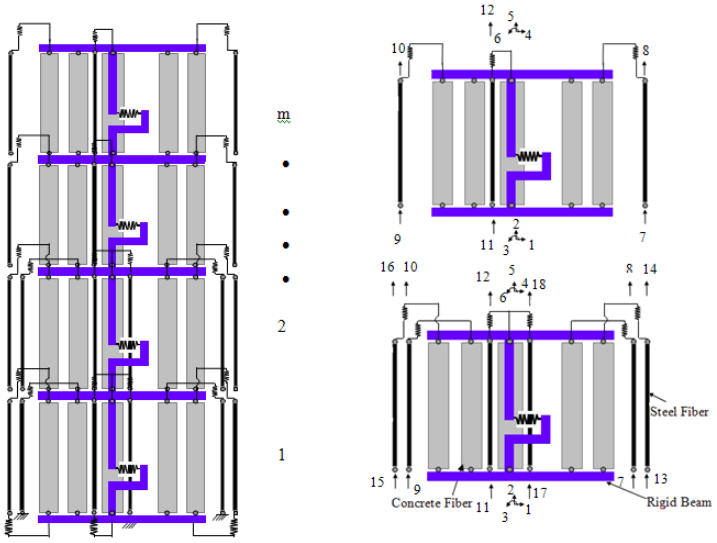

Figure 6.1. (a) Sample Model Assembly (b) Model Elements Used within and Outside the Lap Splice Region.

For representing the behavior of the bond slip springs, two alternative calibration methods were used. In the first method, along the entire length of a column, the monotonic bond stress vs. slip envelopes defined for splitting mode of failure in partially-confined concrete (Harajli *et al*., 2004, Harajli and Mabsout, 2002) were used (Figure 6.2) to account for the partial confinement effect of widely-spaced ties. The hysteretic rules proposed by Harajli (2009) was adopted for the cyclic response (Figure 6.3).

In the second methodology, the bond slip springs were calibrated to address the possibility that the transverse reinforcement would restrain the widening of splitting cracks locally, close to the tie. Bond slip springs close to tie locations were assigned constitutive bond slip relationships representing slip failure, whereas the springs between the ties were

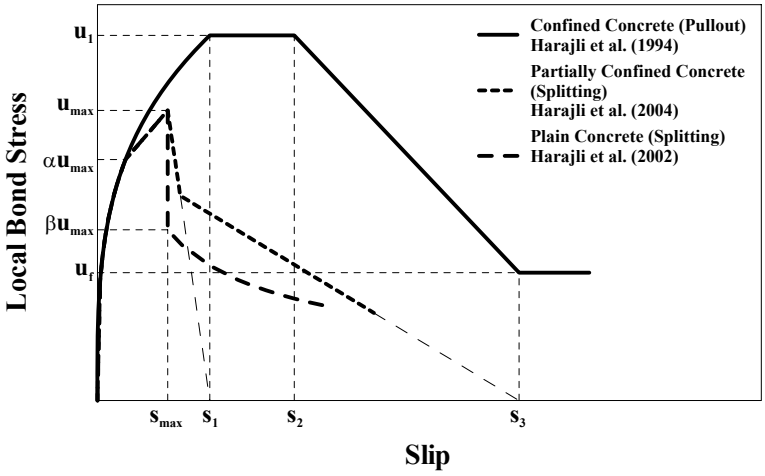

Figure 6.2. Monotonic Bond Stress vs. Envelopes (Harajli *et al.*,1994, 2002, 2004).

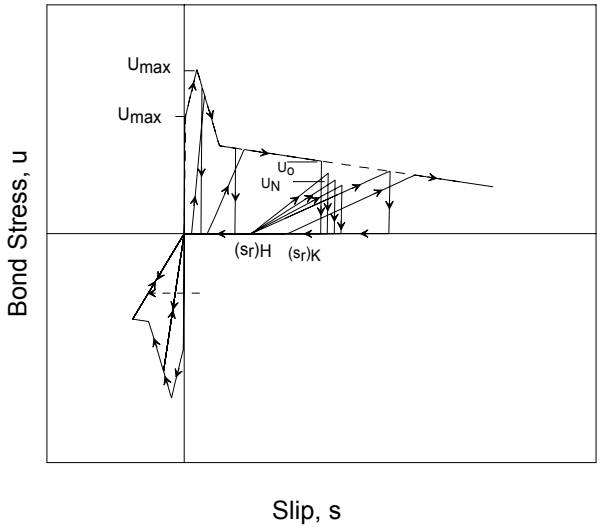

Figure 6.3. Cyclic Constitutive Bond Stress vs. Slip Relationship for Splitting Failure.

assigned constitutive bond slip relationships representing splitting failure in partially-confined concrete. For example, for the columns tested by Melek and Wallace (2004), transverse reinforcement provided along the splice length of the column specimens is only 28% of that required amount to prevent a splitting failure. Therefore the splitting constitutive relationship for partially-confined concrete (Harajli, 2009) were used along only 72% of the splice length (where the partial confinement was assumed to be due to the presence of the pedestal at column base), and the pull-out constitutive relationship by Eligehausen *et al*. (1983) (Figure 6.4) was used along the remaining 28%.

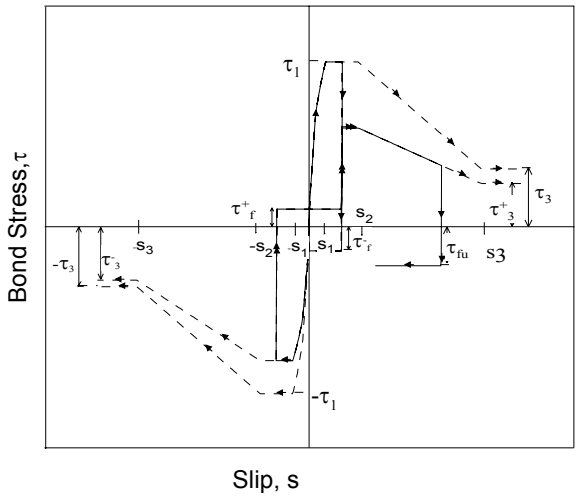

Figure 6.4. Cyclic Constitutive Model for Bond Stress vs. Slip Relationship for Confined Concrete (Eligehausen *et al*., 1983).

For modeling of spliced column with smooth reinforcing bars, since there is no possibility for splitting failure (due to absence of lugs on plain bars), all bond slip springs are assigned the same constitutive bond stress. vs. slip relationship (Figure 6.5) developed by Verderame *et al*. (2009). For 180-degree hooks, the constitutive monotonic envelope proposed by Fabbrocino *et al*. (2004, 2005) was used to relate reinforcing bar stresses to hook end slip deformations. An origin-oriented hysteretic response was assigned to the hooks, due to absence of a cyclic constitutive model in the literature.

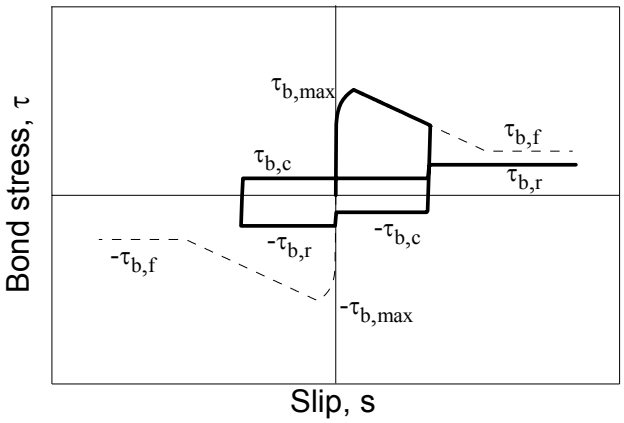

Figure 6.5. Cyclic Bond Stress vs. Slip Relationship for Smooth Reinforcing Bars.

The advanced constitutive relationship proposed by Chang and Mander (1994) (Figure 6.6) is assigned to the concrete macro-fibers of the analytical model, since it allows detailed calibration the monotonic and hysteretic parameters for an improved representation of the stress-strain behavior. This constitutive model provides a direct and flexible approach to incorporate important material behavioral features (for example, hysteretic behavior in tension, progressive gap closure, tension stiffening effects) into the analysis.

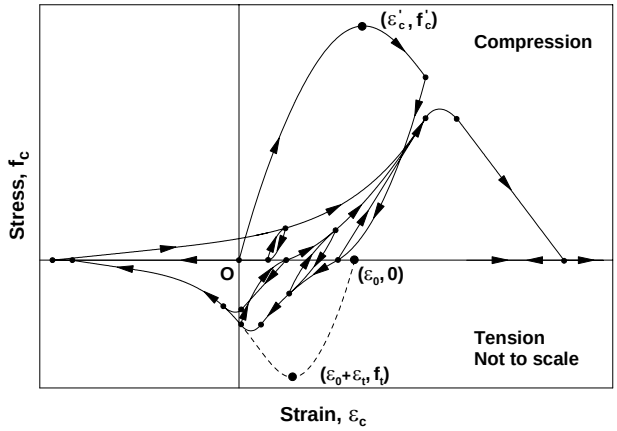

Figure 6.6. Constitutive Material Model for Concrete (Chang and Mander, 1994).

The constitutive model used for reinforcing steel is the Menegotto and Pinto (1973) model, as extended by Filippou *et al*. (1983) to include isotropic strain hardening effects. This constitutive model, although simple in formulation, has been shown to accurately simulate experimental behavior. The model formulation incorporates cyclic degradation of the curvature of the unloading and reloading curves and thus allows the Bauschinger's effect to be represented (Figure 6.7).

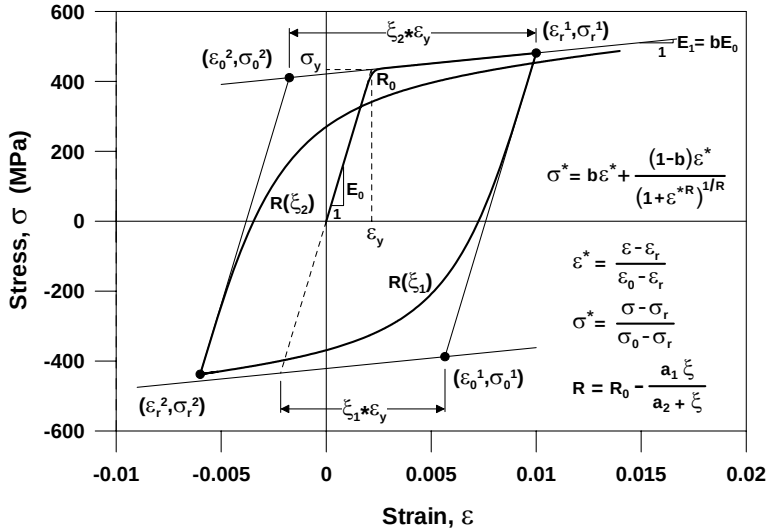

Figure 6.7. Constitutive Material Model for Reinforcing Steel.

6.2. Analytical Model Response

The analytical model, with the properties outlined in the previous section, was implemented in Matlab together with a direct stiffness assembly procedure and an incremental-iterative numerical scheme to perform nonlinear quasi-static (monotonic or cyclic) analysis of the columns with lap splices. The displacement-controlled iterative solution strategy described in Chapter 5 was used for conducting the analyses.

The column specimens tested by Melek and Wallace (2004) were first used to calibrate and evaluate the model reponse. Design and reinforcement details for the column specimens, as well as the loading protocol, are presented in detail in Melek and Wallace (2004), and are summarized in Chapter 7. Details of the model calibration and comparison of the analytical results with experimental data will be presented in Chapters 7 and 8. This chapter focuses on characteristic features of the model response, as well as the sensitivity of the analytical results to changes in model parameters.

Figure 6.8 shows a representative lateral load vs. top displacement response prediction of the model, for a specific column specimen (2S10MI, tested by Melek and Wallace (2004)), with a height of 1.83 meters, 457 mm2 cross section, 8 – #8 (d_b =25.4

mm) longitudinal bars and #3 (9.5 mm diameter) rectangular hoops with 90-degree hooks spaced at 304.8 mm on center along the column height, and an applied axial load of 10% of the axial load capacity of the specimen. A lap splice length of $20d_b$ (508 mm) was used in construction of this specimen. During the test, a standard lateral displacement history

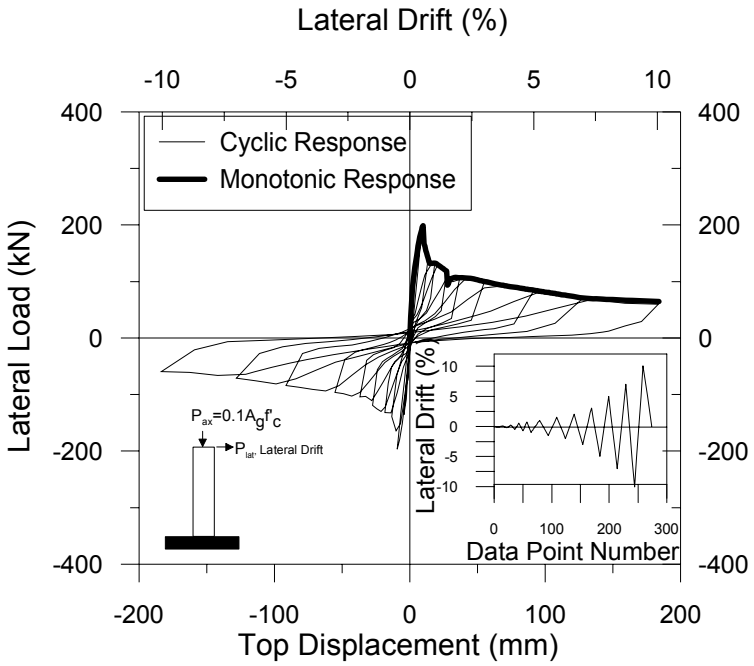

Figure 6.8. Load – Displacement Response Predicted by MVLEM using Harajli (2009).

was applied, which consists of three cycles at each displacement level with monotonically increasing drift levels (0.1, 0.25, 0.5, 0.75, 1.0, 1.5, 2.0, 3, 5, 7, and 10%). In the preliminary analysis, one cycle is applied at each displacement level, for simplicity. For the specimen, the concrete compressive strength was approximately 36 MPa, with a strain at peak stress of 0.002. The yield stress for the longitudinal bars was measured as approximately 510 Mpa. The analytical response presented in the figure is obtained using 25 model elements over the height of the lap splice region, 4 model elements above the lap splice region, 26 uniaxial concrete elements (macro-fibers) along the width of the section, and a value of c = 0.4 for the relative height of the shear spring. The bond stress vs. slip relationship for partially confined concrete by Harajli (2009) is used for all bond slip springs along the entire height of column. As there is no cyclic bond stress degradation present in this relationship (only cyclic stiffness degradation exists), the backbone of cyclic

response prediction follows monotonic response prediction, as shown in Figure 6.8. The analysis results clearly reflect actual characteristics of cyclic bond slip response of a column with a deficient lap splice, including degradation of the lateral load upon slip initiation, stiffness degradation, shape of the load-displacement hysteresis loops, and pinching behavior.

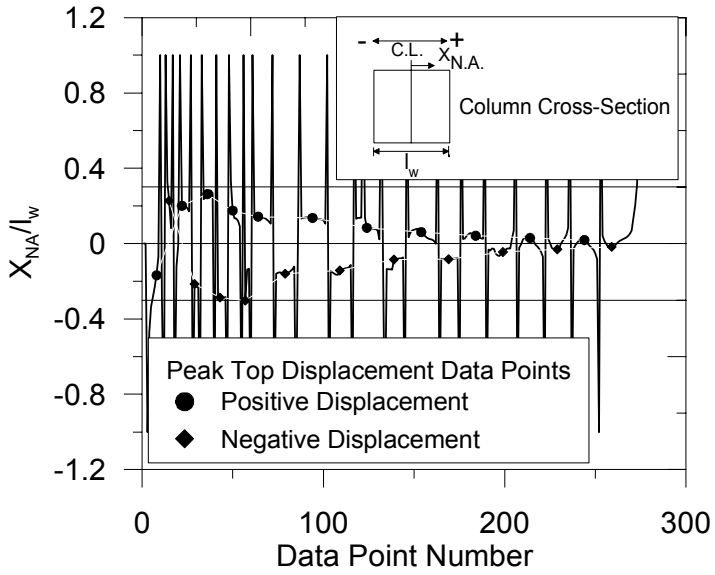

Figure 6.9. Predicted Variation in Position of Neutral Axis.

The model successfully allows variation of the neutral axis depth for a cyclic displacement history applied at the top of the column, as shown in Figure 6.9, which displays the predicted position of the neutral axis in the model element at the base of the column, normalized by the column width. The distance from the centroid of the column cross section to the neutral axis approaches infinity when the lateral displacement (and thus, rotation) of the column approaches zero and reaches its local extreme or limit points (peaks and valleys) at peak displacement (displacement reversal) points.

Figure 6.10 compares the average longitudinal strain histories predicted at the extreme concrete fiber and at the centroid of the column for the element at the base of the column till crushing of concrete, demonstrating the effect of applied displacement history and neutral axis migration on the predicted strains. The longitudinal strains are not symmetric with respect to the zero strain axis, and the strains predicted at the centroid are

tensile for almost the entire loading history, except for a range of small displacements (due to the presence of axial load).

Figure 6.11 shows the cyclic analysis results for the distribution of bond stresses between concrete and the exterior (corner) longitudinal and starter reinforcing bars along lap splice region at 0.25% lateral drift, where as Figure 6.12 shows the monotonic analysis results for the distribution of bond stresses at 0.6% lateral drift, where lateral degradation in the lateral load is initiated. It is clearly seen from Figures 6.11 and 6.12 that unlike the behavior of isolated bars, spliced bars (here longitudinal and starter bars) behave differently in a complex stress transfer mechanism which is correctly represented by the model. Most of the stresses are transferred through longitudinal bars at bottom part of splice and most of the stresses are transferred through starter bars near the top portion of the splice which is visible from these figures also. So model capability in predicting local bond stresses is observed.

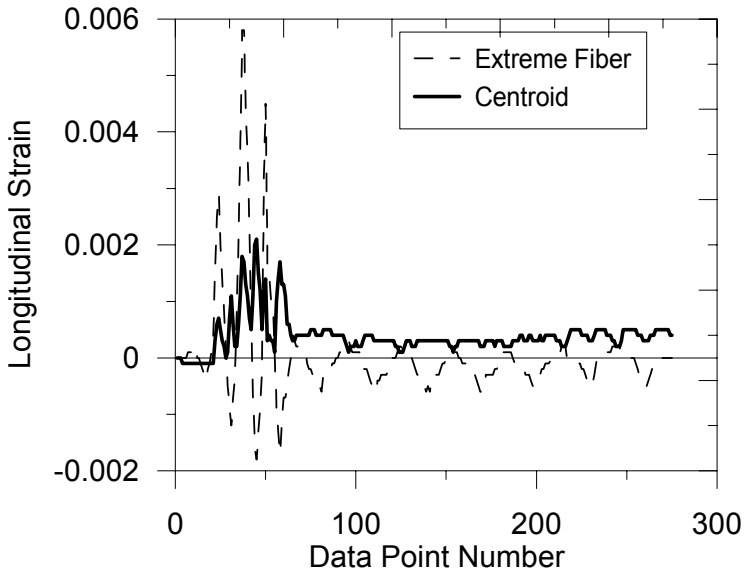

Figure 6.10. Predicted Longitudinal Strain Histories.

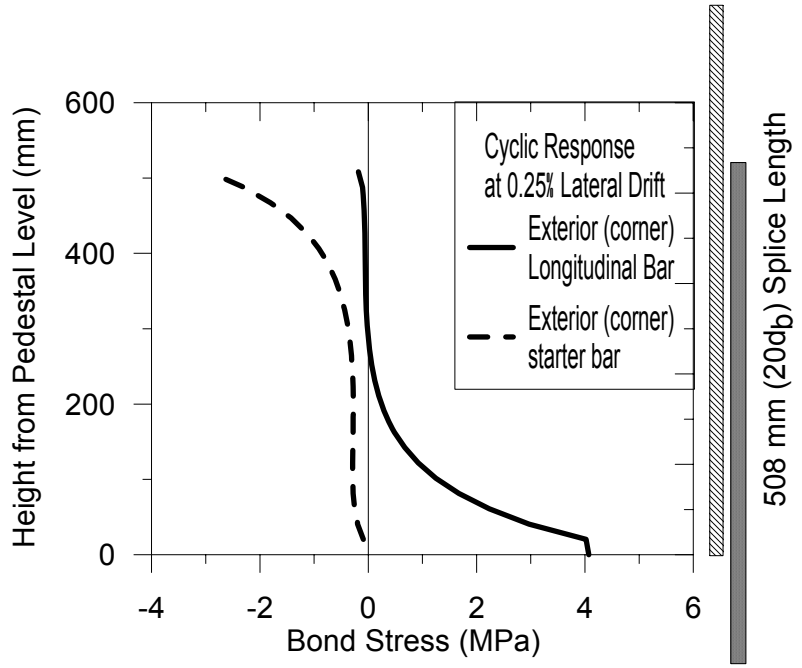

Figure 6.11. Predicted Bond Stress Distribution along the Splice Length for Cyclic. Analysis.

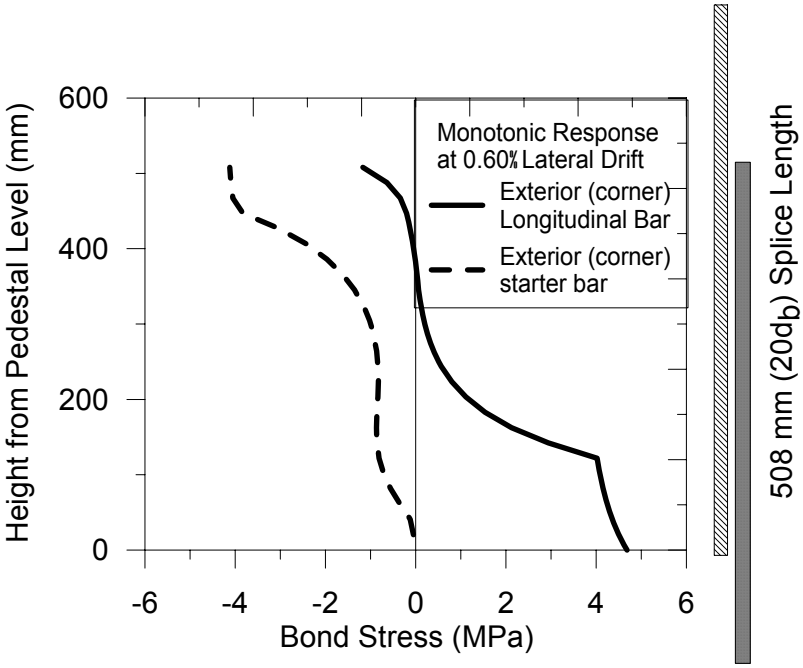

Figure 6.12. Predicted Bond Stress Distribution along the Splice Length for Monotonic Analysis.

Figure 6.13 shows the cyclic analysis results for the distribution of longitudinal steel stresses in exterior longitudinal and starter bars along the lap splice length at 1% lateral drift, where lateral strength degradation starts. Figure 6.14 shows the cyclic analysis results for the history of longitudinal steel strains in exterior longitudinal and starter bars in the model element at the base of the column. As starter bar is fixed at bottom, due to most of the maximum column moment are taken, steel stress are found maximum (also strain as shown in Figure 6.14) in the starter bar near bottom part of column. In the upper part of splice, as most of the moment are taken by longitudinal bar, steel stress are found more in the longitudinal bar (Figure 6.13). So model can able to capture such local phenomenon correctly. The analysis results for column base moment vs. total (accumulated) rotation of the column at the top of the lap splice is shown in Figure 6.15.

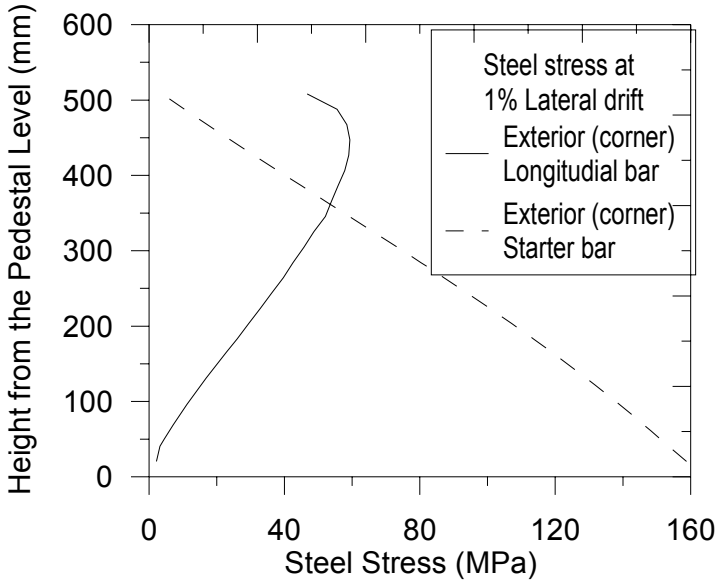

Figure 6.13. Predicted Steel Stress Distribution along the Lap Splice Length.

Figures 6.16 and 6.17 display the analysis results for the same column and using the same model and constitutive material parameters, with the exception of absence of the lap splice. The analysis employed continuous reinforcing bars throughout the full height of

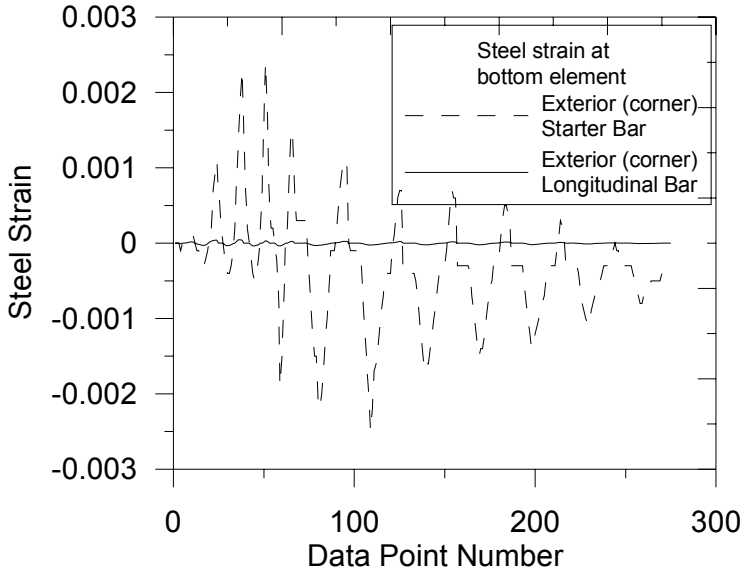

Figure 6.14. Predicted Strain Histories on Reinforcing Steel at Column Base.

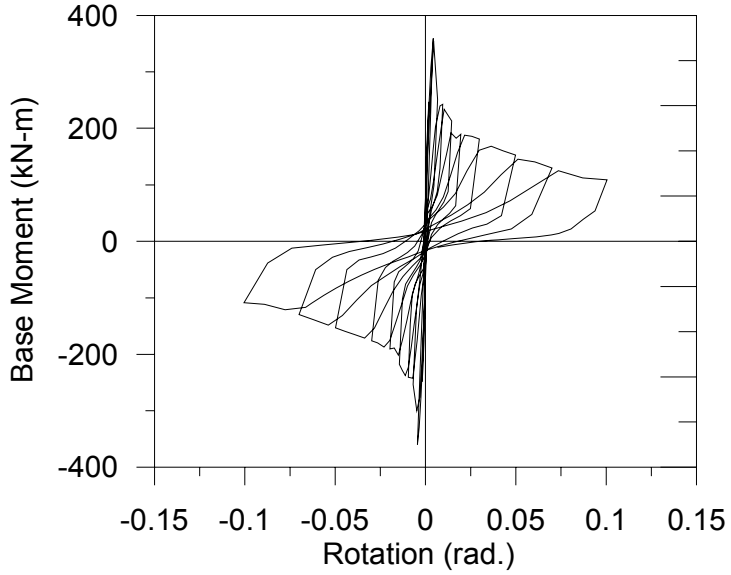

Figure 6.15. Predicted Base Moment vs. Total Rotation along the Lap Splice Length.

column. Comparing the Figure 6.8 with the Figures 6.16 and 6.17, it is observed that column model with lap splice shows more degradation after peak (although the capacities are found same) with clear pinching properties.

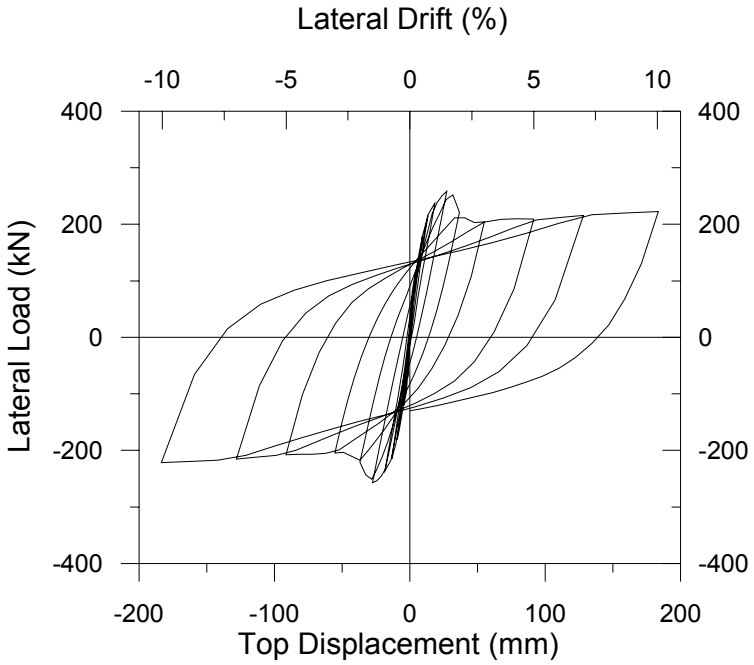

Figure 6.16. Predicted Load – Displacement Response of the Column with Continuous Reinforcing Bars Using Harajli (2009) Bond Slip Relationship for Partially-Confined Concrete.

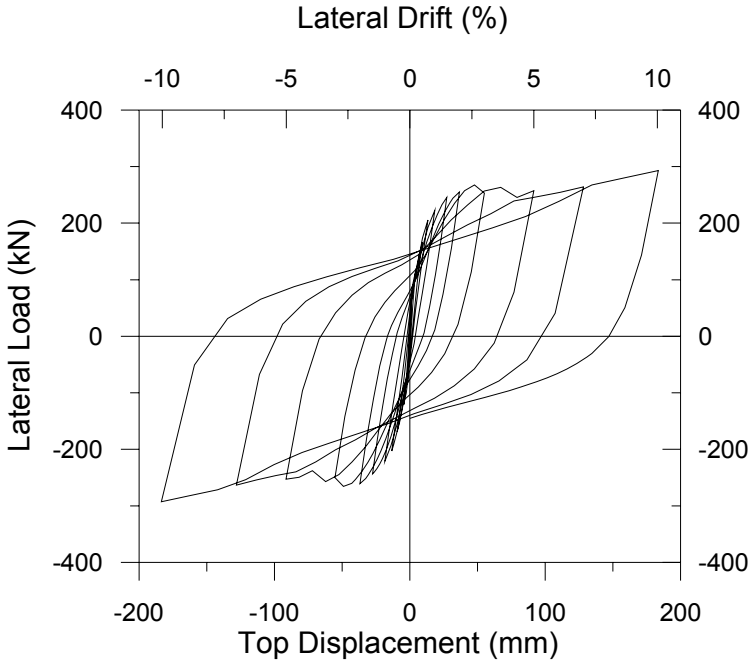

Figure 6.17. Predicted Load – Displacement Response with Continuous Bar without Bond Stress Slip Spring.

Results presented in Figure 6.16 are obtained using the bond stress vs. slip constitutive relationship for partially confined concrete by Harajli (2009). For comparison, Figure 6.17 shows analysis results for the special case of using rigid bond slip springs between reinforcing bars and concrete (flexural response with perfect bond assumption). Comparison of the two analytical responses indicates that although there is no slip failure or no significant slip deformation when continuous reinforcement is used, incorporation of the bond slip springs may marginally change the geometry of the unloading/reloading loops of the cyclic response. The model which includes bond slip springs (Figure 6.16) predicts slightly narrower unloading/reloading loops compared to the model which assumes perfect bond between steel and concrete (Figure 6.17).

So proposed analytical model are capable in predicting cyclic response both at global (lateral load vs. top displacement, moment vs. rotations) and local levels (stress and strain of steel, average concrete strain, position of neutral axis and bond stress distribution) correctly.

6.3. Parametric Sensitivity Studies

Apart from constitutive material and bond slip parameters, the only parameters associated with the analytical model are the number of model elements stacked on top of each other along the height of the column (m), the number of uniaxial concrete elements (macro-fibers) along the column cross section (n), and the parameter defining the relative location of the center of rotation along the height of each model element (c). Sensitivity of the model results to variations of these parameters is addressed in this section. The sensitivity of the model response to the axial load level on a column is also investigated.

Figures 618(a) and 6.18(b) illustrates preliminary lateral load vs. top displacement response predictions for the aforementioned column specimen (Specimen 2S10MI, tested by Melek and Wallace (2004)), using either 8 model elements along the lap splice with thirteen uniaxial concrete elements along the width of the column, or by using 16 model elements along the lap splice with 26 uniaxial concrete elements along the width. Four model elements are used above the lap splice region of the column. In both analyses, the pull-out bond stress vs. slip relationship for confined concrete by Eligehausen *et al*. (1983)

was used for the bond slip springs in the vicinity of the stirrups, whereas the splitting bond stress vs. slip relationship for partially-confined concrete by Harajli (2009) was used for the others. For the analysis depicted in Figure 6.18(a), pullout springs were used for 2 of the 8 model elements (1 at the location of each tie), whereas for Figure 6.18(b), pullout springs were used for 4 of the 16 model elements (2 at the location of each tie). For the remaining elements over the entire column length, splitting springs for partially-confined were used for both analyses.

The comparison indicates that increasing the number of concrete macro-fibers or the number of model elements does not change significantly the prediction of the global response (lateral load vs. top displacement); however, use of more elements is valuable in terms of obtaining more detailed information on local behavior, such as the state of stress and strain at a particular location. For example, results shown in Figure 6.18(c) compare the average longitudinal strain histories predicted at the extreme concrete fiber and the cross-sectional centroid of the column at the base. Using more model elements over the height of the column allows for an improved local prediction of the strains. Also, using more concrete macro-fibers along the width of the column allows for a more refined description of the concrete cross section. Therefore, the model incorporates the flexibility to choose how much detail is desired in the analytical results.

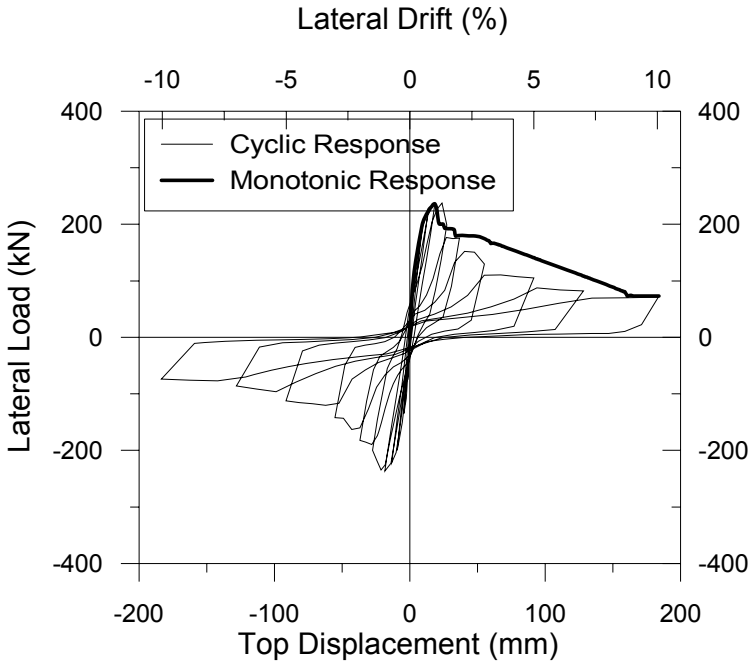

(a) Predicted Load – Displacement Response with 8 Model Elements and 13 Concrete Macro-Fibers.

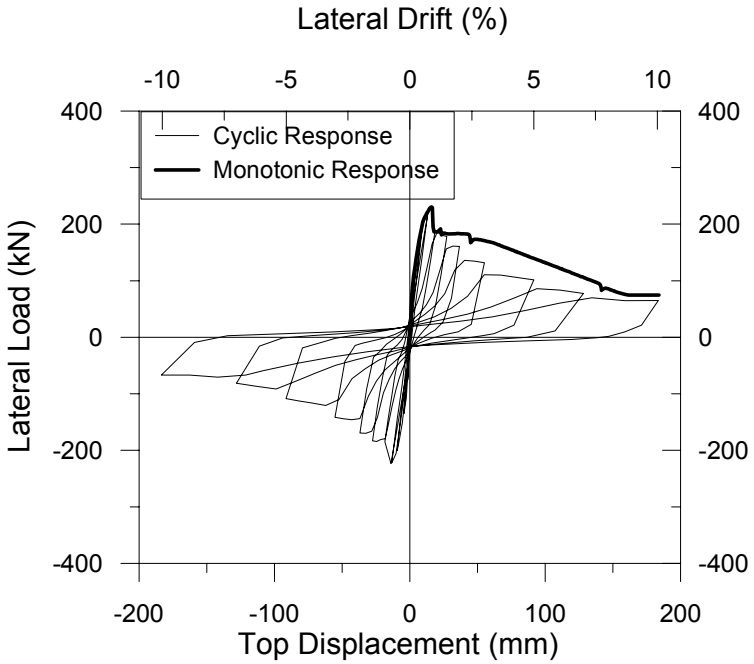

(b) Predicted Load – Displacement Response with 16 Model Elements and 26 Concrete Macro-Fibers.

Figure 6.18. Sensitivity of the Response to Number of Model Elements and Concrete Macro-Fibers.

Analysis results presented in Figure 6.18 also indicate that there is apparent cyclic strength degradation (reduction in lateral load during cyclic loading compared with monotonic loading), when pullout and splitting springs are used in combination. The backbone of the analytical cyclic response is reduced, compared with the monotonic response. This is due to the cyclic bond stress degradation in the pullout constitutive model by Eligehausen, *et al*. (1983), which is not present in the splitting constitutive model for partially-confined concrete by Harajli (2009). As well, comparing the analysis results presented in Figure 6.8 (using splitting springs only) and Figure 6.18 (using pullout and splitting springs in combination), it is apparent that as there is no significant difference in the analytical responses obtained using these two bond-slip spring calibration methods.

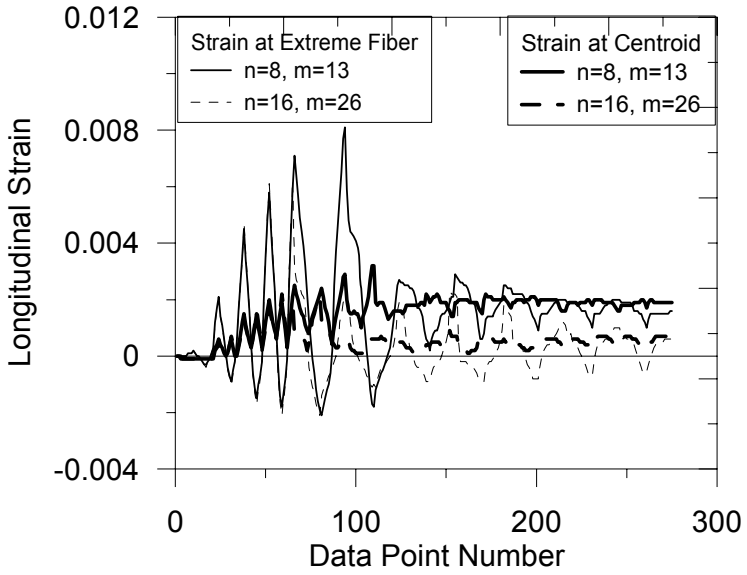

(c) Longitudinal Strain Histories in the Model Element at the Base of the Column.

Figure 6.18. (Continued) Sensitivity of the Response to Number of Model Elements and Concrete Macro-Fibers.

Sensitivity of the analysis results to the parameter defining the relative location of the center of rotation (also the relative location of the horizontal shear spring) along the height of each model element c is illustrated in Figure 6.19. Figure 6.19(a) compares the predicted lateral load vs. top displacement response obtained using a column model with eight model elements (and thirteen concrete macro-fibers) for a value of c = 0.4

recommended by Vulcano *et al*. (1988), and an illustrative extreme value of $c = 0.0$ (center of rotation at the bottom of each model element). Figure 6.19 (b) compares the predicted response for $c = 0.4$ and $c = 0.0$, using a column model with 16 model elements (and 26 concrete macro-fibers). The two analytical responses are very similar, indicating that variation in parameter c does not influence the characteristic shape of the load – displacement response significantly, as long as an adequate number of model elements are stacked on top of each other.

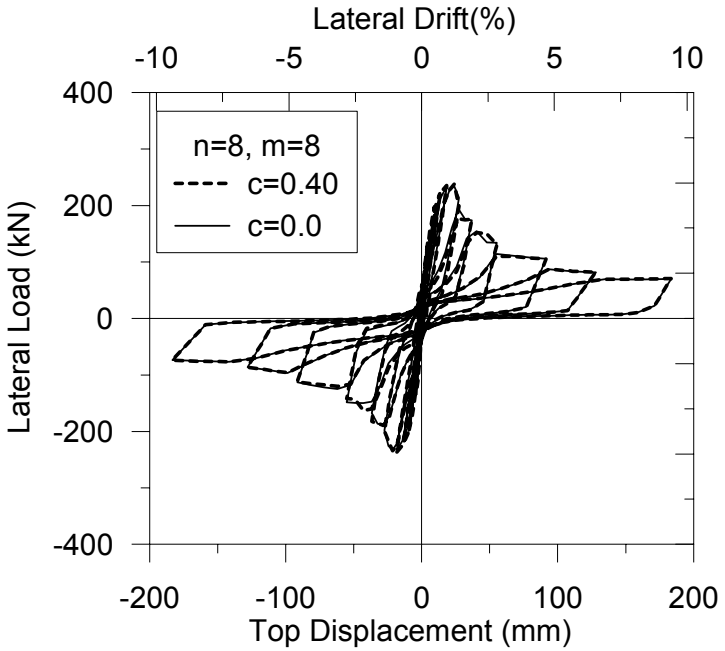

(a) Predicted Load – Displacement Response with 8 Model Elements and 8 Concrete Macro-Fibers.

Figure 6.19. Sensitivity of Response to Parameter c.

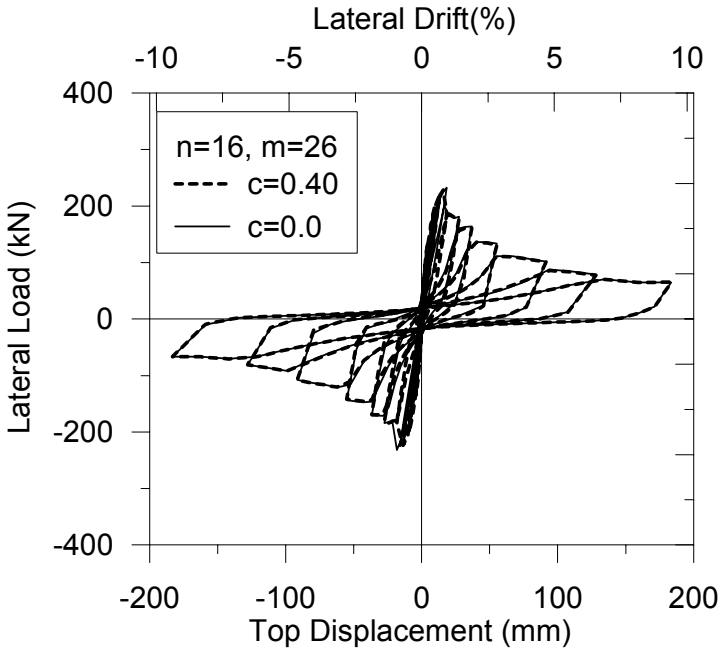

(b) Predicted Load – Displacement Response with 16 Model Elements and 26 Concrete Macro-Fibers.

Figure 6.19. (Continued) Sensitivity of Response to Parameter c.

Sensitivity of the model response to variation of the applied axial load level on the column was also investigated. Figure 6.20 shows a comparison of the analytically predicted lateral load versus top displacement responses of the column for applied axial load levels of 10% , 20% and 30% of the axial load capacity of the column respectively. The model response for zero axial load was presented previously in Figure 6.8. The results clearly display the significant impact of axial load on the column response. The analytical model successfully captures the influence of the axial load level on the flexural and bond slip behavior of columns with lap splices.

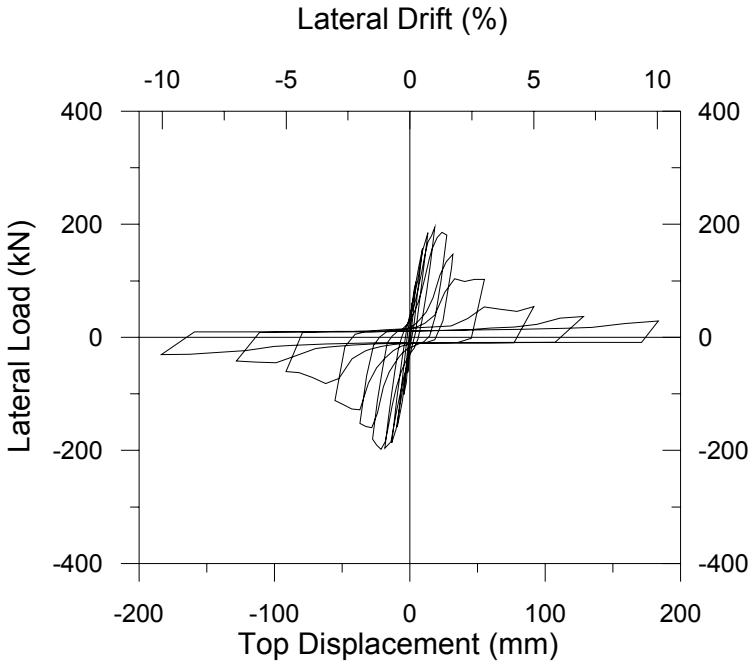

(a) Predicted Load – Displacement Response for an Axial Load Level of 10% of the Axial Load Capacity.

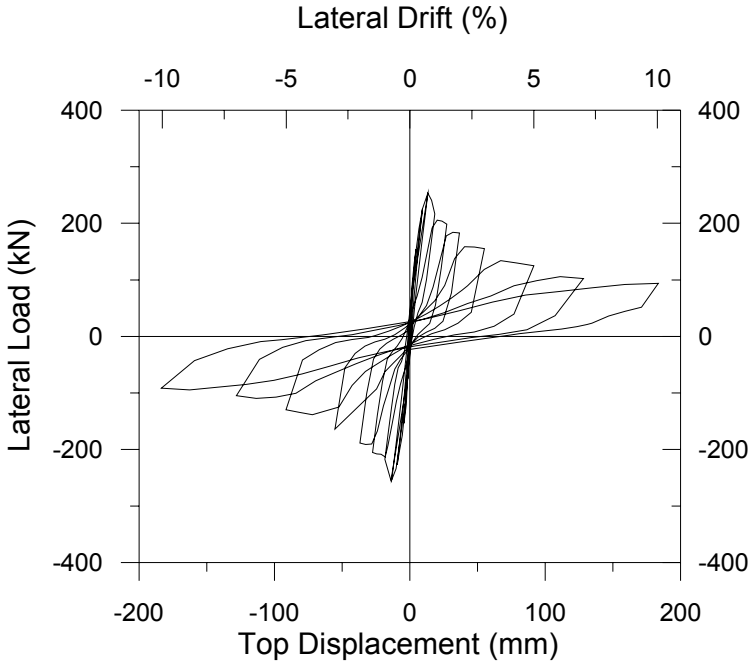

(b) Predicted Load – Displacement Response for an Axial Load Level of 20% of the Axial Load Capacity.

Figure 6.20. Effect of Axial Load Level on Analytical Response.

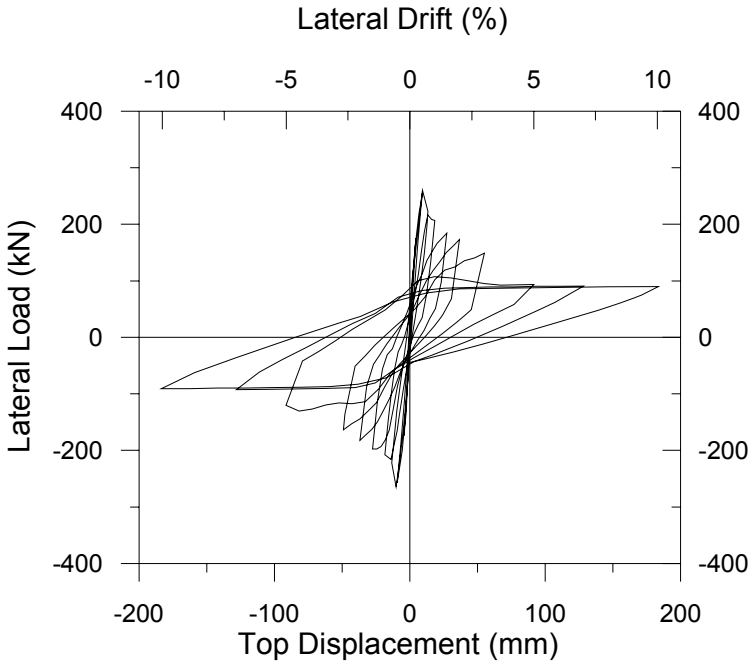

(c) Predicted Load – Displacement Response for an Axial Load Level of 30% of the Axial Load Capacity.

Figure 6.20. (continued) Effect of Axial Load Level on Analytical Response.

Overall, based on the preliminary analysis results presented, it is verified that the analytical model proposed captures important response characteristics associated with the cyclic behavior of reinforced concrete columns with lap splices, the response of which is governed by either bond slip, flexure, or a coupled combination thereof. The analytical model is capable of directly incorporating important behavioral features in the analysis, including shifting of the neutral axis along the column cross-section, the distribution of bond stresses and slip deformations in the starter and longitudinal bars along the lap splice, and the direct effect of axial force (constant and fluctuating) on the analytical response, which are commonly ignored in simple models. Characteristics of the cyclic response, including stiffness degradation, and strength degradation, and hysteretic shape are clearly captured in the analysis results. Deterioration of lateral load due to slip failure and the preceding pinched response are also clearly represented. It is observed that the model global response is not significantly sensitive to model parameters including the number of model elements over the height of a column or the number of concrete macro-fibers along the width of the cross-section, as long as a reasonable number of model elements and

macro-fibers are used in the construction of the model. However, finer discretization of the model provides improved local response predictions. Details on experimental calibration of the analytical model and correlation of model responses, at both global and local response levels, with an extensive test program conducted by Melek and Wallace (2004) are presented in the following chapter.

7. EXPERIMENTAL CALIBRATION AND VERIFICATION OF THE ANALYTICAL MODEL

This chapter provides detail information on physical calibration of the analytical model and comparison of the model results with results of an experimental program on six densely-instrumented column specimens, which incorporate deformed reinforcing bars and deficient lap splices. A brief description of the experimental program, detailed information on calibration of the model, and comprehensive correlations of model results with extensive test data are presented. Analytical results are compared with the experimental measurements, at both global and local response levels. The comparisons are useful for understanding the bond slip response characteristics of reinforced concrete columns with deficient lap splices, as well as for assessment of the effectiveness and accuracy of the analytical model. The comparisons also help illustrate the model capabilities, limitations, and possible improvements.

7.1. Overview of the Experimental Program

The column tests by Melek and Wallace (2004), described in detail in Melek (2006), are used to calibrate and evaluate the analytical model. In this experimental program, six full-scale columns were tested under a variety of conditions. The test specimens consisted of cantilever columns which are monolithically-cast with foundation blocks, which are attached to a strong floor. The specimens are subjected to different levels of axial load and cyclic lateral loads applied at the top of the specimens. The specimen configuration represented half the height of an interior column in a building, extending from column mid-height (where a point of inflection is expected under earthquake loading) to the column-joint interface. Column heights between 1.52 m and 1.83 m, and a 457x457 mm square cross section were used for the test specimens. Brief descriptions of specimen details and the test setup are provided in the following sections. Additional details of the experimental program are available in Melek (2006).

7.1.1. Specimen Details

Column reinforcing details (Figure 7.1), with eight 25.4 mm nominal diameter vertical bars and 9.5 mm diameter hoops with 90-degree hooks spaced at 305 mm on center along the column height, were based on a review of typical reinforcing details in older buildings, and are very similar to the details used in the specimens tested by Lynn *et al*. (1996). As deformed bar was used, there was no slip at the top of the longitudinal bar. In the tests, the column height was selected to ensure the shear strength of the column was sufficient to develop the flexural strength at the base of the column, where the lap splice was located. This was done to ensure that splice failures would be observed. A lap splice length of 20 longitudinal bar diameters ($20d_b$, 508 mm) was used and axial load was held constant during application of a prescribed cyclic lateral displacement history at the top of the column.

The lateral displacement history selected for 5 of the 6 tests is fairly typical, and consists of three cycles at each displacement level, with monotonically increasing drift levels (0.1, 0.25, 0.5, 0.75, 1.0, 1.5, 2.0, 3, 5, 7, and 10%). A lateral displacement history representative of what might be expected in near-fault seismic regions was used for one specimen (2S20HN). The primary test variables were the axial load level (0.1, 0.2 and 0.3 of the column concrete axial load capacity, $A_g f'_c$), the column shear demand at maximum base moment (0.67 to 0.93 of the nominal shear strength, V_n), and the applied displacement history (shown in Table 7.1). The first three specimens (2S10M, 2S20M and 2S30M) were subjected to the standard cyclic lateral displacement history (STD), with the axial load held constant for the duration of the tests at 0.1, 0.2, and 0.3 of Agf'c (534, 1068 and 1601 kN), respectively. A comparison of the provided lap-splice length ($20d_b$) with the lap-splice length required by ACI 318-02 (calculated as $31d_b$), revealed that splice failure (degradation of lateral load capacity) was expected when the bending moment in the column reached approximately 60% to 70% of the nominal

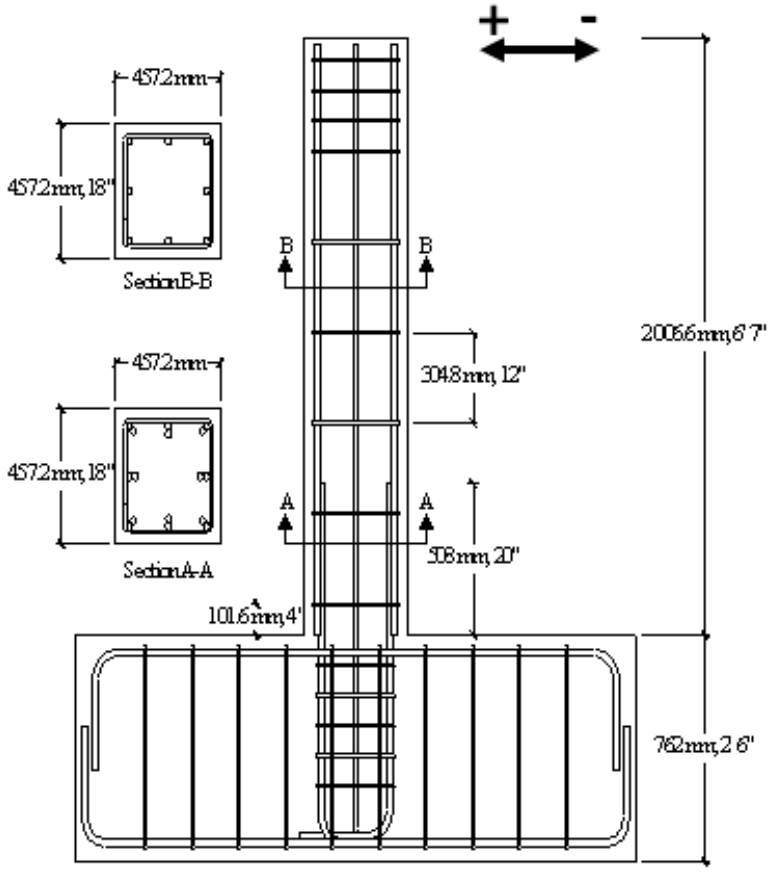

Figure 7.1. Reinforcing Details.

moment capacity; although a review of previous test data (e.g., Lynn *et al*.(1996)) suggested that column longitudinal reinforcement may reach yield in tension. The objective of the three tests (specimens 2S10M, 2S20M and 2S30M) was to assess the influence of axial load on lap splices with moderate shear stress level and widely-spaced transverse reinforcement. Two additional specimens (2S20H and 2S20HN) were tested to investigate the influence of higher shear force and applied displacement history on column behavior, for moderate axial load level (0.20Agf'c). The axial load level and the expected average shear stress (at failure) value were increased for the final specimen (2S30X) to magnify the maximum shear force demand expected during the test to approximately the calculated nominal shear capacity (Table 7.1). The average shear stress level at the expected initiation of splice failure was magnified by decreasing the column height from 1829 mm to 1677mm for specimens S20HI and S20HIN, and to 1524 mm for specimen S30XI.

The specimen identification (ID) labels were similar to those used by Lynn *et al*. (1996); and define the longitudinal steel ratio, the level of the applied axial load, the shear demand level for the lateral load value expected at splice deterioration (Moderate, High and MaXimum), and the applied lateral displacement history. For example, label 2S20HN corresponds to: 2 = 2% longitudinal steel ratio (8-25.4 mm) ; S = Spliced; 20 = 0.20$A_g f'_c$; H = High Shear Demand; N = Near Fault Lateral Displacement History.

Table 7.1. Test matrix.

Specimen	P ($\%A_g f_c'$)	$\frac{l_{s_{provided}}}{l_{s_{required}*}}$	$V_c(kN)$	$V_n(kN)$	$\frac{V_u@M_{EXP}}{V_n}$	Column height(mm)	Displacement history
2S10M	10	0.65	212	201	0.67	1829	STD
2S20M	20	0.65	245	334	0.70	1829	STD
2S30M	30	0.65	278	367	0.78	1829	STD
2S20H	20	0.64	242	331	0.81	1676	STD
2S20HN	20	0.64	242	331	0.81	1676	Near Fault
2S30X	30	0.64	275	363	0.93	1524	STD

*ACI 318-02 Equation (12-1)

7.1.2. Materials

Standard compressive strength tests (ASTM C31-39) on 153mm x 305mm cylinders were conducted 7 and 28 days after concrete casting. In addition, concrete stress – strain tests were also performed at the test dates. Concrete peak compressive stress value was approximately 36 MPa, with a strain at peak stress of 0.002 and 0.0025 for the first and second concrete batches, respectively, used for the two groups of specimens (Figures 7.2 and 7.3).

Stress – strain tests were not conducted for the longitudinal reinforcing bars since bar yielding was not anticipated due to the inadequate splice lengths provided). Geometrical details of longitudinal reinforcing bars are shown on Figure 7.4. It is noted that Grade 60 (Yield strength, 413 MPa) longitudinal reinforcement was used for the specimens,

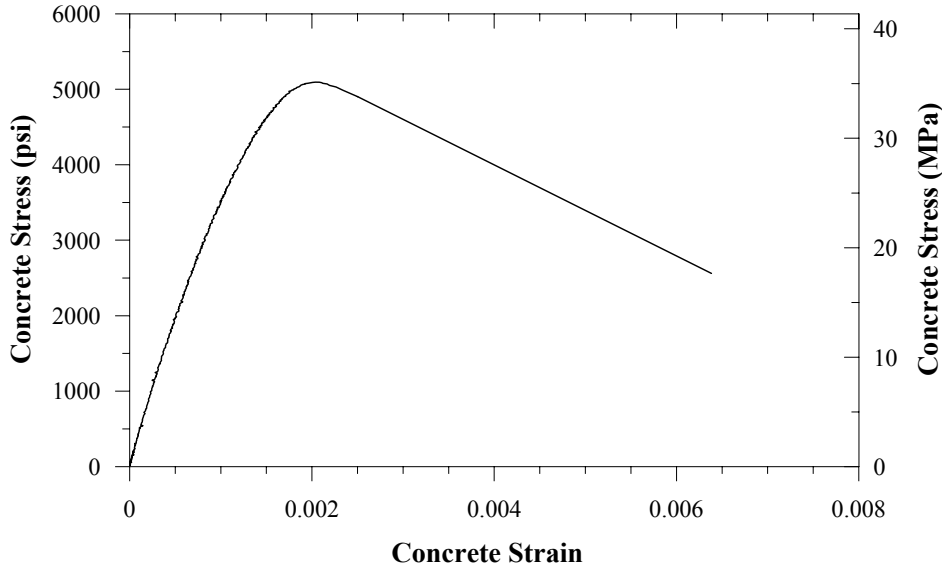

Figure 7.2. Measured Concrete Stress-Strain Relationship for Specimens: 2S10M, 2S20M, and 2S30M.

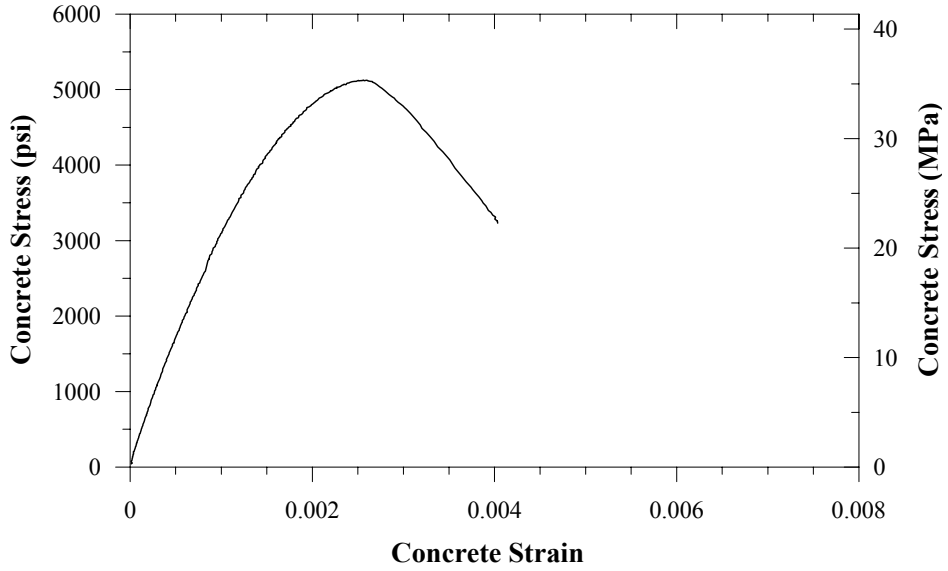

Figure 7.3. Stress-Strain Diagram for Specimens: 2S20H, 2S20HN, and 2S30X.

although Grade 40 (Yield strength, 275 MPa) reinforcement is more common in older buildings, because of the non-availability of Grade 40 reinforcing bars in the market. However, use of Grade 60 reinforcement would actually increase the possibility of splice failure along short lap-splice length ($20d_b$), which was the desired failure mode. The

mechanical properties of the steel and concrete used in the construction of the test specimens are shown in Table 7.2

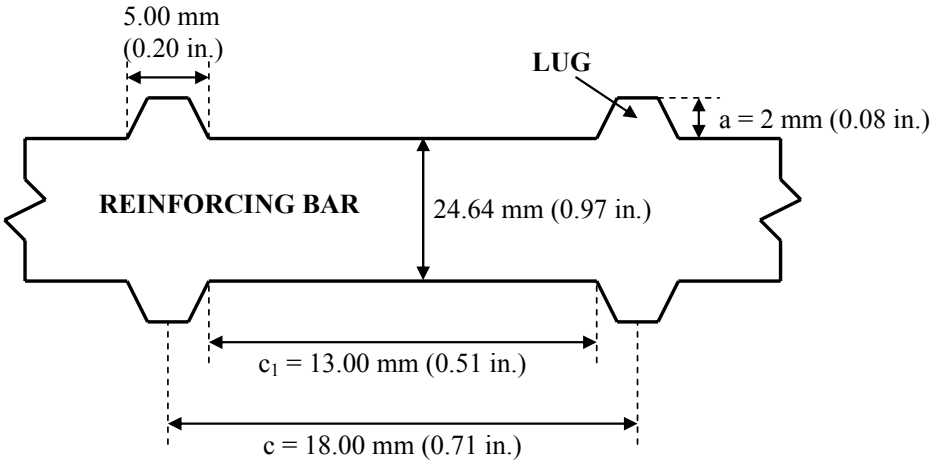

Figure 7.4. Longitudinal Reinforcement Bar Geometry (d_b = 25.4 mm (#8)).

Table 7.2. Material Properties

Material	2S10M-2S20M-2S30M			2S20H-2S20HN-2S30X		
Concrete	$f_c^{/}(Mpa)$	$f_{ct}(Mpa)$	$f_r(Mpa)$	$f_c^{/}(Mpa)$	$f_{ct}(Mpa)$	$f_r(Mpa)$
	36	3.4	3.8	35	-	3.7
Steel	$d_b(mm)$	$f_y(Mpa)$	$f_u(Mpa)$	$d_b(mm)$	$f_y(Mpa)$	$f_u(Mpa)$
(column)	25.4	510	818	25.4	510	818
(starter)	25.4	521	746	25.4	507	807
(ties)	9.5	481	750	9.5	481	750

7.1.3. Test Setup

The test setup used in the experiments is shown in Figure 7.5. The lateral load was applied with a 550 kN hydraulic actuator with 610 mm stroke. The actuator was bolted to the column specimen at one end and to a steel reaction frame at the other end, using rod eye-clevis bracket connections that allow free rotation in the vertical plane of the actuator.

An MTS 407 controller connected to a hydraulic power supply was used to control the actuator load and displacement.

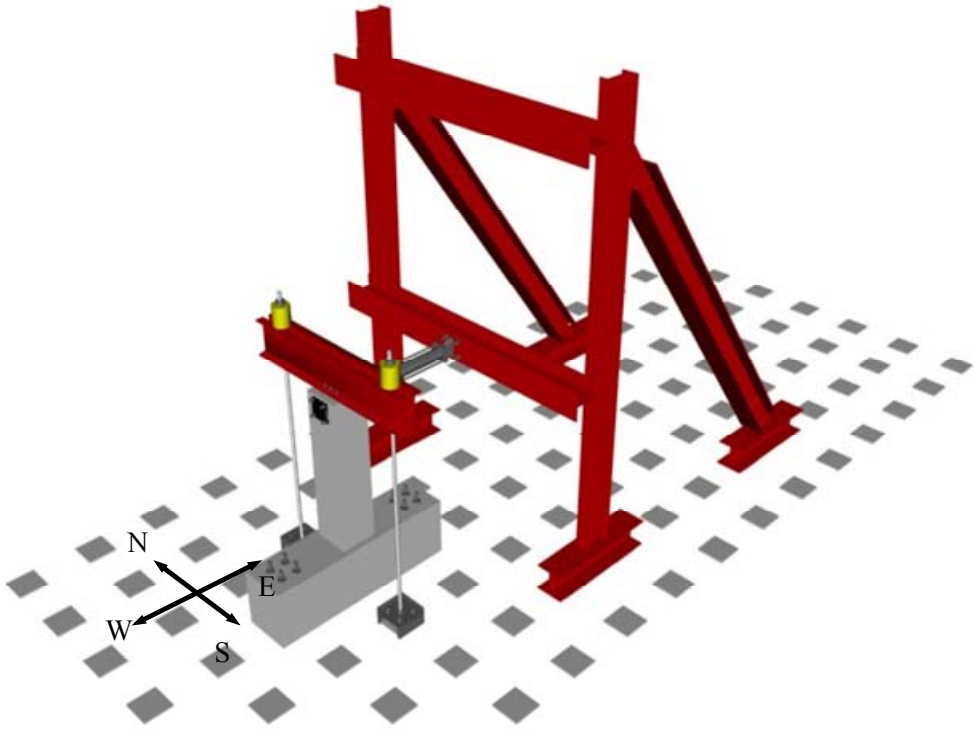

Figure 7.5. Test Setup with Reaction Frame (Melek, 2006).

The axial load on each specimen was held constant for the duration of the applied lateral displacement history. The axial load assembly consisted of two, 889.6 kN ENERPAC hollow plunge cylinders, two 46 mm diameter pre-stressing steel rods, two steel channels, and two 76 mm thick steel plate assemblies. The connection at the top of the column to the axial load assembly was established using 16 mm diameter J-bolts that were anchored in the concrete at the top of the column. The specimens were subjected to axial load by placing the 46 mm diameter threaded rods in tension. The threaded rod was anchored to a 76mm plate, which was anchored to the strong floor with four 32 mm diameter, threaded, high-strength steel tie-down rods. A hand pump with a reservoir was used to pressure the cylinders. During testing, the hydraulic pressure was continuously monitored and adjusted to maintain the desired level of constant axial load (Melek, 2006).

7.1.4. Instrumentation and Data Acquisition

Different types of instrumentation were used to monitor the applied lateral load and displacement, strain on longitudinal and transverse reinforcement, flexural and shear deformations of the column, and pedestal translation and rotation. For each specimen, reinforcing bar strains were measured using 27 longitudinal and 6 transverse reinforcement strain gauges, as shown in Figure 7.6. The strain-gauge-labeling scheme is presented

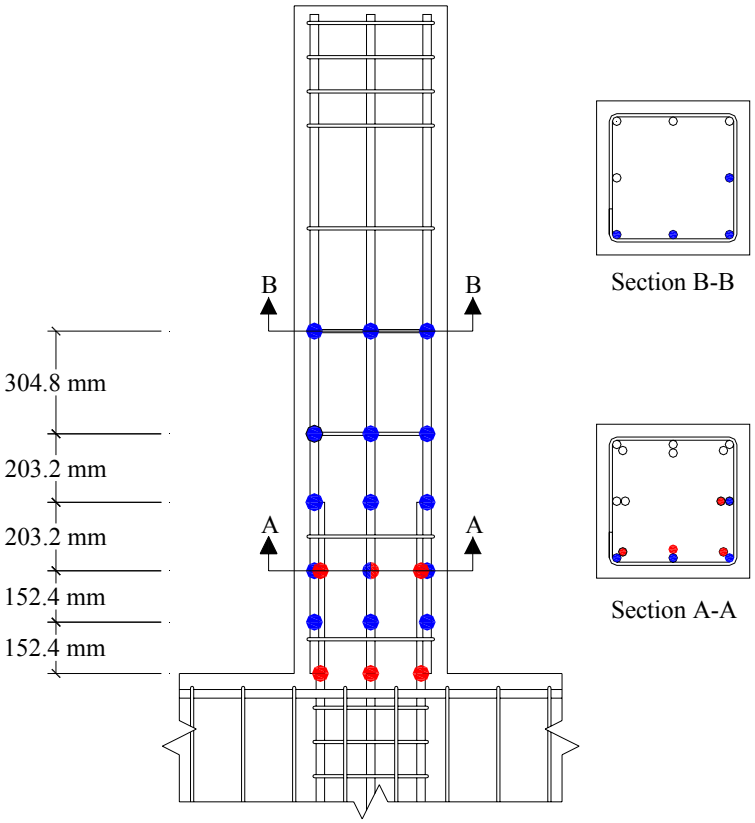

Figure 7.6. Strain Gauge Layout (Melek, 2006).

in Figure 7.7. Column deformations (flexure, shear and lateral displacement) were measured with linear voltage transducers (+/- 1.5 in.; 38 mm). The instrumentation layout was modified slightly between the first set of three specimens and the second set of three specimens. External instrumentation for the first set of three specimens (S10MI, S20MI, and S30MI) consisted of 31 linear transducers, 25 on one side of the specimen to form a grid as shown in Figure 7.8. Four transducers were placed on the opposite face of the

column to obtain rotational response at the column base due to flexure and slip (Figure 7.9).

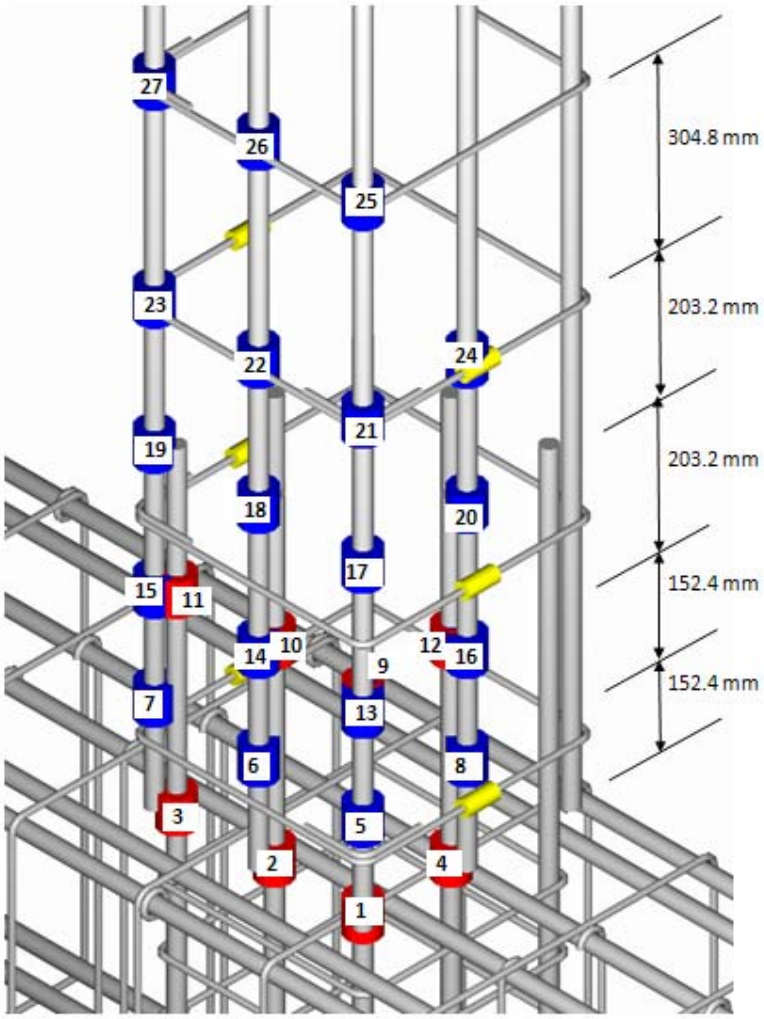

Figure 7.7. Strain Gauge Labeling Scheme (Melek, 2006).

The instrumentation layout was changed for the second set of specimens, where the number of linear potentiometers used was reduced from 31 to 18. Of the 18 linear potentiometers, six pairs were utilized to measure the flexural response (average curvature) of the specimen over the column height (Figure 7.10). The measurement of shear distortions was made possible by using four wire potentiometers (Figure 7.11) that were placed diagonally on the opposite face of the column. Two additional transducers were placed on two ends of the pedestal base to monitor any rotation of the foundation system. The external instrumentation layout and the labeling scheme are given in Figures 7.12 and

7.13, respectively. Potentiometers were connected to the reinforced concrete column with 6 mm – diameter fine threaded rods which were placed in the forms prior to concrete placement.

Figure 7.8. External Instrumentation Grid (2S10M, 2S20M, 2S30M, Melek, 2006).

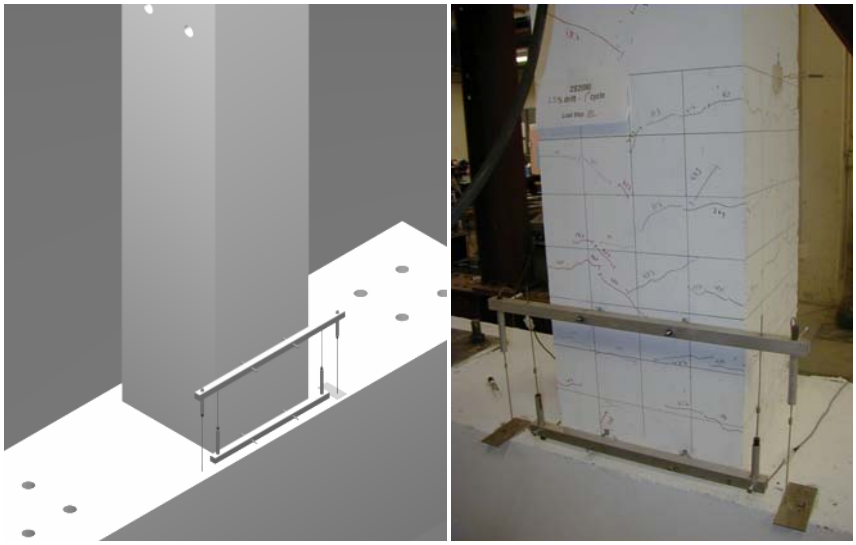

Figure 7.9. Transducers Used to Measure Total and Slip Rotation at Column Base (Specimens 2S10M, 2S20M, 2S30M, Melek, 2006).

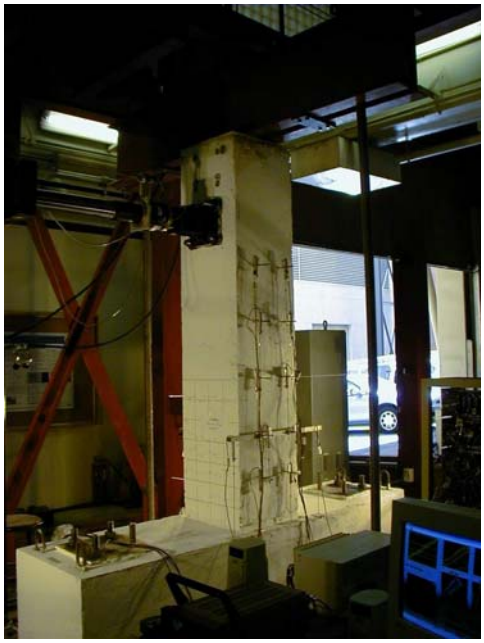

Figure 7.10. External Instrumentation (2S20H, 2S20HN, 2S30X, Melek, 2006).

Figure 7.11. Shear Instrumentation (2S20H, 2S20HN, 2S30X, Melek, 2006).

The lateral load was measured using a 667 kN load cell. The column top lateral displacement was monitored using a transducer (+/- 305mm) mounted on the cylinder. In addition, a wire potentiometer (+/- 508 mm) was mounted between the specimen and a rigid external reference frame to measure the lateral displacement at the point of lateral load application (top displacement). Besides top displacement, mid-height and pedestal lateral displacements were measured relative to the rigid reference frame using wire potentiometers (Figure 7.14).

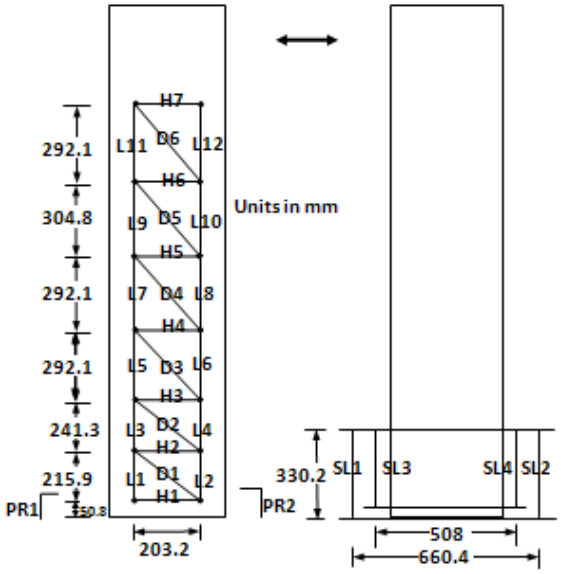

Figure 7.12. External Instrumentation Layout (2S10M, 2S20M, 2S30M).

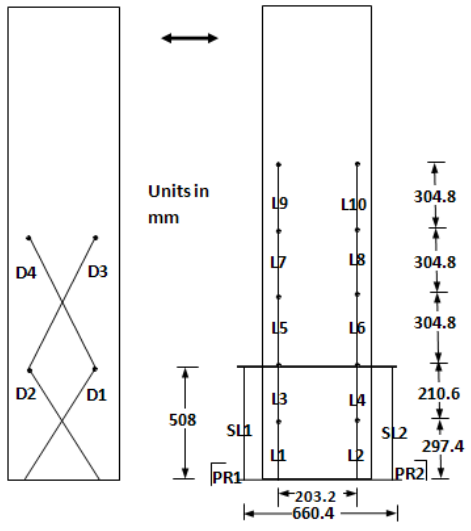

Figure 7.13. External Instrumentation Layout (2S20H, 2S20HN, 2S30X)

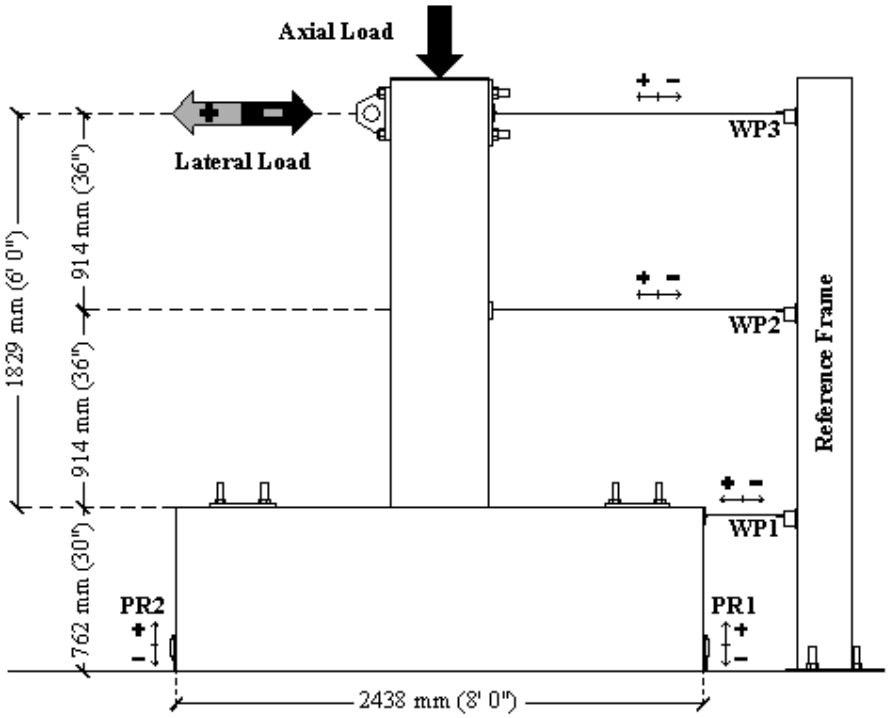

Figure 7.14. Test Specimen with Cable-Extension Position Transducers (Melek, 2006).

7.1.5. Testing Procedure

The specimens were subjected to constant axial load and cyclic lateral loads by the application of a cyclic displacement at the top of the column. Two different lateral displacement histories were applied to specimens, a standard history and a near-fault history. The standard displacement history is fairly typical (Figure 7.15), and consisted of three cycles at each displacement level with monotonically increasing drift levels (0.1, 0.25, 0.5, 0.75, 1.0, 1.5, 2.0, 3, 5, 7, and 10%).

The specimen subjected to the near-fault displacement history was cycled three times at 0.1, 0.25, 0.5 and 1.0% drift levels, followed by one half cycle to 1.5% lateral drift level in one direction, followed by monotonically increasing drift in the opposite direction until failure was reached (Figure 7.16).

One objective of the tests was to apply large displacement amplitudes to assess both the loss of lateral load capacity and the loss of axial load-carrying capacity. The latter was

important in evaluating life-safety and collapse prevention performance levels. Due to this consideration, lateral drift cycles were continued after the loss of lateral strength until axial load-carrying capacity was lost.

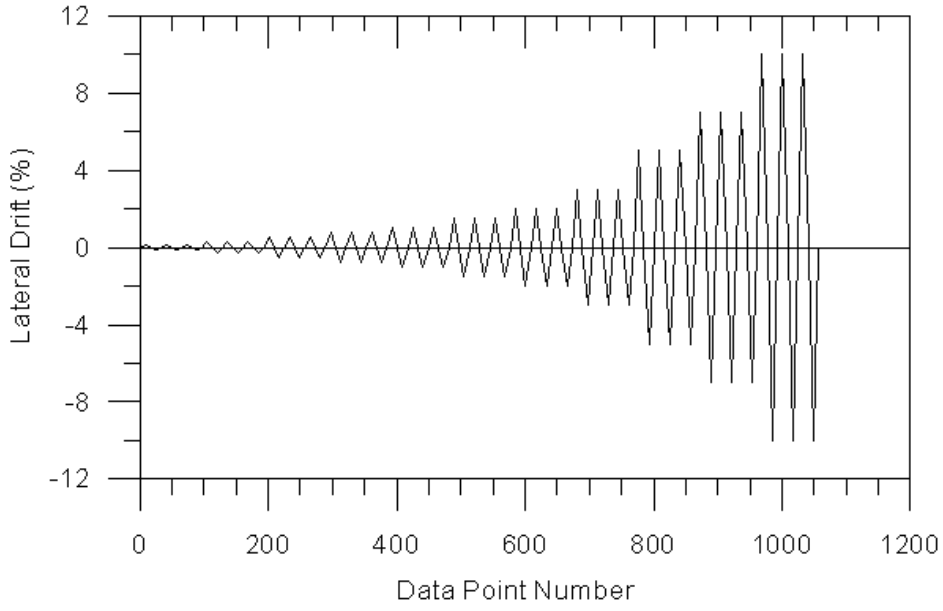

Figure 7.15. Standard Displacement History.

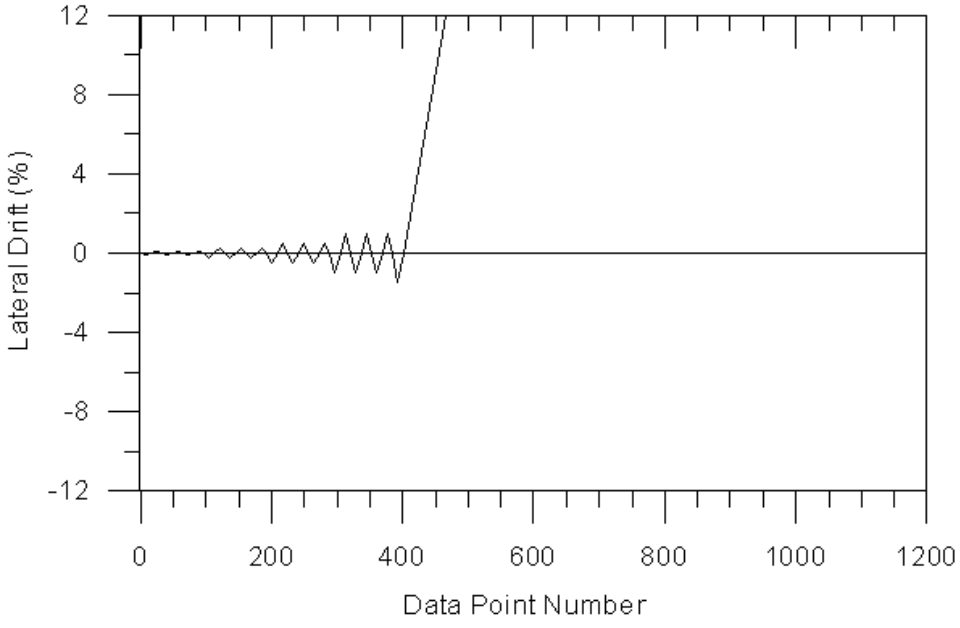

Figure 7.16. Near-Fault Displacement History.

7.2. Calibration of the Analytical Model

For calibration of the analytical model proposed, all six column specimens tested by Melek (2006) was used. Experimental calibration of the geometric, as well as the constitutive parameters of the analytical model, are discussed in the following subsections.

7.2.1. Geometry

Figures 7.17 and 7.18 show a preliminary lateral load – top displacement response prediction obtained using the analytical model, for column specimen 2S10M, using either eight model elements along the lap splice length with thirteen concrete macro-fibers along the width of the column, or using 16 model elements along the lap splice length with 26 concrete macro-fibers along the width. Four model elements are used above the lap splice region for both analyses. For both of these analyses, the splitting bond stress vs. slip relation for partially confined concrete by Harajli (2009) and the pullout bond stress vs. slip relation for confined concrete by Elegehausen *et al*. (1983) are used in a combined manner, where the bond slip springs in the vicinity of the ties are assigned pullout relationships, as described in Chapter 6. Since the comparison indicates that increasing the number of concrete macro-fibers or the number of model elements does not significantly influence the prediction of the global response (lateral load vs. top displacement), for subsequent analysis of all of the six specimens, 8 model elements were used along the lap splice region, 4 model elements were used above the lap splice region, and 13 concrete macro-fibers were used along the width of the columns.

The model elements are discretized along column height to allow consistent deformation comparisons between model and experimental results at all locations where strain gauges and displacement transducers were attached to the specimens during testing. The location and height of each model element is calibrated in such a way that the location of each model element approximately coincides with the location of a strain gauge or displacement sensor. For all analyses, the parameter representing the relative center of rotation of each model element (c) was assigned a value of 0.40.

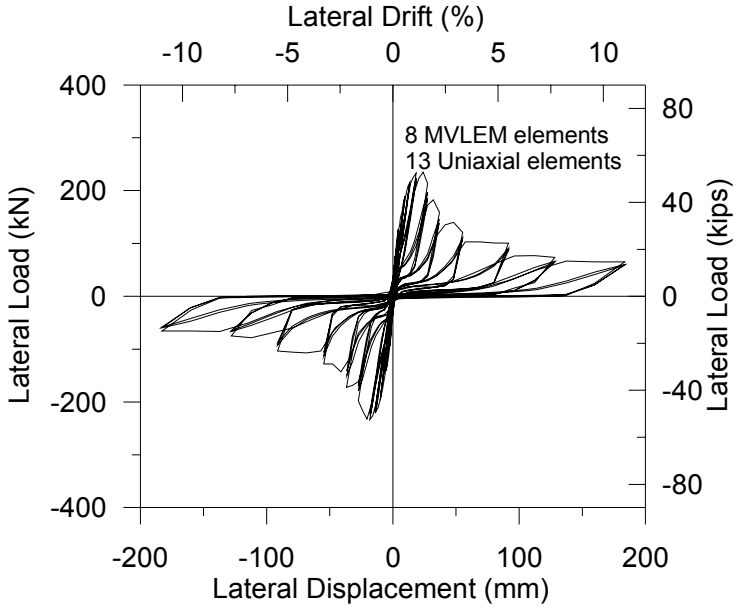

Figure 7.17. Sensitivity of the Model Response to Number of Model Elements and Concrete Macro-Fibers.

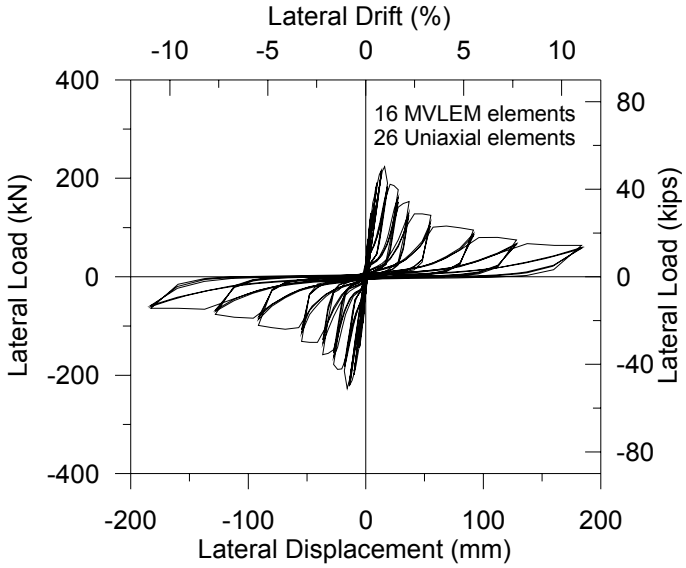

Figure 7.18. Sensitivity of the Model Response to Number of Model Elements and Concrete Macro-Fibers.

7.2.2. Materials

7.2.2.1 Steel Stress-Strain Relation. The constitutive model used for reinforcing steel was calibrated for yield strength, elastic modulus, strain hardening ratio, and cyclic curvature degradation parameters. Yield strength values were calibrated based on uniaxial test results on steel coupon samples of the reinforcing steel used in the construction of the specimens. Since test results for the stress vs. strain behavior of the reinforcement was not available, typical values of E0 = 200 GPa and b = 2% was used for the elastic modulus and the strain hardening ratio, respectively. The values $R0 = 20$, $a1 = 18.5$, and $a2 = 0.15$ (accounting for the cyclic degradation of the curvature coefficient R and thus the Bauschinger effect), originally suggested by Menegotto and Pinto (1983), were used in the calibration. Table 7.3 summerizes the constitutive parameters used in the analysis for reinforcing steel. Since longitudinal bar yielding was not observed during these tests, the steel yield strength and strain hardening ratio values were not modified for consideration of tension stiffening effects on the reinforcement.

Table 7.3. Calibrated Constitutive Parameters for Concrete and Steel

Material	Parameter	Specimens 2S10M-2S20M-2S30M	Specimens 2S20H-2S20HN-2S30X
Concrete in compression	$f_c^{/}(Mpa)$	36	35
	$\varepsilon_c^{/}$	0.002	0.0025
	$E_c(Mpa)$	27577	21000
	ε_{cr}	0.0025	0.0032
	r	5.02	7
Concrete in tension	$f_t(Mpa)$	3.4	3.4
	ε_t	0.00008	0.00008
	$E_c(Mpa)$	27577	21000
	ε_{cr}	0.0035	0.0035
	r	1.20	1.20
Reinforcing bar (Column, starter and ties)	$f_y(Mpa)$	510 (column), 521 (starter) and 481 (ties)	510 (column), 507 (starter) and 481 (ties)
	$E_0(Gpa)$	200	200
	b	0.02	0.02

7.2.2.2 Concrete Stress – Strain Relations The monotonic envelope curves of the Chang and Mander (1994) constitutive model for compression and tension were calibrated for values of peak compressive and tensile stress (f'_c and f_t), strains at peak stress (ε'_c and ε_t), elastic modulus E_c, the parameter r defining the shape of the envelope curves, and the normalized strain parameter x_{cr} (or ε_{cr}) controlling the post peak slope of the envelope curves.

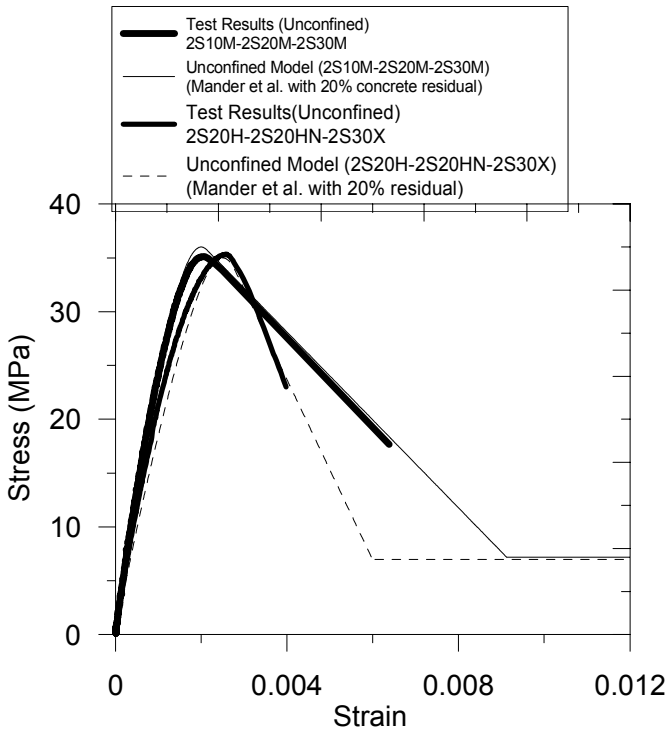

Figure 7.19. Calibration of Concrete Constitutive Model for Compression.

The envelope curve for unconfined concrete in compression was calibrated using results of monotonic stress-strain tests, conducted at time of testing, on standard 152 mm x 304 mm cylinder specimens of the concrete used in the construction for the first (2S10M, 2S20M, 2S30M) and second batches (2S20H, 2S20HN, 2S30X) of concrete (Figure 7.19), with a 20% residual stress value defined for the envelope curve for improving the stability of the analysis. The parameters used for the calibration of the monotonic envelopes for unconfined concrete in compression and tension are presented in Table 7.3. Stress – strain relations for confined concrete were not used in modeling of these columns, since the amount of transverse reinforcement used in the specimens did not provide effective

confinement. The concrete tensile strength was determined from the relationship $f_t = 0.31\sqrt{f'_c}$ (MPa), and a value of 0.00008 was selected for the strain ε_t at peak monotonic tensile stress, as suggested by Belarbi and Hsu (1994). The shape of the monotonic tension envelope was calibrated (via the parameters r and x_{cr}) to reasonably represent the average post-crack stress – strainship relation proposed by Belarbi and Hsu (1994) for considering the effects of tension stiffening on concrete. The hysteretic stress-strain rules defined by Chang and Mander (1994), modified slightly as described by Orakcal (2004), were used to simulate the cyclic behavior of unconfined concrete implemented in model.

7.2.2.3 . Shear Force - Deformation Relation. The trilinear envelope curve of the origin-oriented force–deformation relationship, which was adopted for the horizontal shear springs in the model elements, were calibrated based on the empirical relationships proposed by Sezen (2002), as described in Chapter 3. The calibrated envelope parameters for each of the six column specimens are listed in Table 7.4. It must be mentioned that during testing, none of the column specimens experienced shear failure or significant shear deformations.

Table 7.4. Shear Force – Deformation Envelope Parameters for the Horizontal Shear Springs.

Column	(mm.)			(kN)			
	δ_{cr}	δ_y	δ_n	V_{cr}	V_y	V_n	V_p
2S10M	0.03	0.80	3.96	33.4	208.7	237.0	251.0
2S20M	0.03	0.81	3.96	33.4	246.5	267.9	276.5
2S30M	0.03	0.80	3.96	33.4	278.6	294.1	296.6
2S20H	0.03	0.81	3.63	36.0	263.6	282.5	305.0
2S20HN	0.03	0.81	3.63	36.0	263.6	282.5	305.0
2S30X	0.03	0.80	3.30	39.6	328.0	333.2	364.0

7.2.2.4 Bond Stress – Slip Relations.Envelope parameters of the constitutive bond stress – slip relationships adopted in the analytical model, for splitting failure by Harajli *et al*. (1994, 2004, 2009) and for pullout failure (in the vicinity of the ties) by Eligehausen *et al*.

(1983), were calibrated as proposed originally in the constitutive relationship formulations. The calibrated parameters are listed in Table 7.5.

Table 7.5. Calibrated Bond Stress – Slip Parameters for Splitting and Pullout.

Parameter	s_1 *mm*	s_2 *mm*	s_3 *mm*	u_1 *Mpa*	u_3 *Mpa*	$u_{\max}$ *Mpa*	u_{ps} *Mpa*	$s_{\max}$ *mm*	s_0 *mm*	α	β
Harajli *et al.* (1994)	1.95	4.55	13	15.42	-	5.74	3.07	0.22	0.15	0.70	0.65
Eligehausen *et al.* (1983)	1.24	3.71	13	14.78	5.48	-	-	-	-	0.40	-

7.3. Comparison of Analytical Results with Test Results

Detailed comparisons were made between the analytical model results and the experimental measurements, at various response levels, for all six of the column specimens tested in the experimental program. Comparisons of various response attributes are discussed in the following subsections.

7.3.1. Lateral Load – Top Displacement Response

The lateral load – top displacement response measurements for the column specimens were processed to eliminate measurement errors related to sliding and uplift of the specimen pedestal and the effect of the horizontal component of the axial load on lateral load at higher drift levels. The corrected lateral load – top displacement measurements were considered in the comparisons.

Figures 7.20 to 7.31 compare the measured and predicted lateral load – top displacement responses for all six column specimens. It can be observed in the figures that the general characteristics of the measured response agree very well with the calculated response. All specimens exhibit similar responses, with sudden lateral strength degradation at a drift levels between 1% and 1.5%, both in measured and calculated results. It is also observed that the peak lateral load reached for each specimen is

influenced by the level of the applied axial load, where the the lateral load capacity increases with higher axial load levels.

The lateral load capacity and the lateral stiffness of the columns are well-represented for most of the lateral drift levels. It can be seen that the model provides a reasonably accurate estimate of the global response for all columns, although the model tends to slightly underestimate the lateral displacement values at peak load. It must be mentioned that the hysteresis laws of implemented analytical stress-strain relations for steel and concrete, shear, and bond stress-slip relations are controlled by several parameters that account for cyclic properties of the response, including stiffness degradation upon unloading, pinching of the hysteresis loops and strength decay upon repeated loading cycles. Overall, the comparisons indicate that the cyclic properties of the analytical responses are in agreement with the measured cyclic behavior.

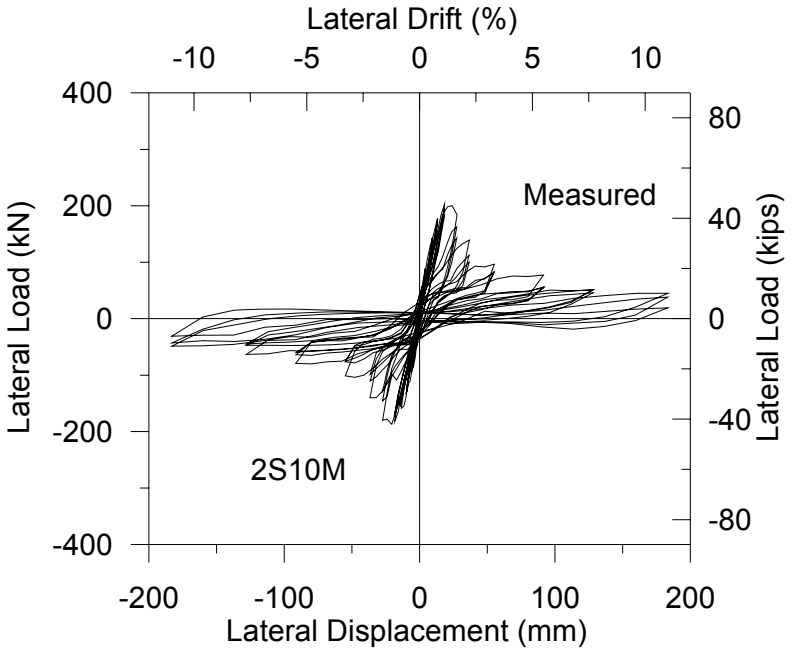

Figure 7.20. Measured Lateral Load Top Displacement Relationship for Specimen 2S10M.

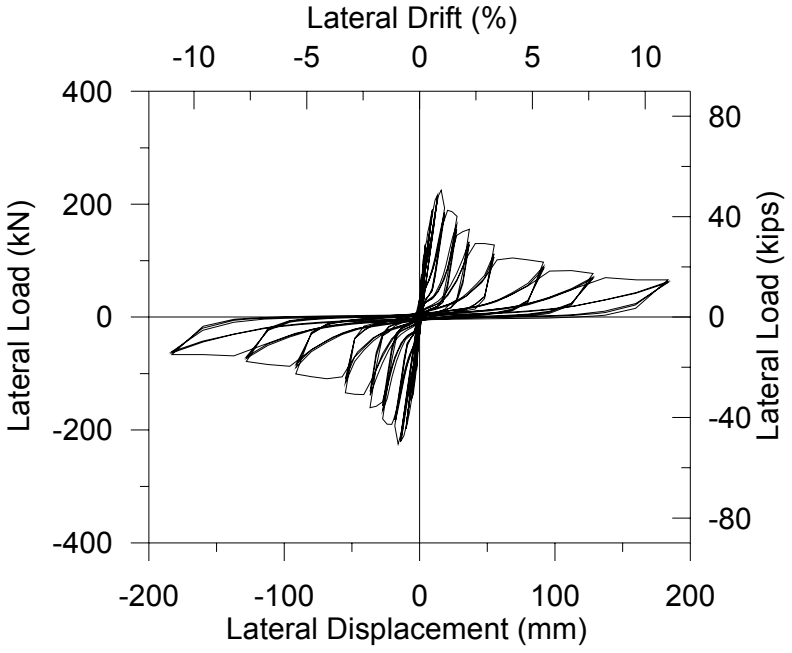

Figure 7.21. Calculated Lateral Load Top Displacement Relationship for Specimen 2S10M.

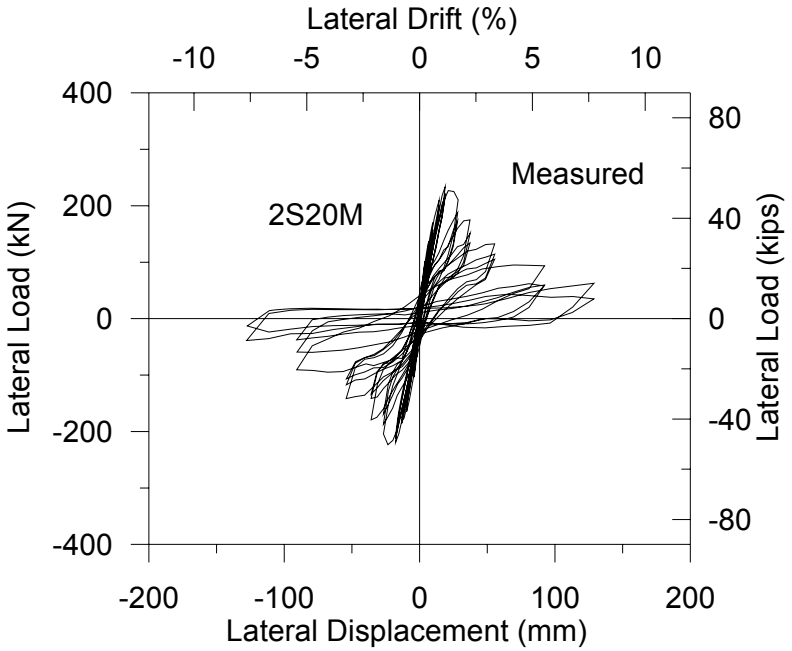

Figure 7.22. Measured Lateral Load Top Displacement Relationship for Specimen 2S20M.

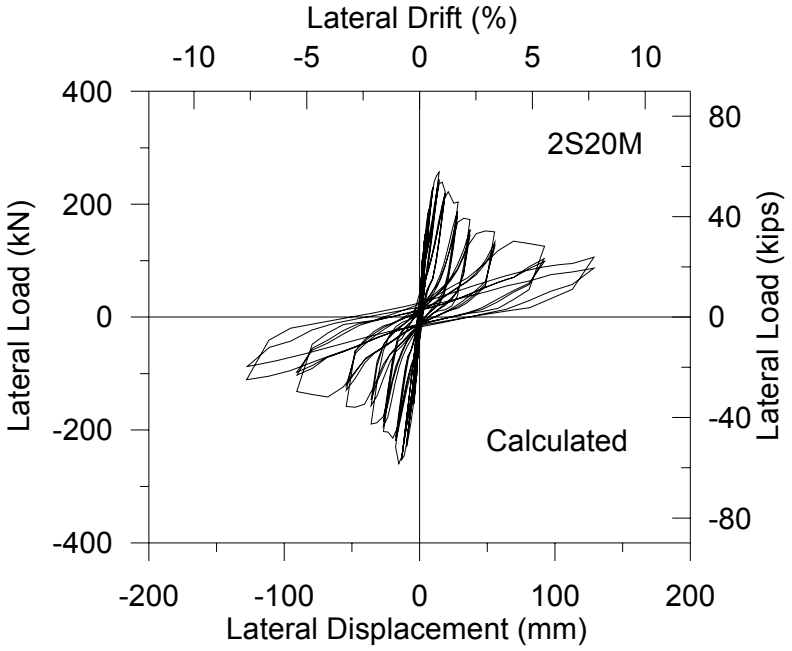

Figure 7.23. Calculated Lateral Load Top Displacement Relationship for Specimen 2S20M.

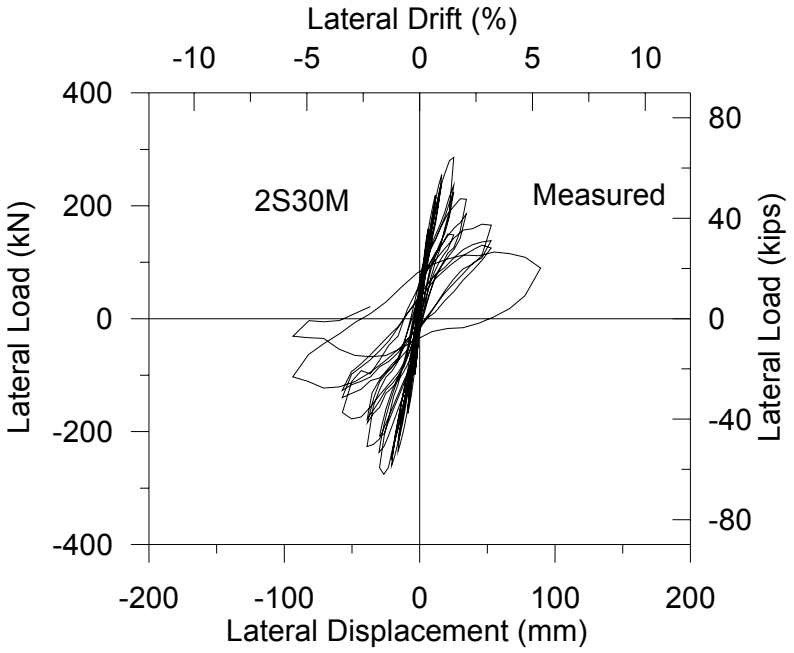

Figure 7.24. Measured Lateral Load Top Displacement Relationship for Specimen 2S30M.

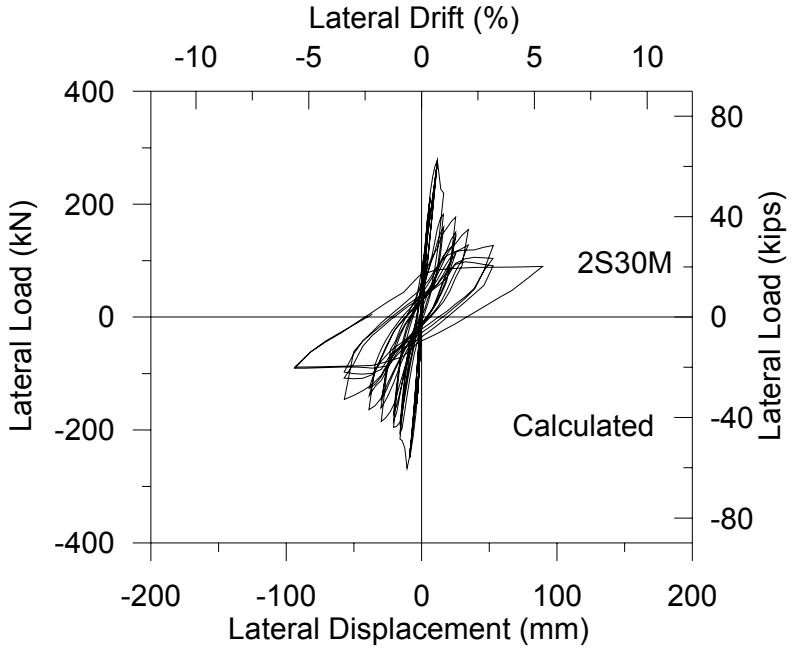

Figure 7.25. Calculated Lateral Load Top Displacement Relationship for Specimen 2S30M.

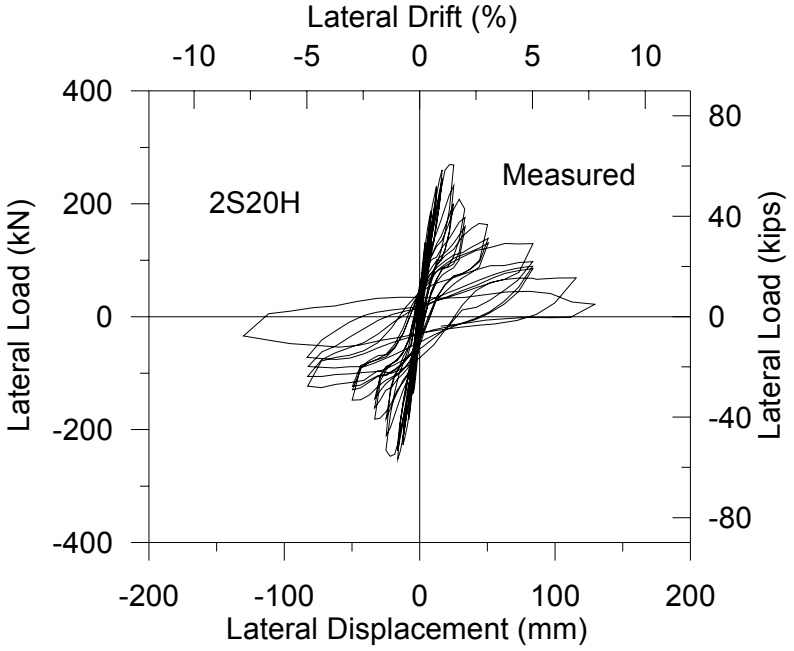

Figure 7.26. Measured Lateral Load Top Displacement Relationship for Specimen 2S20H.

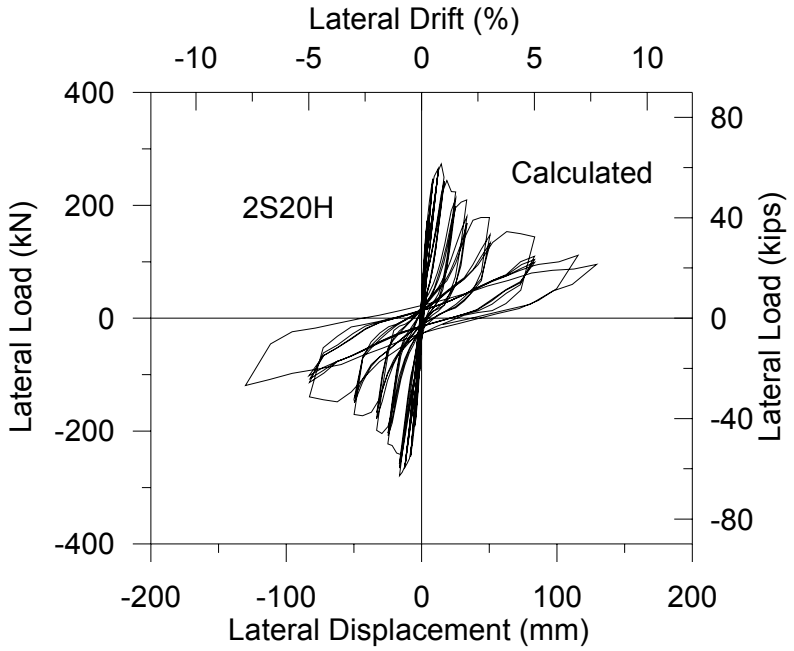

Figure 7.27. Calculated Lateral Load Top Displacement Relationship for Specimen 2S20H.

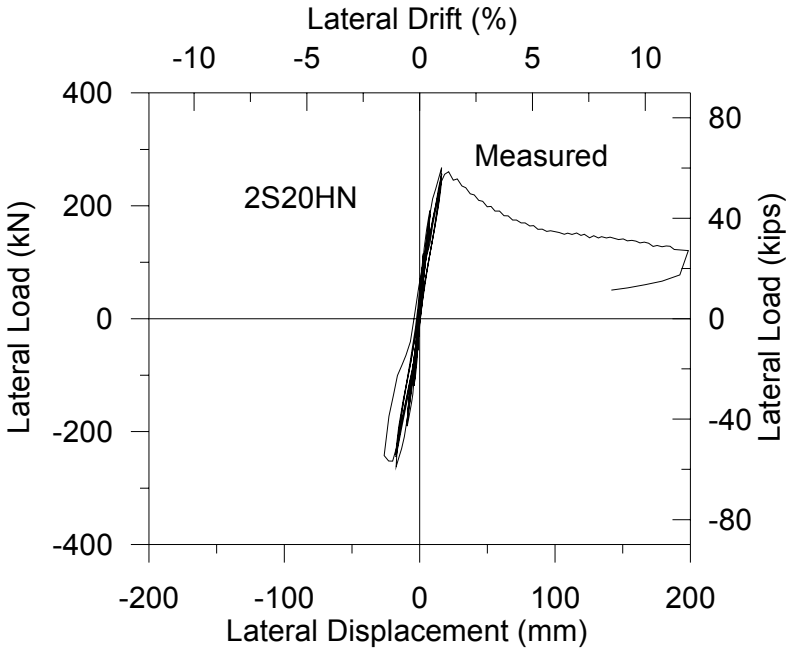

Figure 7.28. Measured Lateral Load Top Displacement Relationship for Specimen 2S20HN.

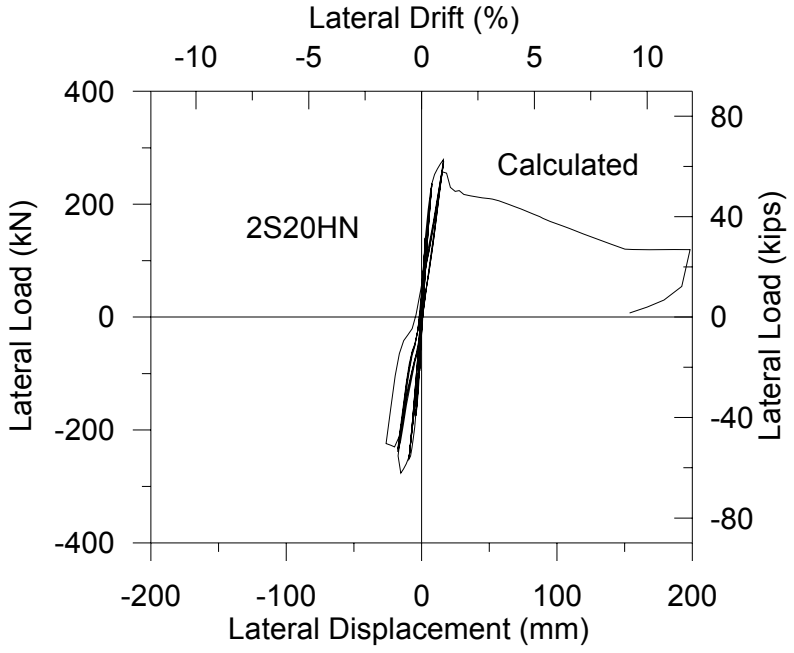

Figure 7.29. Calculated Lateral Load Top Displacement Relationship for Specimen S20HN.

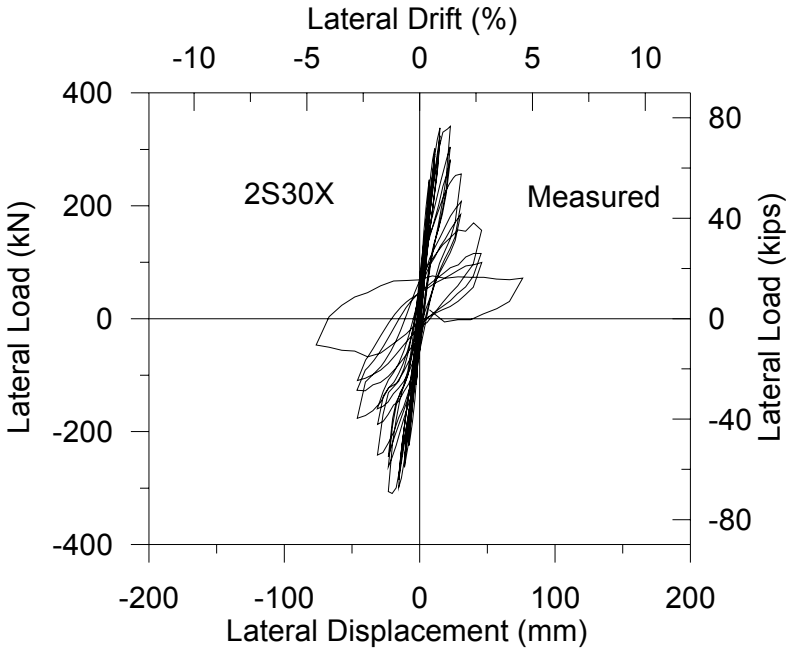

Figure 7.30. Measured Lateral Load Top Displacement Relationship for Specimen 2S30X.

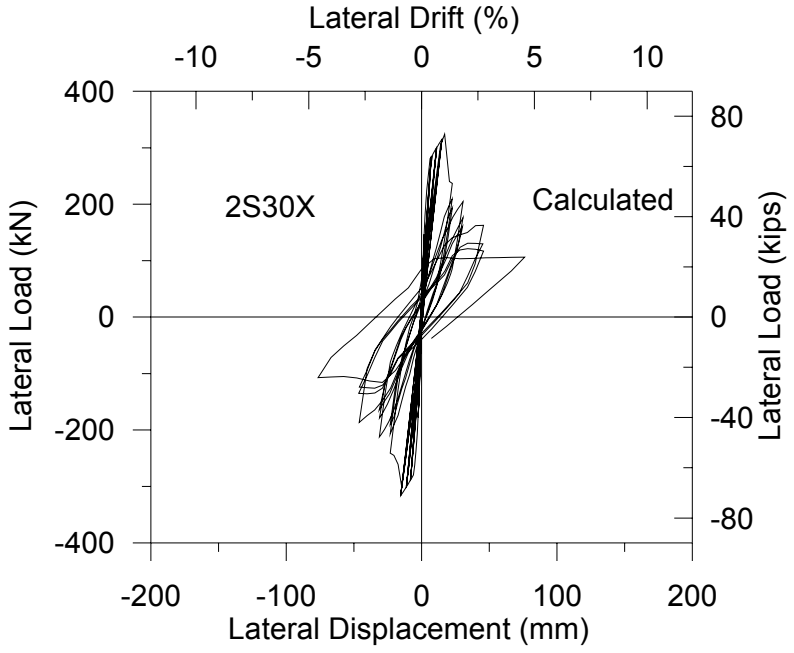

Figure 7.31. Calculated Lateral Load Top Displacement Relationship for Specimen 2S30X.

7.3.2. Rotation Histories at Different Locations

Total rotations predicted by the model due to combined effects of flexural and slip deformations were compared with the measued rotations for all six specimens at different locations (at column base, at the top of the lap splice, and in-between). Rotations predicted by the model due to slip deformation only (with flexural rotations excluded) were also compared with the experiment results. Figures 7.32 to 7.38 present total rotation comparisons at column base for all six column specimens. Figures 7.39 to 7.46 compare the total rotations at the top of the lap splice regions, with the exception of Figure 7.41, which compares total rotation at a distance of 330 mm from the column base for specimen '2S10M'. Figures 7.47 to 7.52 compare pure slip rotations (with flexural contribution excluded) at the top of lap splice region for all specimens. The results are discussed in the following paragraphs.

It is first necessary to describe the methodology used to calculate the rotation measured in the tests, as well as the way rotations are defined in the analysis results. In the tests, for specimens 2S20H, 2S20HN and 2S30X, total rotations at the top of the splice were determined by calculating the difference in the axial (vertical) displacements measured by the two displacement sensors (SL1 and SL2 as shown in Figure 7.13), and dividing the difference in the axial displacements by the distance between the sensors (660 mm). To calculate the total rotation at a distance of 330 mm from column base for specimens 2S10M, 2S20M and 2S30M, the, same procedure was adopted, as shown in Figure 7.12.

Also in the test data, in order to obtain the total rotation at the base of specimens 2S10M, 2S20M and 2S30M, the difference in the axial displacements measured by the two linear displacement sensors (SL3 and SL4 as shown in Figure 7.12) were divided by the distance between the sensors (508 mm), and this value was subtracted from the total rotation at a distance of 330.20 mm from column base.

In order to calculate the total rotation at column base for specimens 2S20H, 2S20HN and 2S30X, the difference in the axial displacements measured by the two displacement sensors L2 and L1 (shown in Figure 7.13) was divided by the distance between the sensors

(203.20 mm) to obtain a first rotation value. Next, the difference in the axial displacements measured by the two displacement sensors L4 and L3 were divided by the distance between the sensors (203.20 mm) to obtain a second rotation value. Finally the rotation at base was obtained by subtracting the sum of these two values from the total rotation at the top of the lap splice. Finally, in the test data, in order to obtain the total rotation at top of the lap splice for specimens 2S10M, 2S20M and 2S30M, the two rotation values calculated in a similar manner to specimens 2S20H, 2S20HN and 2S30X, with the total rotation values at column base.

In the analysis results, total rotations at different locations on the columns are directly obrained from the rotational degrees of freedom of the model, as flexural and slip deformations are coupled in the model results. However, since pure slip deformations along the splice can contribute significantly to column top displacement; rigid body rotation of the column due to slip deformations over the splice length can also be obtained from the model results. In the analysis results, slip rotation values were extracted by subtracting the rotations associated with the longitudinal deformations of the uniaxial steel elements from the the total rotations at the rotational degrees of freedom of the model

Figures from 7.32 to 7.38 compare analytical and experimental results for the total rotation histories at the base of all column specimens (2S10M, 2S20M, 2S30M, 2S20H, 2S20HN and 2S30X). The comparisons indicate that analytical model captures the experimental results, with the only exception of specimen 2S10M (Figures 7.32 and 7.33). Analysis results presented in Figures 7.32 and 7.33 were obtained using 8 model elements in the lap splice region with 13 concrete macro-fibers and 12 model elements in the lap splice region with 26 concrete macro-fibers, respectively. For this particular specimen, accuracy of the predicted response is apparently sensitive to discretization of the model, probably due to strain localization effects associated with crushing of concrete.

Figures 7.39 to 7.46 compare analytical and experimental total rotation histories at the top of the lap splice for all column specimens (2S10M, 2S20M, 2S30M, 2S20H, 2S20HN and 2S30X). A reasonable level of agreement is observed in these figures between the measued and calculated rotation histories. Analysis results shown in Figures 7.39 and 7.40 were obtained using 8 model elements in the lap splice region with 13

concrete macro-fibers and 12 model elements in the lap splice region with 26 concrete macro-fibers, respectively. As the two analysis results are close, strain localization effects do not seem to be governing the response predictions for this case.

Figure 7.41 compares the analytical and experimental total rotation histories at a distance of 330 mm from column base, for specimen 2S10M.

Correlation of measured and calculated slip rotations (with flexural contributions excluded) at the top of the lap splice region are also reasonably well as shown in Figures from 7.47 to 7.52. Overall, the analytical model has proved to be efficient in predicting rotations (both due to slip deformations and the combined effect of flexural and slip deformations) at different locations, for all of the column specimens investigated.

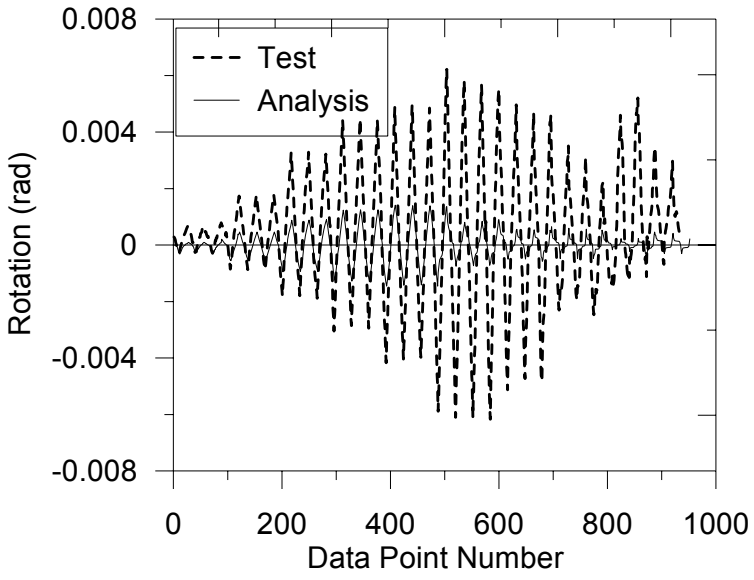

Figure 7.32. Comparison of Measured and Calculated Total Base Rotation Histories for Specimen 2S10M (Analysis with 8 Model Elements and 13 Macro-Fibers).

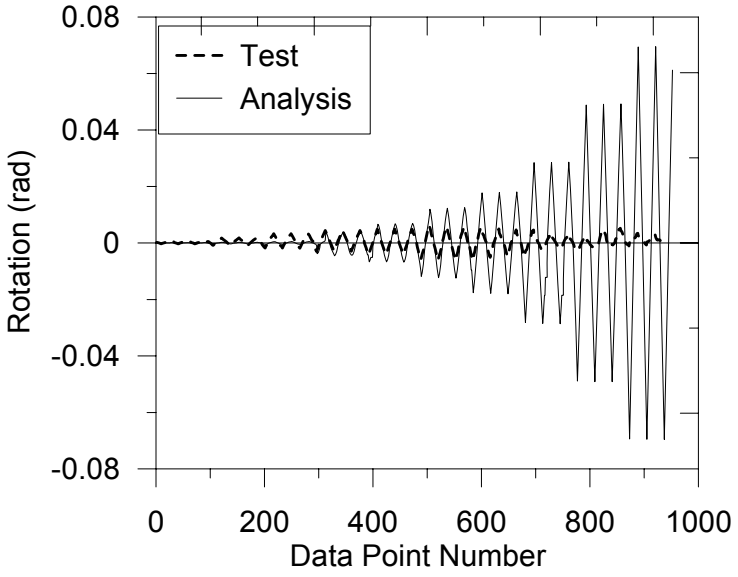

Figure 7.33. Comparison of Measured and Calculated Total Base Rotation Histories for Specimen 2S10M (Analysis with 12 Model Elements and 26 Macro-Fibers).

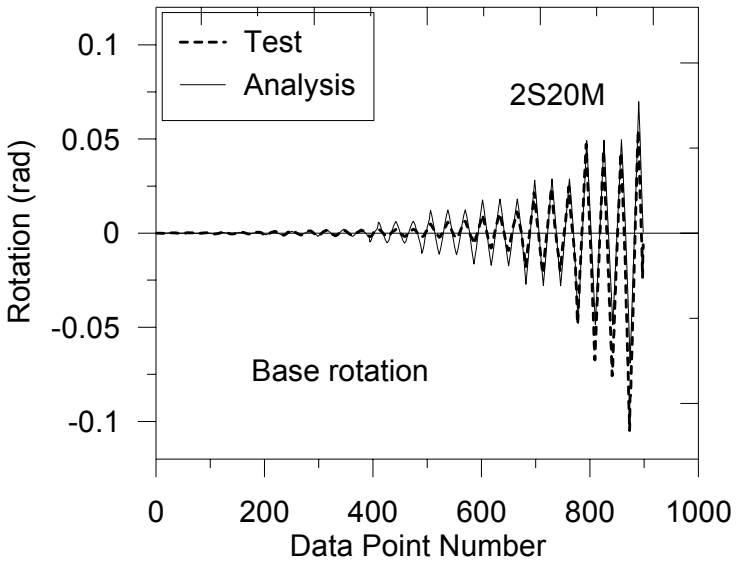

Figure 7.34. Comparison of Measured and Calculated Total Base Rotation Histories for Specimen 2S20M.

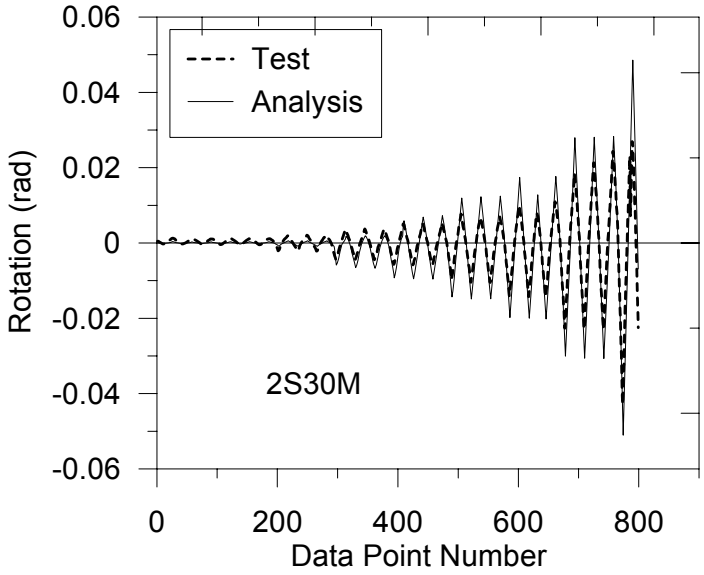

Figure 7.35. Comparison of Measured and Calculated Total Base Rotation Histories for Specimen 2S30M.

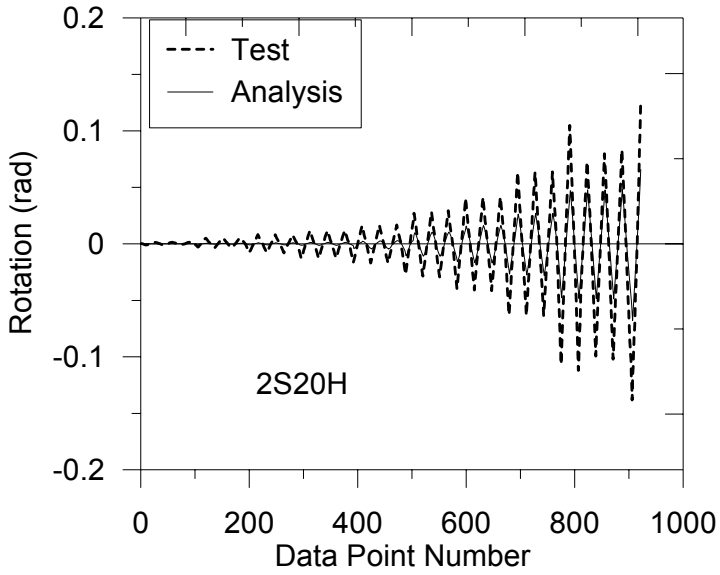

Figure 7.36. Comparison of Measured and Calculated Total Base Rotation Histories for Specimen 2S20H.

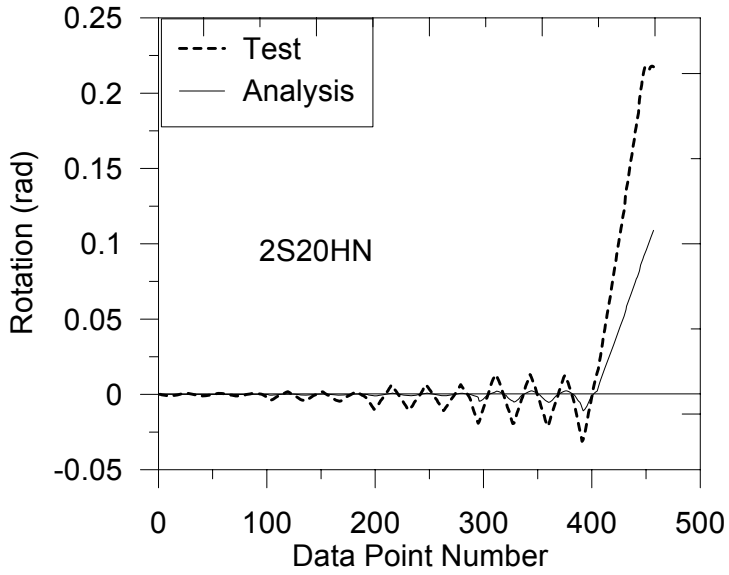

Figure 7.37. Comparison of Measured and Calculated Total Base Rotation Histories for Specimen 2S20HN.

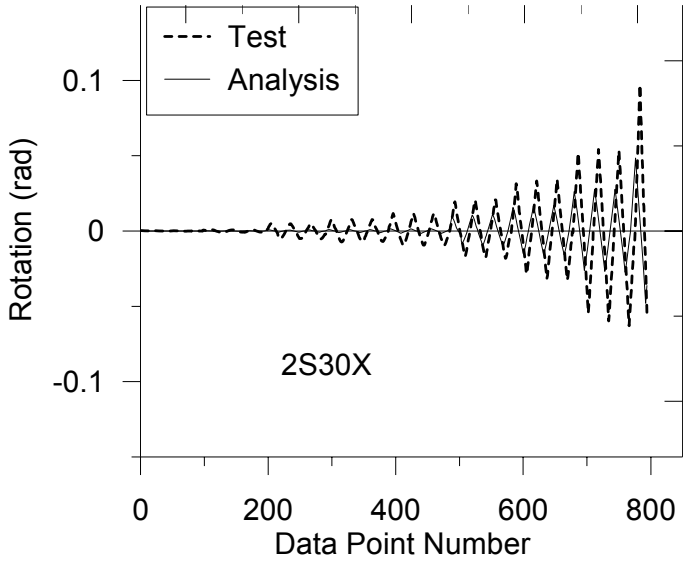

Figure 7.38. Comparison of Measured and Calculated Total Base Rotation Histories for Specimen 2S30X.

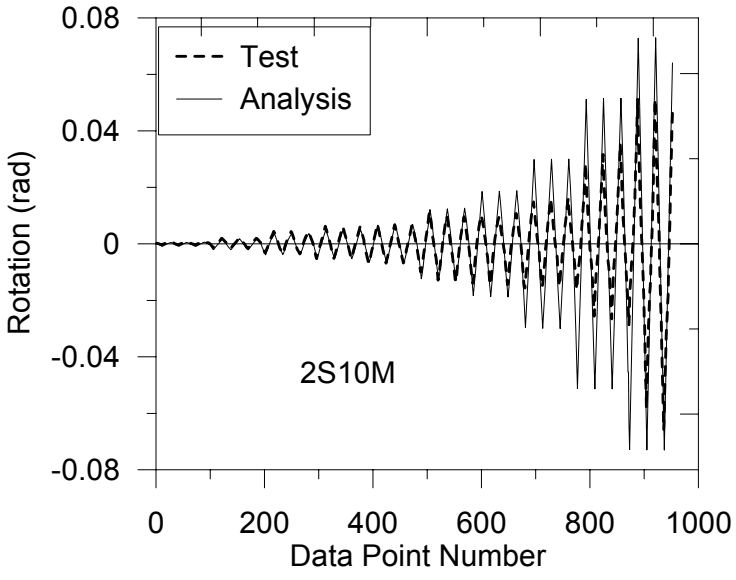

Figure 7.39. Comparison of Measured and Calculated Total Rotation Histories at Top of Splice for Specimen 2S10M (Analysis Done with Less Elemnts and Uniaxial Fibers).

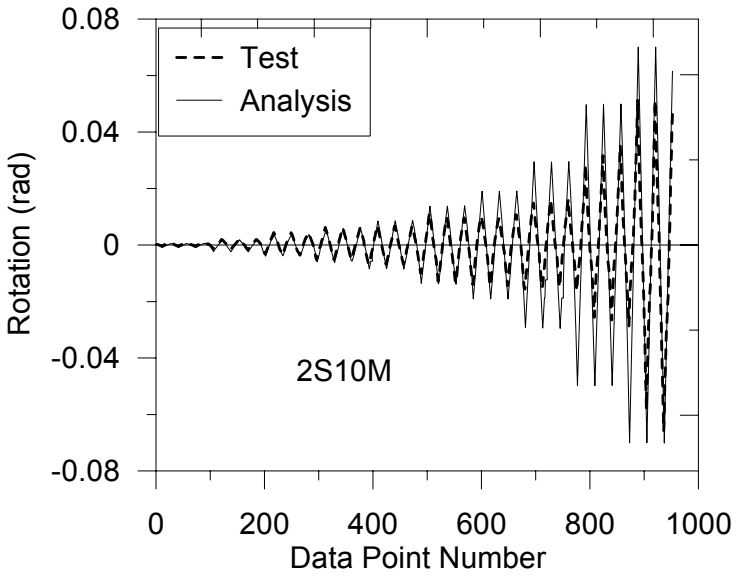

Figure 7.40. Comparison of Measured and Calculated Total Rotation Histories at Top of Splice for Specimen 2S10M (Analysis Done with More Elemnts and Uniaxial Fibers).

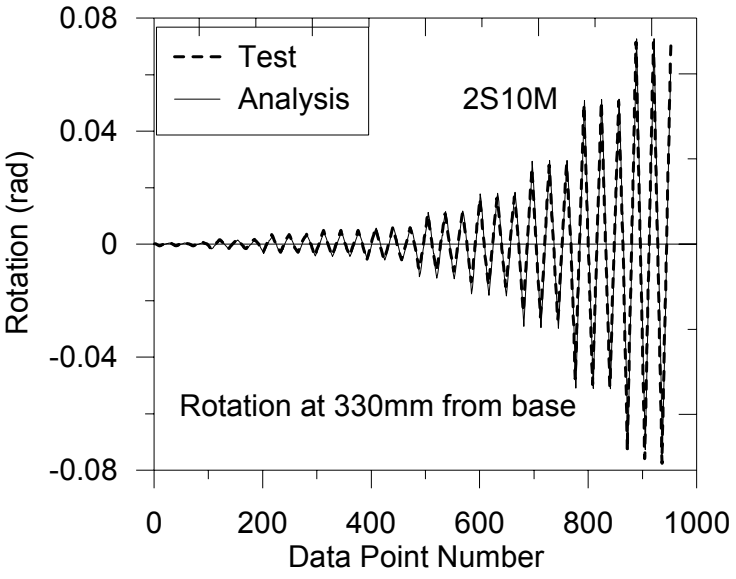

Figure 7.41. Comparison of Measured and Calculated Total Rotation Histories at 330 mm from Column Base for Specimen 2S10M.

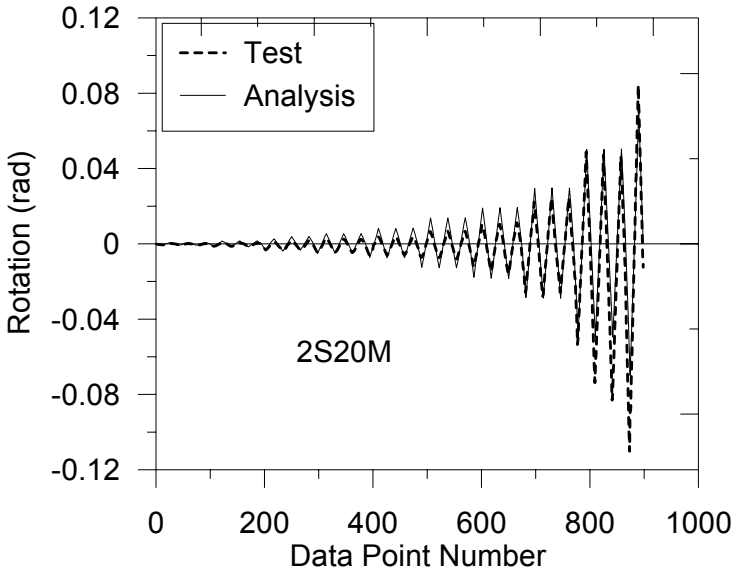

Figure 7.42. Comparison of Measured and Calculated Total Rotation Histories at Top of Splice for Specimen 2S20M.

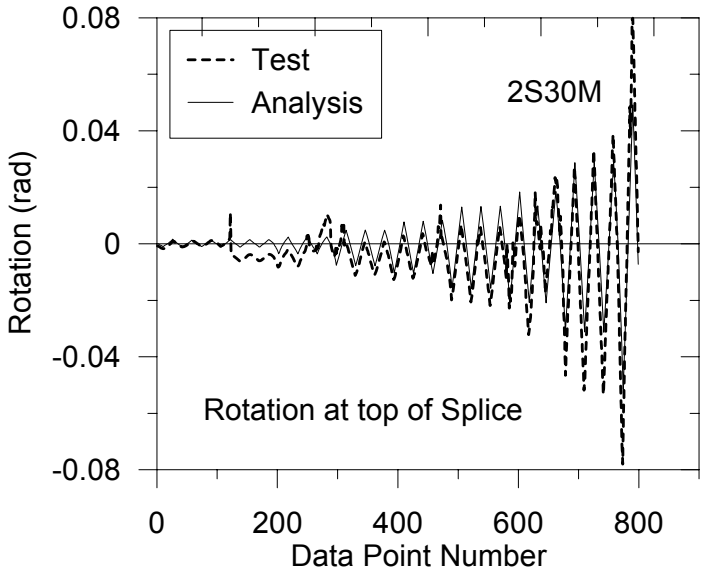

Figure 7.43. Comparison of Measured and Calculated Total Rotation Histories at Top of Splice for Specimen 2S30M.

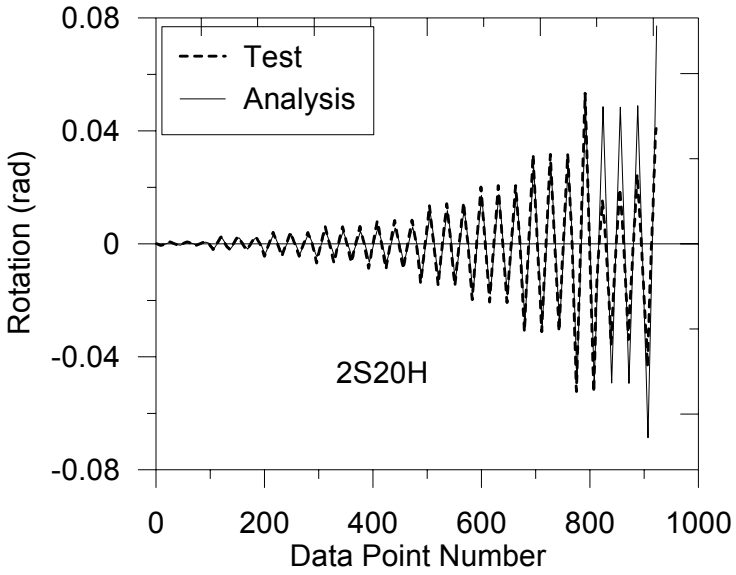

Figure 7.44. Comparison of Measured and Calculated Total Rotation Histories at Top of Splice for Specimen 2S20H.

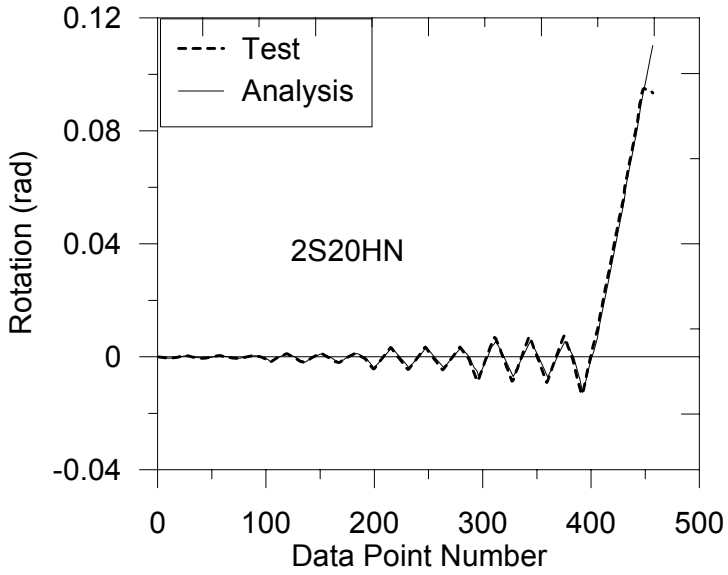

Figure 7.45. Comparison of Measured and Calculated Total Rotation Histories at Top of Splice for Specimen 2S20HN.

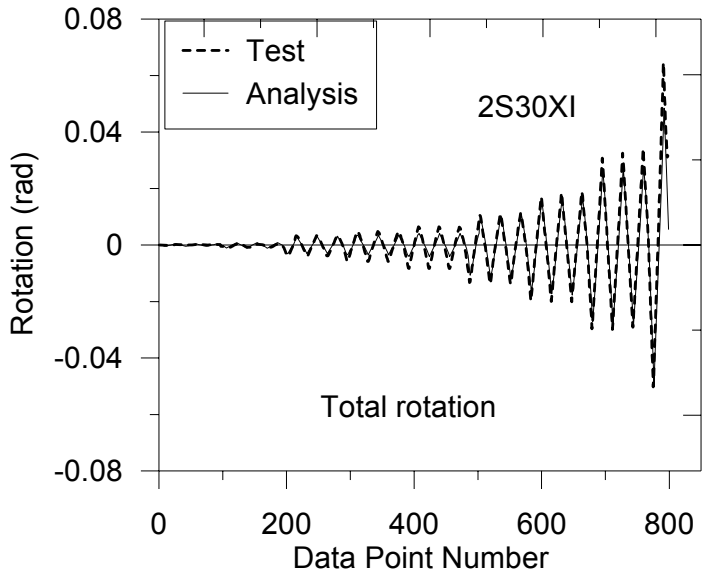

Figure 7.46. Comparison of Measured and Calculated Total Rotation Histories at Top of Splice for Specimen 2S30X.

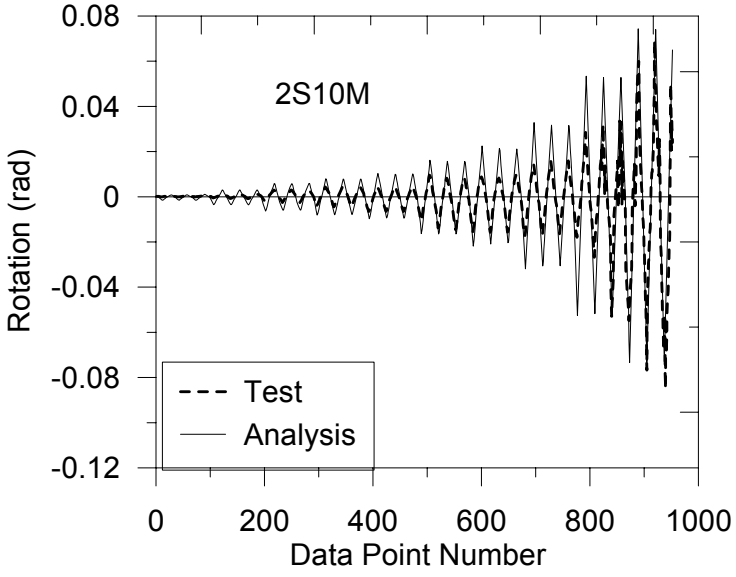

Figure 7.47. Comparison of Measured and Calculated Slip Rotation Histories at Top of Splice for Specimen 2S10M.

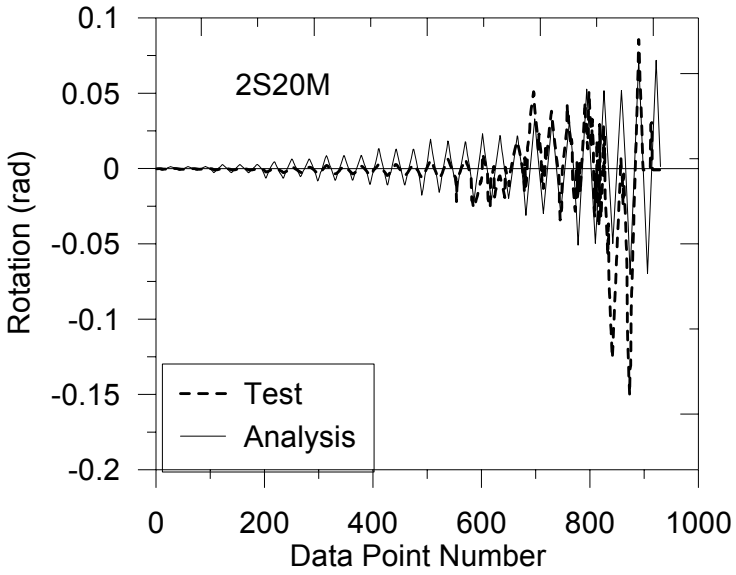

Figure 7.48. Comparison of Measured and Calculated Slip Rotation Histories at Top of Splice for Specimen 2S20M.

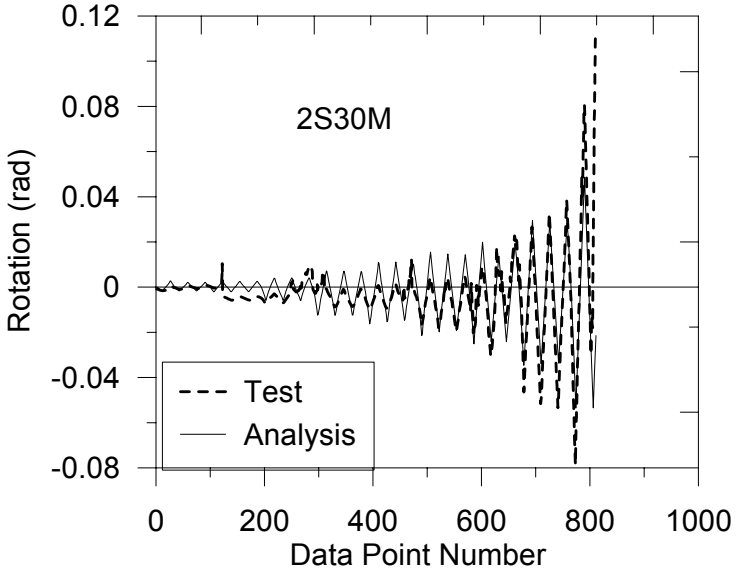

Figure 7.49. Comparison of Measured and Calculated Slip Rotation Histories at Top of Splice for Specimen 2S30M.

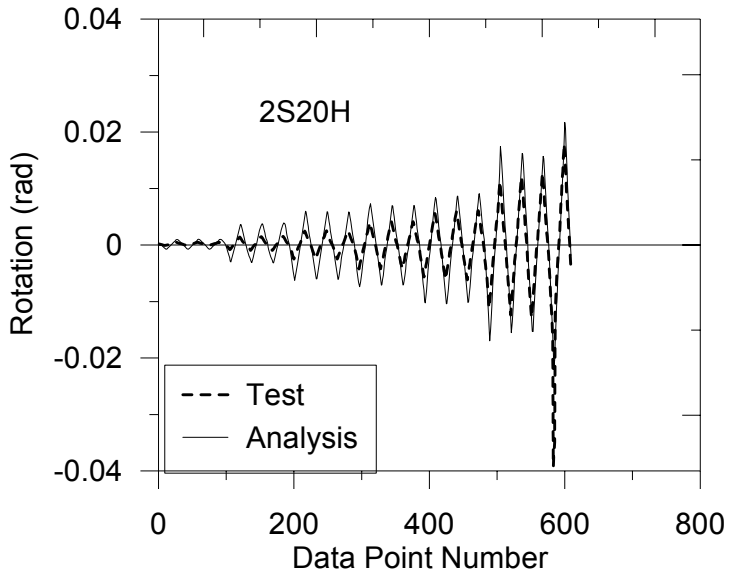

Figure 7.50. Comparison of Measured and Calculated Slip Rotation Histories at Top of Splice for Specimen 2S20H.

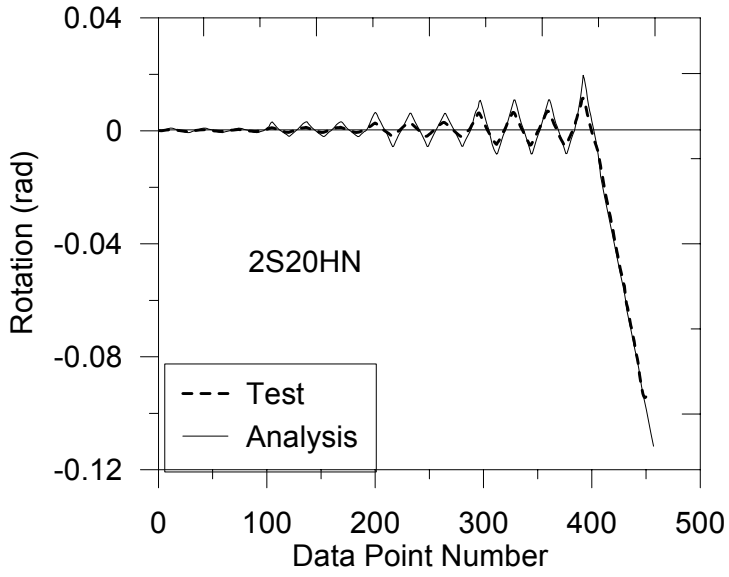

Figure 7.51. Comparison of Measured and Calculated Slip Rotation Histories at Top of Splice for Specimen 2S20HN.

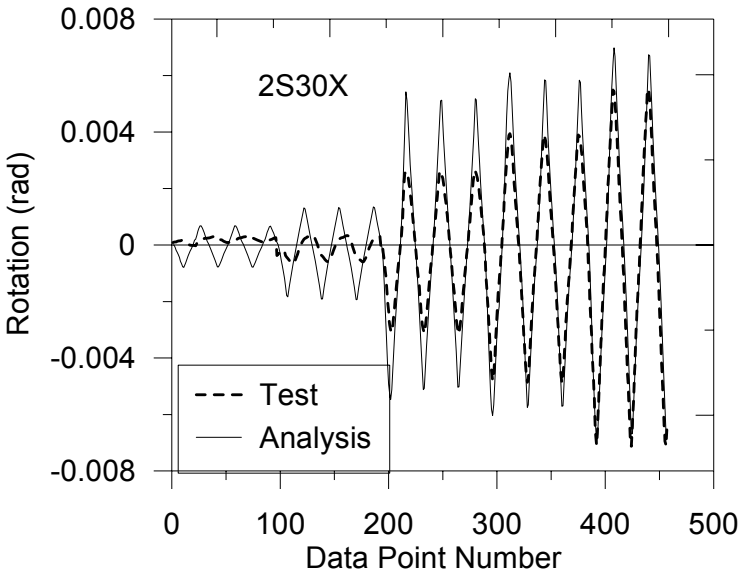

Figure 7.52. Comparison of Measured and Calculated Slip Rotation Histories at Top of Splice for Specimen 2S30X.

7.3.3. Reinforcing Steel Strain Distributions and Histories

Along the lap splice regions of the test specimens, three strain gauges were affixed to the exterior (corner) longitudinal bars, whereas two gauges were affixed to the exterior (corner) starter bars (starter bars being the bars anchored into the pedestal), as depicted in Figure 7.7. It can be deduced that longitudinal strains are equal to zero at the tips of the longitudinal and starter bars. Damage on the specimens and during testing led to failure of the strain gauges, generally at approximately 3% lateral drift (data point 770); therefore, readings for higher drift ratios are not available for most of the strain gauges.

Figures 7.53 to 7.58 compare the measured and calculated longitudinal strain distributions along the lap splice on exterior longitudinal and starter bars of three specimens (2S10M, 2S20M and 2S30M) at selected lateral drift levels. Figures 7.59 to 7.73 compare the analytically-obtained longitudinal strain histories with the steel strain history measurements of the strain gauges, located at different locations on the longitudinal and starter bars for different column specimens. In general, the test measurements and model results show reasonable agreement (considering the typical scatter observed in strain

gauge measurements in reinforced concrete member tests based on proximity of a strain gauge to a crack), up to a drift level of 1% (data point 450), after which lateral load degradation starts with the initiation of bond deterioration along splice length,

It must be mentioned that steel strain predictions obtained using the analytical model for the interior (side) longitudinal and starter bars were not as good. The strains measured on the interior bars were significantly different than the strains on the exterior (corner) bars at the same drift levels, as reported by Melek and Wallace (2004). This may indicate that bond stresses acting on interior bars (side bars) within a splice may be different than those acting on exterior bars. The bond stress vs. slip constitutive relationship by Harajli (1994, 2004, 2009) for splitting of partially-confined concrete was originally developed based on test results for corner bars, and maybe incapable of accurately representing bond stresses acting on middle bars (side bars) of a column cross-section. A constitutive bond-stress vs. slip relation specifically applicable to side bars of a reinforced concrete cross section, is not available in the literature.

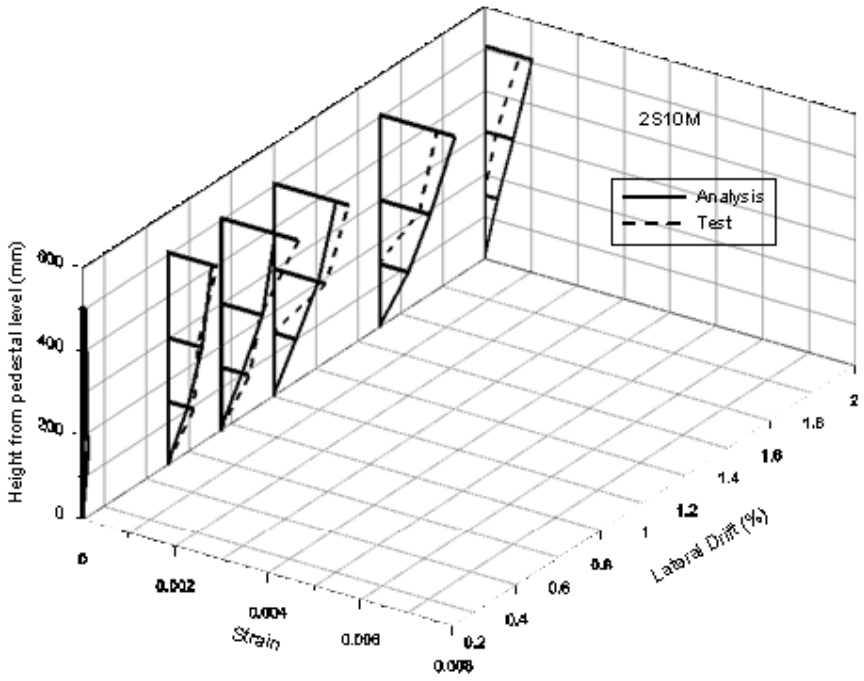

Figure 7.53. Comparison of Measured and Calculated Steel Strain Distributions along Lap Splice on Exterior Longitudinal Bar of Specimen 2S10M.

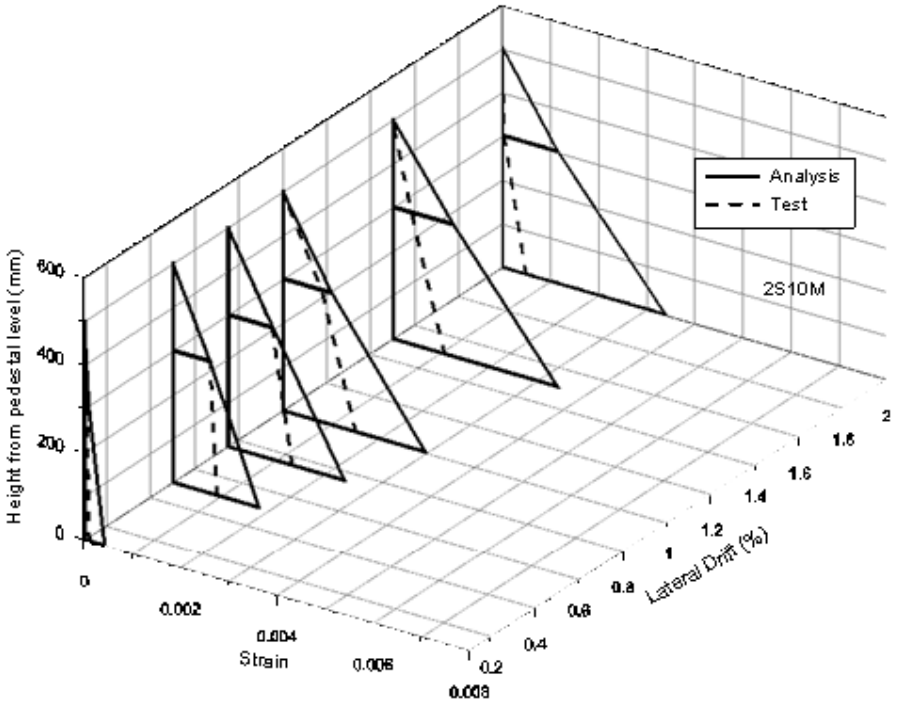

Figure 7.54. Comparison of Measured and Calculated Steel Strain Distributions along Lap Splice on Exterior Starter Bar of Specimen 2S10M.

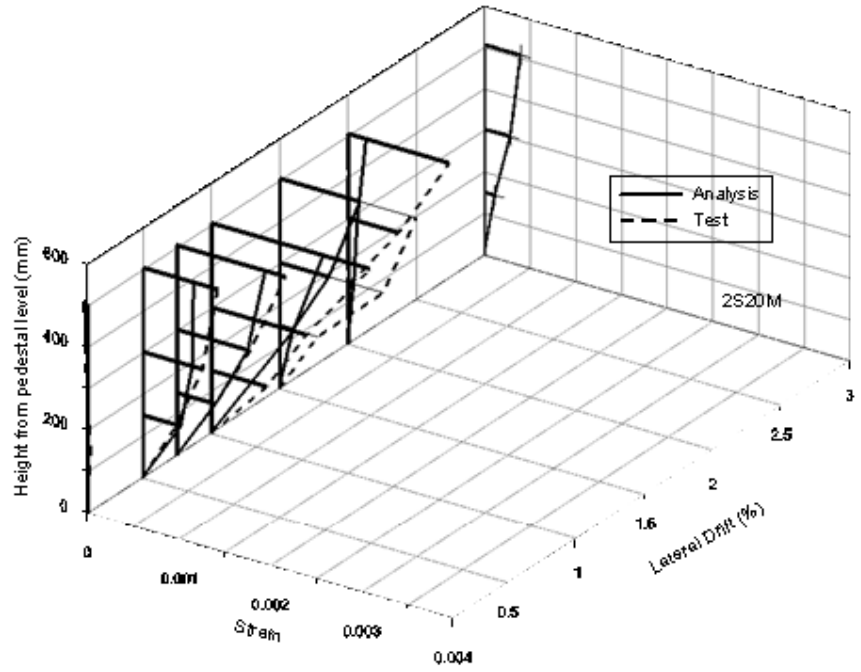

Figure 7.55. Comparison of Measured and Calculated Steel Strain Distributions along Lap Splice on Exterior Longitudinal Bar of Specimen 2S20M.

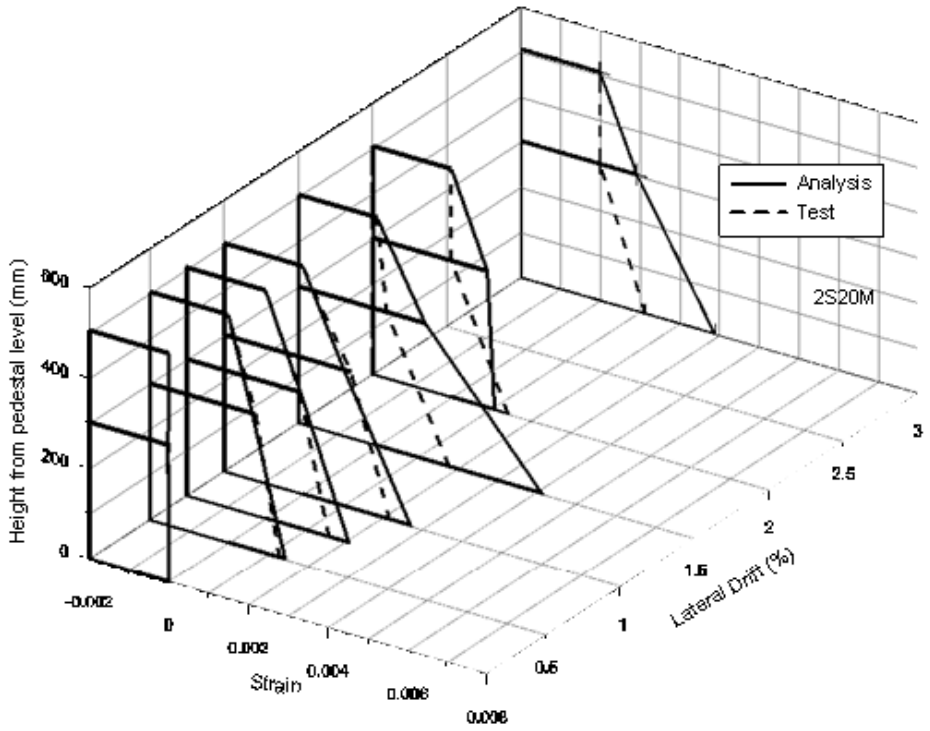

Figure 7.56. Comparison of Measured and Calculated Steel Strain Distributions along Lap Splice on Exterior Starter Bar of Specimen 2S20M.

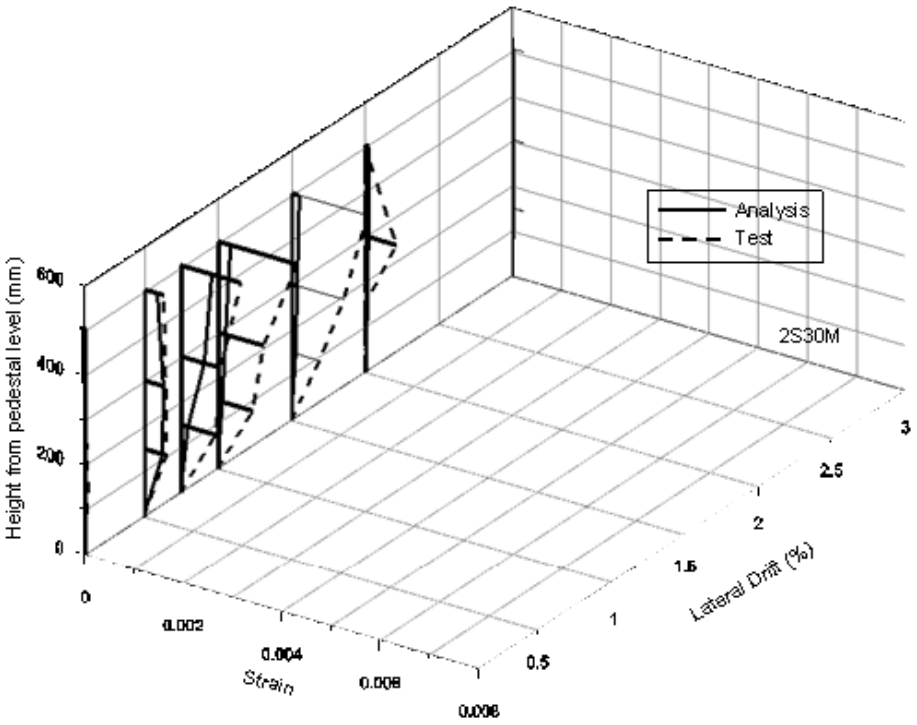

Figure 7.57. Comparison of Measured and Calculated Steel Strain Distributions along Lap Splice on Exterior Longitudinal Bar of Specimen 2S30M.

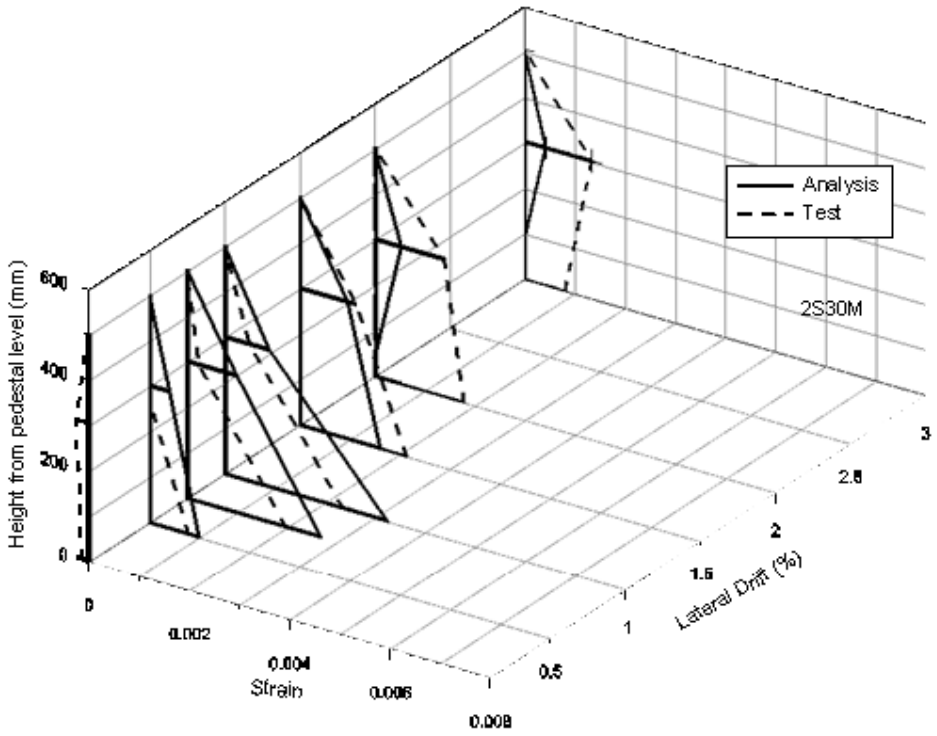

Figure 7.58. Comparison of Measured and Calculated Steel Strain Distributions along Lap Splice on Exterior Starter Bar of Specimen 2S30M.

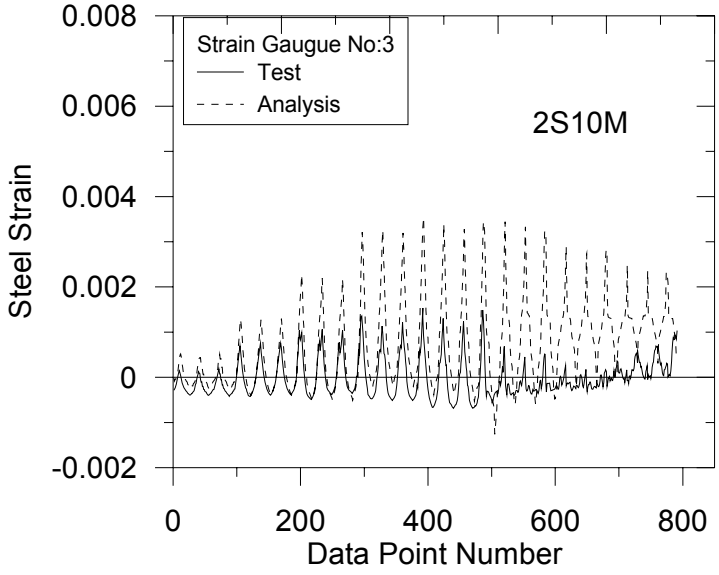

Figure 7.59. Comparison of Measured and Calculated Steel Strain Histories at Location of Strain Gauge No. 3 for Specimen 2S10M.

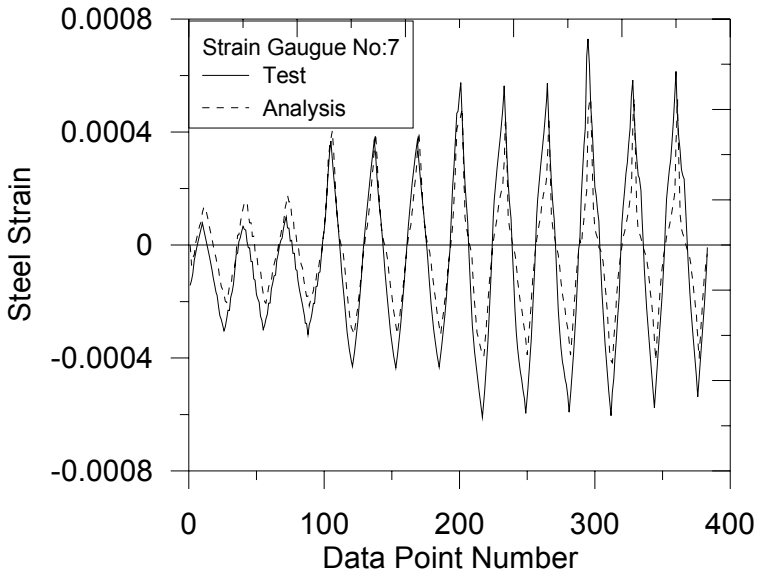

Figure 7.60. Comparison of Measured and Calculated Steel Strain Histories at Location of Strain Gauge No. 7 for Specimen 2S10M.

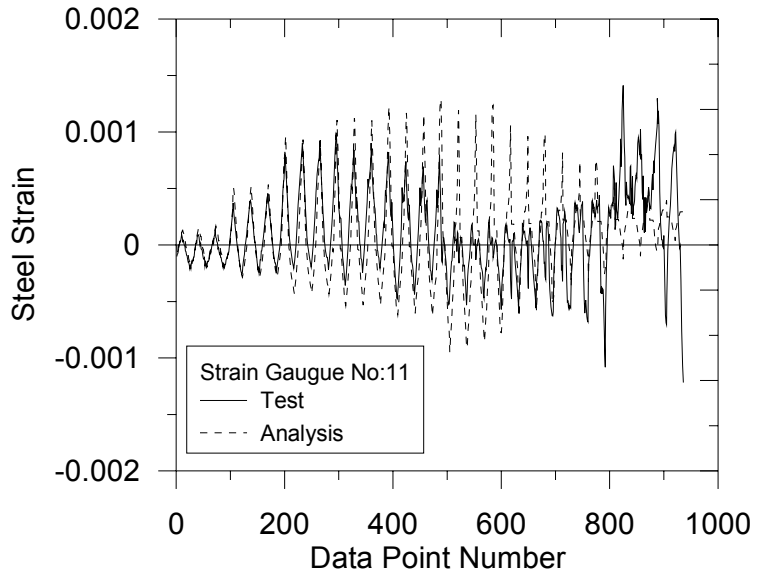

Figure 7.61. Comparison of Measured and Calculated Steel Strain Histories at Location of Strain Gauge No. 11 for Specimen 2S10M.

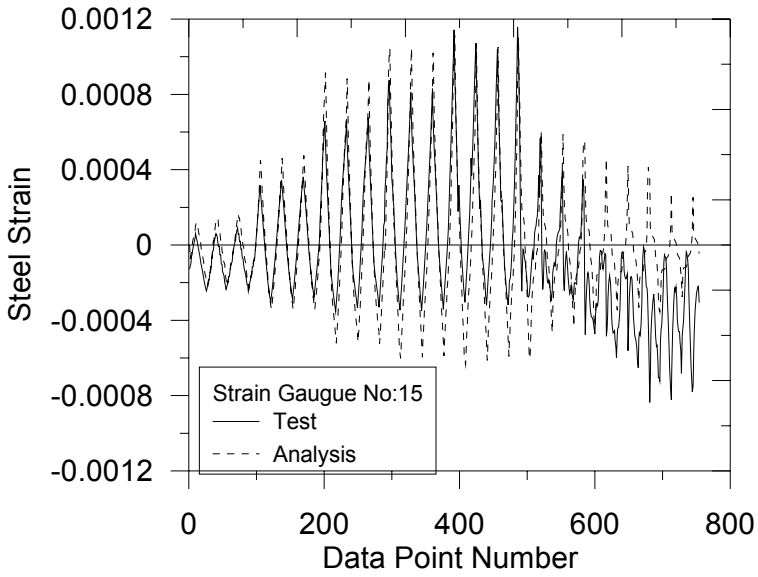

Figure 7.62. Comparison of Measured and Calculated Steel Strain Histories at Location of Strain Gauge No. 15 for Specimen 2S10M.

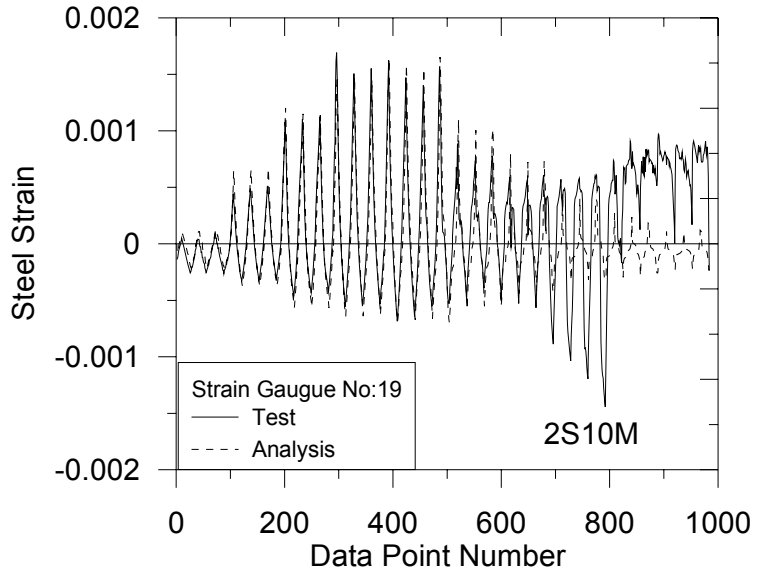

Figure 7.63. Comparison of Measured and Calculated Steel Strain Histories at Location of Strain Gauge No. 19 for Specimen 2S10M.

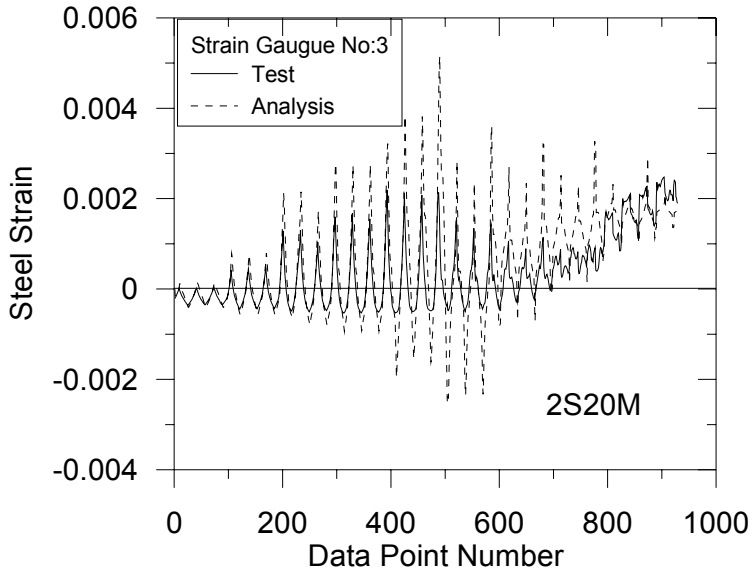

Figure 7.64. Comparison of Measured and Calculated Steel Strain Histories at Location of Strain Gauge No. 3 for Specimen 2S20M.

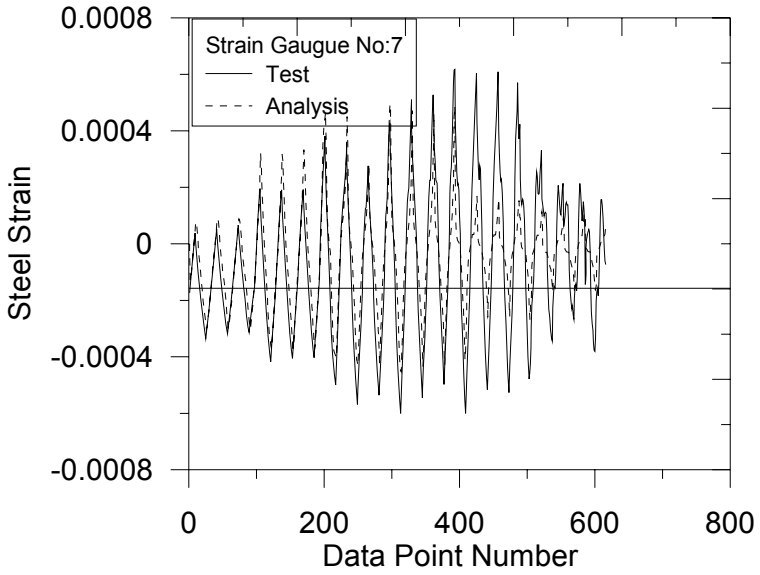

Figure 7.65. Comparison of Measured and Calculated Steel Strain Histories at Location of Strain Gauge No. 7 for Specimen 2S20M.

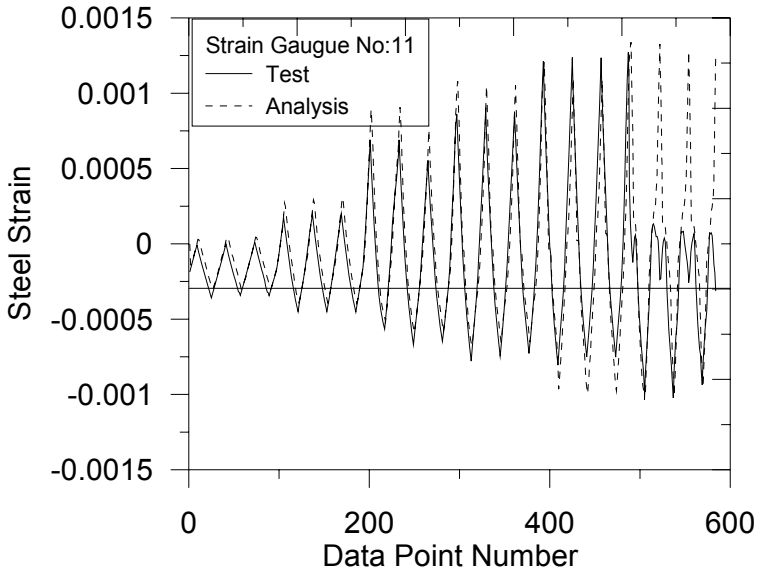

Figure 7.66. Comparison of Measured and Calculated Steel Strain Histories at Location of Strain Gauge No. 11 for Specimen 2S20M.

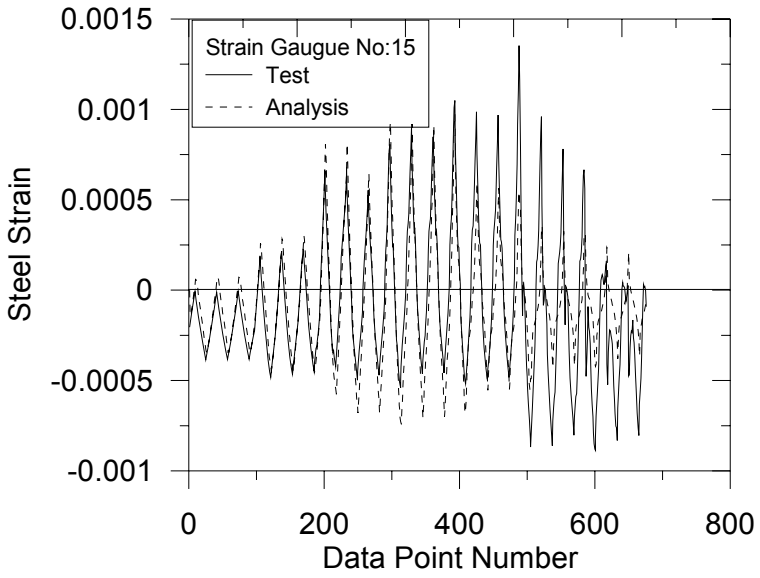

Figure 7.67. Comparison of Measured and Calculated Steel Strain Histories at Location of Strain Gauge No. 15 for Specimen 2S20M.

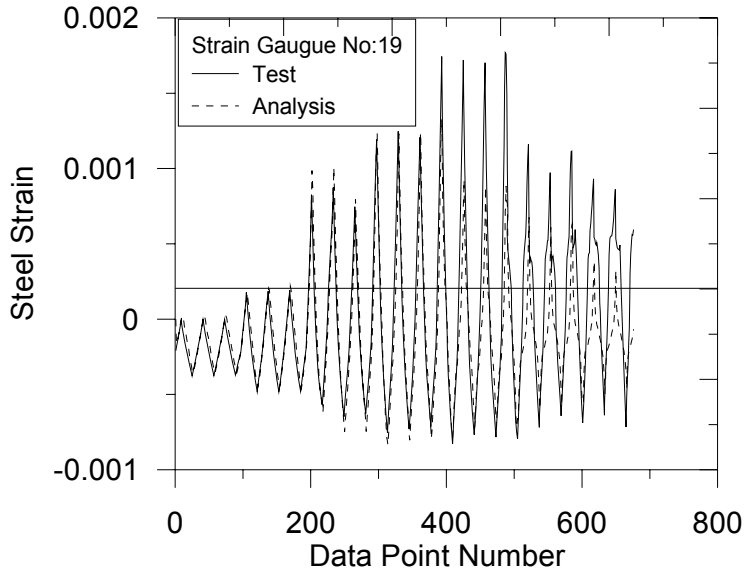

Figure 7.68. Comparison of Measured and Calculated Steel Strain Histories at Location of Strain Gauge No. 19 for Specimen 2S20M.

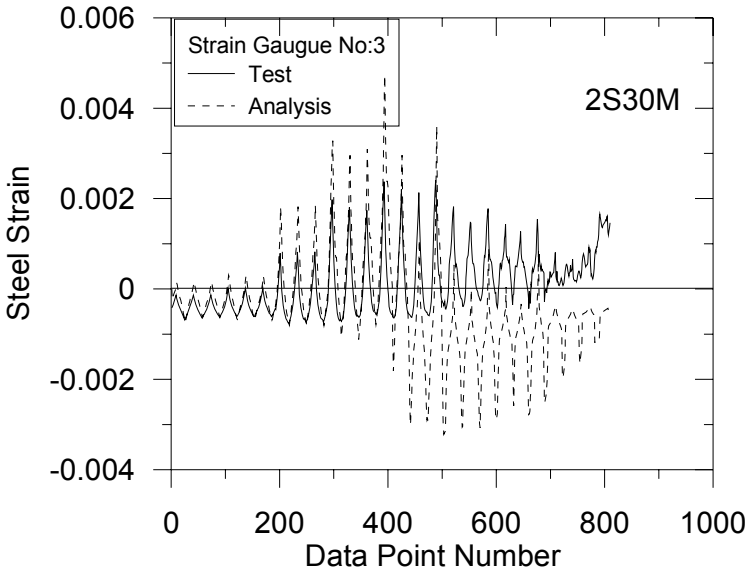

Figure 7.69. Comparison of Measured and Calculated Steel Strain Histories at Location of Strain Gauge No. 3 for Specimen 2S30M.

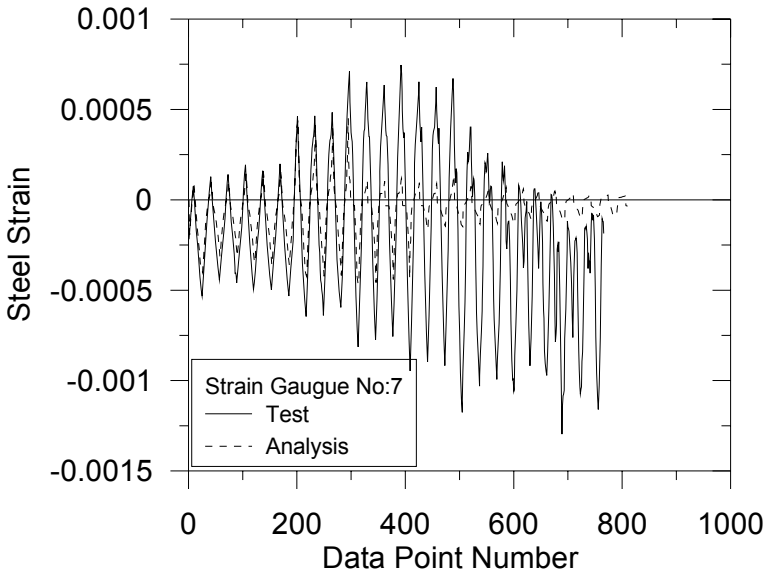

Figure 7.70. Comparison of Measured and Calculated Steel Strain Histories at Location of Strain Gauge No. 7 for Specimen 2S30M.

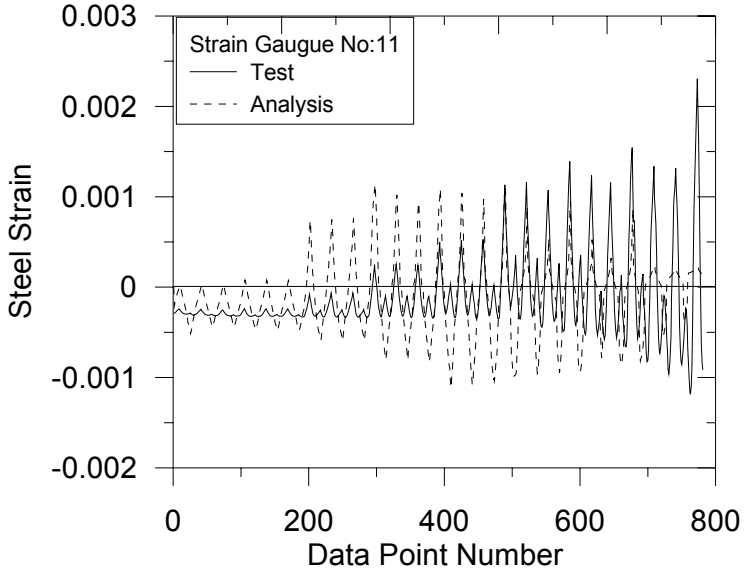

Figure 7.71. Comparison of Measured and Calculated Steel Strain Histories at Location of Strain Ggauge No. 11 for Specimen 2S30M.

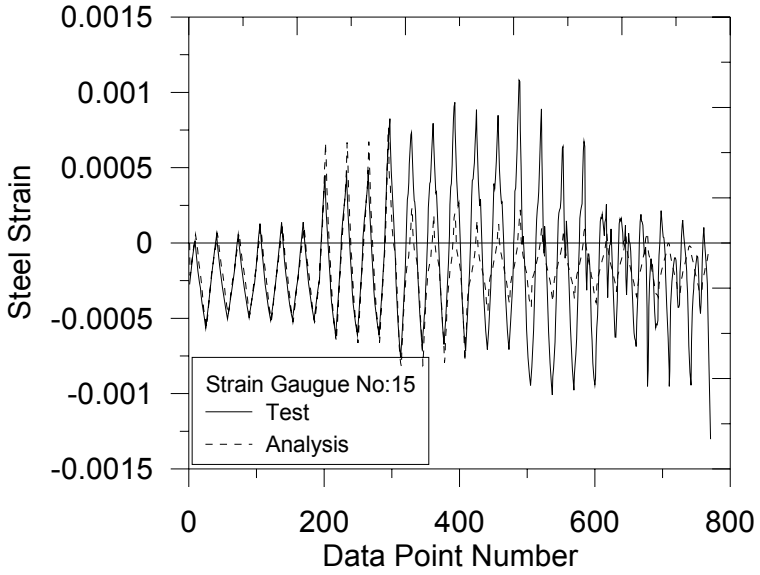

Figure 7.72. Comparison of Measured and Calculated Steel Strain Histories at Location of Strain Gauge No. 15 for Specimen 2S30M.

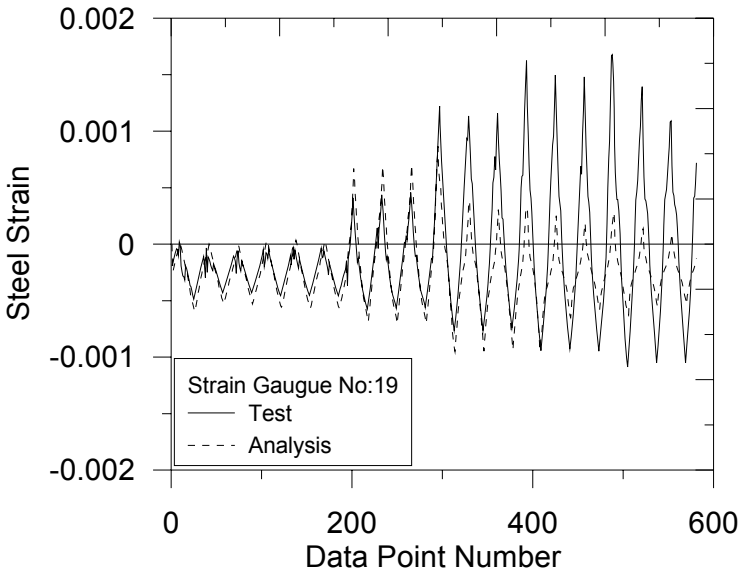

Figure 7.73. Comparison of Measured and Calculated Steel Strain Histories at Location of Strain Gauge No. 19 for Specimen 2S30M.

7.3.4. Concrete Strain Profiles and Average Longitudinal Strain Histories

Figures 7.74 to 7.83 compare the measured and predicted longitudinal strain profiles (due to deformation of concrete) as well as the neutral axis position, along the width of the column specimens at different lateral drift levels.

The concrete strain profiles at a distance of 330mm from the base of column specimens 2S10M, 2S20M and 2S30M, were calculated using measurements of the displacement sensors SL1 and SL2 (shown in Figure 7.12) at peak positive and negative top displacement (top displacement reversal) data points, for selected drift levels (Figures 7.74 to 7.79). The concrete strain profiles at a distance of 508 mm from the base (at the top of the lap splice region) of column specimens 2S20H and 2S30X, were also calculated using measurements of the displacement sensors SL1 and SL2 (shown in Figure 7.13) at peak positive and negative top displacement (top displacement reversal) data points, for selected drift levels (Figures 7.80 to 7.83). It must be noted that the specimens exhibited sudden lateral load degradation dur to splice failure, at drift levels between 1% and 1.5%.

Average longitudinal strain histories measured by individual displacement sensors (connected to concrete) were also compared with the analysis results, as shown in Figures Figures 7.84 to 7.93. location of displacement sensors SL1 and SL2 are shown in Figures 7.12 and 7.13) for all column specimens. The analytical longitudinal strain value at the location of each displacement sensor was calculated via a simple geometric transformation, using the displacements at the model degrees of freedom. Data from the displacement sensors SL1 and SL2 were not available during the entire loading history, since the sensors were removed at different times before the end of the tests, in order to prevent damage on the sensors during to crushing of concrete.

Overall, comparisons presented in Figures 7.74 to 7.93 indicate that analytical model is capable of providing reasonably accurate predictions of the concrete strain profiles (as well as the neutral axis depth), and the average longitudinal strain histories at specific locations, especially for lateral drift levels not exceeding 1.5%. At larger drift levels, together the rapid degradation in load degradation due to splice failure, progressive crushing of concrete was observed at the base of all of the column specimens, which

naturally impaired the accuracy of the model in predicting the concrete strain profiles and longitudinal strain histories.

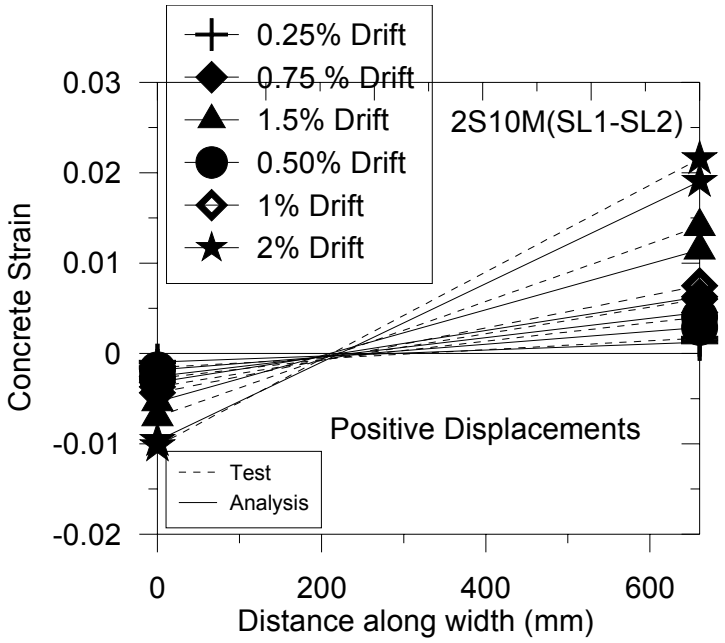

Figure 7.74. Comparison of Measured and Calculated Concrete Strain Profiles by Displacement Sensors (SL1-SL2) for Specimen 2S10M Under Drift Levels.

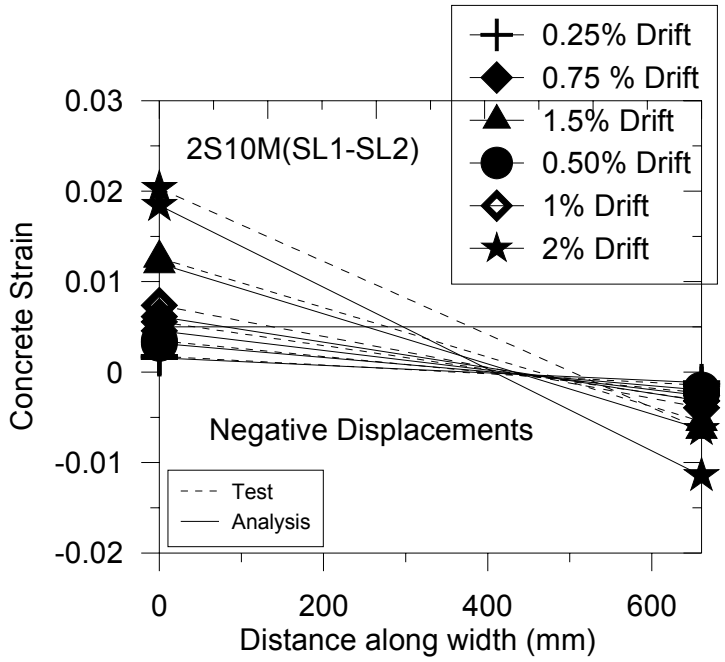

Figure 7.75. Comparison of Measured and Calculated Concrete Strain Profiles by Displacement Sensors (SL1-SL2) for Specimen 2S10M Under Drift Levels.

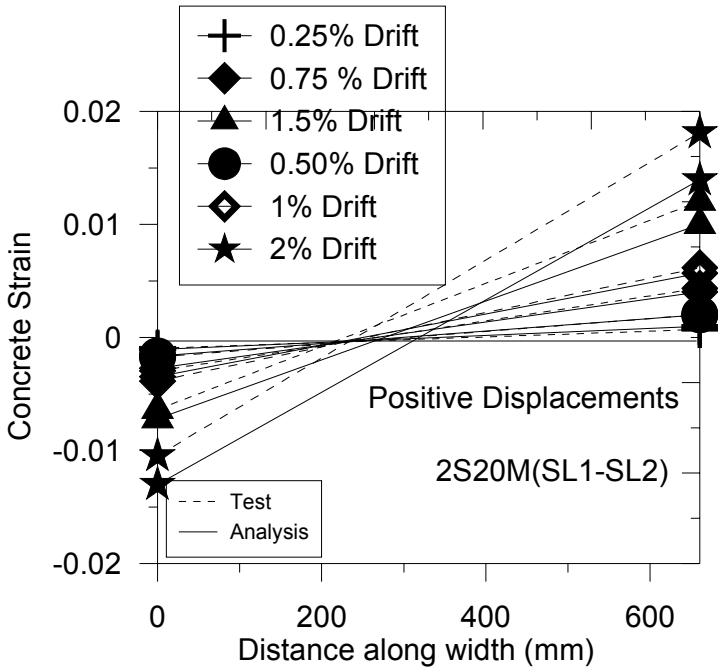

Figure 7.76. Comparison of Measured and Calculated Concrete Strain Profiles by Displacement Sensors (SL1-SL2) for Specimen 2S20M Under Drift Levels.

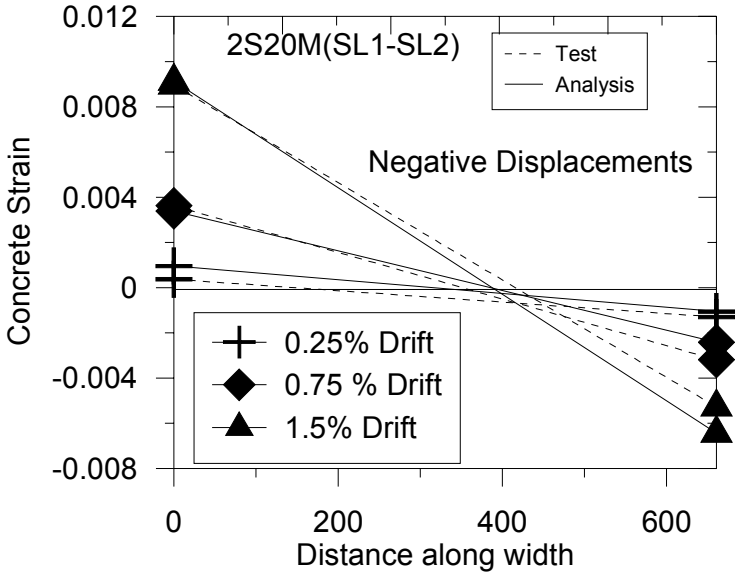

Figure 7.77. Comparison of Measured and Calculated Concrete Strain Profiles by Displacement Sensors (SL1-SL2) for Specimen 2S20M Under Drift Levels.

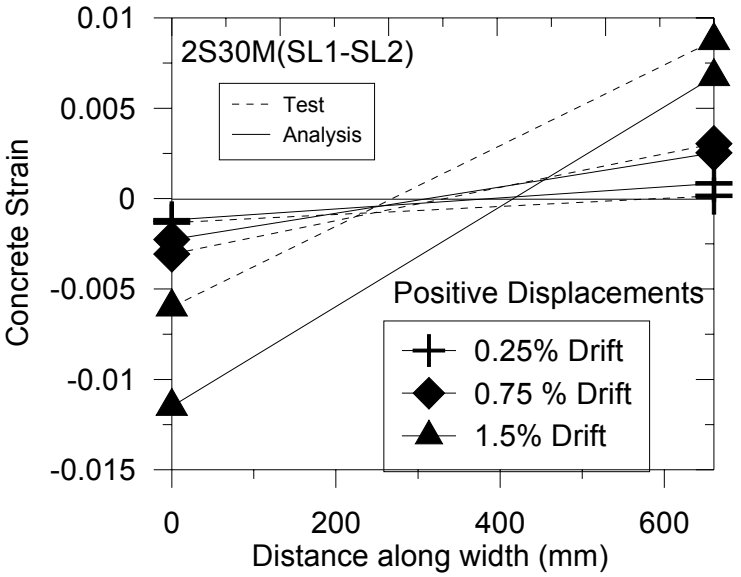

Figure 7.78. Comparison of Measured and Calculated Concrete Strain Profiles by Displacement Sensors (SL1-SL2) for Specimen 2S30M Under Drift Levels.

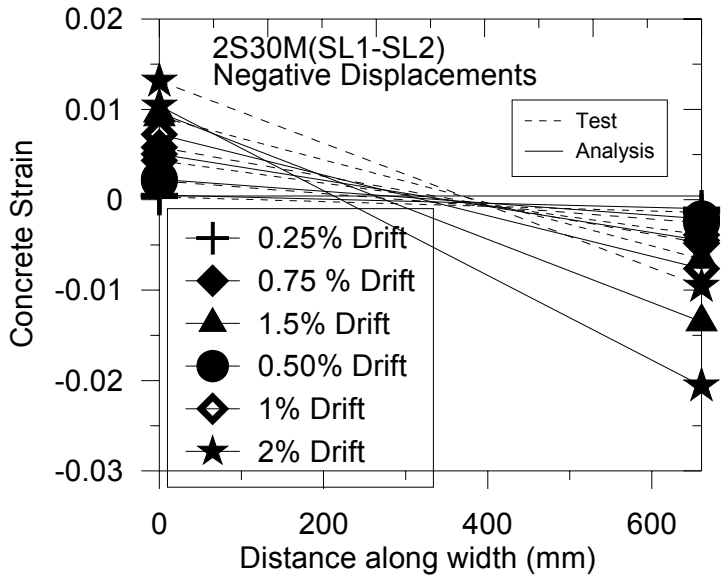

Figure 7.79. Comparison of Measured and Calculated Concrete Strain Profiles by Displacement Sensors (SL1-SL2) for Specimen 2S30M Under Drift Levels.

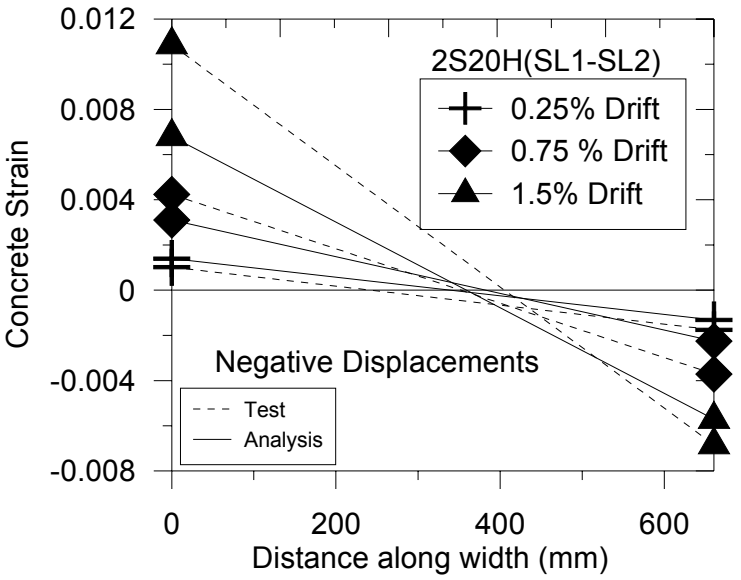

Figure 7.80. Comparison of Measured and Calculated Concrete Strain Profiles by Displacement Sensors (SL1-SL2) for Specimen 2S20H Under Drift Levels.

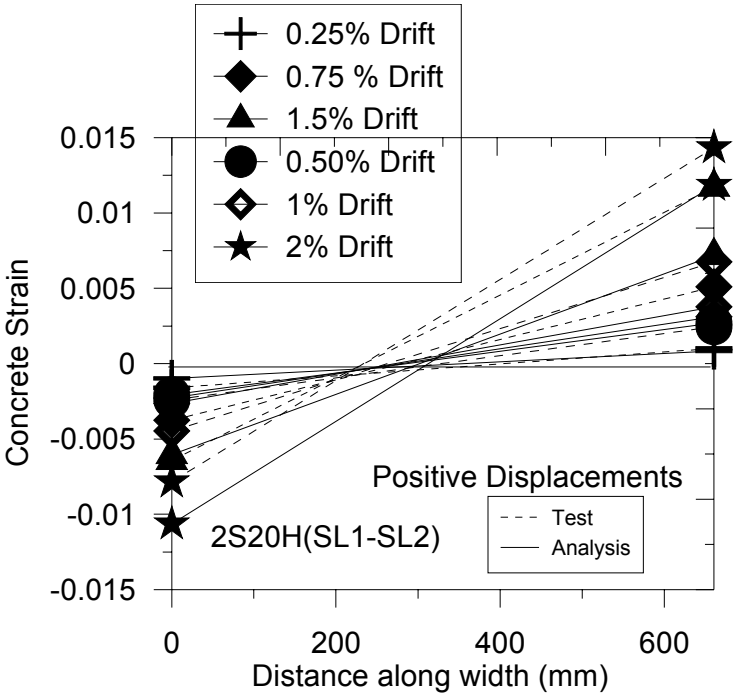

Figure 7.81. Comparison of Measured and Calculated Concrete Strain Profiles by Displacement Sensors (SL1-SL2) for Specimen 2S20H Under Drift Levels.

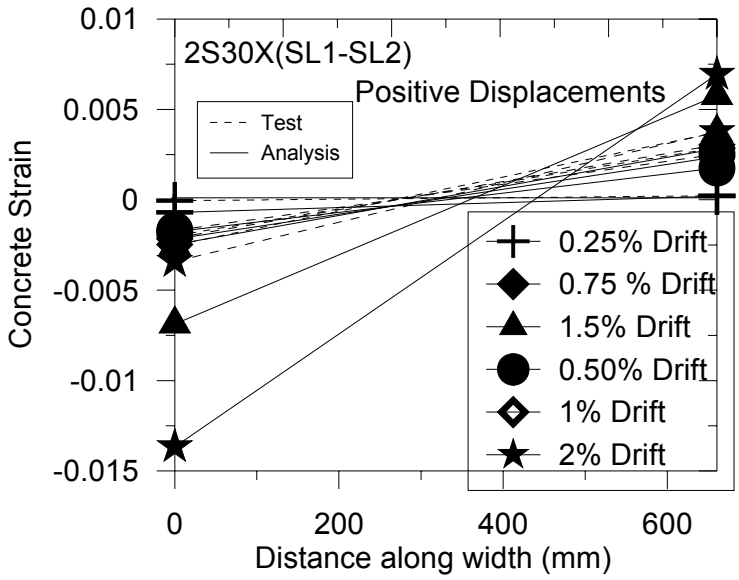

Figure 7.82. Comparison of Measured and Calculated Concrete Strain Profiles by Displacement Sensors (SL1-SL2) for Specimen 2S30X Under Drift Levels.

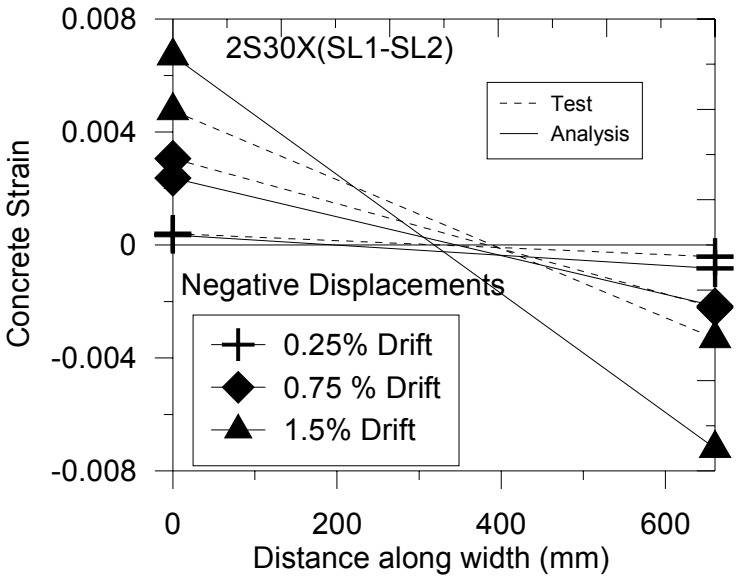

Figure 7.83. Comparison of Measured and Calculated Concrete Strain Profiles by Displacement Sensors (SL1-SL2) for Specimen 2S30X Under Drift Levels.

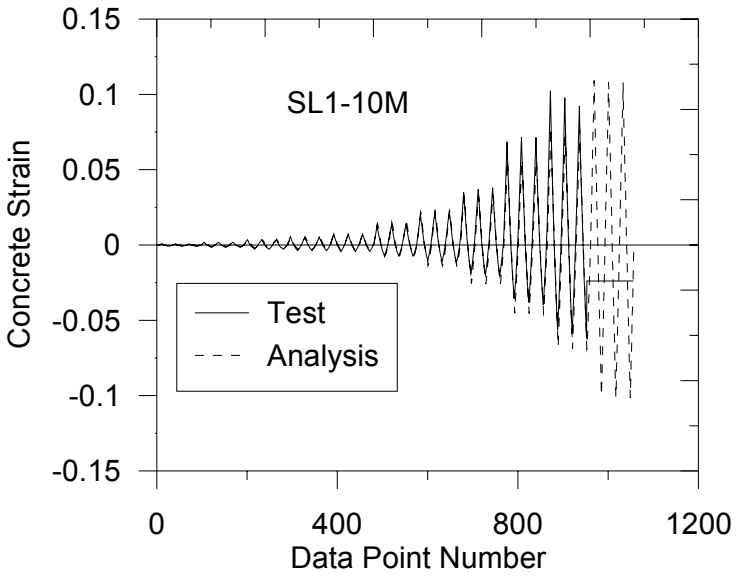

Figure 7.84. Comparison of Measured and Calculated Average Longitudinal Strain Histories, at the Location of Displacement Sensor SL1, for Specimen 2S10M.

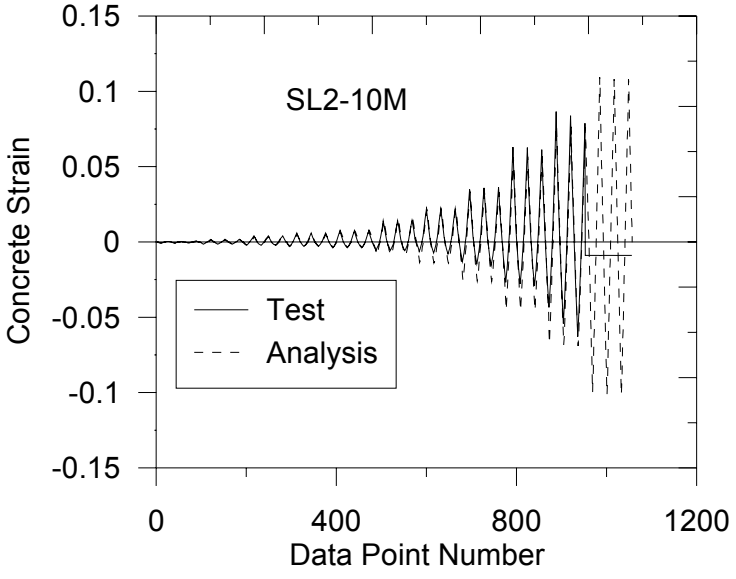

Figure 7.85. Comparison of Measured and Calculated Average Longitudinal Strain Histories, at the Location of Displacement Sensor SL2, for Specimen 2S10M.

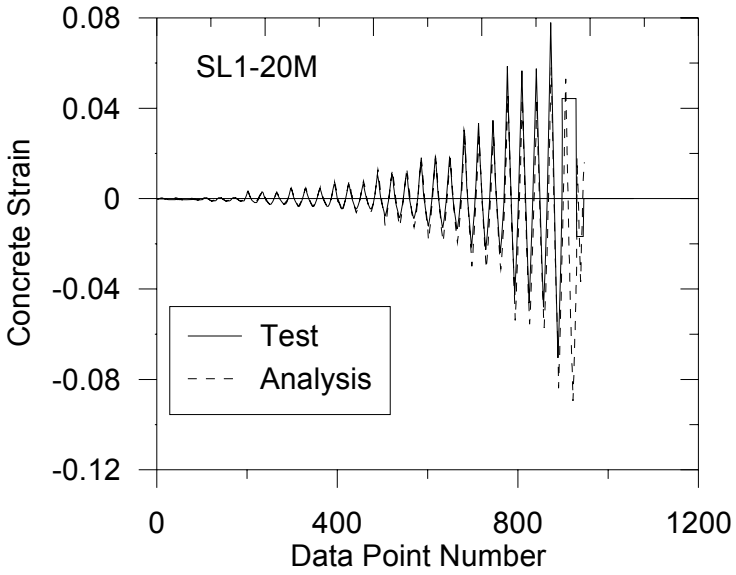

Figure 7.86. Comparison of Measured and Calculated Average Longitudinal Strain Histories, at the Location of Displacement Sensor SL1, for Specimen 2S20M.

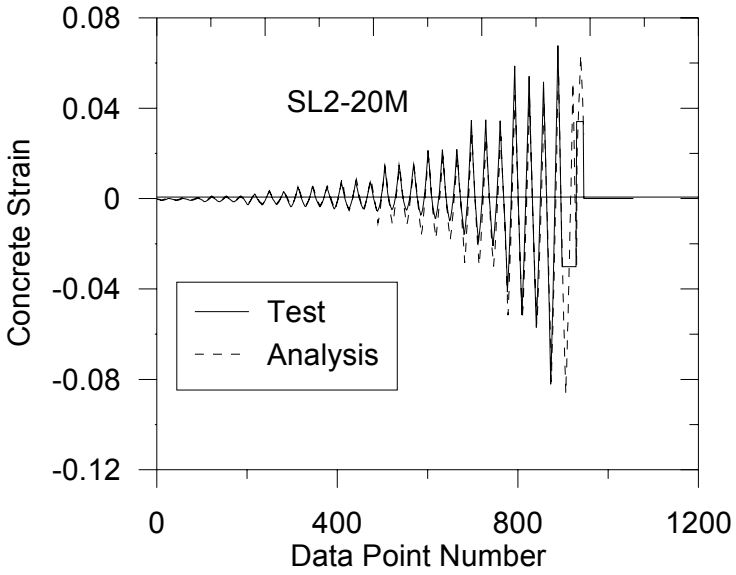

Figure 7.87. Comparison of Measured and Calculated Average Longitudinal Strain Histories, at the Location of Displacement Sensor SL2, for Specimen 2S20M.

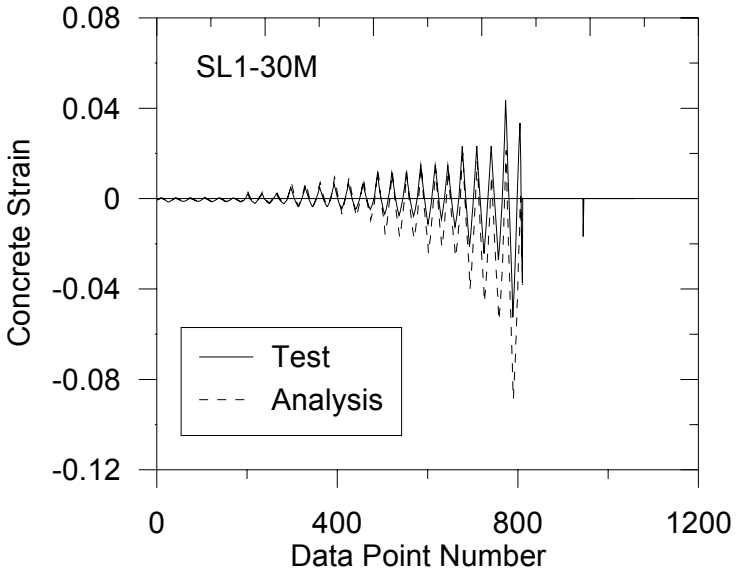

Figure 7.88. Comparison of Measured and Calculated Average Longitudinal Strain Histories, at the Location of Displacement Sensor SL1, for Specimen 2S30M.

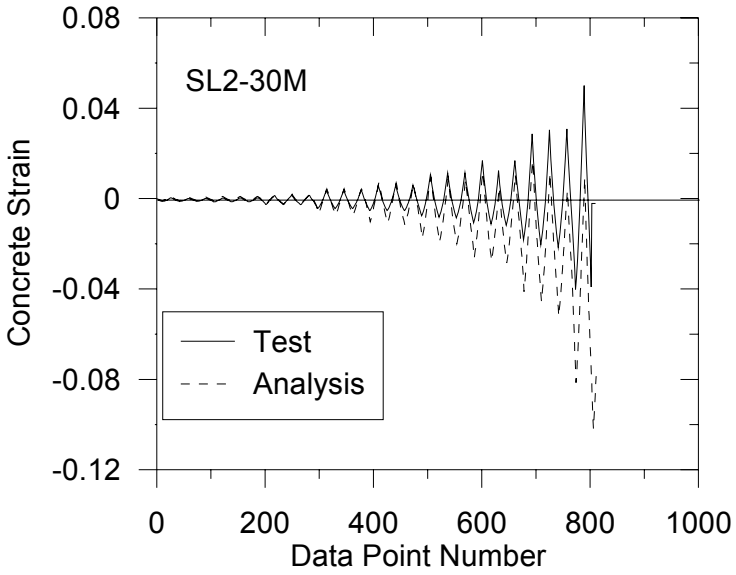

Figure 7.89. Comparison of Measured and Calculated Average Longitudinal Strain Histories, at the Location of Displacement Sensor SL2, for Specimen 2S30M.

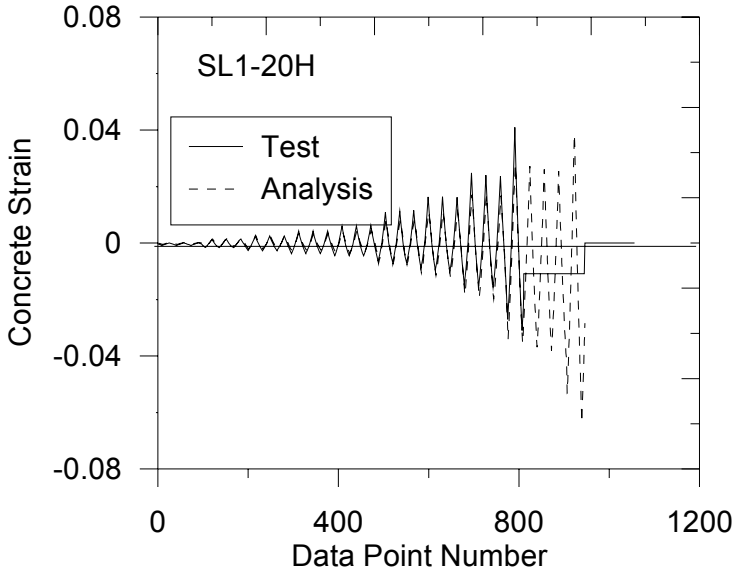

Figure 7.90. Comparison of Measured and Calculated Average Longitudinal Strain Histories, at the Location of Displacement Sensor SL1, for Specimen 2S20H.

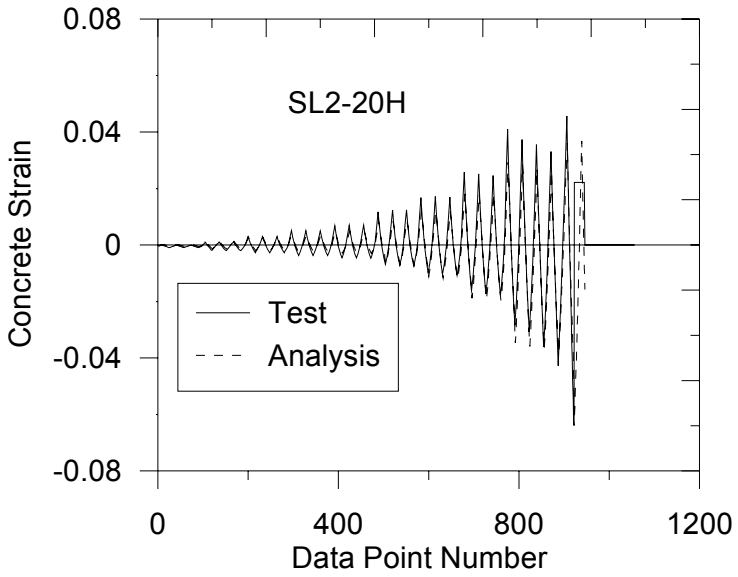

Figure 7.91. Comparison of Measured and Calculated Average Longitudinal Strain Histories, at the Location of Displacement Sensor SL2, for Specimen 2S20H.

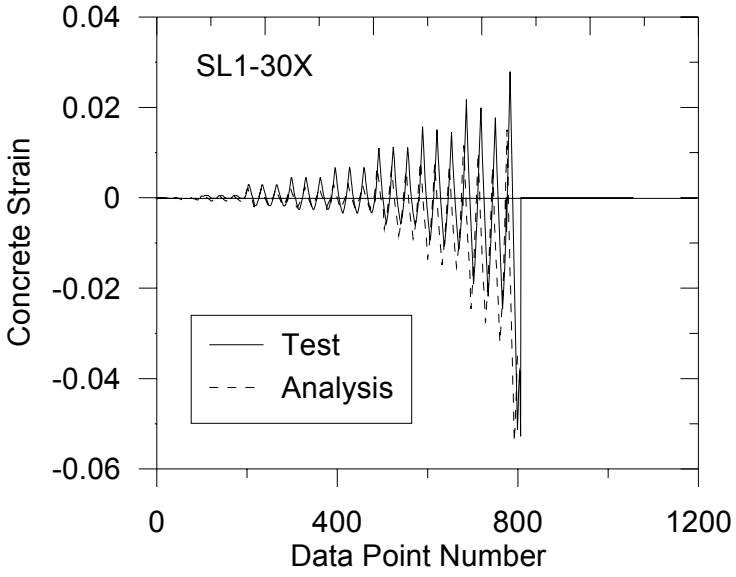

Figure 7.92. Comparison of Measured and Calculated Average Longitudinal Strain Histories, at the Location of Displacement Sensor SL1, for Specimen 2S30X.

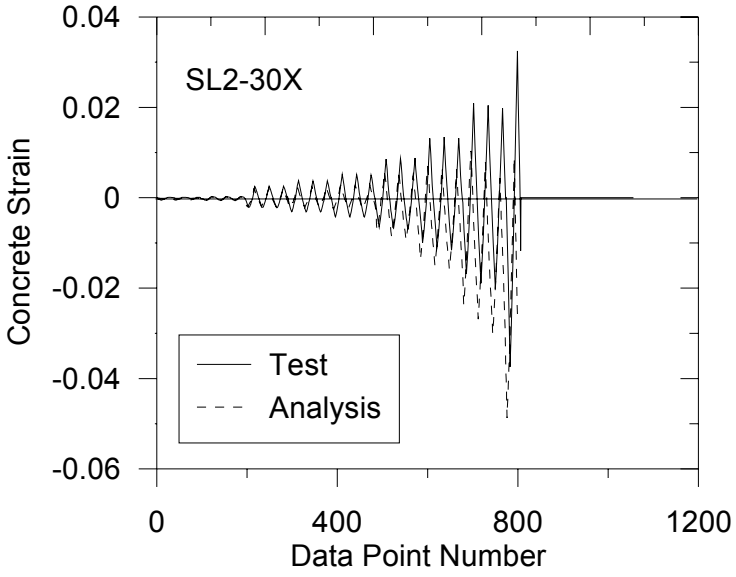

Figure 7.93. Comparison of Measured and Calculated Average Longitudinal Strain Histories, at the Location of Displacement Sensor SL2, for Specimen 2S30X.

7.3.5. Neutral Axis Position History

The model successfully represents the variation in the position of the neutral axis measured within the lap splice region of the column specimens, during the cyclic lateral loading history applied throughout the tests, as shown in Figures from 7.94 to 7.103. Figures 7.94 to 7.99 compare the predicted position of the neutral axis from the column centroid, normalized by the column width, at a distance of 330 mm from the base of column specimens 2S10M, 2S20M and 2S30M, with the measured neutral position obtained using measurements from displacement sensors SL1 and SL2 shown in Figure 7.12. Figures 7.100 to 7.103 compare the predicted position of the neutral axis from column centroid, normalized by the column width, at a distance of 508 mm from the base of the column specimens 2S20H and 2S30X, with the measured neutral position obtained using measurements from displacement sensors SL1 and SL2 shown in Figure 7.13. For all results, the distance from the column centroid to the neutral axis position approaches infinity when the top lateral displacement (and thus, rotation) of the column approaches zero, and reaches its local extreme or limit points (peaks and valleys) at peak displacement (displacement reversal) points. The experimental and analytical neutral axial position histories show similar variation and reach similar values at peak (displacement reversal) points, as observed in the figures. The occasional erratic values in the experimental results are due to distortion of the displacement sensors due to local crushing of concrete at locations where the sensors are connected.

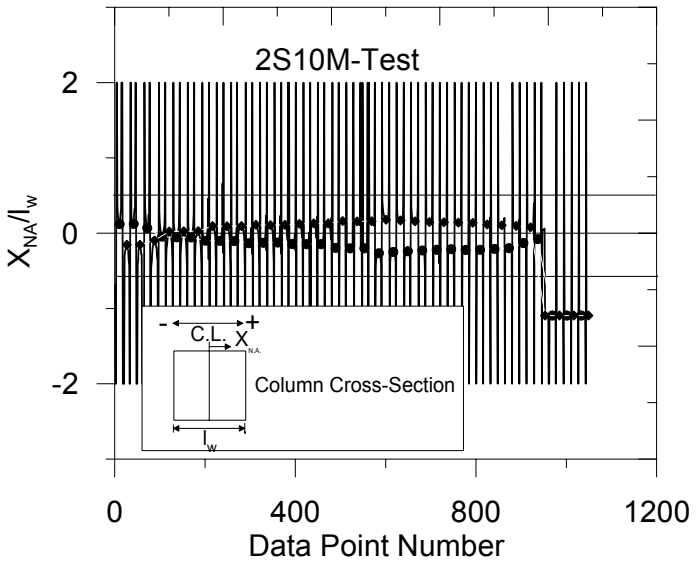

Figure 7.94. Experimental Variation in Position of Neutral Axis for Specimen 2S10M.

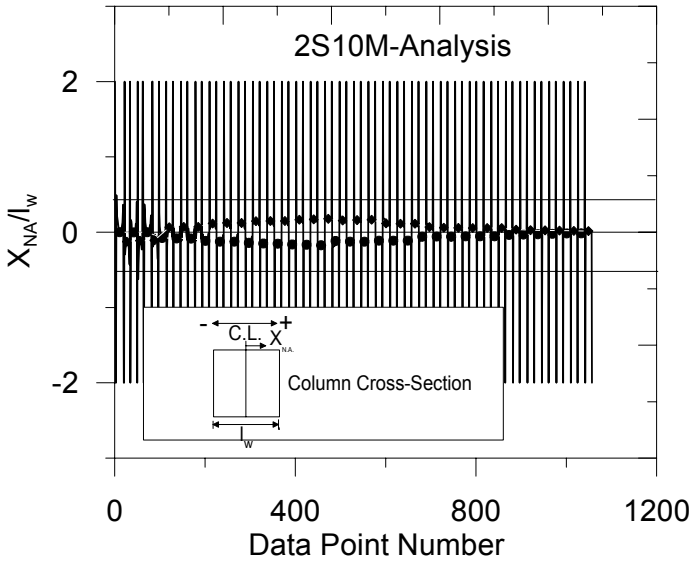

Figure 7.95. Analytical Variation in Position of Neutral Axis for Specimen 2S10M.

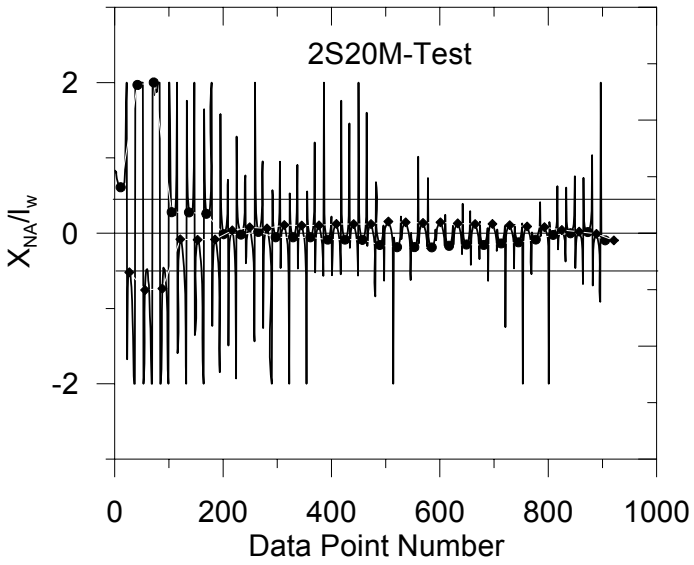

Figure 7.96. Experimental Variation in Position of Neutral Axis for Specimen 2S20M.

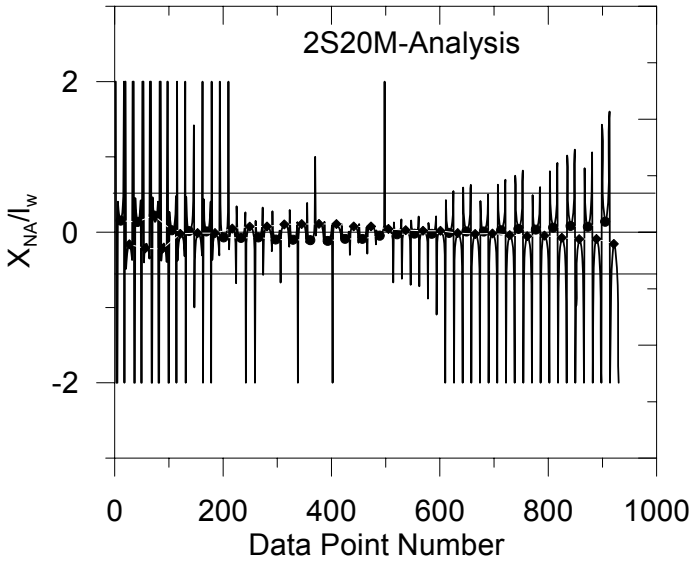

Figure 7.97. Analytical Variation in Position of Neutral Axis for Specimen 2S20M.

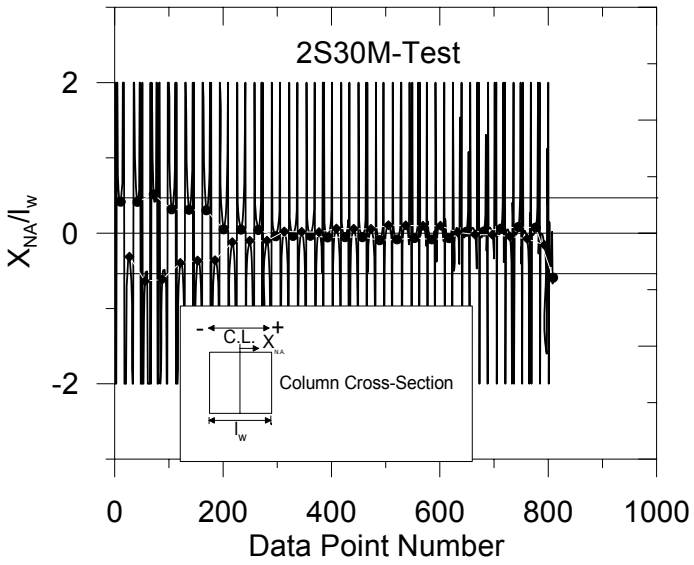

Figure 7.98. Experimental Variation in Position of Neutral Axis for Specimen 2S30M.

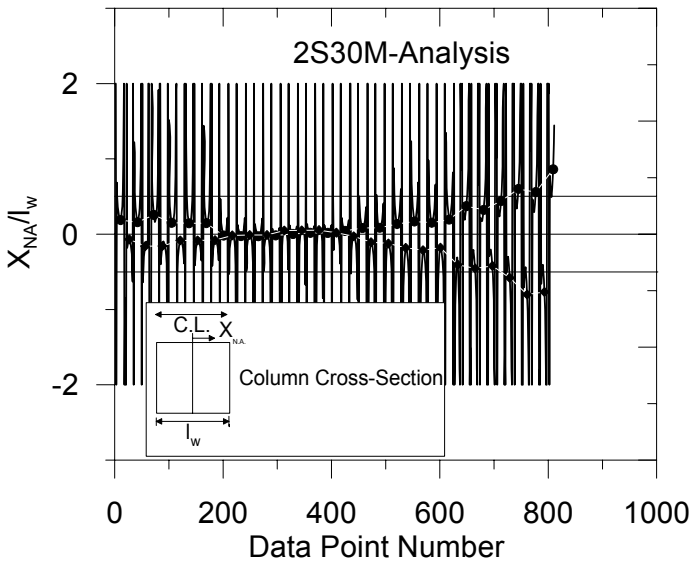

Figure 7.99. Analytical Variation in Position of Neutral Axis for Specimen 2S30M.

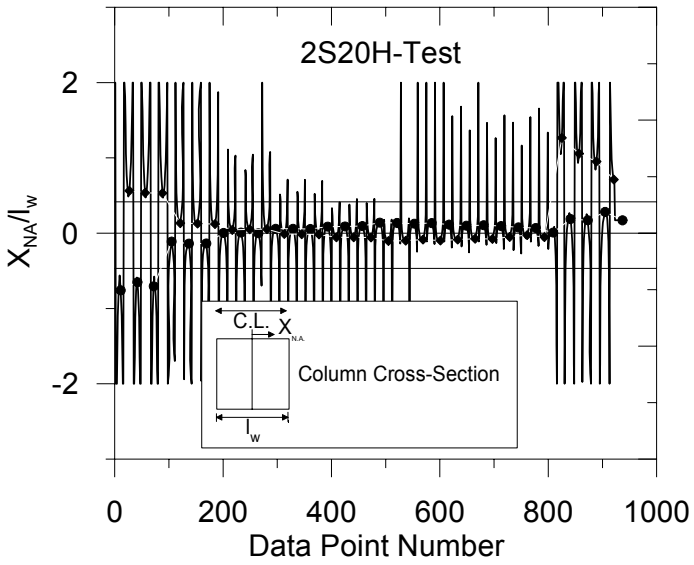

Figure 7.100. Experimental Variation in Position of Neutral Axis for Specimen 2S20H.

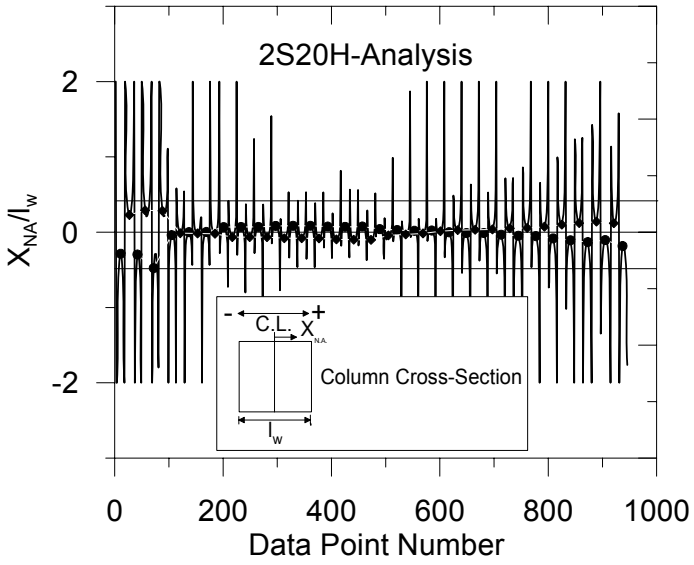

Figure 7.101. Analytical Variation in Position of Neutral Axis for Specimen 2S20H.

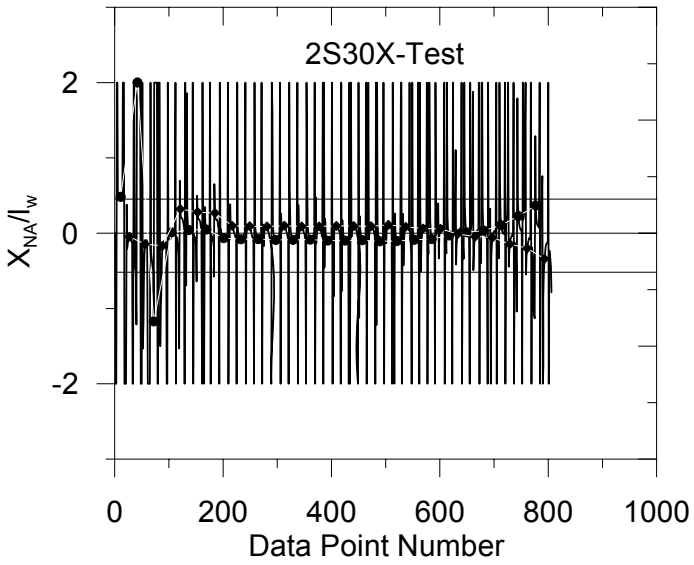

Figure 7.102. Experimental Variation in Position of Neutral Axis for Specimen 2S30X.

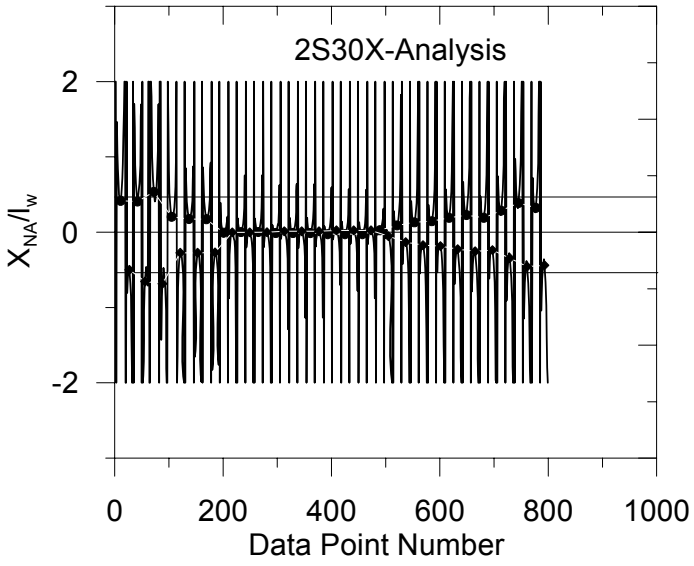

Figure 7.103. Analytical Variation in Position of Neutral Axis for Specimen 2S30X.

7.3.6. Average Bond Stresses along Spliced Bars

The model results are also compared with "processed" test measurements, in terms of the average bond stresses (along the lap splice region) between reinforcing steel and surrounding concrete, for both starter and longitudinal bars, as shown in Figures 7.104 to 7.123. The experimental average bond stress (u) values were calculated using the variation in the longitudinal steel stresses in the bars, calculated using the strains measured by the strain gauges on the bars. To convert the measured steel strains (ε) into longitudinal steel stresses (f_s), a simple hysteretic elasto – plastic stress – strain relationship was used for the reinforcing steel, as proposed by Melek (2006). The longitudinal steel stresses were then transformed into average bond stress values along the lap splice using the relation:

$$u = \frac{f_s d_b}{4l} \tag{7.1}$$

where f_s is the change in the longitudinal stress on the bar, d_b is the nominal bar diameter, and l is the length of the splice. In this calculation process, to obtain the average bond stress on a starter bar, measurements of the strain gauge affixed to the starter bar at the column base level (Strain gauge No.3 shown in Figure 7.7) is used. To obtain the average bond stress on a longitudinal bar, measurements of the strain gauge affixed to the longitudinal bar at the top of the splice (Strain gauge No.19 shown in Figure 7.7) is used. In the analytical model results, average bond stress values along the lap splice between concrete and the reinforcing steel bars is obtained in a much more direct manner, by simply taking the weighted average of the bond stresses (weighted with respect to the height of each model element), which develop in the bond slip springs of the model.

Figures 7.104 to 7.123 compare the experimentally–obtained and analytically–predicted average bond stresses along the lap splice (between concrete and the longitudinal or starter bars) vs. the top lateral displacement of each column specimen. As the experimental bond stress values were processed from strain gauge measurements, the results are only presented until the data point when the strain gauge was damaged.

The level of correlation between the analytical and experimental results can be deemed reasonable, considering the typical scatter observed in strain gauge measurements in reinforced concrete member tests based on proximity of a strain gauge to a crack. The analytical model seems to capture the general pattern of the average bond stress vs. top displacement behavior of the column specimens, and the maximum average bond stress values for some of them. Both the analytical results and experimental measurements indicate that the average bond stress levels along the lap splice on the longitudinal and starter bars are somewhat different; and it is possible that relatively larger bond stresses will develop on the starter bars.

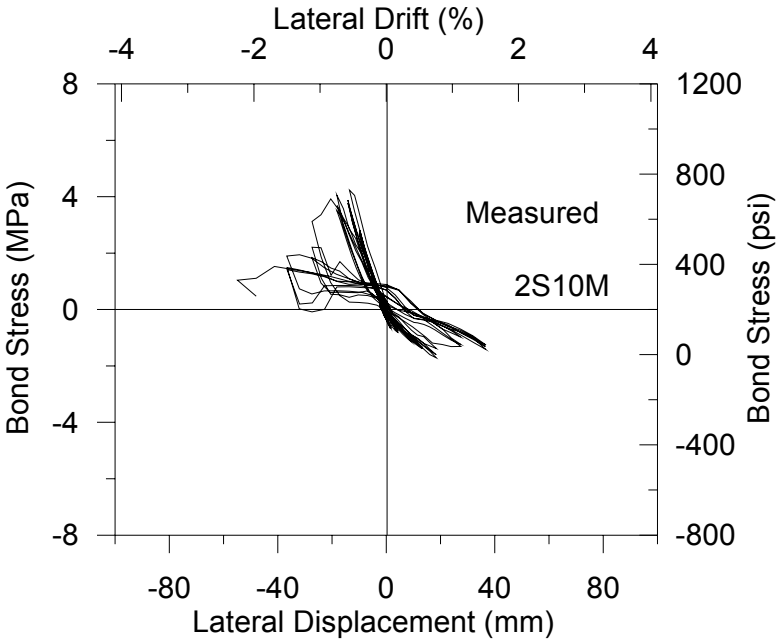

Figure 7.104. Experimental Average Bond Stress on Longitudinal Bar along Lap Splice vs. Top Displacement for Specimen 2S10M.

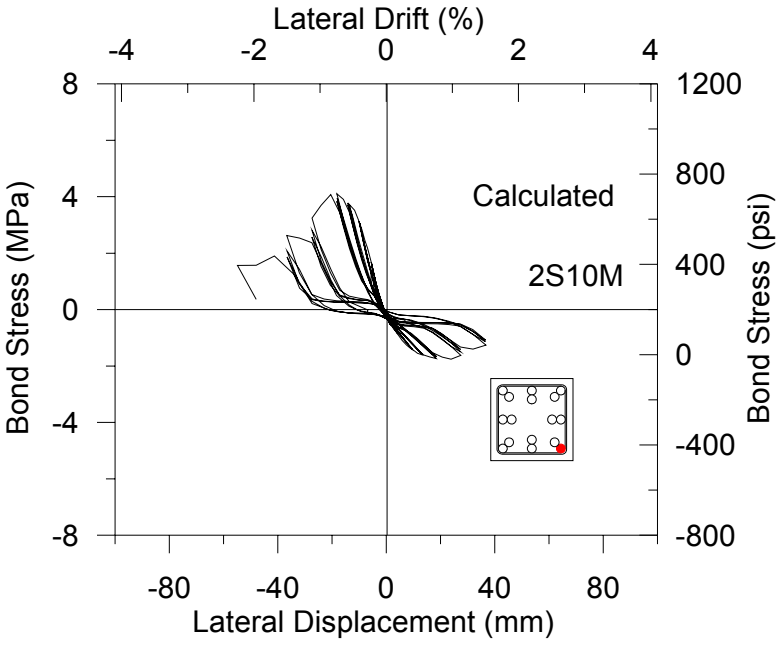

Figure 7.105. Analytical Average Bond Stress on Longitudinal Bar along Lap Splice vs. Top Displacement for Specimen 2S10M.

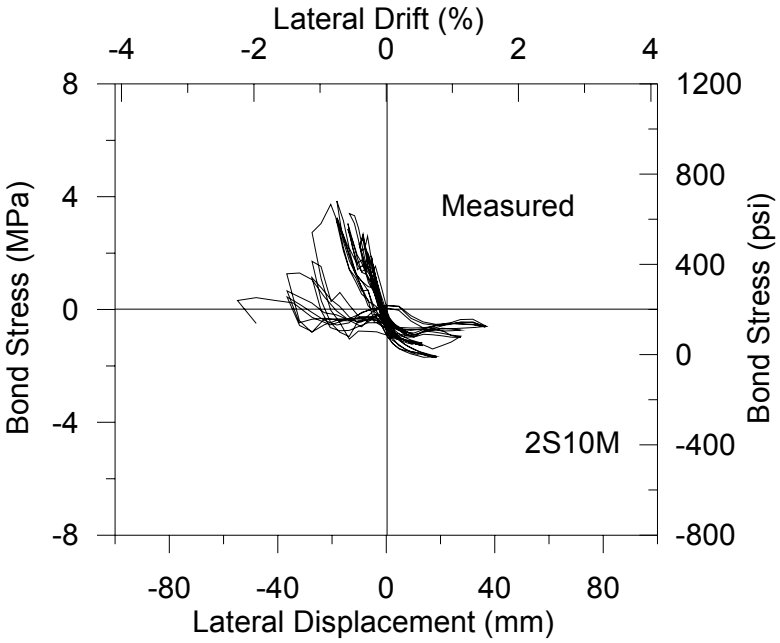

Figure 7.106. Experimental Average Bond Stress on Starter Bar along Lap Splice vs. Top Displacement for Specimen 2S10M.

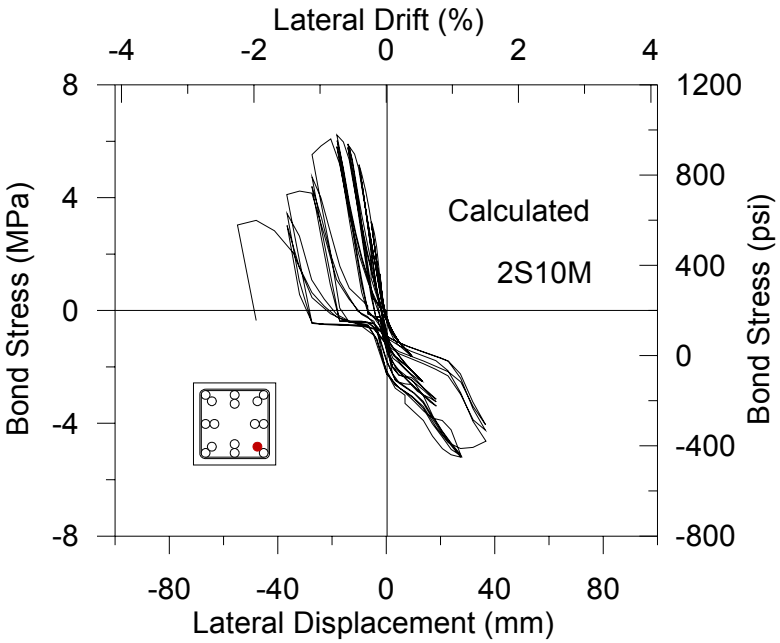

Figure 7.107. Analytical Average Bond Stress on Starter Bar along Lap Splice vs. Top Displacement for Specimen 2S10M.

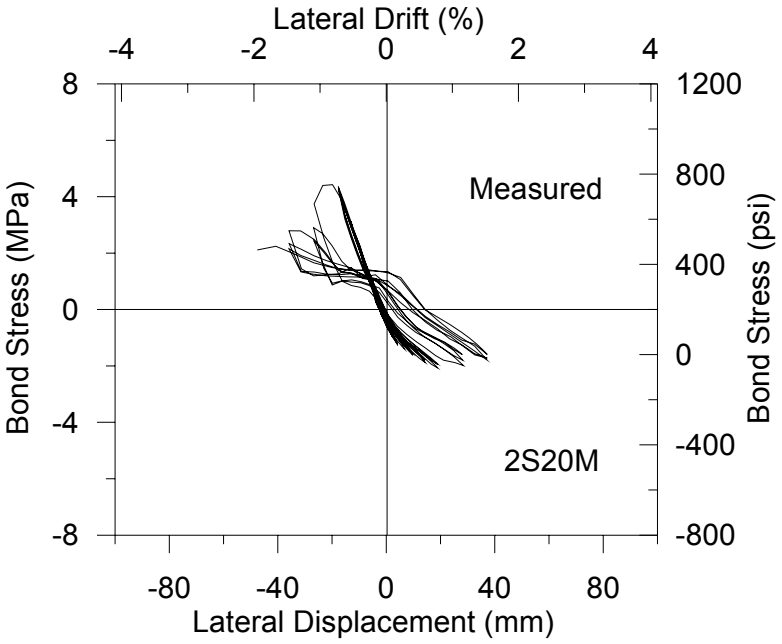

Figure 7.108. Experimental Average Bond Stress on Longitudinal Bar along Lap Splice vs. Top Displacement for Specimen 2S20M.

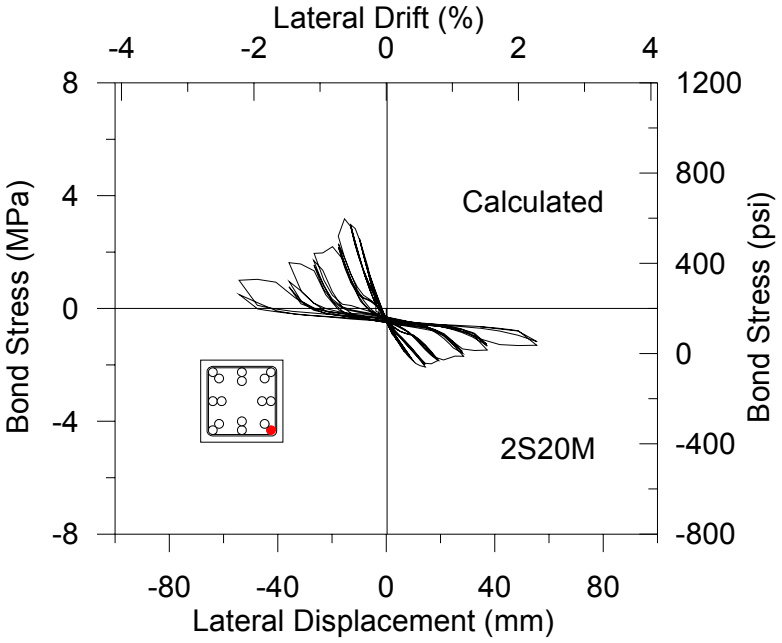

Figure 7.109. Analytical Average Bond Stress on Longitudinal Bar along Lap Splice vs. Top Displacement for Specimen 2S20M.

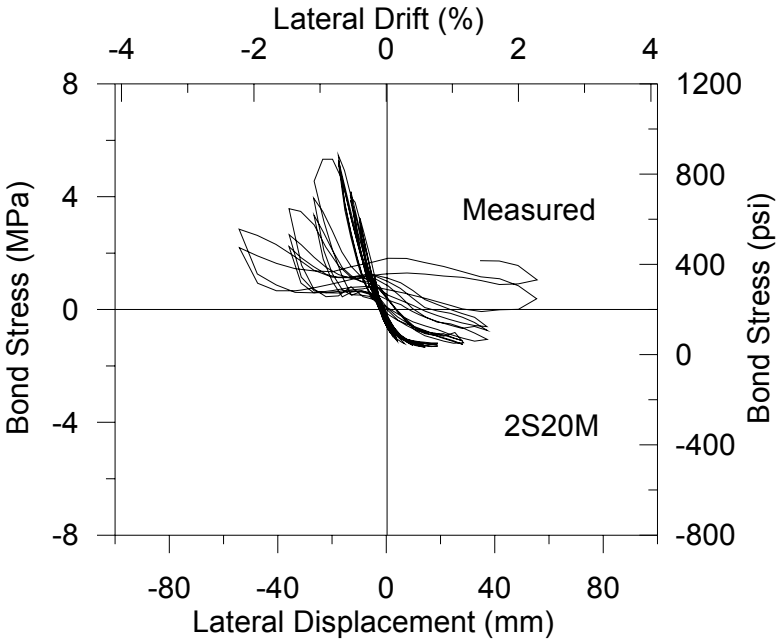

Figure 7.110. Experimental Average Bond Stress on Starter Bar along Lap Splice vs. Top Displacement for Specimen 2S20M.

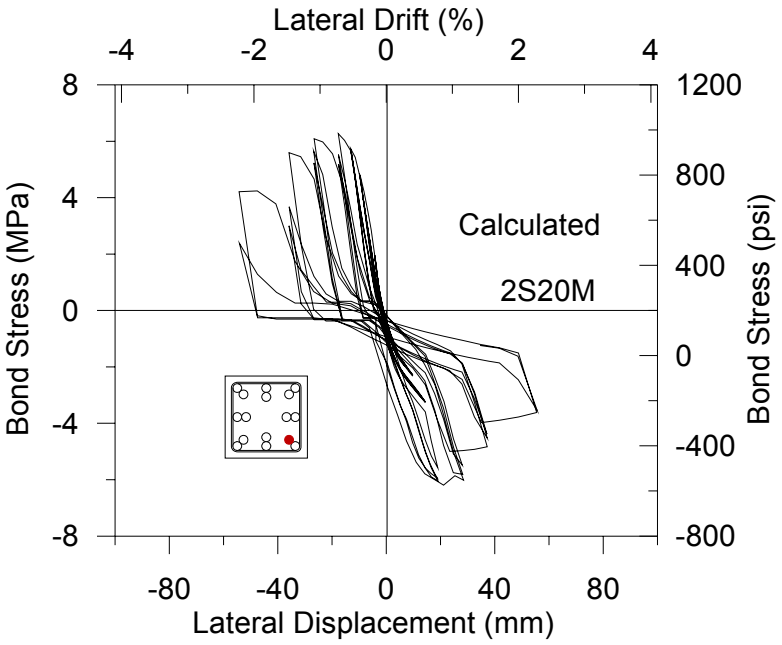

Figure 7.111. Analytical Average Bond Stress on Starter Bar along Lap Splice vs. Top Displacement for Specimen 2S20M.

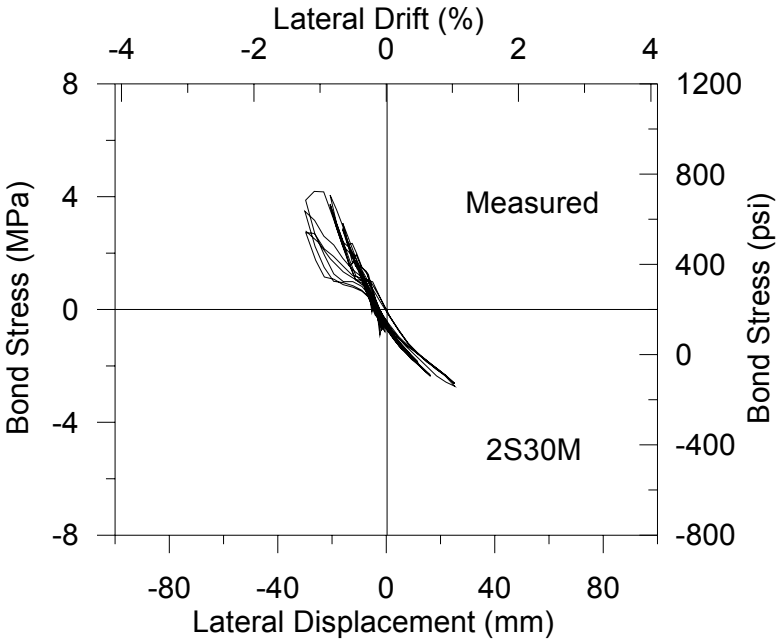

Figure 7.112. Experimental Average Bond Stress on Longitudinal Bar along Lap Splice vs. Top Displacement for Specimen 2S30M.

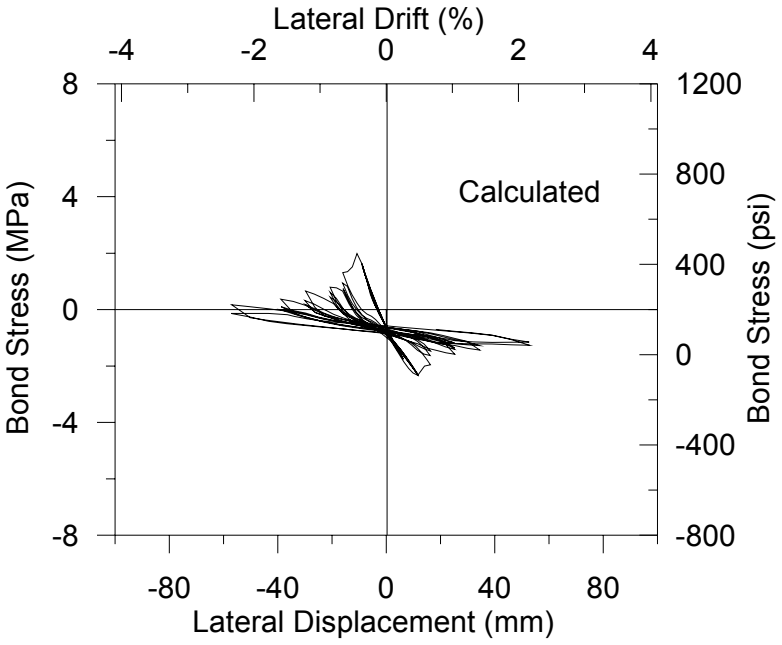

Figure 7.113. Analytical Average Bond Stress on Longitudinal Bar along Lap Splice vs. Top Displacement for Specimen 2S30M.

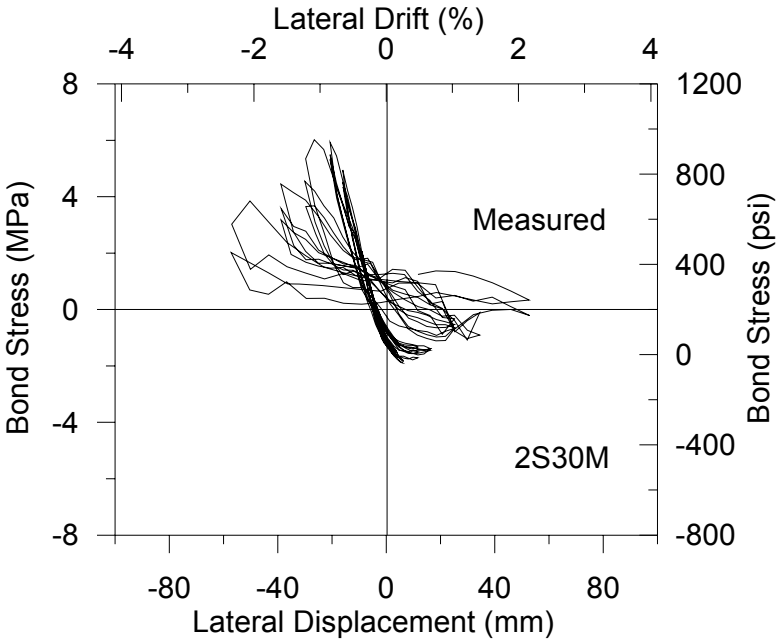

Figure 7.114. Experimental Average Bond Stress on Starter Bar along Lap Splice vs. Top Displacement for Specimen 2S30M.

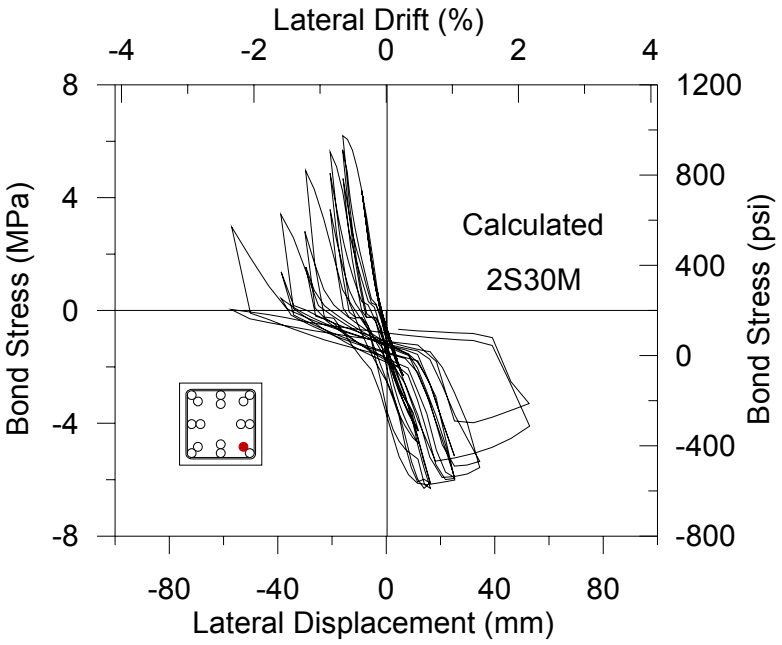

Figure 7.115. Analytical Average Bond Stress on Starter Bar along Lap Splice vs. Top Displacement for Specimen 2S30M.

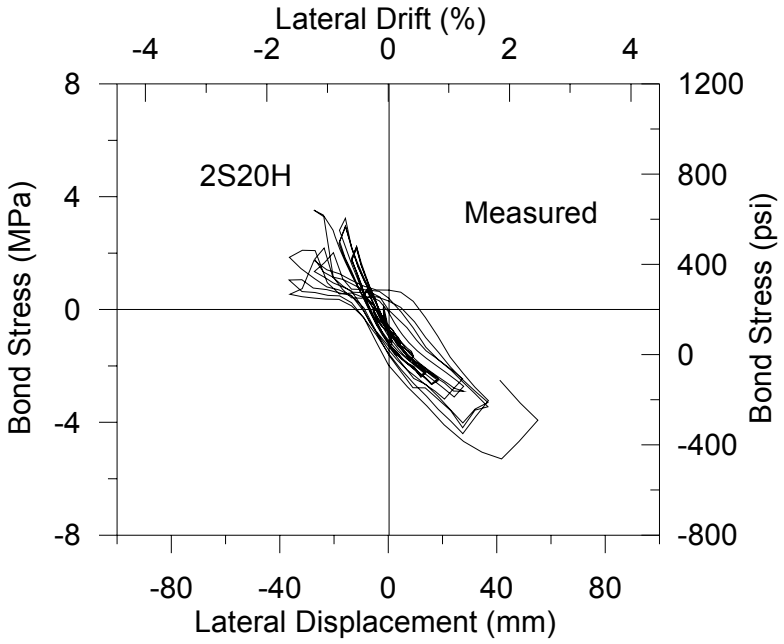

Figure 7.116. Experimental Average Bond Stress on Longitudinal Bar along Lap Splice vs. Top Displacement for Specimen 2S20H.

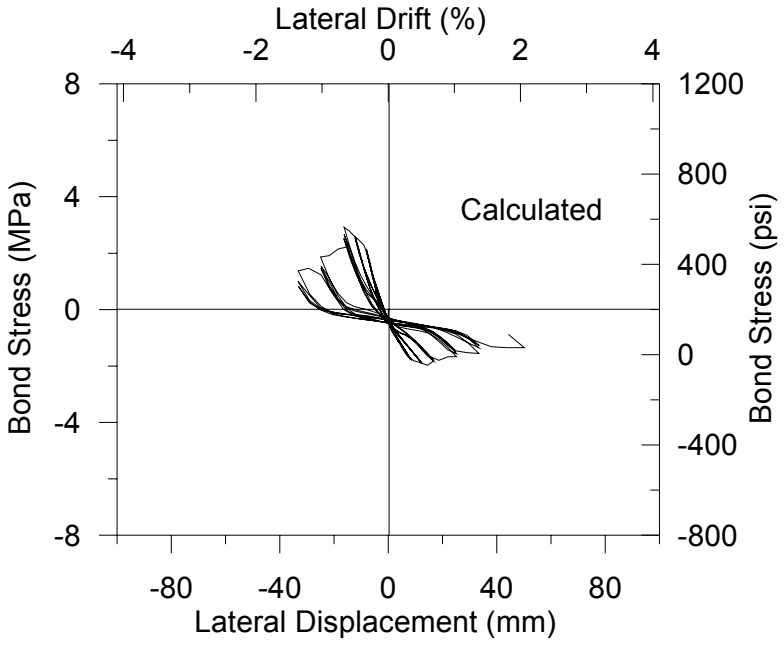

Figure 7.117. Analytical Average Bond Stress on Longitudinal Bar along Lap Splice vs. Top Displacement for Specimen 2S20H.

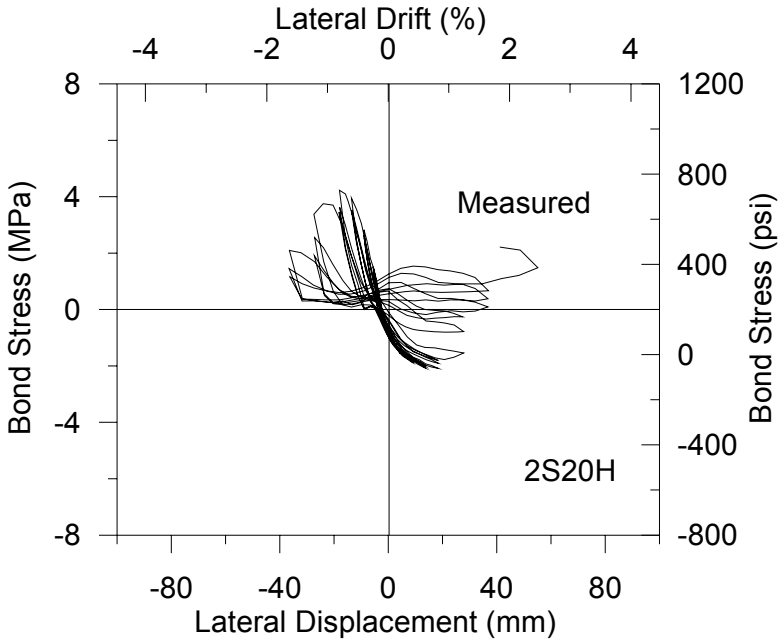

Figure 7.118. Experimental Average Bond Stress on Starter Bar along Lap Splice vs. Top Displacement for Specimen 2S20H.

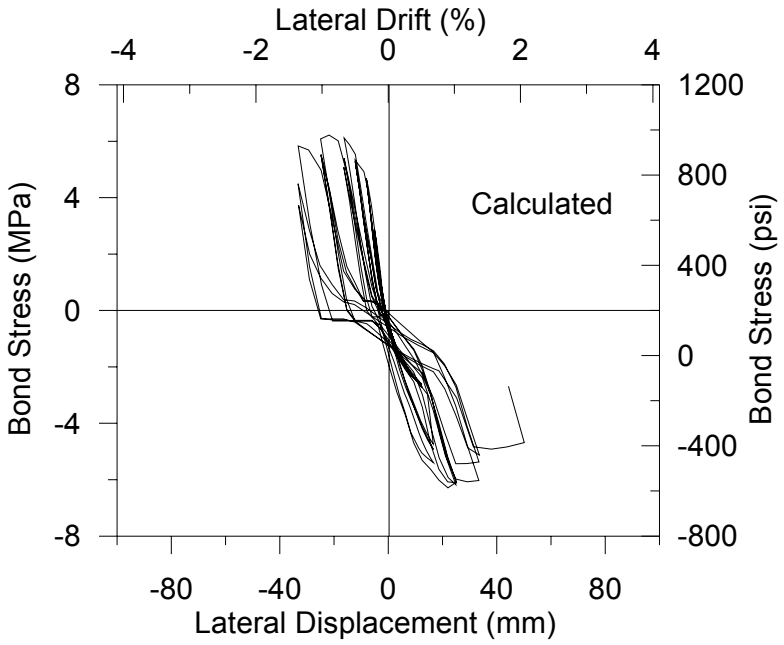

Figure 7.119. Analytical Average Bond Stress on Starter Bar along Lap Splice vs. Top Displacement for Specimen 2S20H.

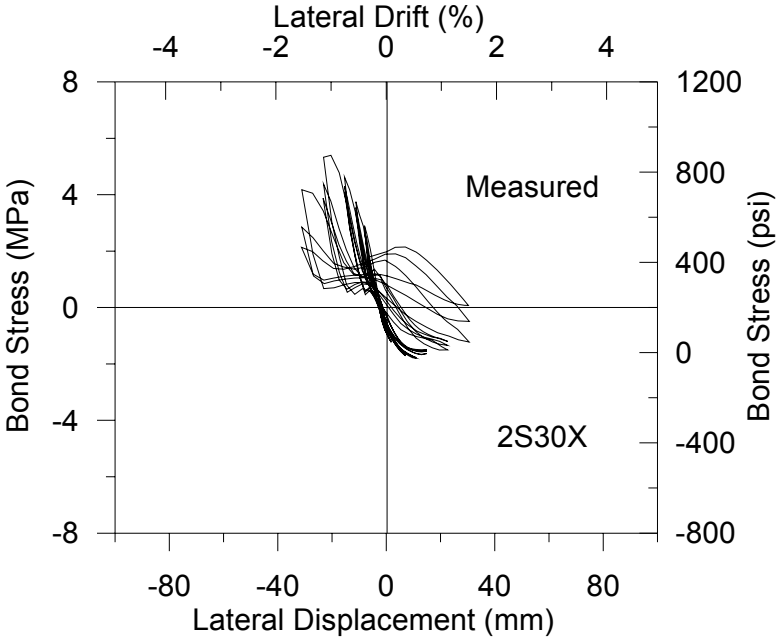

Figure 7.120. Experimental Average Bond Stress on Starter Bar along Lap Splice vs. Top Displacement for Specimen 2S30X.

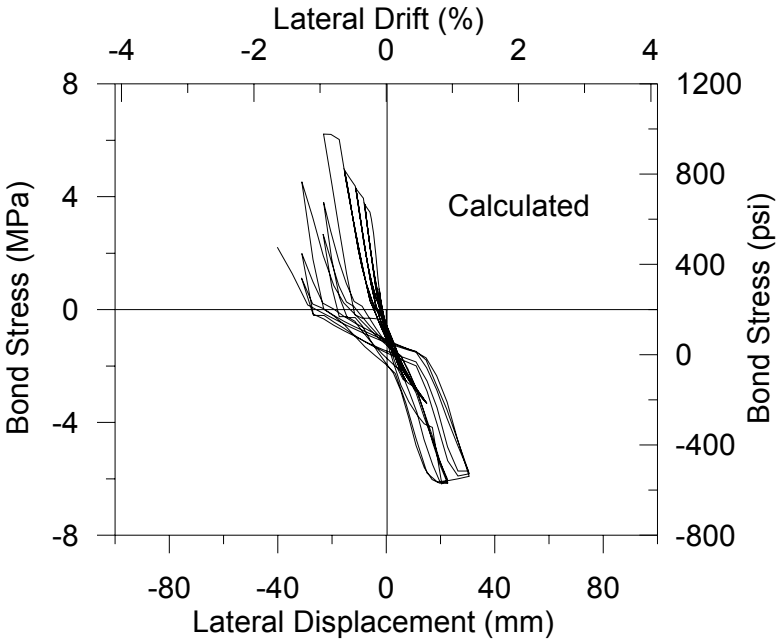

Figure 7.121. Analytical Average Bond Stress on Starter Bar along Lap Splice vs. Top Displacement for Specimen 2S30X.

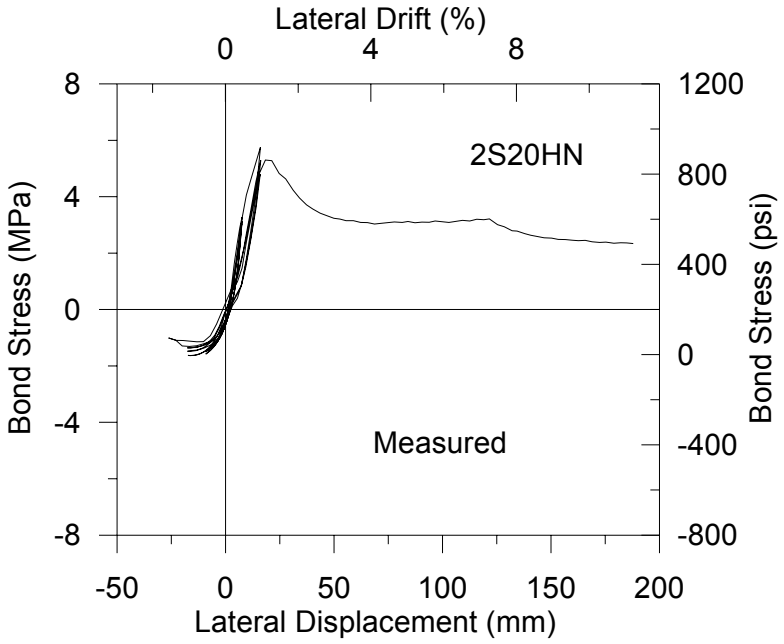

Figure 7.122. Experimental Average Bond Stress on Starter Bar along Lap Splice vs. Top Displacement for Specimen 2S20HN.

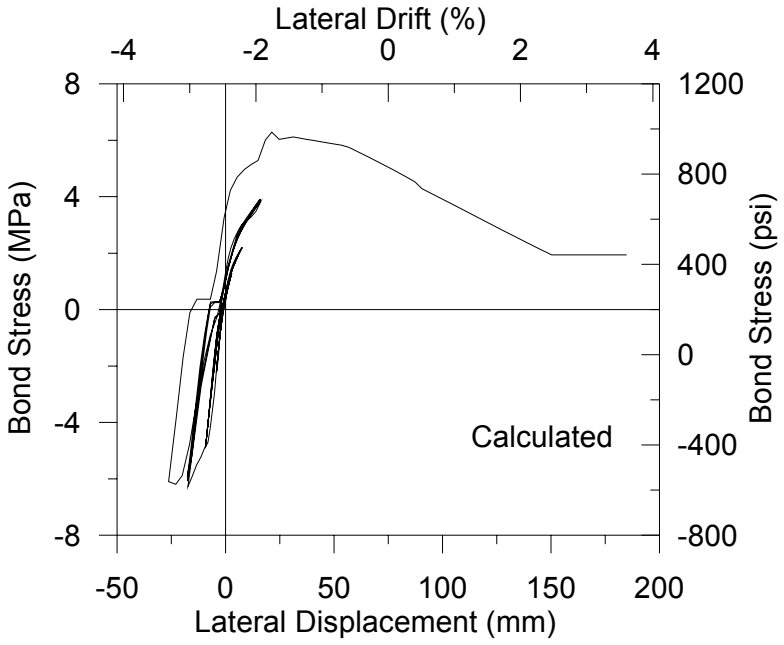

Figure 7.123. Analytical Average Bond Stress on Starter Bar along Lap Splice vs. Top Displacement for Specimen 2S20HN.

Overall, the detailed comparisons presented in this chapter indicate that the analytical model was effective in predicting the cyclic behavior of the column specimens investigated in the experimental program by Melek (2006). The model provides accurate predictions of global response characteristics including the lateral load capacity, strength degradation, stiffness degradation, ductility, pinching properties, and other cyclic attributes of the lateral load vs. top displacement behavior. Rotations due to flexure and slip at different locations of the column specimens were also predicted well by the model. Local response and deformation predictions of the model (steel strain distributions, concrete strain profiles, neutral axis position, and average bond stresses along the lap splice) are also representative of the experimental measurements, with a reasonable level of accuracy. In the next chapter, the analytical model predictions are compared with the results of additional experimental studies, which are available in the literature, conducted on column specimens with various configurations and anchorage conditions.

8. FURTHER EXPERIMENTAL VERIFICATION OF THE ANALYTICAL MODEL

The scope of this chapter is further experimental verification of the analytical model, for a more broad set of reinforced concrete column configurations. Response predictions obtained using the analytical model are compared with additional experimental observations available in the literature, for various column specimens with both deformed and plain reinforcing bars, and with both deficient lap splices and continuous longitudinal reinforcement. A total of 24 column tests conducted by 10 research groups are considered in comparison of the analytical and experimental responses. Comparisons are made at only the global response level (lateral load vs. top displacement), due to the absence of digital test data and information on local response measurements.

8.1. Overview of Experimental Studies

A number of experimental studies have been selected for comparing the model predictions with the results of tests conducted on various types of column specimens with either deformed or plain reinforcing bars, and with various lap splice lengths, cross sections, material properties and reinforcement conditions, subjected to different axial load levels and lateral loading patterns.

Two column specimens (Specimen-1 and Bousias) tested by Low and Moehle (1987) and Bousias *et al*. (1995), both with continuous longitudinal reinforcement, were selected to investigate the accuracy of the model in representing the so-called for strain penetration effects (effect of bond slip deformations in the anchorage region of the reinforcement) on column response. Five splice-deficient column specimens (FC1, FC4, FC5, FC14 and FC15) tested by Aboutaha *et al*. (1994, 1996) with different cross sections, concrete compressive strengths, and longitudinal reinforcement amounts were chosen for additional comparisons. Three splice-deficient column specimens (C14, C20 and C16) tested by Harajli and Dagher (2008), with different material properties and reinforcement configurations, (C14 and C20 have three layers of longitudinal reinforcement, whereas C16 has four layers of longitudinal reinforcement in the direction of bending) were also

selected for the comparisons. One specimen (AB1) by Elgawady *et al*. (2010), was also considered, since it incorporated four layers of longitudinal reinforcement in the direction of bending. One other specimen (2SLH18) by Lynn *et al*. (1996) was chosen to investigate the model effectiveness when the column is subjected to a double – curvature bending moment distribution. To consider further variation in specimen properties and loading conditions, one specimen (L0) by Harries *et al*. (2006) and two specimens (AF(COG0)B1 and AF(COG0)B2) by Yildiz (2006) were selected for the response comparisons.

Furthermore, to investigate the effectiveness of the analytical model in predicting the responses of columns with smooth reinforcing bars (as well as 180-degree hooks), four column specimens (C270A1, C270B1, C540A1 and C540B1) tested by Verderame *et al*. (2008) were chosen. Five additional column specimens (LS-25φ-N1, LS-35φ-N1, LS-44φ-N1, LS-55φ-N1 and LS-CON-N1) tested by Yilmaz (2009), with plain pars and different lap splice lengths. The properties of the test specimens used in comparison of the analytical predictions of the model with experimental results are presented in Table 8.1. In the table, the column height (l) values represent the effective height from the column base to the point where the lateral loading is applied.

Table 8.1. Dimensions and Properties of Column Specimens Investigated.

Researcher	Column	Column dimensions			Longitudinal Rein.			Transverse Rein.		Concrete	Axial Load (%)
		b, mm	h, mm	l, mm	Amount	l_s, mm	F_y,Mpa	Amount	f_y, Mpa	Fc, Mpa	
Low-Moehle	Specimen 1	127	165	692.2	6 No. 2 &4 No.3	178** ($23d_b$)	450	13mm dia at 129mm		36.54	5
Bousias	Bousias	250	250	1490	8, 16 mm	480** ($30d_b$)	460	8 mm dia at 70 mm		30.75	15
Aboutaha	FC1	914.4	457.2	2743.2	16 No. 8	609.6 ($24d_b$)	434	9.5mm dia at 407mm	400	32.4	0
	FC4	914.4	457.2	2743.2	16 No. 8	609.6 ($24d_b$)	434	9.5mm dia at 407mm	400	19.65	0
	FC5	914.4	457.2	2743.2	16 No. 8	609.6 ($24d_b$)	434	9.5mm dia at 407mm	400	20.54	0
	FC14	685.8	457.2	2743.2	12 No. 8	609.6 ($24d_b$)	434	9.5mm dia at 407mm	400	28.75	0
	FC15	457.2	457.2	2743.2	8 No. 8	609.6 ($24d_b$)	434	9.5mm dia at 407mm	400	28.75	0
Harajli and Dagher	C14	400	200	1400	8, 14 mm	420 ($30d_b$)	550	8mm dia at 200mm		39	0
	C20	400	200	1400	6, 20mm	600 ($30d_b$)	617	8mm dia at 200mm		32	0
	C16	400	200	1400	8, 16mm	480 ($30d_b$)	528	8mm dia at 200mm		40	0
Elgawady	AB1	381	254	1803	12 No. 4	445 ($35d_b$)	331	6.3mm dia at 125mm	372	31	0
Lynn	2SLH18	457.2	457.2	2946.4	8 No. 8	331 ($20d_b$)	331	9.5mm dia at 457mm	400	33.1	12
Harries	L0	458	458	2400	8 No. 7	490 ($22d_b$)	460	9.5mm dia at 150mm	438	24.6	25
Yildiz	AF(C0G0)B1	240	180	850	4 , 12 mm	180 ($15d_b$)	500	8mm dia at 120mm		27.6	10
	AF(C0G0)B2	240	180	850	4 , 12 mm	180 ($15d_b$)	500	8mm dia at 120mm		28.77	10
Verderame	C270A1	300	300	1570	6, 12 mm	480 ($40d_b$)	355	8m dia at 100mm	430	25	12
	C270B1	300	300	1570	6, 12 mm	*	355	8m dia at 100mm	430	25	12
	C540A1	300	300	1570	6, 12 mm	480 ($40d_b$)	355	8m dia at 100mm	430	25	24
	C540B1	300	300	1570	6, 12 mm	*	355	8m dia at 100mm	430	25	24
Yilmaz	LS-25φ-N1	300	200	1650	4, 14 mm	350 ($25d_b$)	285	10mm dia at 100mm /200mm	307	10	0
	LS-35φ-N1	300	200	1650	4, 14 mm	490 ($35d_b$)	285	10mm dia at 100mm /200mm	307	10	0
	LS-44φ-N1	300	200	1650	4, 14 mm	616 ($44d_b$)	285	10mm dia at 100mm /200mm	307	10	0
	LS-55φ-N1	300	200	1650	4, 14 mm	770 ($55d_b$)	285	10mm dia at 100mm /200mm	307	10	0
	LS-CON-N1	300	200	1650	4, 14 mm	*	285	10mm dia at 100mm /200mm	307	10	0

*Continuous longitudinal reinforcements

**Anchorage length

8.2. Analytical Model Formulation

The general model formulation described in Chapter 3 is applicable to most of the column specimens with lap splices, investigated in this chapter. However, it was necessary to modify this formulation in order to represent the configuration of some of the specimens (AB1, 2SLH18, Specimen-1, Bousias, LS-25φ-N1, LS-35φ-N1, LS-44φ-N1, LS-55φ-N1, C270A1, and C540A1), as described below.

Most of the selected column specimens consist of two or three layers of longitudinal reinforcement with one layer located middle of the cross section, which is compatible with the general model formulation (with three layers of reinforcement) shown in Figure 3.1. However, to incorporate four layers of longitudinal reinforcement in the bending direction, as seen in specimens C16 (Figure 8.20) and AB1 (Figure 8.27), it was necessary to modify the original column model formulation slightly to incorporate the additional layer of reinforcement.

To model the response of specimen 2SLH18 (Figure 8.30), which is subjected to double – curvature bending moment distribution and zero rotation at the top, necessary modifications were applied to the direct stiffness assembly procedure used in the formulation of the analytical model.

Modifications to the original model formulation were also required for specimens 'Specimen-1'(Figure 8.1) and 'Bousias' (Figure 8.4), to simulate the effects of "strain penetration" (bond slip deformations in the anchorage zone) on the behavior of these specimens. The lap splice region in the original model formulation were transformed into the anchorage zone, via fixing the concrete displacement degrees of freedom located at the top of the rigid beams in this region.

For modeling of the column specimens with plain bars and 180-degree hooks, the bottom hooks on the longitudinal bars were represented by steel stress – hook end slip springs connecting the bottom rigid beam of the second model element from column base, to the longitudinal bars in the splice. The hook springs were not assigned to the very first model element at the base of the column, to allow the uplift of the longitudinal bar hook

from the column-pedestal interface. The top hooks on the starter bars at the top level of the splice or on the longitudinal bars at the top level of the column were also represented by steel stress – hook end slip springs, connecting the top rigid beam of the respective model element, to the longitudinal bars. This modeling approach was used to analyze specimens LS-25φ-N1, LS-35φ-N1, LS-44φ-N1, LS-55φ-N1, C270A1, and C540A1.

8.3. Calibration of the Analytical Model

Experimental calibration of the geometric, as well as the constitutive parameters of the analytical model, for the column test investigated in this chapter, are discussed in the following subsections.

8.3.1. Geometry

It is discussed in Chapter 6, that neither the number of model elements nor the number concrete macro-fibers used in the analytical model have a significant influence on the global response prediction, as long as an adequate number of elements and fibers are used to describe the geometric details of a column. The optimum number of model elements and concrete macro-fibers used to calibrate the model for the column specimens investigated in this chapter are discussed in the following paragraphs.

Twenty six macro-fibers are used along column width to represent the concrete cross section of the majority of the columns specimen model. Eight model elements along the lap splice length and 4 model elements above the lap splice region are assigned to the analytical model, for most of the columns specimens with deficient lap splices (Specimens FC1, FC4, FC5, FC14 , FC15, C14, C20, AF (COG0)B1, AF(COG0)B2, and AB1).

.

For other specimens, either less or more number of model elements and macro-fibers were used in calibration, based on the results of preliminary analyses, depending on the level of detail of the specimen geometry, or the level of complexity of the response. Four model elements along the lap splice length and two elements above the lap splice region are selected to model column specimens LS-25φ-N1, LS-35φ-N1, LS-44φ-N1 and LS-

55φ-N1 (Yilmaz, 2009). Six model elements and 52 macro-fibers were used along the entire length of column specimen LS-CON-N1, with continuous longitudinal reinforcement. Four model elements along the lap splice length and two elements above the lap splice, are selected for specimens C270A1 and C540A1 (Verderame *et al*., 2009). Six model elements are used along the whole length of specimens C270B1 and C540B1 with continuous reinforcement. Sixteen model elements along the lap splice and 4 elements above the lap splice region are for the column specimens, C16 and 2SLH18. For specimen L0, four model elements along the lap splice and two elements above the lap splice region are used.

Three separate analytical models are built for each of the two specimens 'Specimen-1' and Bousias', with continuous longitudinal reinforcement, which were tested to observe strain penetration effects in the anchorage zone (foundation). The first model included eight elements in the anchorage zone (with rigid concrete degrees of freedom) and four elements along the height of the column.The second and third models only included four elements along the height of each column to simulate its behaviour without incorporating bond slip deformations (strain penetration) in the anchorage zone. The third model incorporates rigid bond slip springs, representing the perfect bond assumption between concrete and reinforcing steel.

8.3.2. Materials

8.3.2.1 Steel Stress-Strain Relation. The constitutive model used for reinforcing steel was calibrated for yield strength, elastic modulus, strain hardening ratio, and cyclic curvature degradation parameters. The monotonic parameters of the model were calibrated based on the values for the specimens investigated. For cases where test results for the stress – strain behavior of the reinforcement was not available, typical values of E_0 = 200 GPa and b = 2% was used for the elastic modulus and the strain hardening ratio, respectively. The values $R0$ = 20, $a1$ = 18.5, and $a2$ = 0.15 (accounting for the cyclic degradation of the curvature coefficient R and thus the Bauschinger effect), originally suggested by Menegotto and Pinto (1983), were used in the calibration. Table 8.2 summarizes the constitutive parameters used in the analysis for reinforcing steel.

Table 8.2. Calibrated Constitutive Parameters for Confined Concrete and Steel.

Specimen	Concrete in compression					Concrete in tension					Reinforcing bar		
	$f_c^{/}$ Mpa	$\varepsilon_c^{/}$	E_c Mpa	ε_{cr}	r	f_t Mpa	ε_t	E_c (Mpa)	ε_{cr}	r	f_y Mpa	E_0 Gpa	b
Specimen 1	36.54	0.0025	28713	0.003	5.02	1.87	0.00008	28713	∞	1.2	408	210	0.002
Bousias	36	0.0025	28500	0.004	2.50	1.86	0.00008	28500	∞	1.2	421	200	0.02
FC1	32.40	0.0024	27038	0.003	5.02	1.76	0.00008	27038	∞	1.2	390	200	0.02
FC4	19.65	0.0019	21056	0.002	5.02	1.37	0.00008	21056	∞	1.2	390	200	0.02
FC5	20.55	0.002	21532	0.002	5.02	1.40	0.00008	21532	∞	1.2	390	200	0.02
FC14-FC15	28.75	0.0023	25469	0.003	5.02	1.66	0.00008	25469	∞	1.2	390	200	0.02
C14	39	0.0026	29664	0.004	5.02	1.94	0.00008	29664	∞	1.2	496	200	0.02
C20	32	0.0024	26870	0.003	5.02	1.75	0.00008	26870	∞	1.2	566	200	0.02
C16	40	0.0027	30041	0.004	5.02	1.96	0.00008	30041	∞	1.2	480	200	0.02
AB1	34	0.0025	27697	0.004	5.02	1.81	0.00008	27697	∞	1.2	292	200	0.02
2SLH18	33.10	0.0024	27328	0.003	5.02	1.78	0.00008	27328	∞	1.2	297	200	0.008
L0	24.60	0.0021	23560	0.003	5.02	1.54	0.00008	23560	∞	1.2	400	200	0.02
AF(C0G0)B 1	27.60	0.0022	24954	0.003	5.02	1.63	0.00008	24954	∞	1.2	446	200	0.0015
AF(C0G0)B 2	28.77	0.0023	25478	0.003	5.02	1.66	0.00008	25478	∞	1.2	446	200	0.0015
C270A1, C270B1, C540A1, C540B1	29	0.0023	16454	0.004	2	1.67	0.00008	25580	∞	1.2	300	200	0.002
LS-25φ-N1 LS-35φ-N1 LS-44φ-N1 LS-55φ-N1 LS-CON-N1	12	0.0015	16454	0.002	5.02	0.99	0.00008	16454	∞	1.2	250	183	0.004

8.3.2.2 Concrete Stress-Strain Relations. The monotonic envelope curves of the Chang and Mander (1994) constitutive model for compression and tension were calibrated for values of peak compressive and tensile stress (f'_c and f_t), strains at peak stress (ε'_c and ε_t), elastic modulus E_c, the parameter r defining the shape of the envelope curves, and the normalized strain parameter x_{cr} controlling the post peak slope of the envelope curves.

The envelope curve for unconfined concrete in compression was calibrated using reported results of monotonic stress-strain tests, conducted at time of testing, for the concrete used in the construction of the specimens, with a 20% residual stress value defined for the envelope curve for improving the stability of the analysis. The parameters

used for the calibration of the monotonic envelopes for unconfined concrete in compression and tension are presented in Table 8.2. Stress – strain relations for confined concrete were not used in modeling of these columns, since the amount of transverse reinforcement used in the specimens did not provide effective confinement. The concrete tensile strength was determined from the relationship $f_t = 0.31\sqrt{f'_c}$ (Mpa), and a value of 0.00008 was selected for the strain ε_t at peak monotonic tensile stress, as suggested by Belarbi and Hsu (1994). The shape of the monotonic tension envelope was calibrated (via the parameters r and x_{cr}) to reasonably represent the average post-crack stress – strainship relation proposed by Belarbi and Hsu (1994) for considering the effects of tension stiffening on concrete. The hysteretic stress-strain rules defined by Chang and Mander (1994), modified slightly as described by Orakcal (2004), were used to simulate the cyclic behavior of unconfined concrete implemented in model.

8.3.2.3 Shear Force-Deformation Relation. The trilinear envelope curve of the origin-oriented force–deformation relationship, which was adopted for the horizontal shear springs in the model elements, was calibrated based on the empirical relationships proposed by Sezen (2002), as described in Chapter 3. It must be mentioned that during testing, none of the column specimens experienced shear failure or significant shear deformations.

8.3.2.4 Bond Stress Slip Relations. The parameters of the cyclic constitutive bond stress – slip relationship for splitting failure in partially-confined concrete by Harajli *et al*. (1994, 2004, 2009), were calibrated as proposed originally in the constitutive relationship formulations, for most of the splice-deficient column specimens with deformed reinforcing bars. For the specimen ‘FC4’, where splitting springs were used in combination with pull-out springs (in the vicinity of the ties), parameters of the cyclic bond stress – slip relationship for pull-out failure in confined concrete by Eligehausen *et al*. (1983) were calibrated as proposed in the original constitutive formulation. Pull-out springs following the original constitutive relationship by Eligehausen *et al*. (1983) were also used in the anchorage zones (foundations) of ‘Specimen-1’ and ‘Bousias’, for consideration of slip deformations in the anchorage region (strain penetration effects).

The cyclic bond stress – slip constitutive relationship representing the pullout behaviour of plain reinforcing bars, developed by Verderame *et al*. (2009), was calibrated, using the original constitutive formulation, for column specimens LS-25φ-N1, LS-35φ-N1, LS-44φ-N1, LS-55φ-N1, LS-CON-N1 C270A1, C270B1, C540A1 and C540B1. The original monotonic steel stress vs. hook end slip constitutive model by Fabbrocino *et al*. (2004) for 180-degree hooks was also used for modeling of these specimens, with adaptation of origin-oriented cyclic rules, as described in Chapter 3.

Table 8.3(a) lists the constitutive bond stress – slip parameters used for the column models which incorporated both splitting and pullout bond slip springs whereas the parameters used for the column models splitting springs only, are listed in Table 8.3(b). Table 8.4 presents the constitutive bond stress – slip parameters used for modelling of the columns with plain reinforcing bars.

Table 8.3. Calibrated Constitutive Bond Stress – slip Parameters Used for the Specimens with Deformed Bars.

(a) Specimens Analyzed Using Both Pullout and Splitting Springs.

Specimen	Parameter	s_1 mm	s_2 mm	s_3 mm	u_1 (Mpa)	u_3 (Mpa)	$u_{\max}$ (Mpa)	u_{ps} (Mpa)	$s_{\max}$ mm	s_0 mm	α	β
FC4	Harajli *et al*. (1994) Unconfined	1.95	4.55	3	11.39	-	4.15	2.18	0.22	0.15	0.70	0.65
	Eligehausen *et al*. (1983)	1.00	3.00	10.5	10.93	4.05	-	-	-	-	0.40	-
Specimen-1	Harajli *et al*. (1994)	1.95		13	15.42	-	5.74	3.07	0.27	0.15	0.70	0.65
	Eligehausen *et al*. (1983)	1.24	3.71	13	14.78	5.48	-	-	-	-	0.40	-
Bousias	Harajli *et al*. (1994)	1.95		13	15.42		5.74	3.07	0.27	0.15	0.70	0.65
	Eligehausen *et al*. (1983)	1.24	3.71	13	14.78	5.48					0.40	

Table 8.3. Calibrated Constitutive Bond Stress – Slip Parameters Used for the Specimens with Deformed Bars (Cont.).

(b) Specimens Analyzed Using Splitting Springs Only.

Parameter of Harajli *et al.* (1994)	s_1 (mm)	s_3 (mm)	u_1 (Mpa)	$u_{\max}$ (Mpa)	u_{ps} (Mpa)	$s_{\max}$ (mm)	s_0 (mm)	α	β
FC1	1.95	13	14.63	5.46	2.94	0.22	0.15	0.70	0.65
FC5	1.95	13	11.65	4.35	2.34	0.22	0.15	0.70	0.65
FC14-FC15	1.95	13	13.78	5.09	2.68	0.22	0.15	0.70	0.65
C14	1.95	13	16	6.22	3.52	0.23	0.15	0.70	0.65
C20	1.95	13	14.54	4.67	2.78	0.21	0.15	0.70	0.65
C16	1.95	13	16	8.46	4.70	0.32	0.15	0.70	0.65
2SLH18	1.50	10	14.70	7.14	3.63	0.25	0.15	0.70	0.65
L0	1.95	13	12.75	5.17	2.74	0.23	0.15	0.70	0.65
AF(C0G0)B1 AF(C0G0)B2	1.50	10	13.50	8.60	5.10	0.40	0.15	0.70	0.65
AB1	1.95	13	14.31	5.09	2.85	0.22	0.15	0.70	0.65

Table 8.4. Calibrated Constitutive Bond Stress – Slip Parameters Used for the Specimens with Smooth Bars.

Parameter of Verderame *et al.* (2009)	$s_{\max}$ (mm)	s_1 (mm)	$\tau_{b,\max}$ (Mpa)	$\tau_{b,f}$ (Mpa)	$\tau_{b,c}$ (Mpa)	$\tau_{b,r}$ (Mpa)	α
C270A1, C270B1, C540A1, C540B1	0.38	3.17	1.55	0.65	0.25	0.45	0.26

8.4. Comparison of Model Results with Experimental Results

In this section the response predictions obtained using the analytical model, are compared with the experimental results. Comparisons are made at only the global lateral load vs. top displacement response level due to the absence of digital test data and information on local response measurements. The comparisons are presented and discussed individually, for each test program.

8.4.1. Low and Moehle (1987) Specimen:

Low and Moehle (1987) tested a series of reinforced concrete cantilever columns with rectangular cross sections. The columns were subjected to a constant axial load and cyclic lateral displacements. One of these columns, labeled Low-Moehle "Specimen 1", with continuous longitudinal reinforcement, is selected here for investigating the efficiency of the model in simulating strain penetration effects. The specimen geometry is shown in Figure 8.1. The column was subjected to a constant axial compression of 44.5 kN (corresponds to approximately 5%Agf'c), and a cyclic lateral displacement history in the weak direction of the column cross section.. The anchorage length of the longitudinal reinforcement in the specimen foundation (pedestal) was 178mm, corresponding to 23 longitudinal bar diameters.

Figure 8.2 shows the experimental response of 'Specimen 1' which was used by Spacone and Limkatanyu (2000), to validate the formulation of a reinforced concrete beam element model, which incorporates bond slip deformations. The correlation between experimental and analytical results obtained by Spacone and Limkatanyu (2000) was quite satisfactory.

Figure 8.3 presents three different analytical results obtained using the present model. The solid line represents results of the first modeling approach (Model 1), where bond slip deformations in both the column and in the anchorage zone (strain penetration) are considered. The second model (Model 2), the results of which are represented by the dashed line with narrow spacing, considers bond slip deformation in the column only,

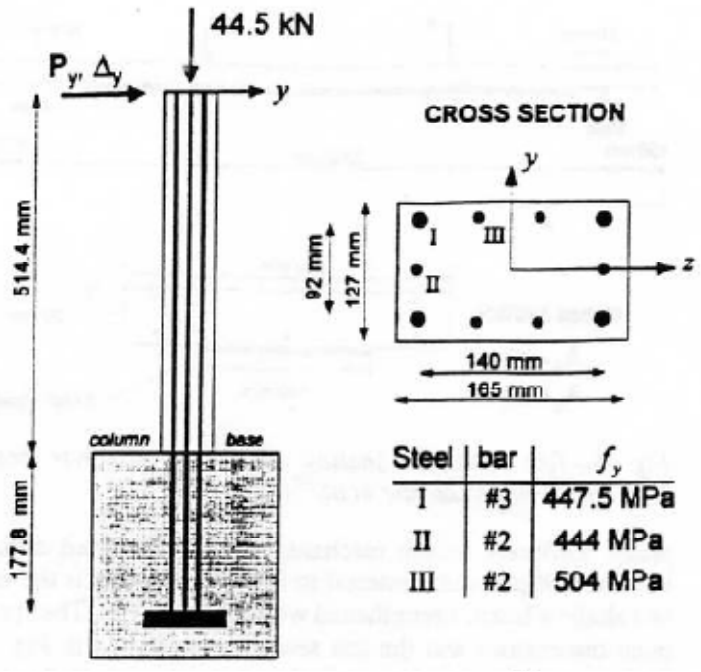

Figure 8.1. Geometry and Loading Conditions for 'Specimen 1' (Low and Moehle, 1987).

neglecting the strain penetration effects. In the third model (Model 3), represented by the dashed line with wide spacing, all bond slip and strain penetration effects are neglected (perfect bond condition).

All three models capture the column lateral load capacity accurately. In Models 2 and 3, the pre-yield stiffness in the analytical results is overestimated, since column base rotations due to the strain penetration effects are ignored. Moreover, the models that do not consider column bond slip and strain penetration (model 2 and model 3) obviously tend to overestimate the hysteretic energy dissipation (cumulative area under the load – displacement loops) of the specimen. During unloading, initial unloading is followed by closing of the cracks, reloading, and yielding of the longitudinal steel in tension. With the model considering bond slip deformations in both the column and the anchorage zone (model 1), when the column unloads, closing of the crack is accompanied by slip of reinforcing bars at the column base. This gives a more flexible response, and yielding of the reinforcing bars in tension is delayed.

From Figure 8.3, it can be deduced that the hysteretic behavior of reinforced concrete columns, subjected to severe seismic excitations, is dependent on the bond interection between steel and concrete, even if no anchorage failure takes place.

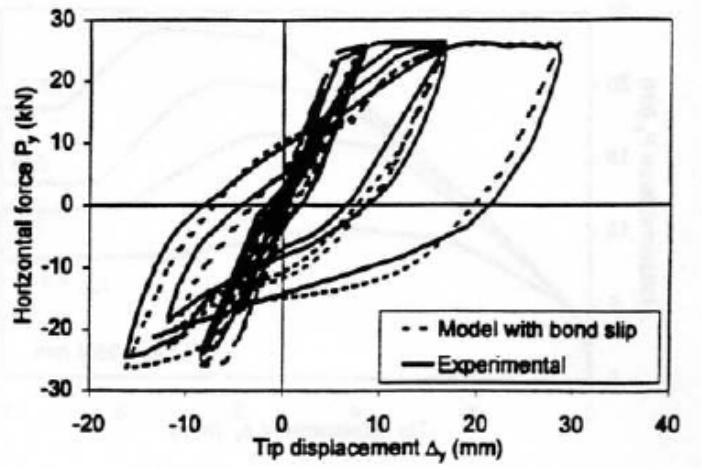

Figure 8.2. Experimental and Previous Analytical Responses of 'Specimen 1' (Spacone and Limkatanya, 2000).

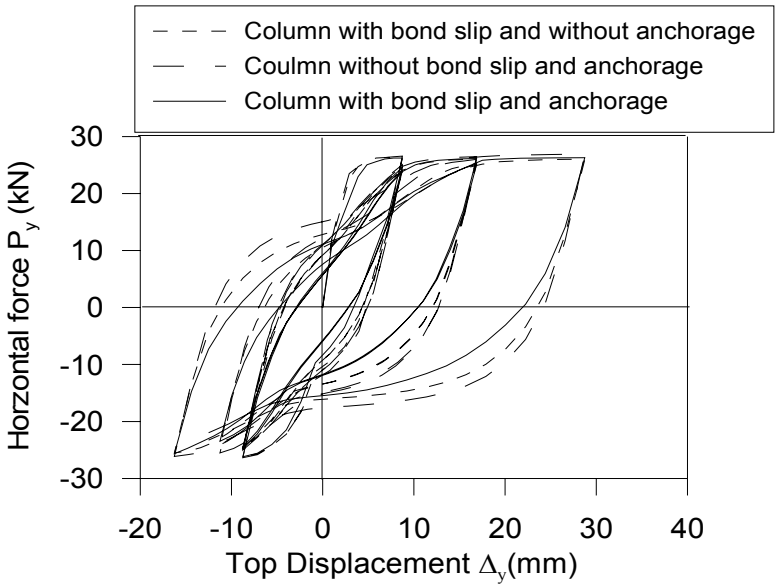

Figure 8.3. Analytical Response Prediction for 'Specimen 1'.

8.4.2. Bousias *et al*. (1995) Specimen:

Figure 8.4 illustrates details of the column specimen tested by Bousias *et al*. (1995). The specimen was 1490 mm long, with a cross section of 250 mm by 250 mm, and anchorage length of 480 mm (30db) in the foundation; and was subjected to a constant axial load 300 kN and a variable cyclic lateral load acting at the top. A concrete cover of 15 mm was provided on all faces. The longitudinal reinforcement consisted of 3 bars 16 mm in diameter, placed at the sides, and 2 bars 16 mm in diameter placed at the center. The concrete compressive strength was 30.7 MPa, and the yield strength of reinforcing steel was 460 MPa. The elastic modulus measured for the longitudinal steel was approximately 210,000 MPa.

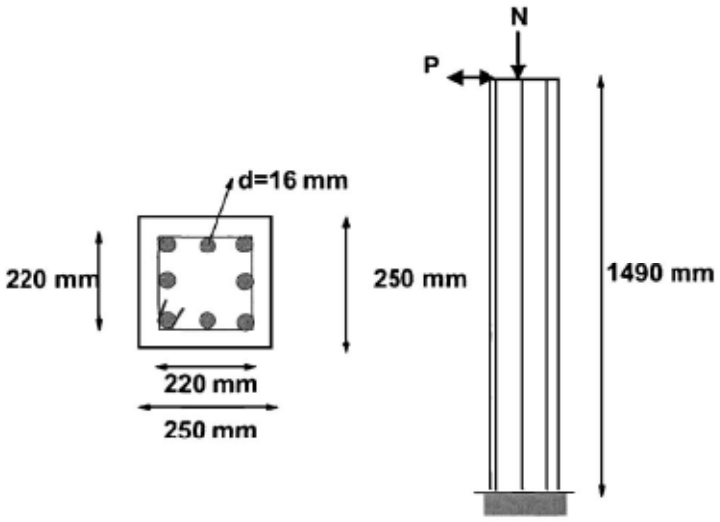

Figure 8.4. Bousias Specimen (Bousias *et al*., 1995).

Figure 8.5 shows the comparison of lateral load – displacement responses between the test results and the analytical study conducted by Ayoub (2006). Although the finite element model formulated by Ayoub (2006) captured the column lateral load capacity, the hysteretic shape of the unloading and reloading loops and especially the pinching properties of the response were not represented well by the analytical model by Ayoub (2006).

Similarly with the ‘Specimen 1’by Low and Moehle (1987), three models were generated using the present analytical model for this specimen, the predictions of which are presented in Figure 8.6. The model formulation considering bond slip deformations in the both column and in the anchorage zone accurately predicts the cyclic attributes of the measured response, including lateral load capacity, shape of the hysteretic loops, cyclic stiffness degradation, cyclic energy dissipation capacity, and pinching behavior.

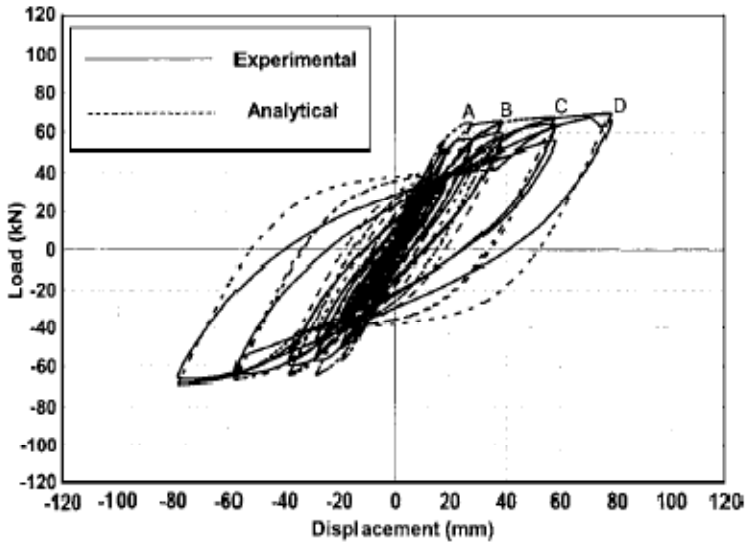

Figure 8.5. Experimental and Previous Analytical Results Response of 'Bousias (1995)' Specimen (Ayoub, 2006).

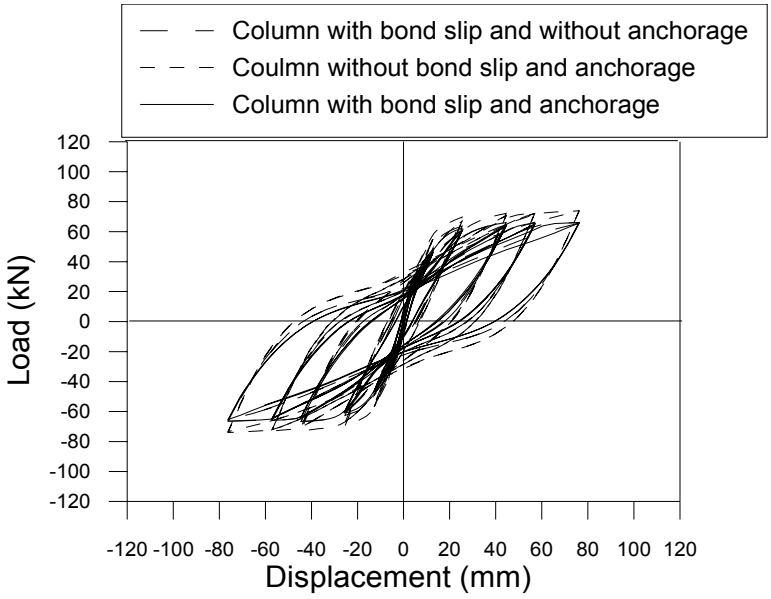

Figure 8.6. Analytical Response Prediction for 'Bousias (1995)' Specimen.

8.4.3. Aboutaha (1994) and Aboutaha *et al*. (1996) Specimens:

Aboutaha (1994) and Aboutaha *et al*. (1996) conducted a series of tests on cantilever-type column specimens (Figure 8.7), representing half the height column, subjected to bending under double curvature, within a real building frame. All of the column specimens were 2.74 m high from the top of footing to the point of load application, to ensure flexural dominated behavior. Cyclic lateral loads were applied at the top of the column. All columns were loaded in the weak direction. Lateral loads were increased in 22.25 KN increments until significant inelastic displacement was observed. Lateral displacements were then increased in increments corresponding to 0.5% drift ratios. The columns were laterally loaded with two complete cycles at every load or drift ratio level. No axial load was applied. Longitudinal bars were all spliced at the base of the column as shown in Figure 8.7. The lap splice length corresponded to 24 bar diameters. A concrete cover 38 mm was provided for all transverse ties. For all the test specimens, the

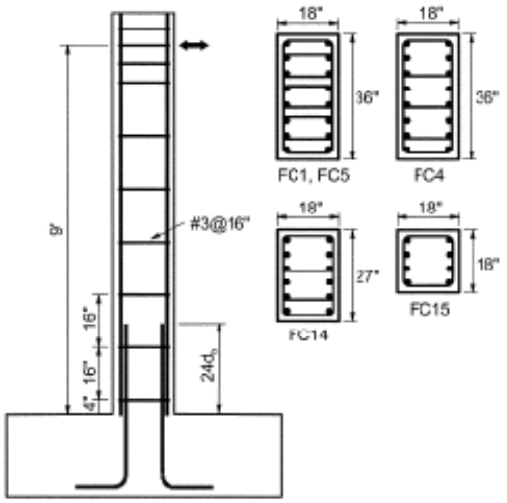

Figure 8.7. Details of Test Specimens (Aboutaha, 1994, Aboutaha *et al*. ,1996).

longitudinal reinforcement bars were 25.4 mm dia. (Yield strength, 413 Mpa) reinforcement. Transverse ties were with 9.5 mm dia (Yield strength, 276 Mpa) bars, spaced at 406 mm.

Five specimens (FC1, FC4, FC5, FC14 and FC15) were tested to consider the effect of varying concrete compressive strength, amount of longitudinal and transverse reinforcement, and cross-sectional dimensions on the behavior.

Figures 8.8, 8.10, 8.13, 8.16, and 8.18 show the measured responses for specimens FC1, FC4, FC5, FC14, and FC15, respectively. For specimen FC4, splice failure was associated with the formation of vertical splitting cracks along the full height of the splice. Strain readings showed that the strain levels in the longitudinal bars was just below yielding, prior to splice failure. Hence, splice failure occurred before development of the flexural yield capacity of the column. Specimen FC4 demonstrated very poor ductility and energy dissipation characteristics. Specimen FC1 also experienced a splice failure. However, specimen FC1 reached its flexural capacity, and maintained it up to a drift ratio of approximately 2%, prior to splice failure. The improved performance of specimen FC1 was attributed to its higher concrete compressive strength, and the presence of cross ties on every longitudinal bar. Until 1.5% drift ratio, specimen FC1 experienced stable hysteretic loops. At 2% drift ratio, the specimen showed dramatic loss in strength and stiffness. Splice failure after yielding of the main longitudinal bars, and the gradual (as opposed to sudden) extension of the vertical splitting cracks was attributed to the relatively higher concrete compressive strength, compared to the design value. For specimen FC5, vertical splitting cracks extended to almost half the height of the splice, as the lateral load level was approximately 156 kN. Splice failure occurred when the vertical splitting cracks extended over the full length of the lap splice, at a lateral load level of 40 kips. The splice failure of specimens FC14 and FC15 was very brittle, with very rapid loss in strength and stiffness, and occurred prior to flexural yielding.

In the analytical responses obtained using the present model for all of these column specimens, the lateral load capacities are predicted very well, as shown in Figures 8.8 to 8.19. The lateral displacement values corresponding to peak lateral load are also generally well-captured, although the model tends to underestimate the displacement at peak load, for some cases. General characteristics of the cyclic response, including the shape of the hysteretic loops, pinching properties, and degradation in the lateral load in post peak region are all captured reasonably well. However, for specimen FC1 (Figure 8.9), the analytical model estimates a more rapid degradation in the lateral load due to splice failure, as

opposed to the experimentally observed flexural yielding prior to splice failure. This discrepancy may be attributed to no reduction in the bond stresses in the constitutive bond slip relationships adopted in the model, associated with bar yielding.

Specimen FC4 was analyzed using two model formulations, the first of which incorporates splitting springs (for partially-confined concrete) only, whereas the second formulation also included pullout springs (for confined concrete) within the vicinity of the ties. As described previously in Chapter 6. Results of the two model formulations presented in Figures 8.11 and 8.12 illustrate that for this specimen, using the second model formulation (splitting and pullout springs used together) provides an improved prediction of the response. Consideration of the tension stiffening effects (reduction in the effective yield strength of reinforcing steel, modification of the strain hardening ratio, and modification of the post-crack stress – strain behavior of concrete) does not significantly improve the analytical response prediction for specimen FC5, as illustrated by the two analysis results, shown in Figures 8.14 and 8.15.

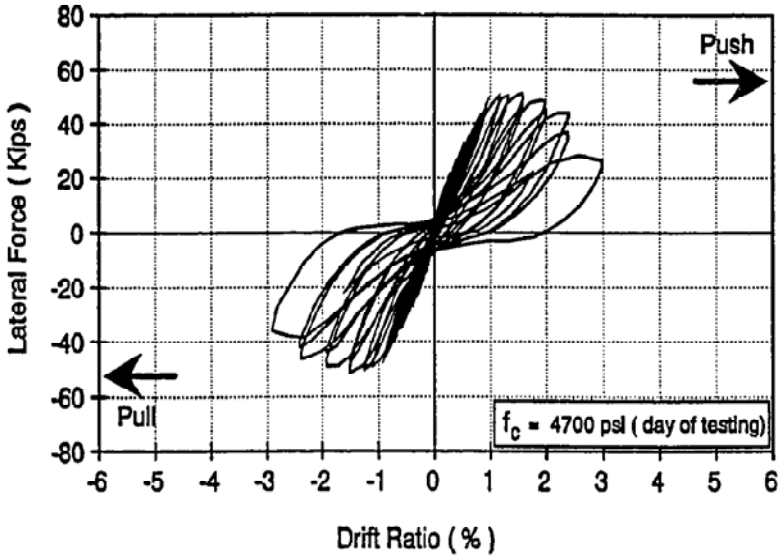

Figure 8.8. Experimental Response of Specimen FC1 (Aboutaha *et al*., 1996).

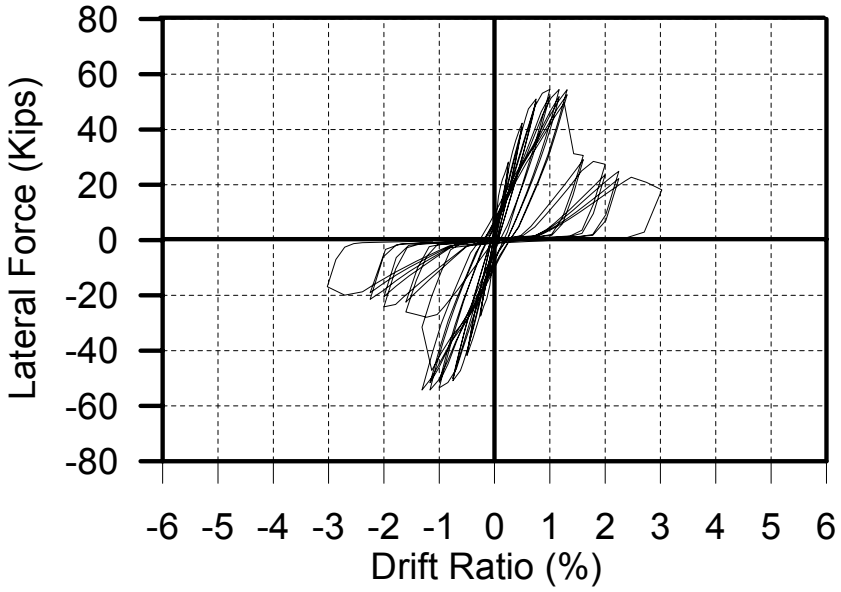

Figure 8.9. Analytical Response of Specimen FC1,with Splitting Springs Only.

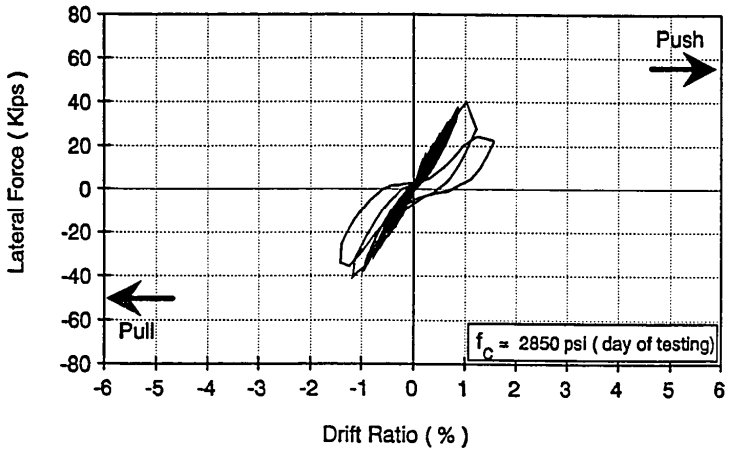

Figure 8.10. Experimental Response of Column Specimen FC4 (Aboutaha *et al*., 1996).

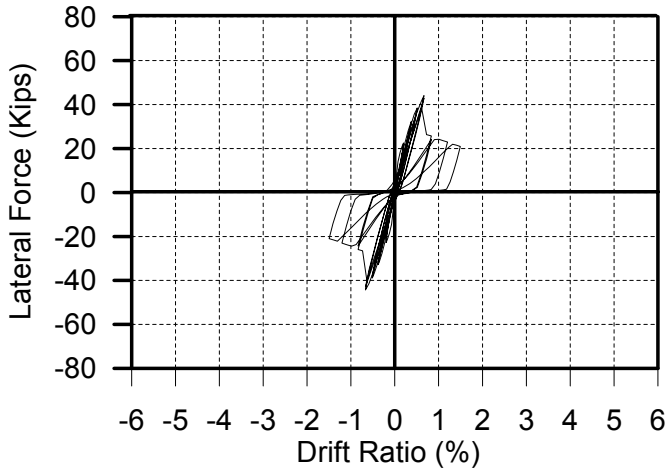

Figure 8.11. Analytical Response of Specimen FC4, with Splitting Springs Only.

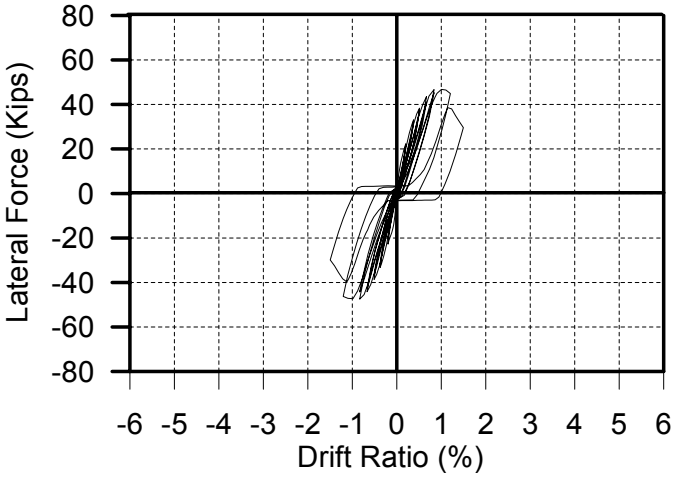

Figure 8.12. Analytical Response of Specimen FC4, with Both Pullout and Splitting Springs.

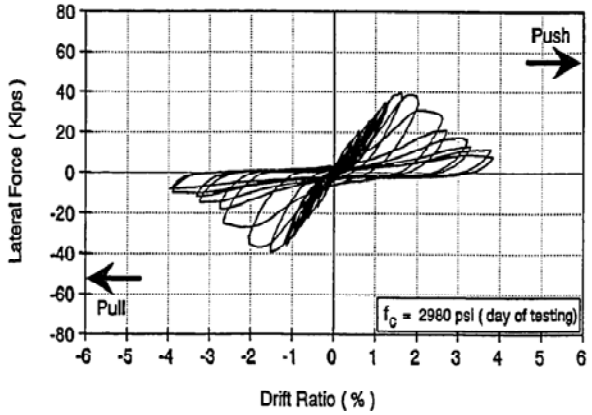

Figure 8.13. Experimental Response of Specimen FC5 (Aboutaha *et al*., 1996).

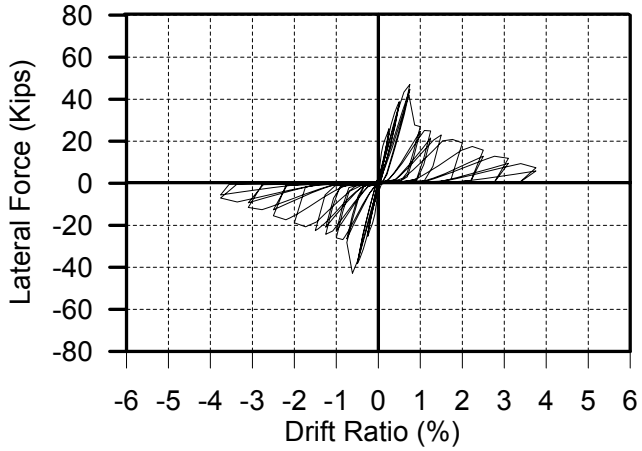

Figure 8.14. Analytical Response of Specimen FC5, Considering Tension Stiffening.

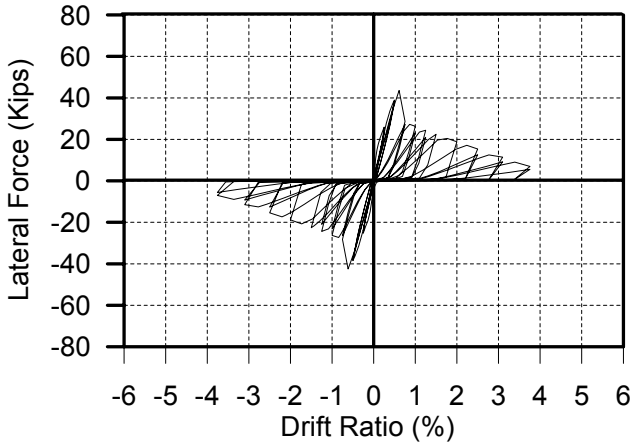

Figure 8.15. Analytical Response of Specimen FC5, not Considering Tension Stiffening.

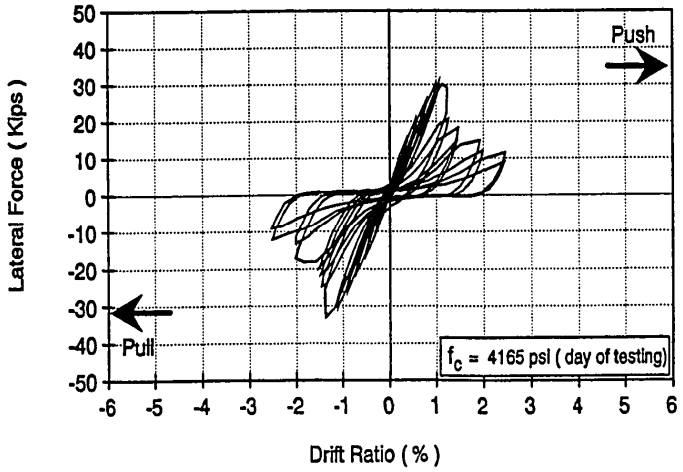

Figure 8.16. Experimental Response of Specimen FC14 (Aboutaha *et al.*,1996).

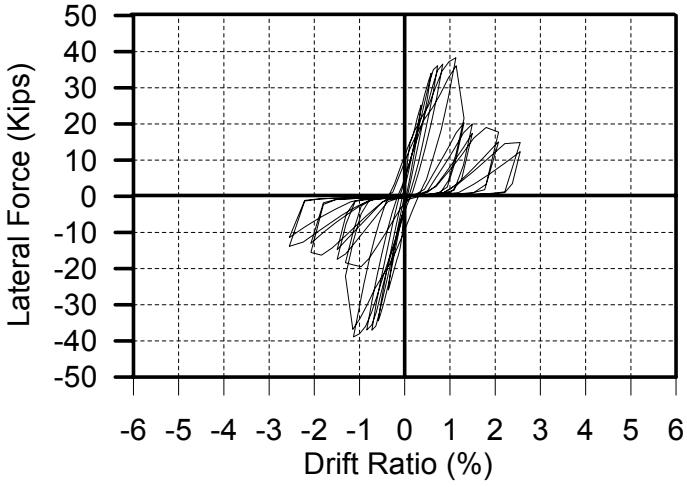

Figure 8.17. Analytical Response of Specimen FC14.

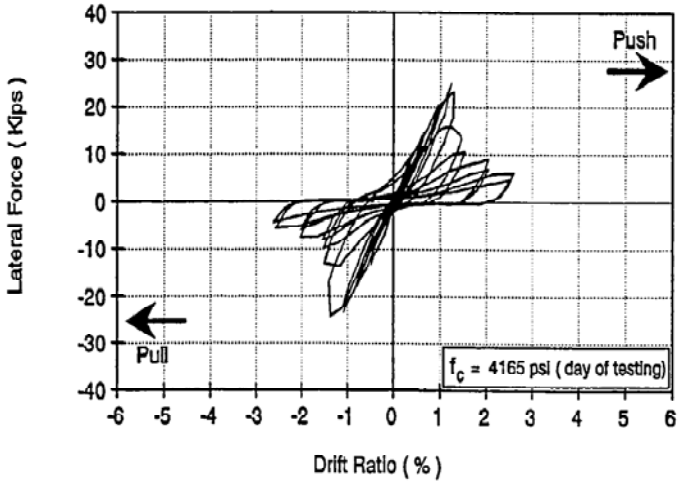

Figure 8.18. Experimental Response of Specimen FC15 (Aboutaha *et al.* ,1996).

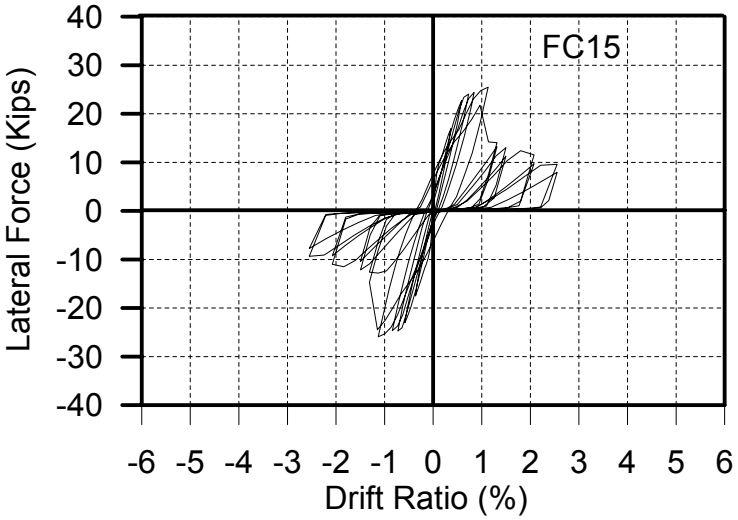

Figure 8.19. Analytical Response of Specimen FC15.

8.4.4. Harajli and Dagher (2008) Specimens:

Harajli and Dagher (2008) tested a series of full-scale column specimens with lap-spliced reinforcement at the base. The three column specimens C14, C16, and C20 had longitudinal reinforcement diameters of 14, 16, and 20 mm, respectively. Figure 8.20

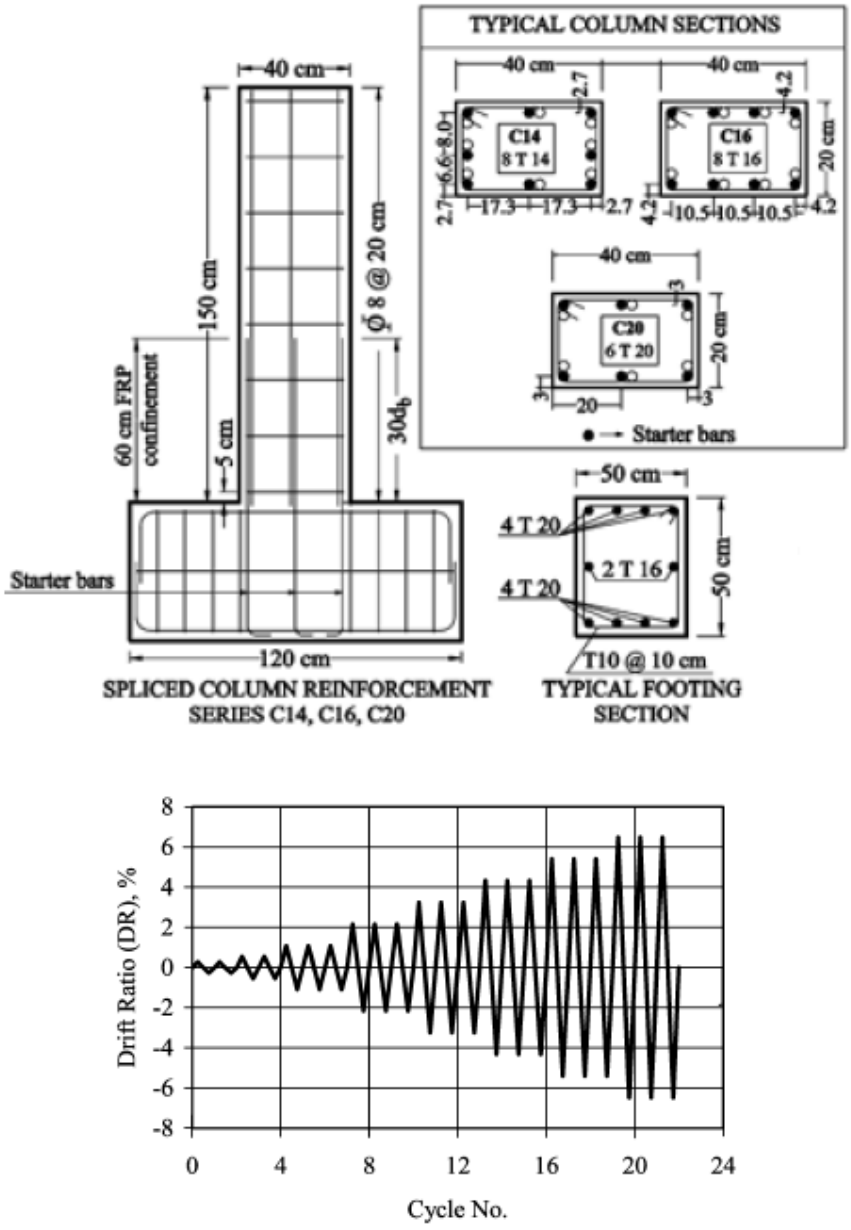

Figure 8.20. Details of Test Columns and Load History (Harajli and Dagher, 2008).

shows details of the three specimens. The area of longitudinal reinforcement produced reinforcement ratios of 0.015 (for C14), 0.02 (for C16), and 0.023 (for C20). The longitudinal reinforcing bars of the specimens were lap-spliced with starter bars of the same diameter, anchored inside the footing using standard 90-degree hooks. The splice length for all columns was selected at 30 bar diameters. The side cover c_s and bottom cover c_b of the spliced bars in the column sections were chosen to produce a range of values of c/d_b, that would induce splitting bond failure before steel yielding. The horizontal loads were applied at a discance of 1.40 m above the column base. All specimens were subjected to the same lateral load history shown in Figure 8.20. The drift cycles were increased sequentially with three fully reversed cycles applied at each target drift level up to a maximum drift ratio of ±6%. As the focus of the tests was to investigate the splitting bond strength of spliced column reinforcement, and since the splitting bond strength of spliced bars depends primarily on the tension stresses on the spliced bars, the specimens were tested under flexure only, with no axial load applied on the specimens.

Figures 8.21, 8.23 and 8.25 show the experimental responses for column specimens C14, C20 and C16 respectively. All specimens developed splitting cracks at the bottom during relatively early stages of the response. The splitting cracks first developed at the base of the columns, and propagated upwards along the full splice length, as the lateral drift increased. Splitting bond failure caused concrete spalling along the splice length and substantial slip of the starter bars at the column-footing interface.

Figures 8.22, 8.24, and 8.26 present the analytical responses obtained using the present model for column specimens C14, C20, and C16, respectively, considering tension stiffening effects on concrete and reinforcing bars. The lateral load capacities of specimens C14 and C20 were overestimated by the analytical model, whereas a better lateral load capacity prediction was obtained for specimen C16. General characteristics of the cyclic response, including the shape of the hysteretic loops, pinching properties, and degradation in the lateral load in post peak region are captured reasonably well for all specimens.

During the tests, these specimens were observed to fail under a combined effects of longitudinal bar yielding and slip failure along the splice. The analytical model also predicts such a coupled yielding–slip response for the specimens. However, the reason that

the model overestimates the lateral load capacity of specimens C14 and C20 may be attributed to the fact no reduction was applied to the bond stress values in the constitutive bond slip relationships adopted in the model, associated with bar yielding. Eligehausen *et al*. (1983) states that when a deformed reinforcing bar yields in tension, the bond stresses acting on the bar are reduced, since the diameter of the bar rapidly decreases, due to Poisson's effects, after yielding in tension. The opposite was also stated to be true, for a reinforcing bar yielding in compression. However, the Poisson's effect on bond stresses was not considered in the original hysteretic constitutive bond stress vs. slip model developed by Eligehausen *et al*. (1983), and was therefore not adopted in the present analytical model study. Such an improvement in the constitutive bond slip relationship may improve the analysis results and lateral load capacity predictions for these column specimens.

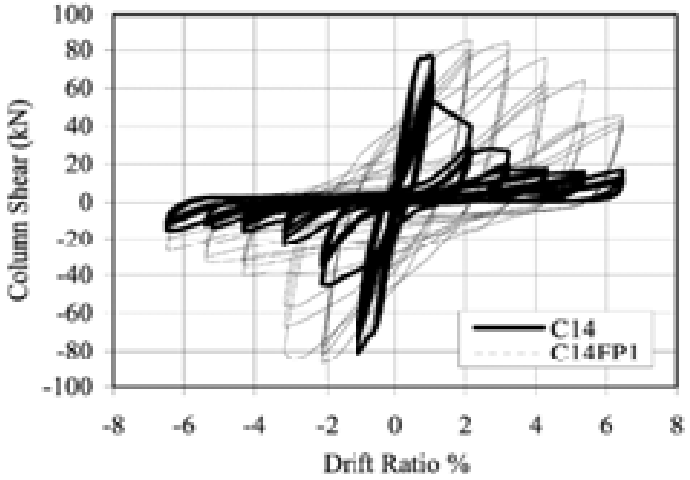

Figure 8.21. Experimental Response of Specimen C14 (Harajli and Dagher, 2008).

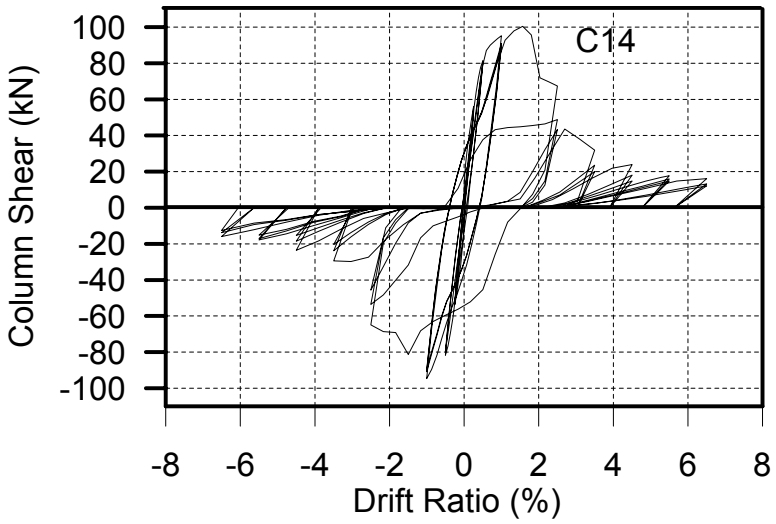

Figure 8.22. Analytical Response of Specimen C14.

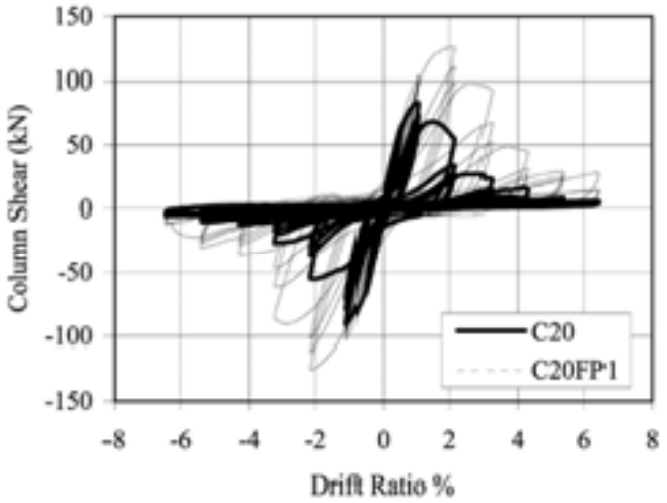

Figure 8.23. Experimental Response of Specimen C20 (Harajli and Dagher, 2008).

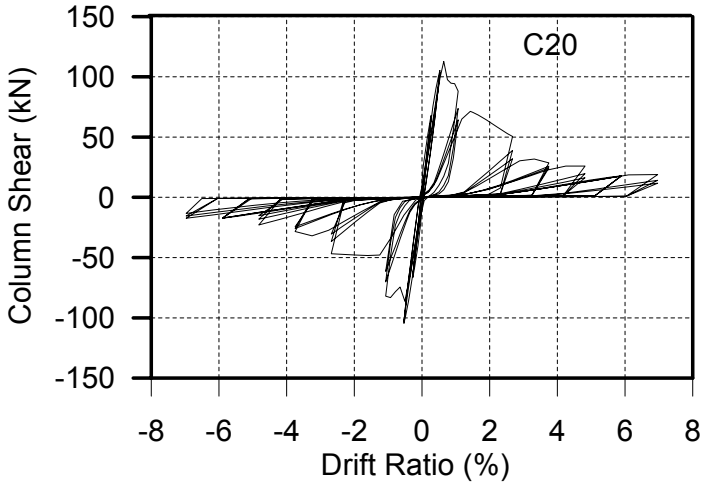

Figure 8.24. Analytical Response of Specimen C20.

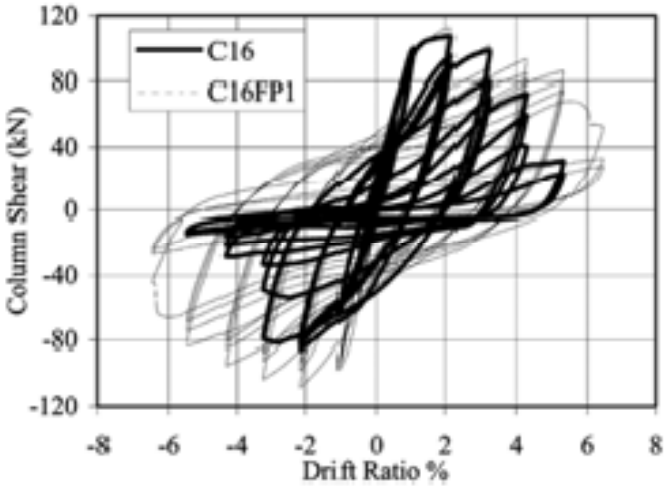

Figure 8.25. Experimental Response of Specimen C16 (Harajli and Dagher, 2008).

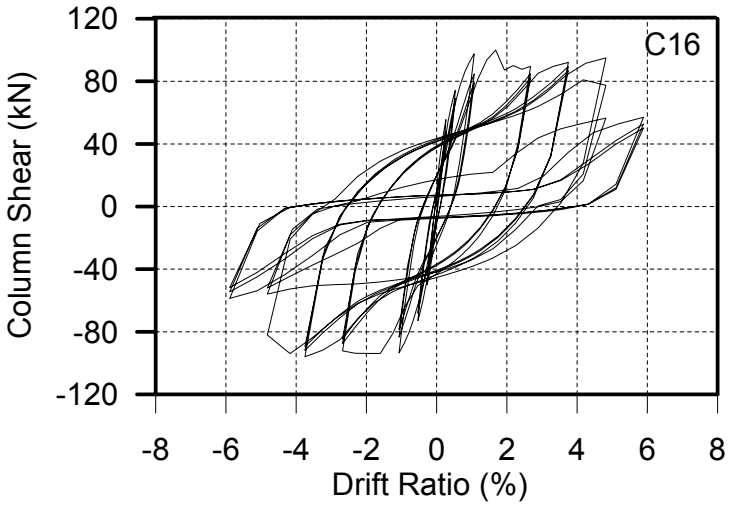

Figure 8.26. Analytical Response of Specimen C16.

8.4.5. Elgawady *et al*. (2010) Specimen:

Elgawady *et al*. (2010) investigated the cyclic behavior of eight 4/10-scale reinforced concrete column specimens representing the properties of columns in existing bridges constructed in the state of Washington prior to 1971. All specimens were tested under constant axial load and incrementally increasing lateral loading cycles. Two modes of failure were observed for the column specimens, which are low-cycle fatigue failure of longitudinal reinforcement and slip failure of the lap splice. In the column specimens, longitudinal bars were lap spliced (over a length of 35 bar diameter), at the base of the column with the starter bars extending from the foundation. Column specimens had a height of 2.03 m and a cross section of 254 mm x 381 mm. All specimens had an approximate longitudinal reinforcement ratio of 1.2%, provided with 12.5 mm – diameter deformed rebars, and 6.3 – mm diameter smooth mild steel ties at 125 mm spacing as transverse reinforcement The specimens were subjected to reverse cyclic lateral loading, applied at 1803 mm from column base, with increasing levels of lateral displacements. The concrete of the specimens had an average compressive strength of 31 MPa, measured at the time of testing. A yield strength of 331 MPa was measured for the longitudinal reinforcement. Mild steel with a measured yield strength of 372 MPa was used for the transverse reinforcement. Details of the specimens are illustrated in Figure 8.27.

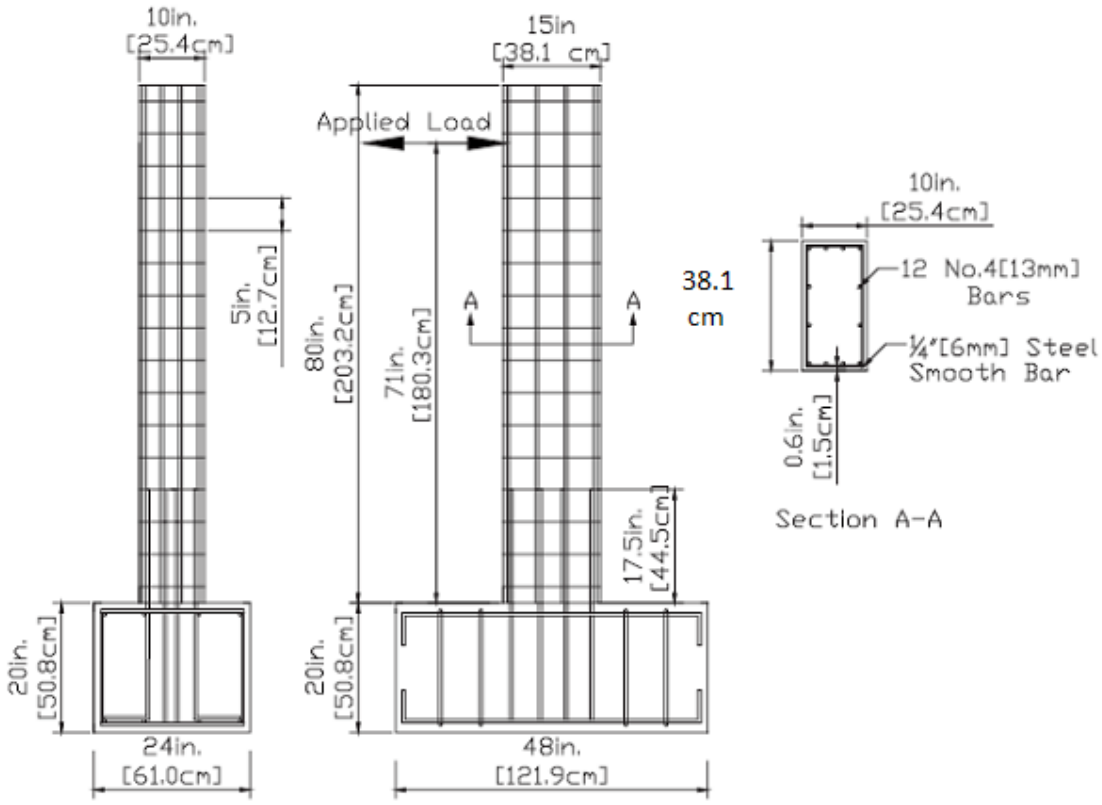

Figure 8.27. Typical Dimensions and Reinforcement for a Test Specimen (Elgawady *et al*., 2010).

Figure 8.28 shows the experimental lateral load – top displacement relationship of specimen AB1. During the test, the specimen ultimately failed due to low-cycle fatigue of the longitudinal reinforcement. At a drift ratio of 1.7%, spalling of the concrete cover and buckling of the longitudinal bars at the base of the column were initiated. During the last loading cycles, the longitudinal bars ruptured due to a low-cycle fatigue effects, leading to more than 20% drop in the lateral load capacity of the specimen. Figure 8.29 shows the analytical response prediction for the specimen AB1, obtained using the present model, considering tension stiffening effects on the response. The lateral load capacity of the column is accurately predicted by the model. Hysteretic characteristics of the response are also well-represented, except the last three cycles of loading where reinforcement buckling and low-cycle fatigue effects influence the experimental response. Therefore, the model predictions may be improved, upon incorporating buckling and low-cycle fatigue effects in the constitutive relationship adopted in the model for reinforcing steel.

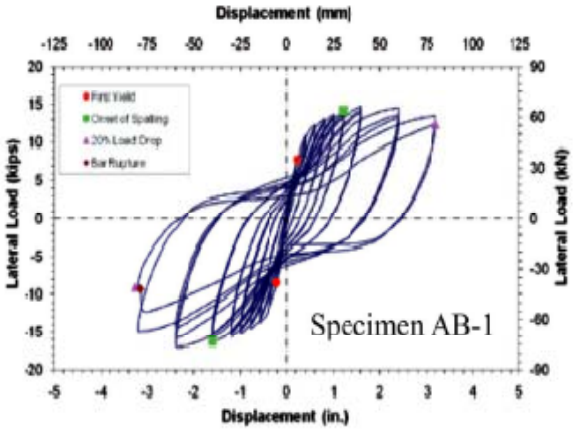

Figure 8.28. Experimental Response of Specimen AB-1 (Elgawady *et al*., 2010).

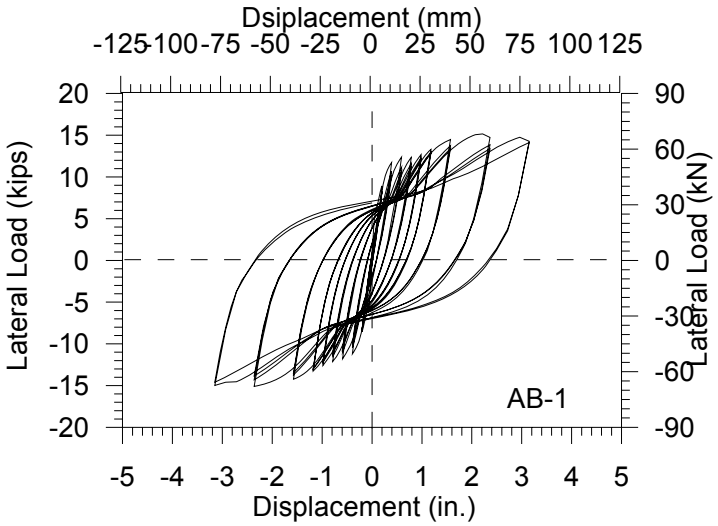

Figure 8.29. Analytical Response of Specimen AB-1.

8.4.6. Lynn *et al*. (1996) Specimen:

Lynn *et al*. (1996) conducted tests on eight full-scale column specimens representing typical detailing used in the United States prior to the 1970s. The specimens were subjected to reversed cyclic lateral displacements, while the axial load was held constant for the duration of the test, at a level corresponding to approximately 12% of the axial load capacity of the columns. Observed failure modes included localized crushing of concrete, buckling of reinforcement, splitting bond failure at the lap splice, shear failure, and axial load collapse. One of the specimens, labeled as 2SLH18 (Figure 8.30), incorporated a lap splice at the base. The lap splice length corresponded to 20 longitudinal bar diameters. The specimen had a clear height of 2946 mm, and a 457.2 mm – square cross-section. A clear cover of 50 mm was used. Figure 8.30 shows the reinforcement details of the specimen and the loading used to impose zero top rotation and double – curvature bending moments on the specimen. Lateral loads were applied by an actuator attached horizontally between the loading frame and the reaction frame, with the loading axis passing through the column mid-height. The vertical actuators were controlled to maintain constant axial load zero rotation at the top of the column.

Comparing the experimental and analytical responses presented in Figures 8.31 and 8.32, it is observed that the model predicts the response features of the specimen, except the degradation in the lateral load for larger drift levels. During testing, the specimen exhibited considerable flexural deformation before failure, associated with yielding of the longitudinal bars. Since the response of this specimen was not dominated by bond slip failure of the lap splice, the analytical model incorporating tension stiffening effects provided a better prediction of the behavior. During the test, considerable damage was observed in the splice region due to combined flexural and shear deformations. The analytical model does not capture the lateral load degradation in the later loading cycles, since it does not incorporate a robust approach to simulate nonlinear shear deformations through coupling of inelastic flexural and shear responses. This may also be the reason why the hysteretic loops in the analytical response are somewhat wider. Using an improved modeling methodology to simulate nonlinear shear responses and shear – flexure interaction effects may improve the model predictions for such a type of failure mode.

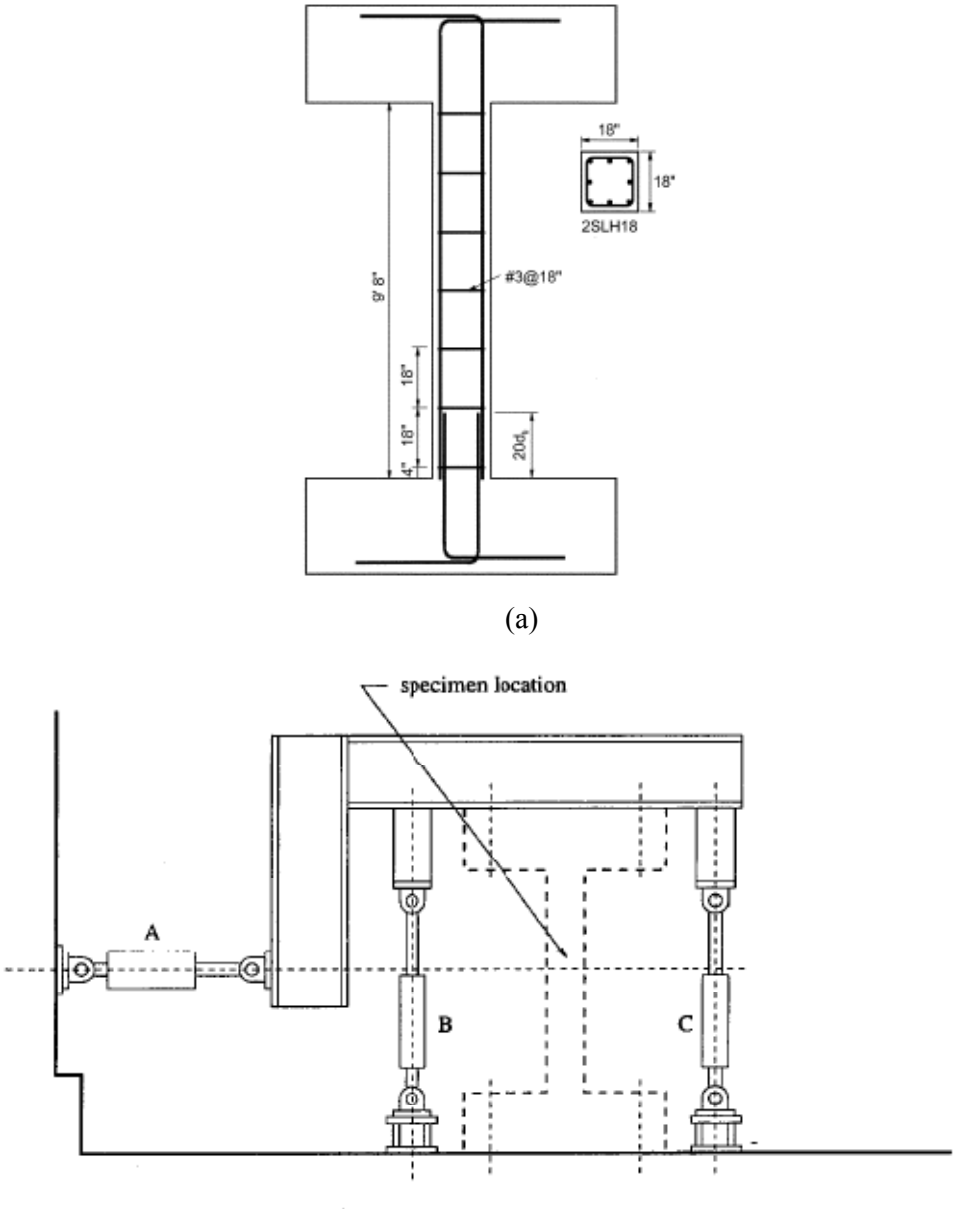

Figure 8.30. (a) Column Details (b) Loading assembly (Lynn *et al*., 1996).

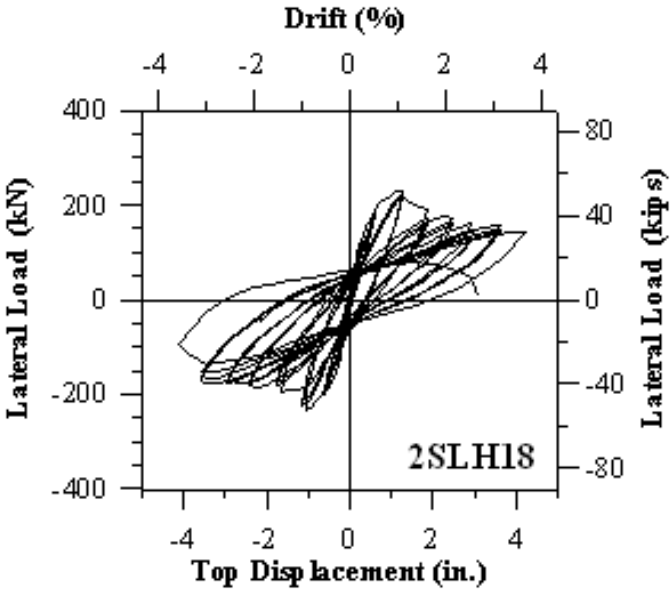

Figure 8.31. Experimental Response of Specimen 2SLH18 (Lynn *et al*. ,1996).

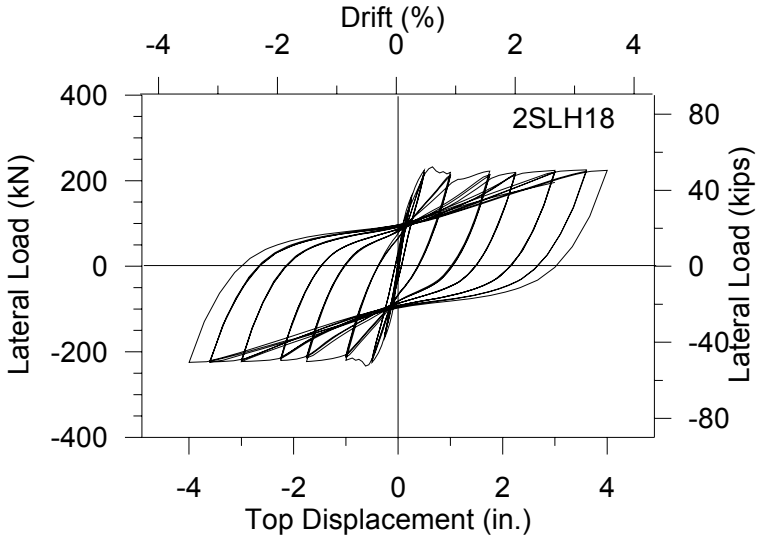

Figure 8.32. Analytical Response of Specimen 2SLH18, Considering Tension Stiffening.

8.4.7. Harries *et al*. (2006) Specimen:

The full scale column specimen, 'L0' (Figure 8.33), tested by of Harries *et al*. (2006), incorporated a 22 bar diameter lap splice length, and was tested under combined axial and cyclic lateral loads. The column specimen was initially designed so that the lap splice would cause bond slip failure prior to achieving the flexural capacity of the column. The column specimens had 458 mm square cross sections with eight 22 mm – diameter longitudinal reinforcing bars. 9.5 mm – diameter ties with 356 mm spacing were located over a height of 1780 mm from the base of the column. These ties incorporated deficient 90-degree hooks. The axial load level applied during testing was approximately 25% of the column axial load capacity, and was maintained constant throughout the cyclic lateral load history, using a regulated system of hydraulic rams. The reversed cyclic lateral loads were applied to the column specimen at a height of 2440 mm, which was selected to ensure a sufficiently high moment-to-shear ratio to result in flexure-dominated column behavior. The columns were tested as cantilevers with the lateral loads applied at the top, approximately representing the half the height of an actual column in a building frame, for which the point of inflection is located at the mid-height. Three loading cycles were at each load level corresponding to 1/3 and 2/3 of the expected flexural yield capacity, followed by three cycles at each lateral displacement level corresponding to 1.0, 1.5, 2.0, 2.5, 3.0, 4.0, 5.0, 6.0, 7.0, 8.0, and 10.0 times the expected yield displacement.

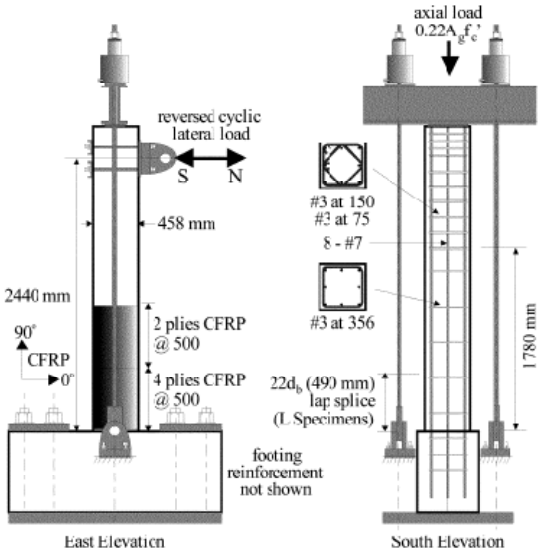

Figure 8.33. Column Reinforcement Details and Test Setup (Harries *et al*., 2006).

Figures 8.34 and 8.35 respectively show the experimental and analytical responses for the specimen, both of which are which are typical of columns having splice lengths insufficient to develop the yield strength of the longitudinal bars. In test, at 36 mm lateral displacement, (for which the lateral load capacity of 190 kN was recorded), the longitudinal cracks in the lap splice region widened and crushing of the concrete at the base of the column was observed. Widening of the longitudinal cracks indicated sudden slip deformation along the splice. Failure was ultimately characterized by significant widening of the vertical splitting cracks in the lap splice region, together with crushing of concrete. Overall, the analytical response prediction is in good agreement with the observed behavior. The lateral load capacity, hysteretic properties, and pinching characteristics of the response are all captured by the analytical model, with reasonable accuracy.

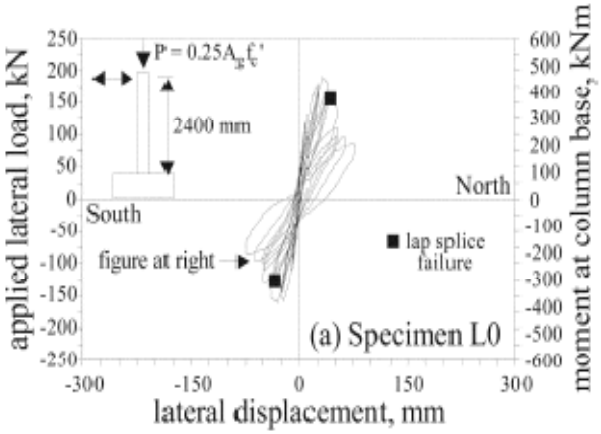

Figure 8.34. Experimental Response of Specimens L0 (Harries *et al*., 2006).

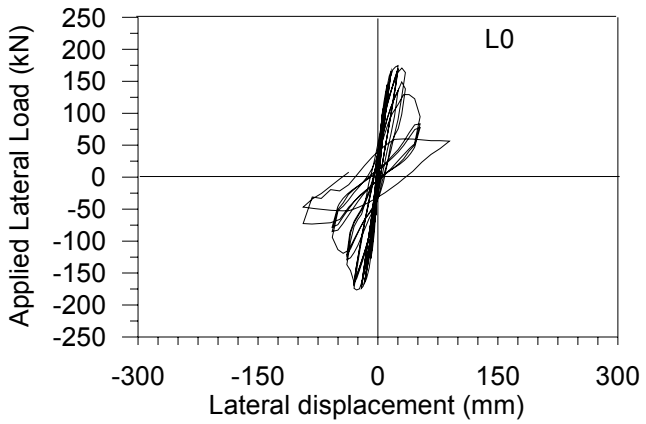

Figure 8.35. Analytical Response of Specimen L0, Considering Tension Stiffening.

8.4.8. Yildiz (2006) Test:

Yildiz (2006) conducted an experimental program on reinforced concrete columns with deficient detailing and low material quality, representing older non-ductile buildings in Turkey. Two of her specimens (Specimens AF(COG0)B1 and AF(COG0)B2) incorporated deficient lap splices, with splice lengths equal to 15 bar diameters, and were subjected to constant axial and reversed cyclic lateral loads. All test specimens were designed such that shear failure would be avoided. However, all specimens possessed inadequate confinement. Details of the specimens are presented in Table 8.1 and Figure 8.36.

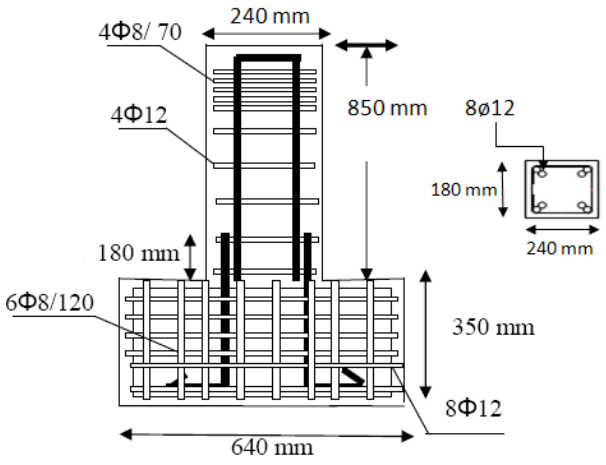

Figure 8.36. Column Reinforcement Details (Yildiz, 2006).

Figures 8.37 and 8.39 show the experimental responses measured respectively for specimens AF(COG0)B1 and AF(COG0)B2, whereas Figures 8.38 and 8.40 present the analytical response predictions for the respective specimens. In both analytical response predictions, the lateral load capacity of each specimen is overestimated by a small margin. Other response characteristics including the shape of the hysteresis rules, cyclic degradation in lateral load in the post-peak region of the response, lateral displacement at peak lateral load values, and pinching properties, are all well-represented in the analysis results.

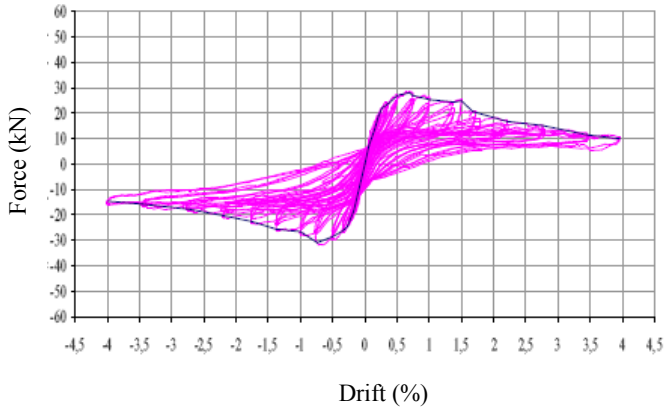

Figure 8.37. Experimental Response of Specimen AF (C0G0) B1 (Yildiz, 2006).

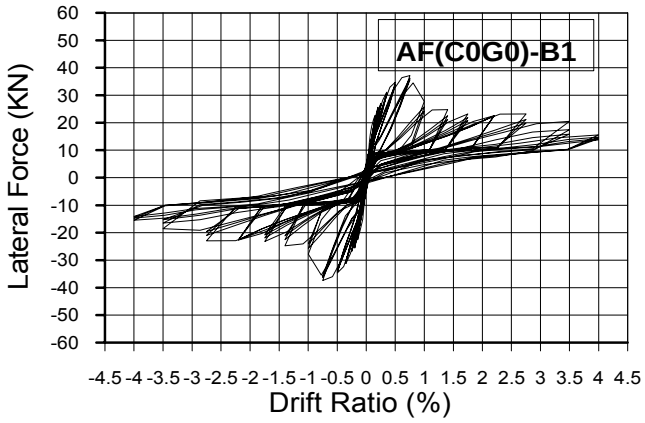

Figure 8.38. Analytical Response of Specimen AF (C0G0) B1.

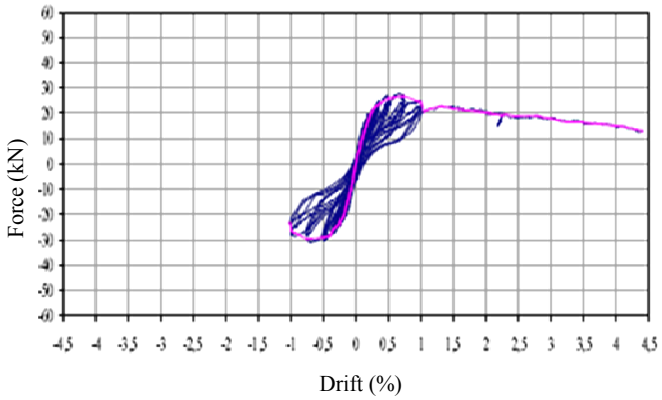

Figure 8.39. Experimental Response of Specimen AF (C0G0) B2 (Yildiz, 2006).

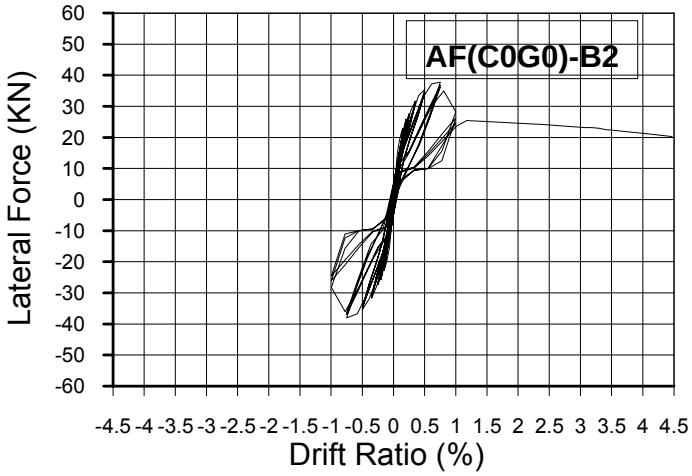

Figure 8.40. Analytical Response of Specimen AF (C0G0) B2.

8.4.9. Verderame *et al*. (2008) Test:

Verderame *et al*. (2008) conducted experiments on reinforced concrete column specimens incorporating with smooth reinforcing bars. Two types of specimens were considered, depending on the longitudinal reinforcement details at column base. Type A specimens had lap-spliced and hooked bars with 40 bar diameter long splice length (Figure 8.41(a)), whereas continuous longitudinal bars were provided for Type B specimens (Figure 8.41(b)). Two different levels of axial load (270 kN and 540 kN) were applied to represent the loading conditions of two columns in a prototype building. For the specimen types investigated in detail in the present study (C-270A1 and C-540A1 with lap splices and 180-degree hooks; C-270B1 and C-540B1 with continuous reinforcement), the specimens were 2000 mm high, with a 300 mm by 300 mm square cross-section. Longitudinal reinforcement consisted of six 12 mm – diameter smooth bars, while 8 mm – diameter ties were spaced at 100 mm spaced. Reinforcing steel was mild and ductile with a yielding stress of 355 MPa and ultimate stress of 470 MPa, with a fracture strain value of 0.27. Concrete used had a cylindrical compressive strength of approximately 25 MPa. Cyclic lateral loads were applied at a height of 1570 mm from the top of the specimen foundations. Maximum lateral displacements of ±100 mm were applied on the specimens, and the specimens were cycled three times at 15 target drift levels, as reported in Figure 8.41(c). Details of the test specimens are presented in Figure 8.41 and Table 8.1.

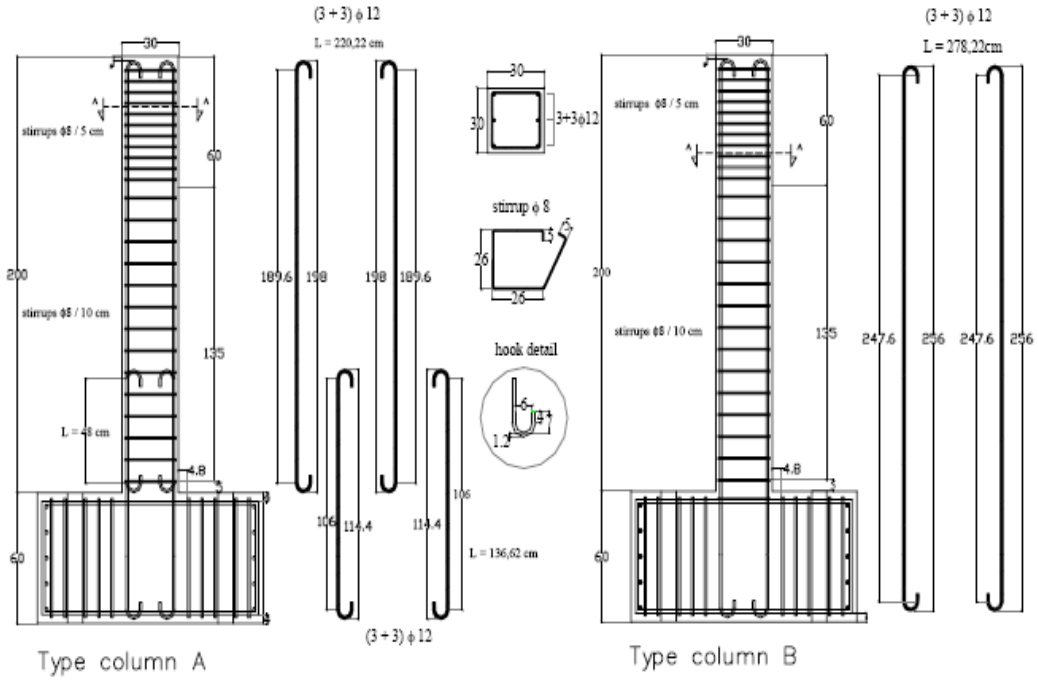

(a) (b)

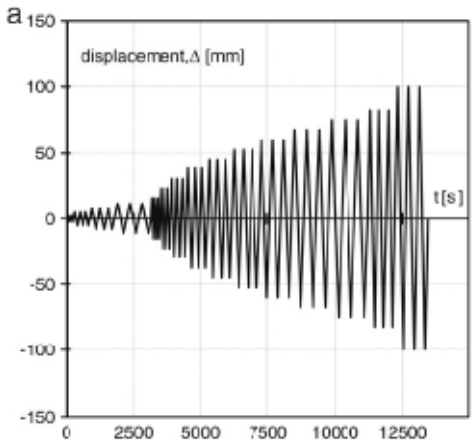

(c)

Figure 8.41. (a),(b) Geometry and Reinforcement Details of Column Specimens, (c) Lateral Load History (Verderame *et al*., 2008).

Figure 8.42 illustrates the experimental response measured for specimen, C270-A1, which shows a gradual lateral load degradation (due to progressive spalling of concrete) and pronounced pinching effects in the behavior. The experimental response of specimen C-270B1 is shown in Figure 8.46. For this specimen, apart from the overall gradual degradation in lateral load and moderate pinching behavior, the last drift cycle (±100 mm) is characterized by a further degradation of lateral load, related to buckling of the reinforcing bars on the compression side. Figure 8.48 and 8.52 displays the experimental response of specimens C- 540A1 and C-540B1, which also experienced gradual degradation in lateral load during the tests, due to progressive crushing and spalling of concrete. The failure mode of all of specimens was flexure – dominated, and splice failures were not observed for the specimens (C-270A1 and C-540A1) with deficient lap splices and hooks.

Experimental responses presented in Figures 8.42 and 8.46 indicate that the lateral load capacities measured for the specimen with the lap splice (C-270A1) and the specimen with continuous reinforcement (C-270B1), are similar in magnitude. This behavior is also observed in the analytical responses shown in Figures 8.43 and 8.47. The analyses of the results of Figures 8.43 and 8.47 are found assigning the hook springs connecting the bottom rigid beam of the second model element from column base, to the longitudinal bars in the splice. (to allow the uplift of the longitudinal bar hook from the column-pedestal interface). However, although the analytical model captures the lateral load capacities of the specimens, the gradual degradation of the lateral load capacity with increasing drift is not represented in the analysis results. As well, the experimental results (Figures 8.42 and 8.46) reveal that the specimen with the lap splice (C-270A1) experiences a more pronounced pinching behavior, compared to the specimen with continuous reinforcement (C-270B1). Such a tendency is not represented in the analytical responses (Figures 8.43 and 8.47).

For further investigation, Figures 8.44 and 8.50 present the analytical responses for the lap spliced specimens C-270A1 and C-540A1, under the condition that the hook springs of the longitudinal bars of the splice are assigned to the very first model element at the base of the column . In these analysis results, the lateral load capacities of the column

specimens are significantly overestimated, compared with the analytical responses obtained using the hook springs.

The lateral capacities measured during test were also similar for the spliced column specimen (C-540A1) and the specimen with continuous reinforcement (C-540B1), both subjected to high–level axial load (Figures 8.48 and 8.52). This behavior is also observed in the analytical responses shown in Figures 8.49 and 8.53. However, although the analytical model captures the lateral load capacities of the specimens, the gradual degradation of the lateral load capacity with increasing drift is again not represented in the analysis results.

Both the experimental and analytical responses indicate that the overall level of pinching in the response is influenced by the level of axial load, where higher axial load results in less pronounced pinching. As well, both the analytical and measured responses indicate that the lateral load capacity of each specimen is influenced by the level axial load, where the lateral load capacity increases with increased axial load level, for the specimens investigated. The analytical and experimental responses are also compatible in the sense that the analytical results obtained for the specimens with lap splices do not predict bond slip failure of the splice, due to the presence of the 180-degree hooks on the starter and longitudinal bars.

The discrepancies in the analytical model predictions may be recovered upon implementing realistic hysteretic rules in the bar stress vs. end slip deformation constitutive model for the 180-degree hook (which is not available in the literature), as well as incorporating the modifications to consider local buckling (as suggested by Prota *et al*. ,2009) in the constitutive stress – strain relationship of the reinforcing bars.

The constitutive relationship implemented in the analytical model for reinforcing steel (Menegotto and Pinto, 1973) may need to be improved to represent the behavior of plain bars, as suggested by Prota *et al*. (2009). Prota *et al*. (2009) proved that cyclic stress – strain behavior of plain bars is symmetric in tension and compression when the *L/D* ratio of the bar (L being the stirrup spacing and D being the longitudinal bar diameter) is smaller than 8, and that it becomes non-symmetrical due to buckling of the bar, as the *L/D* ratio

increases. Comparing the experimental stress – strain behavior of deformed and smooth bars investigated by Prota *et al*. (2009), it also appears that the shape of the hysteretic stress – strain loops may differ among deformed and plain bars. However, the differences diminish and the shape of the hysteretic loops become increasingly similar as *L/D* ratios increase. The *L/D* ratio of the smooth bars used in the column specimens of Verderame *et al*. (2008) is 8.33.

In the other extreme, if the hooks at the bottom of longitudinal bars are removed from the analytical model for the lap spliced specimens C-270A1 and C-540A1, the analytical responses would have been as presented in Figures 8.45 and 8.51, respectively, clearly identifying the necessity to include the hook springs in the analytical model formulation.

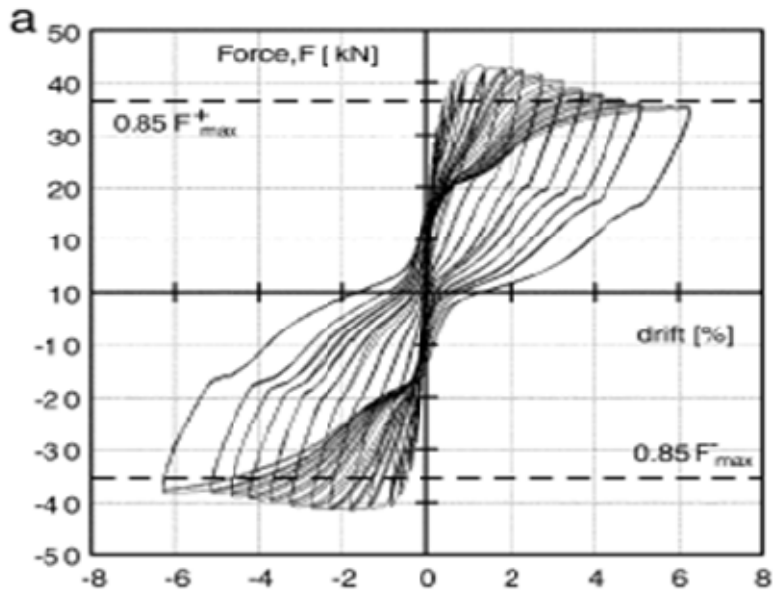

Figure 8.42. Experimental Response of Specimen C-270 A1 (Verderame *et al*., 2008).

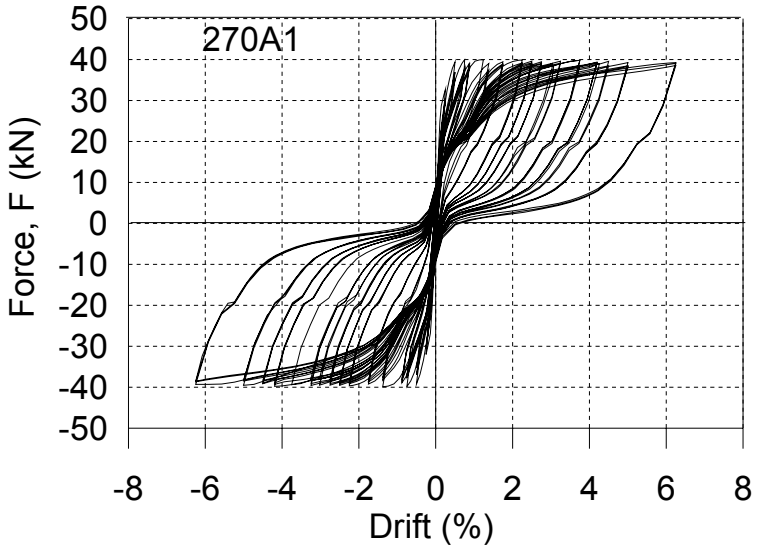

Figure 8.43. Analytical Response of Specimen C-270 A1.

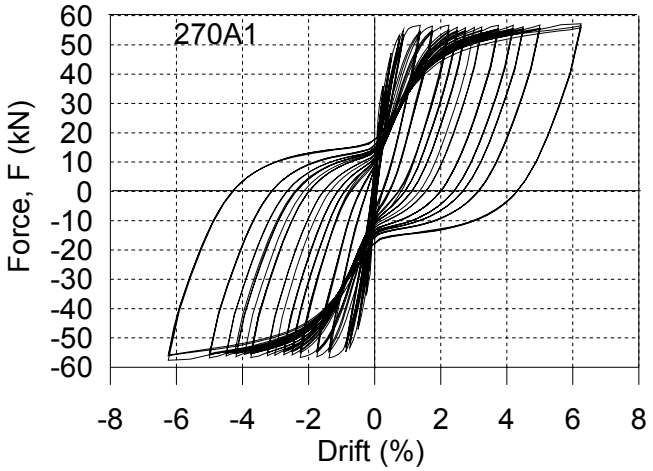

Figure 8.44. Analytical Response of Specimen C-270 A1, with Hook Asigned at the Base of the Column.

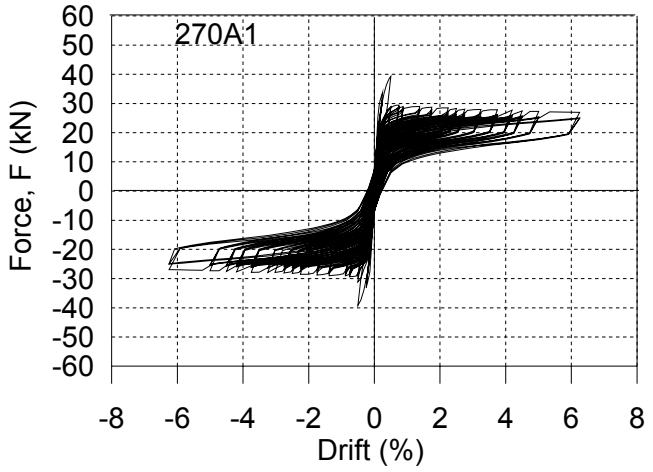

Figure 8.45. Analytical Response of Specimen C-270 A1, with no Hook at Column Base.

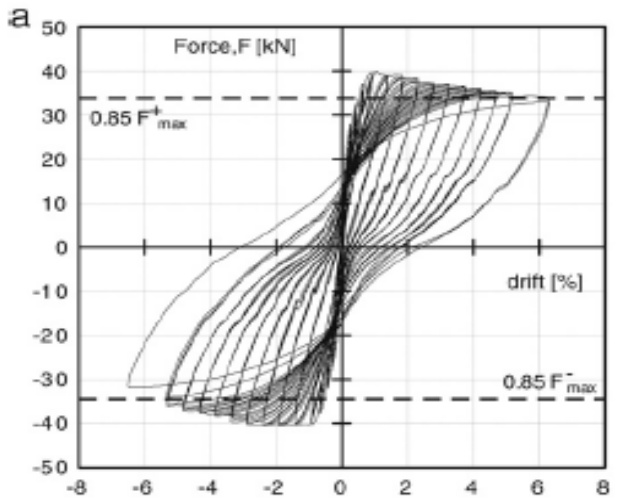

Figure 8.46. Experimental Response of Specimen C-270 B1 (Verderame *et al*., 2008).

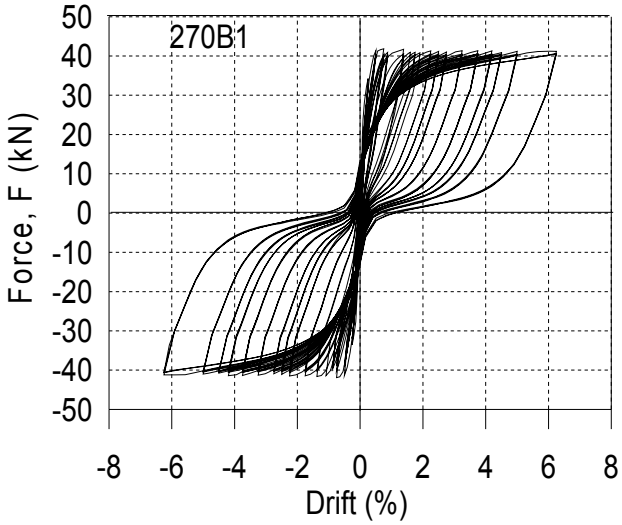

Figure 8.47. Analytical Response of Specimen C-270 B1.

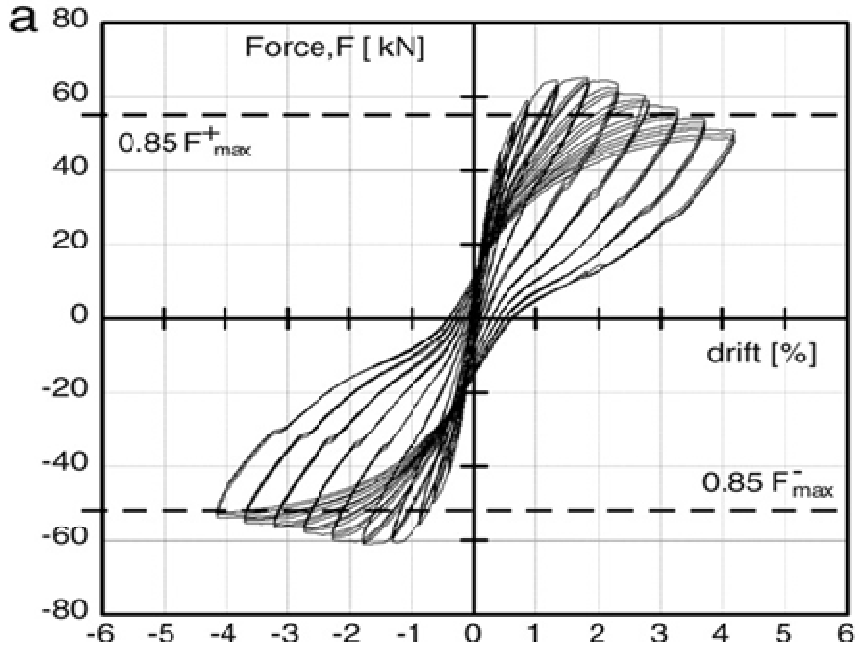

Figure 8.48. Experimental Response of Specimen C-540 A1 (Verderame *et al*., 2008).

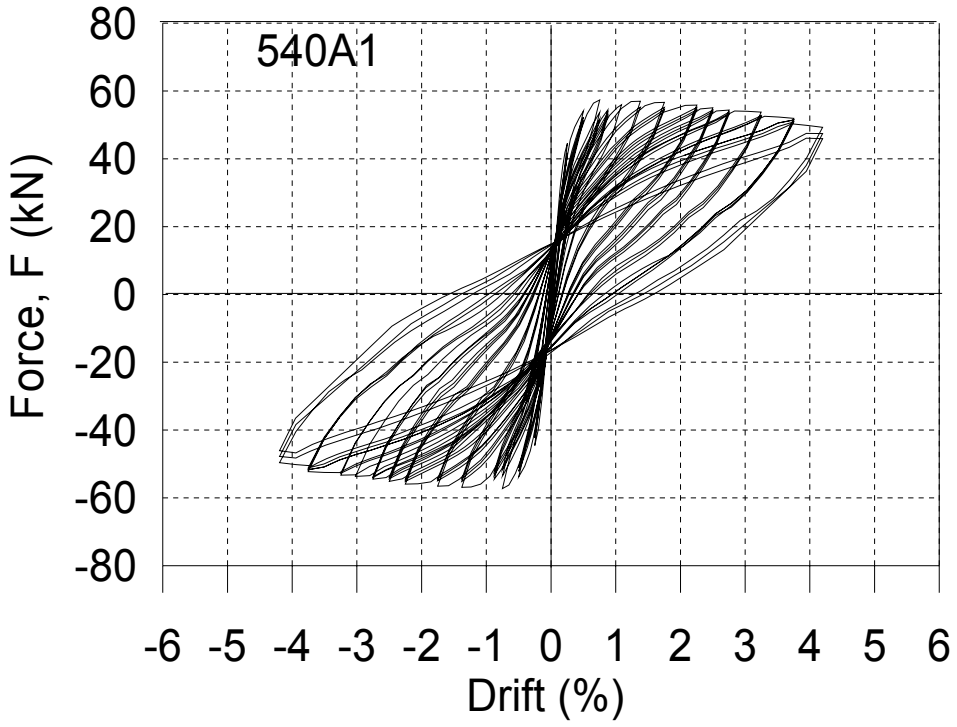

Figure 8.49. Analytical Response of Specimen C-540 A1.

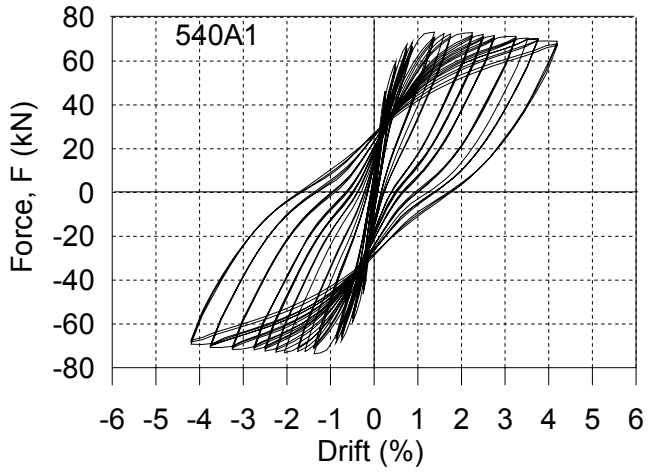

Figure 8.50. Analytical Response of Specimen C-540 A1, with Hook Asigned at the Base of the Column.

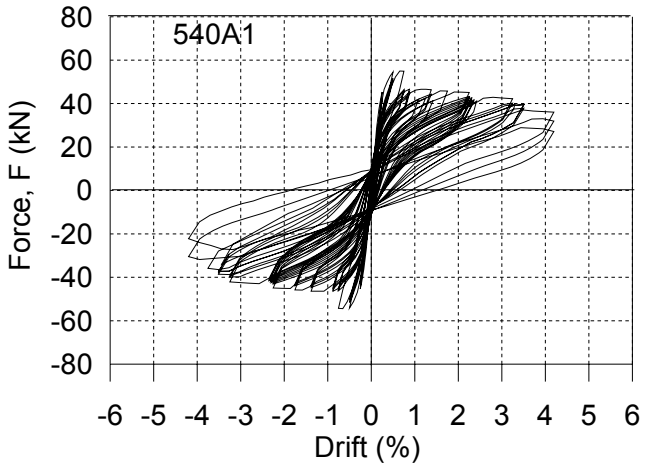

Figure 8.51. Analytical Response of Specimen C-540 A1, with no Hook at Column Base.

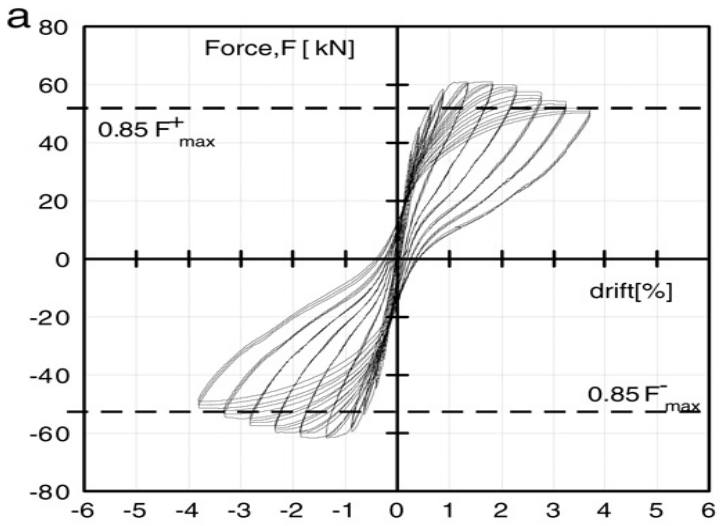

Figure 8.52. Experimental Response of Specimen C-540 B1 (Verderame *et al*., 2008).

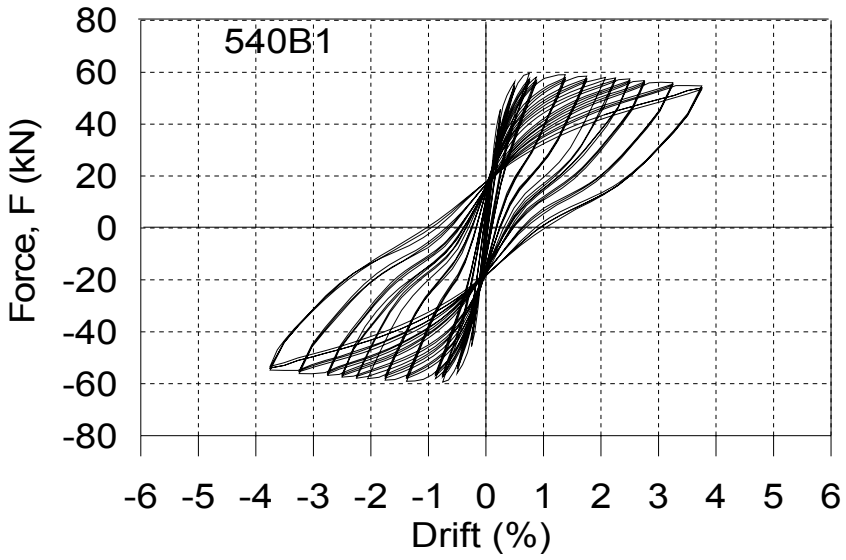

Figure 8.53. Analytical Response of Specimen C-540 B1.

8.4.10. Yilmaz (2009) Specimens:

Yilmaz (2009) investigated the effect of deficient lap splices with plain bars 180-degree hooks, as well as the influence of low concrete compressive strength on the lateral load behavior of reinforced concrete columns in typical poorly-constructed buildings in Turkey. In his experimental study, the column specimens incorporated 14 mm – diameter (φ) smooth longitudinal bars, 10 mm – diameter poorly detailed and wide-spaced ties, and an average concrete compressive strength of approximately 12 MPa. In construction of four specimens, different lap splice lengths (25φ, 35φ, 44φ, 55φ) were used, and one specimen incorporated continuous longitudinal reinforcement. The column specimens were tested under zero axial load and reversed-cyclic lateral loading. Figures 8.54, 8.55 and 8.56 present the isometric view, plan view and cross sectional views of a representative column specimen. The lateral drift history imposed on the specimens is presented in Figure 8.57. Figure 8.58 shows 28-day compressive stress strain relationships measured on cylindrical specimens of the concrete used in the construction of the specimens, Figure 8.59 illustrates the stress – strain test results conducted on samples of the 14-mm-diameter plain reinforcing bar. Average yield and ultimate stress values for the longitudinal reinforcement were reported as 285 Mpa and 440 MPa, respectively. Figures 8.60 and 8.61 illustrate the damage observed on specimens LS-44φ-N1 and LS-55φ-N1, respectively, at large drift levels. Details of the tests are described in the M.Sc. Thesis by Yilmaz (2009).

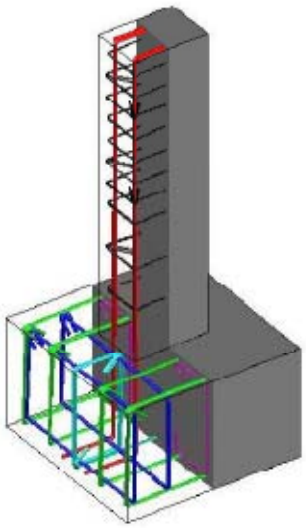

Figure 8.54. Typical Isometric View of a Specimen (Yilmaz, 2009).

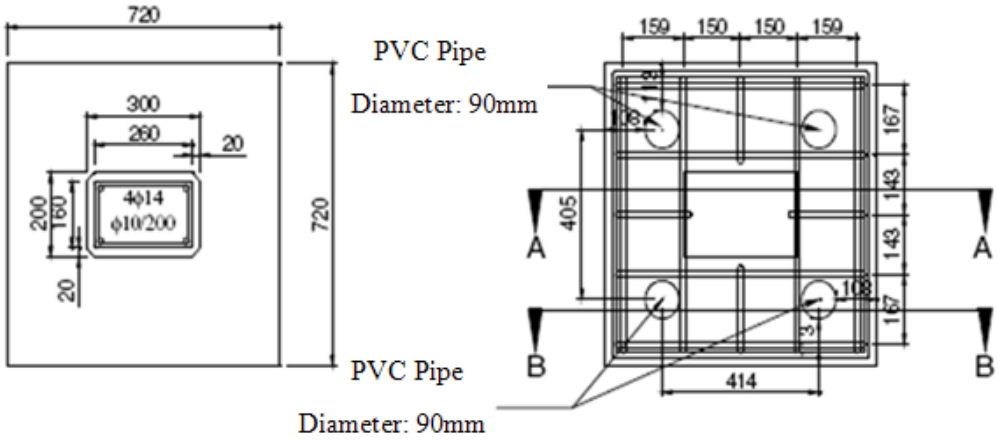

Figure 8.55. Typical Plan View of a Specimen (Yilmaz, 2009).

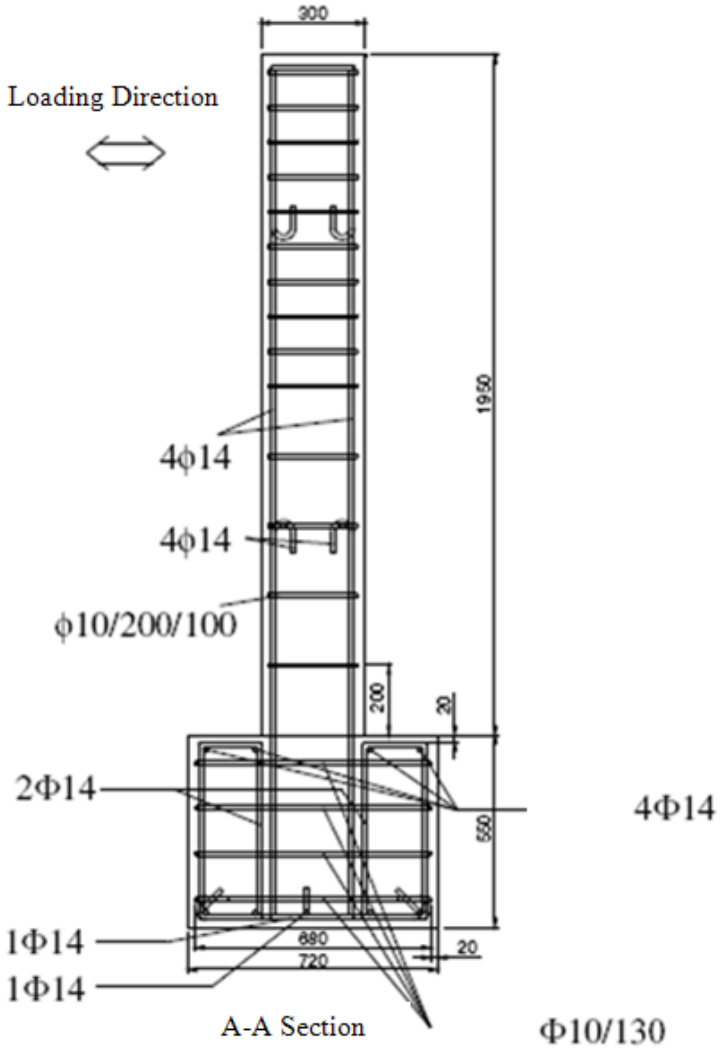

Figure 8.56. Reinforcement Layout (Yilmaz, 2009).

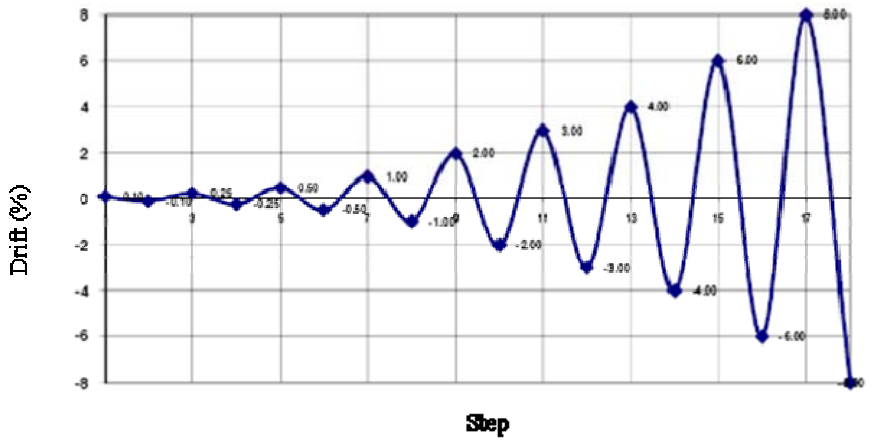

Figure 8.57. Imposed Lateral Drift History (Yilmaz, 2009).

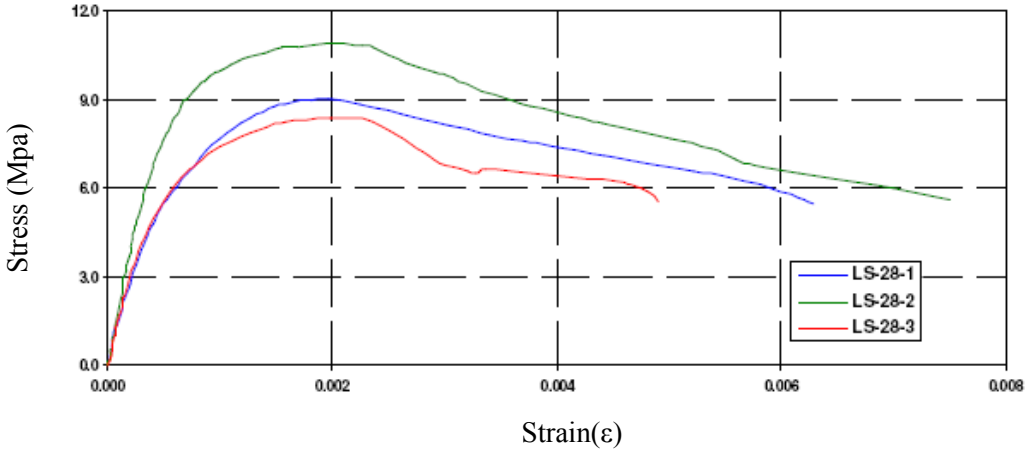

Figure 8.58. Measured Concrete Stress – strain Relationships (Yilmaz, 2009).

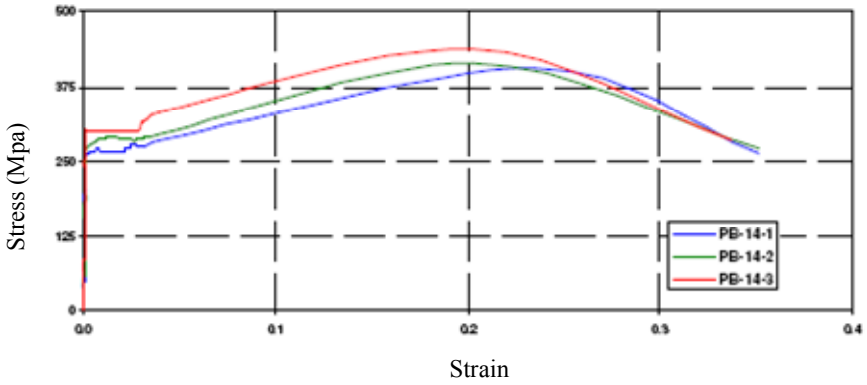

Figure 8.59. Measured Stress – strain Relationships for 14 mm Plain Bars (Yilmaz, 2009).

Figure 8.60. Damage at the Base of Specimen LS-44φ-N1 (Yilmaz, 2009).

Figure 8.61. Damage at the Base of Specimen LS-55φ-N1 (Yilmaz, 2009).

Figures 8.62, 8.64, 8.66, and 8.68 show the experimentally-measured lateral load – top displacement responses of the specimens with increasing lap splice lengths (LS-25φ-N1, LS-35φ-N1, LS-44φ-N1 and LS-55φ-N1), whereas Figure 8.70 displays the experimental response of the column specimen (LS-CON-N1) with continuous longitudinal reinforcement. In all of the five experimental responses, the lateral load capacities are similar. For the specimens with shorter lap splice lengths (LS-25φ-N1 and LS-35φ-N1), the responses exhibit degradation in the lateral load after the peak value is reached, as well as moderate-level pinching behaviour after lateral load degradation initiates. Cyclic behaviour of the other two specimens with lap splices (LS-44φ-N1 and LS-55φ-N1) are very similar to each other, with no degradation in the lateral load after the peak. The hysteretic unloading/reloading loops are progressively wider, and pinching characteristics diminish, as the lap splice length of the specimens increase. General response characteristics of the specimen with continuous longitudinal reinforcement (LS-CON-N1) are similar to those of the specimen with 55-bar-diameter long lap splice (LS-55φ-N1)

The analytical response predictions obtained using the present model (with hook springs incorporated) for all of the five specimens testes, are shown in Figures 8.63, 8.65, 8.67, 8.69 and 8.71. The predicted lateral load capacities of the specimens are similar to each other and reasonably close to the experimentally-measured capacities. In fact, the

analytical responses obtained for the 4 specimens with various lap splice lengths are practically identical.

The analytical model is incapable of capturing the hysteretic properties of the experimentally–measured responses of the lap-spliced specimens, due to the absence of realistic hysteretic rules in the bar stress vs. hook end slip constitutive model for the 180-degree hooks. As well, the degradation in lateral load, observed in the experimental responses is not captured by the analytical model, possible due to the lack of consideration of local buckling (as suggested by Prota *et al*., 2009) in the constitutive stress – strain relationship of reinforcing bars. The stirrup-spacing-to-bar-diameter (*L/D*) ratio of these specimens is approximately 14 (larger than 8), indicating that bar buckling effects can be pronounced for these specimens, as suggested by Prota *et al*. (2009).

Figure 8.72 presents the analytical response obtained for the lap-spliced specimens LS-25ø-N1, under the condition that the hook springs of the longitudinal bars of the splice are assigned to the very first model element at the base of the column. In this analysis result, the lateral load capacity of the column specimens is significantly overestimated, similarly to the case for the specimens tested by Verderame *et al*. (2008).

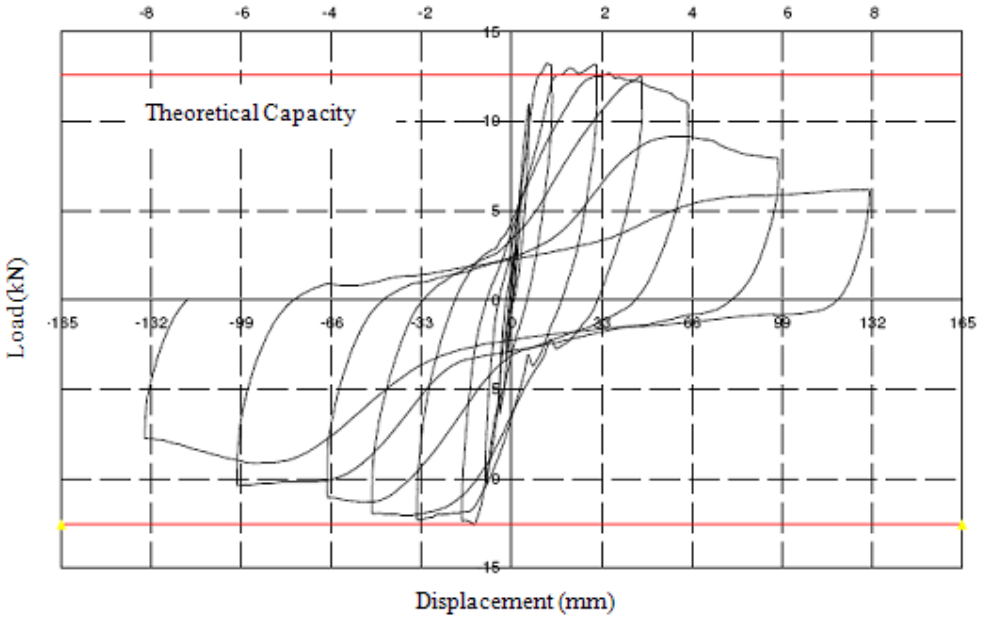

Figure 8.62. Experimental Response of Specimen LS-25ø-N1 (Yilmaz, 2009).

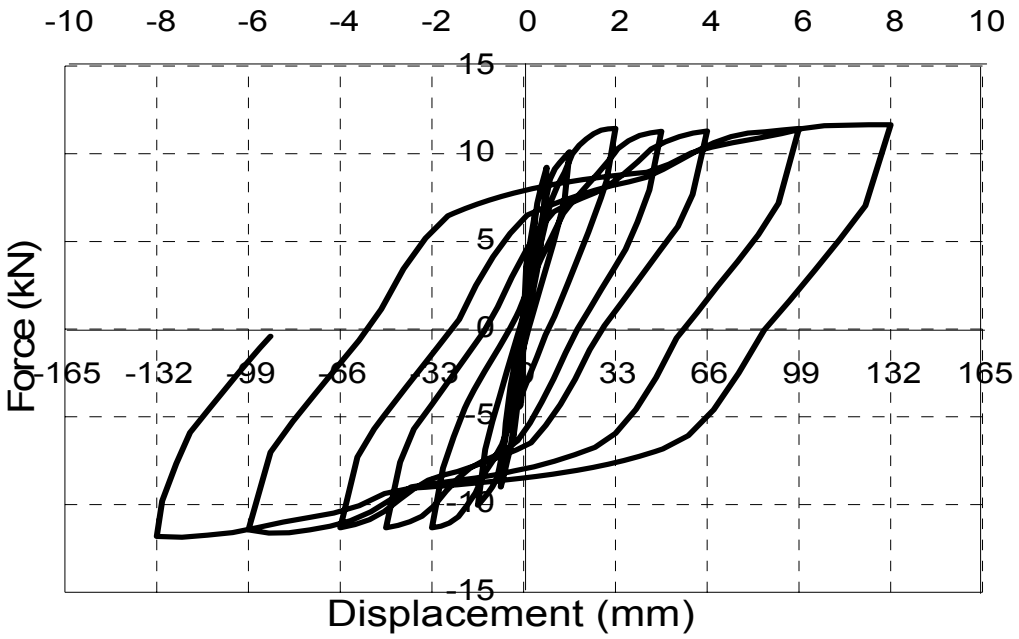

Figure 8.63. Analytical Response of Specimen LS-25ø-N1.

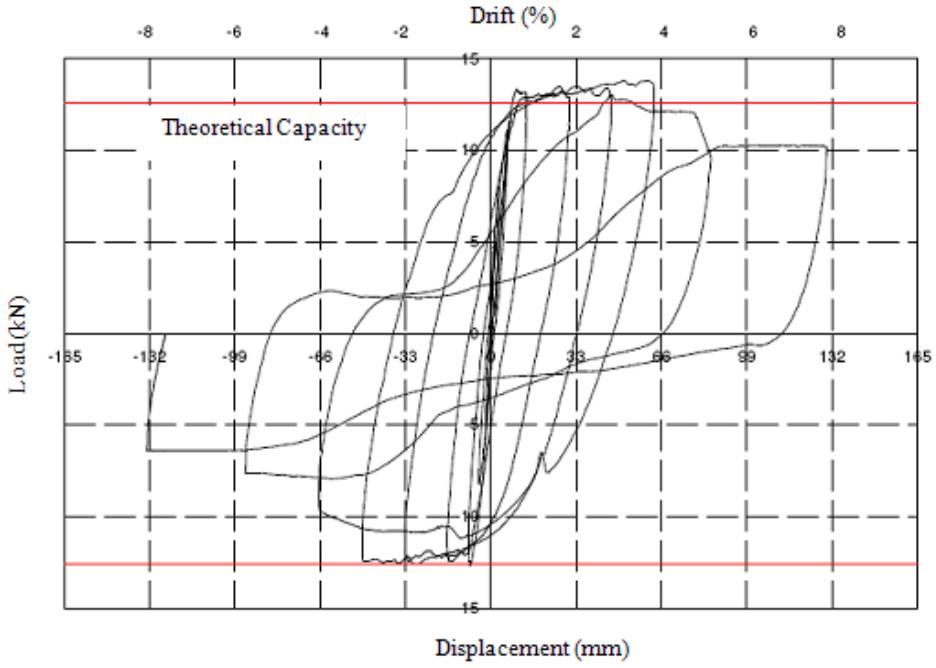

Figure 8.64. Experimental Response of Specimen LS-35ø-N1, (Yilmaz, 2009).

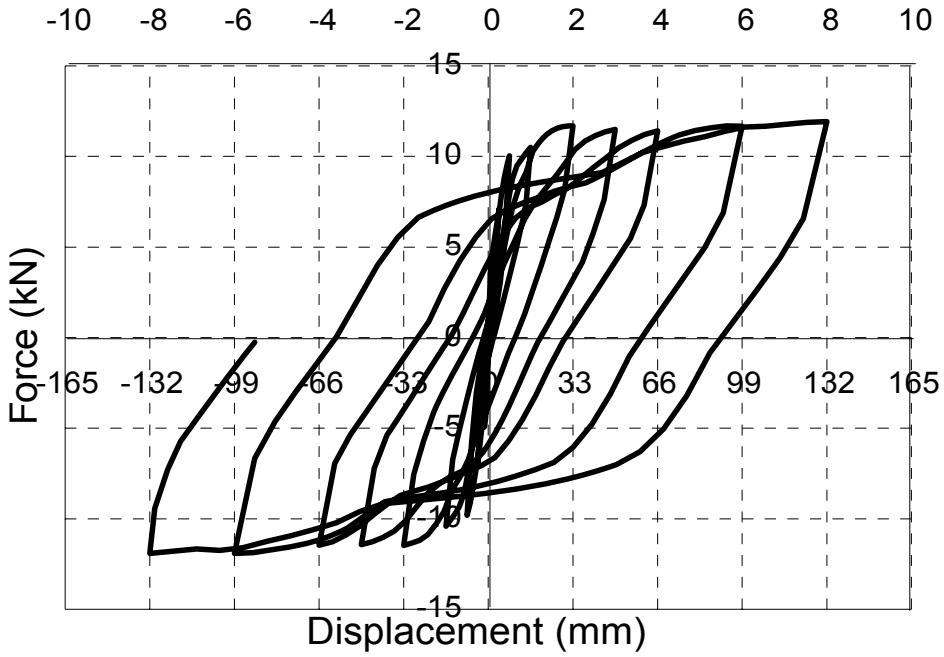

Figure 8.65. Analytical Response of Specimen LS-35ø-N1.

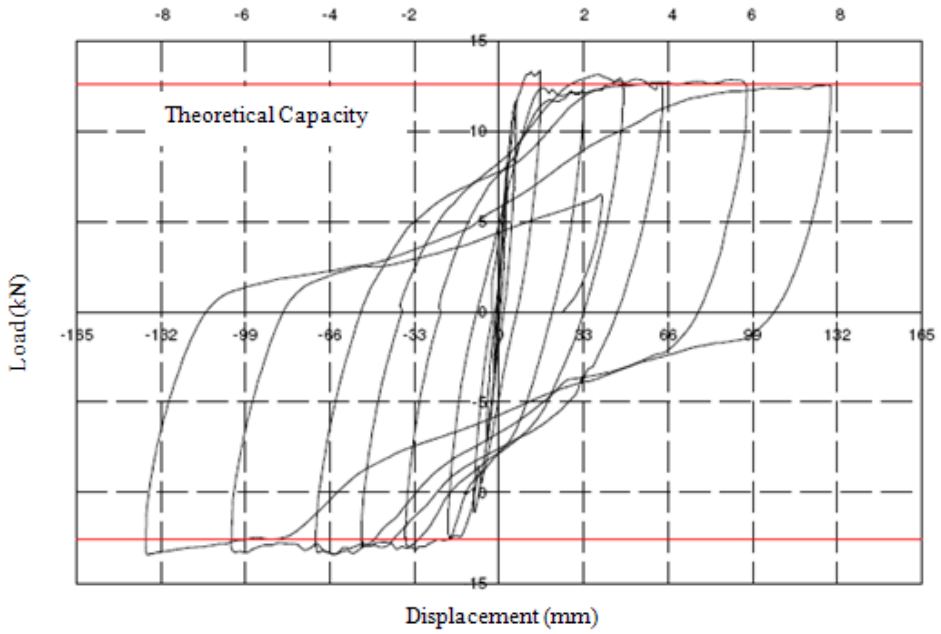

Figure 8.66. Experimental Response of Specimen LS-44ø-N1 (Yilmaz, 2009).

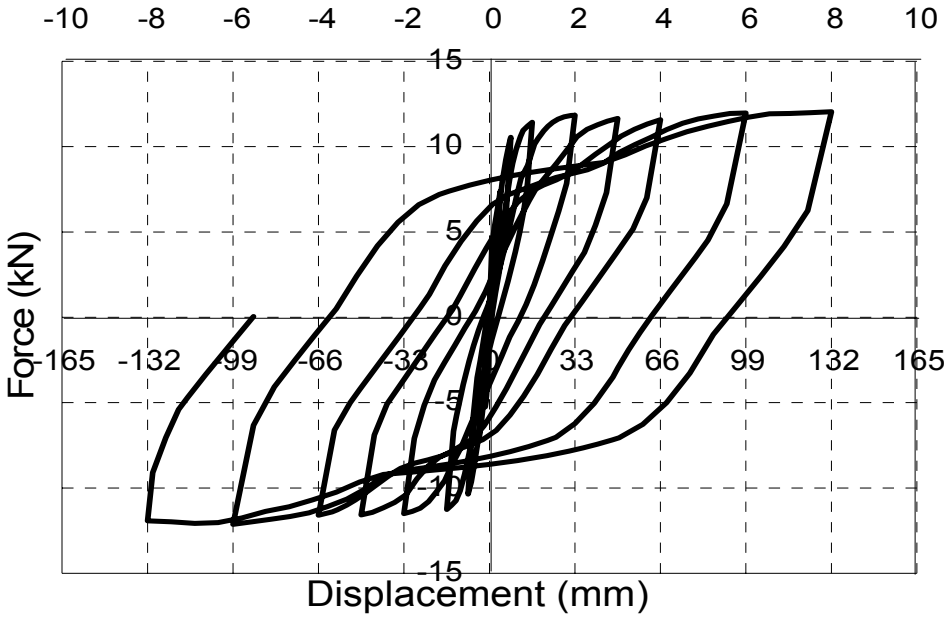

Figure 8.67. Analytical Response of Specimen LS-44ø-N1.

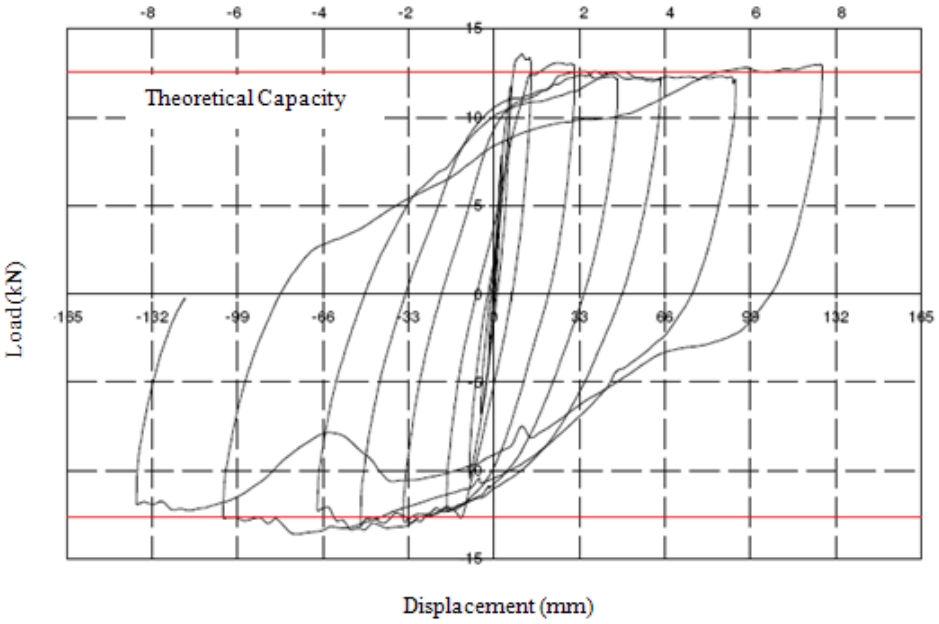

Figure 8.68. Experimental Response of Specimen LS-55ø-N1 (Yilmaz, 2009).

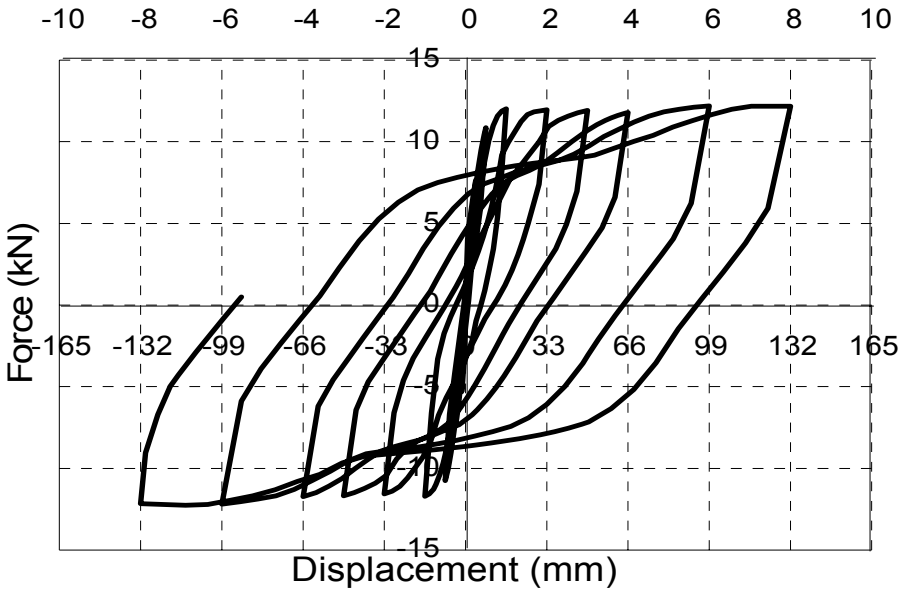

Figure 8.69. Analytical Response of Specimen LS-55ø-N1.

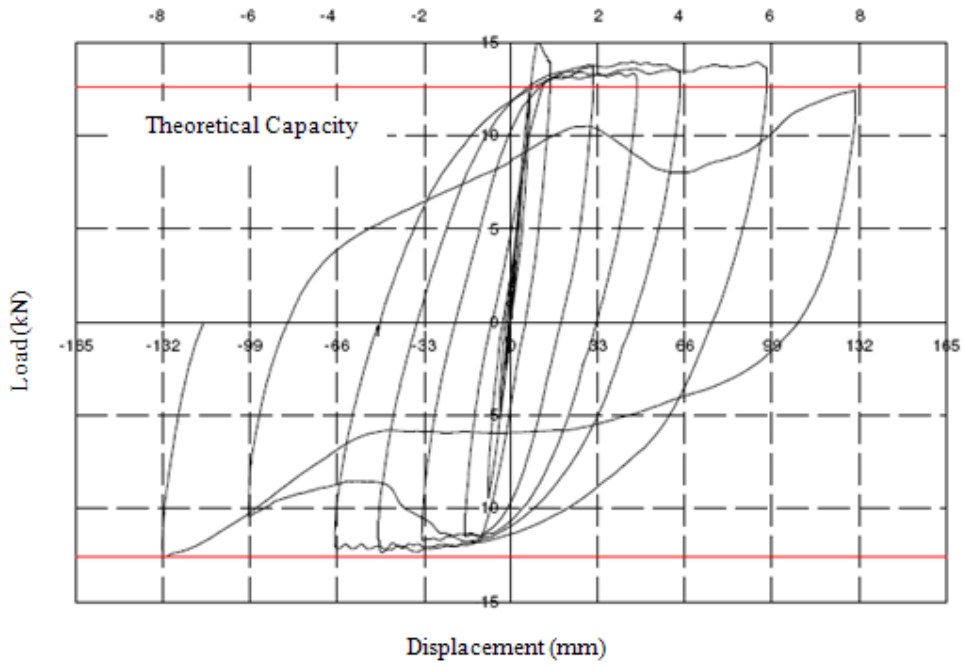

Figure 8.70. Experimental Response of Specimen LS-CON-N1 (Yilmaz, 2009).

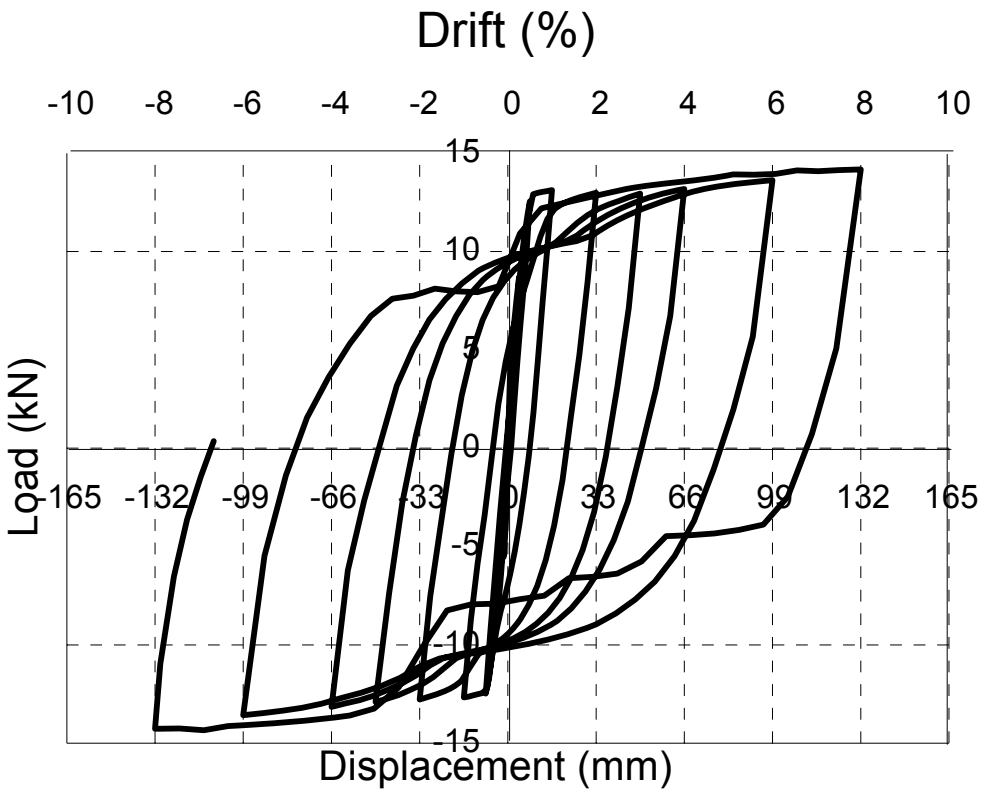

Figure 8.71. Analytical Response of Specimen LS-CON-N1.

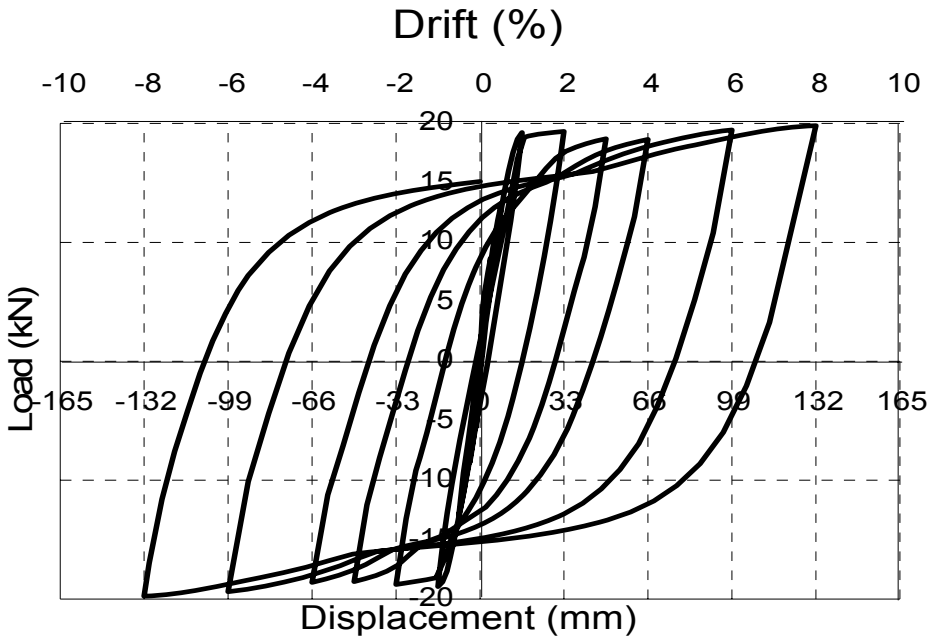

Figure 8.72. Analytical Response of Specimen LS-25ø-N1 with Hook Asigned at the Base of the Column.

9. SUMMARY AND CONCLUSIONS

The objective of this study was to develop a more robust and refined modeling approach to simulate the bond-slip responses observed in reinforced concrete columns under reversed cyclic loading. The proposed modeling methodology involves modifying the formulation of a fiber-based flexural model (i.e., the Multiple Vertical Line Element Model), with the fibers representing the hysteretic flexural behavior of concrete only. Reinforcing bar elements, with uniaxial hysteretic stress–strain relationships of their own, are connected to the concrete fibers through uniaxial bond slip springs, the behavior of which are represented with experimentally-derived hysteretic bond stress vs. slip constitutive relationships available in the literature for the splitting and pullout-type bond slip behavior of both deformed and smooth reinforcing bars, as well as for 180-degree hooks. Through this methodology, local bond slip behavior is incorporated at the fiber level, and full coupling of flexural and bond slip deformations of the model is retained under reversed cyclic loading conditions.

9.1. Model Capabilities and Characteristics

It is verified that the analytical model proposed captures important response characteristics associated with the cyclic behavior of reinforced concrete columns with lap splices, the response of which is governed by either bond slip, flexure, or a coupled combination thereof. The analytical model is capable of directly incorporating important behavioral features in the analysis, including shifting of the neutral axis along the column cross-section, the distribution of bond stresses and slip deformations in the starter and longitudinal bars along the lap splice, and the direct effect of axial force (constant and fluctuating) on the analytical response, which are commonly ignored in simple models. Characteristics of the cyclic response, including stiffness degradation, and strength degradation, and hysteretic shape are clearly captured in the analysis results. Degradation of lateral load capacity due to slip failure and the preceding pinched response are also clearly represented. The model allows monitoring of local responses including longitudinal strains and stresses in concrete and reinforcing steel, as well as bond stresses and slip deformations at any location on the column. Local rotations, strain profiles, and neutral

axis locations, and bond stress distributions along either longitudinal or starter splice bars can also be obtained using the analytical model proposed.

It is observed that the model global response is not significantly sensitive to model parameters including the number of model elements over the height of a column or the number of concrete macro-fibers along the width of the cross-section, as long as a reasonable number of model elements and macro-fibers are used in the construction of the model. However, finer discretization of the model provides improved local response predictions.

9.2. Model Correlation with Detailed Test Data for Specific Column Types

The analytical model was shown to be very effective in predicting the cyclic behavior of the column specimens investigated in the experimental program by Melek (2006), conducted on six reinforced column specimens incorporating deformed reinforcing bars and deficient lap splices. The model provides accurate predictions of global response characteristics including the lateral load capacity, strength degradation, stiffness degradation, ductility, pinching properties, and other cyclic attributes of the lateral load vs. top displacement behavior. Rotations due to flexure and slip at different locations of the column specimens are also well-predicted by the analytical model. Local response and deformation predictions of the model (steel strain distributions, concrete strain profiles, neutral axis position, and average bond stresses along the lap splice) are also representative of the experimental measurements, with a reasonable level of accuracy.

9.3. Model Correlation with General Test Observations for Various Column Types

Global (lateral load–displacement) response predictions obtained using the analytical model were also compared with additional experimental observations available in the literature, for various column specimens with both deformed and plain reinforcing bars, and with both deficient lap splices and continuous longitudinal reinforcement. Overall, the correlation studies conducted further verified that the model can effectively reflect the global response characteristics and failure modes of various column configurations incorporating either deficient lap splices or anchorage-deficient continuous reinforcement.

Bond-slip behavior may depends on scale of specimen. All column specimens (24 column specimens from 10 researchers and 6 detailed column tests from Melek, 2006) except one selected for this study were full-scaled column. Scaling effects are not expcted to influence the experimental behavior of the specimens or the correlation of model results with the experimental results.

The model was shown to accurately represent the influence of bond slip deformations in the anchorage zone (strain penetration effects) on the global cyclic response and pinching characteristics of columns with continuous longitudinal reinforcement.

The coupled flexural yielding and bond slip response observed in some of the lap-spliced columns investigated, were better-represented by the analytical model when pullout springs were used in combination with splitting springs (where pullout spring are assigned in the vicinity of the ties), and the effects of tension stiffening on reinforcing steel behavior were considered. Nevertheless, the analytical model can still potentially overestimate the lateral load capacity of such columns, which may attributed to the fact no reduction was applied to the bond stress values in the constitutive bond slip relationships adopted in the model, associated with yielding of the reinforcing bars in tension. As well, it is deduced the model predictions may be improved, upon incorporating buckling and low-cycle fatigue effects in the constitutive relationship adopted in the model for reinforcing steel.

The analytical model was found to capture the lateral load capacities of the splice-deficient specimens incorporating plain bars and 180-degree hooks; however, the degradation observed during the tests in the lateral load with increasing drift levels, due to local buckling of longitudinal reinforcing bars, was not represented in the model results. The model also fails to provide accurate predictions of the cyclic characteristics and pinching attributes of the response of such columns. The discrepancies in the analytical model predictions may be recovered upon implementing realistic hysteretic rules in the bar stress vs. end slip deformation constitutive model for 180-degree hooks (which is not available in the literature), as well as incorporating the modifications to consider local buckling in the constitutive stress–strain relationship of reinforcing bars.

9.4. Suggested Improvements and Recommendations for Future Studies

(i) For a more accurate prediction of the lateral load capacity of columns experiencing flexural yielding together with bond slip deformations in the lap splice region, reduction of bond stresses associated with yielding of reinforcing bars in tension should be considered in the formulation of the constitutive bond stress – slip relationships adopted in the model,

(ii) The model predictions of cyclic column response may be improved via adaptation of realistic hysteretic rules in the constitutive the bar stress vs. end slip deformation model used for 180-degree hooks, as well as considering local buckling effects in the constitutive stress–strain relationship of the reinforcing bars.

(iii) For response prediction of columns under more generalized loading conditions and modes of failure, the nonlinear shear response of the model needs to be improved, via implementation of a methodology that considers coupling of flexural and shear modes of deformation in a fiber-based model (e.g., Massone *et al*., 2006).

(iv) The present model formulation can be used for predicting nonlinear dynamic responses, via adaptation of an incremental dynamic analysis algorithm that involves numerical integration and the force-controlled Newton-Raphson iteration strategy described in Chapter 5.

Overall, the modeling approach proposed in this study is believed to be a significant improvement, towards realistic consideration of bond slip deformations and anchorage failures on the seismic response and performance of reinforced concrete structures. Implementation of the model into a computational platform (e.g., OpenSees, ref) will provide design engineers improved analytical capabilities to represent the seismic behavior of splice-deficient columns, which is essential for the application of performance-based evaluation methods for existing structures.

REFERENCES

Aboutaha, R.S., 1994, *Seismic Retrofit of Non-Ductile Reinforced Concrete Columns Using Rectangular Steel Jackets*, Ph.D. Thesis, The university of Texas, Austin.

Aboutaha, R., M.D. Engelhardt, J.O. Jirsa and M.E. Kreger, 1996, "Retrofit of Concrete Columns with Inadequate Lap Splices by the Use of Rectangular Steel Jackets", *Earthquake Spectra*, Vol. 12, No. 4, pp. 693-714.

Abrams D., 1913, *Test of Bond Between Concrete and Steel" University of Illinois Bulletin*, Bulletin No. 71.

American Concrete Institute, 2003, *Building Code Requirements for Reinforced Concrete: ACI 318*, Farmington Hills, MI, 1956, 1963, 1995, 1999 and 2002.

Ayoub, A., 2006, "Nonlinear Analysis of Reinforced Concrete Beam-Columns with Bond-Slip", *Journal of Engineering Mechanics*, ASCE, Vol. 132, No. 11, pp. 1177-1186.

Belarbi, H. and T.C.C. Hsu, 1994, "Constitutive Laws of Concrete in Tension and Reinforcing Bars Stiffened by Concrete", *ACI Structural Journal*, Vol. 91, No. 4, pp. 465-474, July-August.

Belmouden, Y. and P. Lestuzzi, 2006, "Analytical Model for Predicting Nonlinear Reversed Cyclic Behavior of Reinforced Concrete Structural Walls", *Engineering Structures*, Vol. 29, pp. 1263-1276.

Bousias, S.N., G. Verzeletti, M.N. Farids and E. Guitierrez, 1995, "Load-Path Effects in Column Biaxial Bending with Axial Force", *Journal for Enviromental Engineering*, Vol. 125, No. 5, pp. 596-605.

Brena, S.F. and B.M. Schlick, 2007, "Hysteretic Behavior of Bridge Columns with FRP-Jacketed Lap Splices Designed for Moderate Ductility Enhancement", *J. Compos. for Constr.*, Vol. 11, No. 6, pp. 565-574.

CEB-FIP, Model Code 1990, 1993, Final Draft, Bulletin d'information No. 213/214.

Chang, G.A. and J.B. Mander, 1994, *Seismic Energy Based Fatigue Damage Analysis of Bridge Columns: Part I—Evaluation of Seismic Capacity*, NCEER Technical Report No. NCEER-94-0006, State University of New York, Buffalo, N.Y.

Cho, J.Y. and J.A. Pincheira, 2006, "Inelastic Analysis of Reinforced Concrete Columns with Short Lap Splices Subjected to Reversed Cyclic Loads", *ACI Structural Journal*, Vol. 103, No. 2, pp. 280-290.

Cho, J.Y. and J.A. Pincheira, 2004, "Nonlinear modeling of RC columns with short lap splices", *13th World Conference on Earthquake Engineering*, Vancouver BC Canada, Paper No. 1506.

Clarke, M.J. and Hancock, G.J., 1990, "A Study of Incremental-Iterative Strategies for Non-Linear Analyses", *International Journal for Numerical Methods in Engineering*, Vol. 29, pp. 1365-1391.

Cosenza E., G. Manfredi and R. Realfonzo, 1997, "Behavior and Modelimg of Bond of FRP Rebars to Concrete", *Journal of Composites for Construction*, Vol. 1, No. 2, pp. 40-51.

Clarke, M.J. and G.J. Hancock, 1990, "A Study of Incremental-Iterative Strategies for Non-Linear Analyses", *International Journal for Numerical Methods in Engineering*, Vol. 29, pp. 1365-1391.

Elgawady, M., M. Endeshaw, D. McLean and R. Sack, 2010, "Retrofitting of Rectangular Columns with Deficient Lap Splices", *Journal of Composites for Construction*, ASCE, Vol. 14, No. 1, pp. 22-35.

Eligehausen, R., E.P. Popov and V.V. Bertero, 1983, *Local Bond Stess-Slip Relationships of Deformed Bars Under Generalized Excitations*, Report No. UCB/EERC, University of California, Berkeley.

Elmorsi, M., M.R. Kianush, and W.K. Tso, 1998, "Nonlinear Analysis of Cyclically Loaded Reinforced Concrete Structures", *ACI Structural Journal*, V. 95, No. 6, pp. 725-739, November-December.

Fabbrocino, G., G.M. Verderame and G. Manfredi, 2005, "Experimental Behavior of Anchored Smooth Rebars in Old Type Reinforced Concrete Buildings", *Engineering Structures*, Vol. 27, pp. 1575-1585.

Fabbrocino, G., G.M. Verderame and G. Manfredi, 2002, "Experimental Behavior of Straight and Hooked Smooth Bars in Existing R.C. Buildings", *12th European Conference on Earthquake Engineering*, Barbican Centre, London, UK.

Fabbrocino, G., G.M. Verderame, G. Manfredi and E. Cosenza, 2004, "Structural Models of Critical Regions in Old-Type R.C. Frames with Smooth Rebars", *Engineering Structures*, Vol. 26, pp. 2137-2148.

Feldman L.R., F.M. Bartlett, 2005, "Bond Strength Variability in Pullout Specimens with Plain Reinforcement", *ACI Structural Journal*, Vol. 102, No. 6, pp. 860-866.

Filippou, F.C., E.G. Popov and V.V. Bertero, 1983, *Effects of Bond Deterioration on Hysteretic Behavior of Reinforced Concrete Joints,* EERC Report No. UCB/EERC-83/19, Earthquake Engineering Research Center, University of California, Berkeley, Calif.

Fischinger, M., T. Vidic, J. Delih, P. Fajfar, H.Y. Zhang and F.B. Damjanic, 1990, "Validation of a Macroscopic Model for Cyclic Response Prediction of RC Walls", *Computer Aided Analysis and Design of Concrete Structures*, Vol. 2, pp. 1131-1142.

Giberson, M.F., 1969, "Two Nonlinear Beams with Definition of Ductility", *Journal of the Structural Division,* ASCE, Vol. 95, No. ST2, pp. 137-157.

Girard, C. and J. Bastien, 2002, "Finite-Element Bond-Slip Model for Concrete Columns under Cyclic Loads", *Journal of Structural Engineering*, ASCE, Vol. 128, No. 12, pp. 1502-1510.

Harajli, M.H. and F. Dagher, 2008, "Seismic Strengthening of Bond-Critical Regions in Rectangular Reinforced Concrete Columns Using Fiber-Reinforced Polymer Wraps", *ACI Structural Journal*, Vol. 105, No. 1, pp. 68-77.

Harajli, M.H., 2008, "Seismic Behavior of RC Columns with Bond-Critical Regions: Criteria for Bond Strengthening Using External FRP Jackets", *J. Compos. for Constr.*, Vol. 12, No. 1, pp. 69-79.

Harajli, M.H., B.S. Hamad and A.A. Rteil, 2002, "Effect of Confinement of Bond Strength between Steel Bars and Concrete", *ACI Structural Journal*, Vol. 99, No. 4, pp. 595-603.

Harajli, M.H.,2009, "Bond Stress-Slip Model for Steel Bars in Unconfined or Steel, FRC, or FRP Confined Concrete under Cyclic Loading", *Journal of Structural Engineering (ASCE)*.

Harajli, M.H., 1994, "Development/Splice Strength of Reinforcing Bars Embedded in Plain and Fiber Reinforced Concrete", *ACI Structural Journal*, Vol. 91, No. 5.

Harajli, M.H., B.S. Hamad and A.A. Rteil, 2004, "Effect of Confinement of Bond Strength between Steel Bars and Concrete", *ACI Structural Journal*, Vol. 101, No. 5, pp. 595-603.

Harajli, M.H. and M.E. Mabsout, 2002, "Evaluation of Bond Strength of Steel Reinforcing Bars in Plain and Fiber-Reinforced Concrete", *ACI Structural Journal*, Vol. 99, No. 4, pp. 509-517.

Harries, K.A, J.R. Ricles, S. Pessiki and R. Sause, 2006, "Seismic Retrofit of Lap Splices in Nonductile Square Columns Using Carbon Fiber-Reinforced Jackets", *ACI Structural Journal*, Vol. 103, No. 6.

Limkatanyu, S. and E. Spacone, 2003, "Effects of Reinforcement Slippage on the Non-Linear Response Under Cyclic Loadings of RC Frame Structures", *Earthquake Engineering and Structural Dynamics*, Vol. 32, pp. 2407-2424.

Low, S.S. and J.P. Moehle, 1987, *Experimental Study of Reinforced Concrete Columns Subjected to Multi-Axial Cyclic Loading*, EERC Report 87/14, Earthquake Engineering Research Center, University of Calirfornia, Berkeley

Lynn, A.C., J.P. Moehle, S.A. Mahin and W.T. Holmes, 1996, "Seismic Evaluation of Existing Reinforced Concrete Building Columns", *Earthquake Spectra*, Vol. 12, No. 4, pp. 715-739.

"Matlab", 2008, The Math-Works, Inc., Natick, Massachusetts.

Mander, J.B., M.J.N. Priestley and R. Park, 1988, "Theoretical Stress- Strain Model for Confined Concrete", *Journal of Structural Engineering*, ASCE, Vol. 114, No. 8, pp. 1804-1826.

Massone, L.M., K. Orakcal and J.W. Wallace, 2006, "Shear-Flexure Interaction for Structural Walls", *American Concrete Institute Special Publication SP 236-7*-Deformation Capacity and Shear Strength of Reinforced Concrete Members under Cyclic Loading, pp. 127-150.

Melek, M., 2006, *Experimental and Analytical Assessment of Columns with Short Lap Splices Subjected to Cyclic Loads*, Ph.D. Thesis, Department of Civil Engineering, University of California, Los Angeles.

Melek, M. and J.W. Wallace, 2004, "Cyclic Behavior of Columns with Short Lap Splices", *ACI Structural Journal*, V. 101, No. 6, pp. 802-811, November-December.

Menegotto, M. and E. Pinto, 1973, "Method of Analysis for Cyclically Loaded Reinforced Concrete Plane Frames Including Changes in Geometry and Non-Elastic Behavior of Elements Under Combined Normal Force and Bending", Proceedings, *IABSE Symposium on Resistance and Ultimate Deformability of Structures Acted on by Well-Defined Repeated Loads*, Lisbon, pp. 15-22.

OpenSees – Open System for Earthquake Engineering Simulation, Pacific Earthquake Engineering Research Center, University of California, Berkeley

Orakcal, K., J.W. Wallace and J.P. Conte, 2004,"Nonlinear Modeling and Analysis of Reinforced Concrete Structural Walls", *ACI Structural Journal*, Vol. 101, No. 3, pp. 688-698, May-June.

Orakcal, K., 2004, *Nonlinear Modeling and Analysis of Slender Reinforced Concrete Walls*, Ph.D thesis, University of California, Los Angeles, Calif.

Orakcal, K. and J.W. Wallace, 2006,"Flexural Modeling of Reinforced Concrete Walls-Experimental Verification", *ACI Structural Journal*, Vol. 103, No. 2, pp. 196-206, March-April.

Pacific Earthquake Engineering Research Center, *OpenSees—Open System for Earthquake Engineering Simulation*, University of California, Berkeley, Calif., http://opensees.berkeley.edu/OpenSees/developer.html, 2011.

Pincheira, J.A., F.S. Dotiwala, J.T. D'Souza, 1999, "Seismic Analysis of Older Reinforced Concrete Columns", *Earthquake Spectra*, Vol. 15, No. 2, pp. 245-272.

Powell, G. and J. Simons, 1981, "Improved Iteration Strategy for Nonlinear Structures", International Journal for Numerical Methods in Engineering, Vol. 17, pp. 1455-1467.

Prota, A., F.D. Cicco and E. Cosenza, 2009, "Cyclic Behavior of Smooth Steel Reinforcing Bars: Experimental Analysis and Modeling Issues", *Journal of Earthquake Engineering*, Vol. 13, pp. 500-519.

Rehm, G., 1969, *Evaluation Criteria for High-Bond Rebars*, Festschrift Rusch.

Riks, E., 1979, "An Incremental Approach to the Solution of Snapping and Buckling Problems", *International Journal of Solids and Structures*, Vol. 15, pp. 529-551.

Reyes, O., 1999, *Modeling of Reinforced Concrete Columns with Short Lap Splices Subjected to Earthquakes*, M.S. Thesis, University of Wisconsin, Madison, Wis.

Reyes, O. and J.A. Pincheira, 1999, "R/C Columns with Lap Splices Subjected to Earthquake", *ASCE Structures Congress*, New Orleans, La., pp. 369-372.

Seckin, M., 1981, *Hysteretic Behavior of Cast-in-Place Exterior-Beam- Column-Slab Sub-assemblies,"* P.hD.Thesis, University of Toronto, Toronto, Ontario, Canada.

Sezen, H., 2002, *Seismic Response and Modeling of Reinforced Concrete Building Columns*, Ph.D. Thesis, Department of Civil and Environmental Engineering, University of California, Berkeley.

Spacone E. and S. Limkatanyu, 2000, "Responses of Reinforced Concrete Members Including Bond-Slip Effects", *ACI Structural Journal*, Vol. 97, No. 6, November-December.

Tassios T.P.,1979, *Properties of Bond Between Concrete and Steel Under Load Cycles Idealizing Seismic Actions*, Comite Euro-International du Beton, Bulletin No. 131, Paris.

Tsai, W.T., 1988, "Uniaxial Compressional Stress-Strain Relation of Concrete", *Journal of Structural Ebgineering*, ASCE, Vol. 114, No. 9, pp. 2133-2136.

Verderame, G.M., G. Fabbrocino and G. Manfredi, 2008 a., "Seismic Response of R.C. Columns with Smooth Reinforcement, Part I: Monotonic Tests", *Engineering Structures*, Vol. 30, pp. 2277-2288

Verderame, G.M., G. Fabbrocino and G. Manfredi, 2008 b., "Seismic Response of R.C. Columns with Smooth Reinforcement, Part II: Cyclic Tests", *Engineering Structures*, Vol. 30, pp. 2289-2300

Verderame G.M., P. Ricci, G.D. Carlo and G. Manfredi, 2009 a., "Cyclic Bond Behavior of Plain Bars. Part I: Experimental Investigation", *Construction and Building Materials*, Vol-23, pp. 3499-3511.

Verderame G.M., G.D. Carlo, P. Ricci and G. Fabbrocino, 2009 b., "Cyclic Bond Behavior of Plain Bars. Part II: Analytical Investigation", *Construction and Building Materials*, Vol-23, pp. 3512-3522.

Vulcano, A., V.V. Bertero and V. Colotti, 1988, "Analytical Modeling of RC Structural Walls. Proceedings", *9th World Conference on Earthquake Engineering*, Tokyo-Kyoto, Japan, pp 41-46.

Wempner, G.A., 1971, "Discrete Approximations Related to Nonlinear Theories of Solids", *International Journal of Solids and Structures*, Vol. 7, pp. 1581-1599.

Xiao, Y. and R. Ma, 1997, "Seismic Retrofit of RC Circular Columns Using Prefabricated Composite Jacketing", *J. Compos. for Constr.*, Vol. 123, No. 10, pp. 1357-1364.

Yildiz, H.A., 2006, *Flexural Strengthening of Reinforced Columns having Lap Splice Problem with Longitudinal FRP Composites*, MS thesis, Kocaeli University, Turkey.

Yankelevsky, D.Z. and H.W. Reinhardy, 1987, "Response of Plain Concrete to Cyclic Tension", *ACI Materials Journal*, Vol. 84, No. 5, pp. 365-373.

Yilmaz H., 2009, *The Effect of Lap Splice Length of Longitudinal bars on the Performance of Low Strength Reinforced Concrete Members Under Lateral Loads*, MS Thesis, Istanbul Technical University, Turkey.